THE GENERATION, ENERGETICS AND PROPAGATION OF INTERNAL TIDES IN THE WESTERN NORTH ATLANTIC OCEAN

by

ROSS MACRAE HENDRY

B.Math., University of Waterloo
(1970)

SUBMITTED IN PARTIAL FULFILLMENT OF THE
REQUIREMENTS FOR THE DEGREE OF
DOCTOR OF PHILOSOPHY

at the

MASSACHUSETTS INSTITUTE OF TECHNOLOGY

and the

WOODS HOLE OCEANOGRAPHIC INSTITUTION

April, 1975

Signature of Author .....
Joint program in Oceanography, Massachusetts Institute of Technology - Woods Hole Oceanographic Institution, and Department of Earth and Planetary Sciences, Massachusetts Institute of Technology, April 1975

Certified by. .....
Thesis Supervisor

Accepted by .....
Chairman, Joint Oceanography Committee in the Earth Sciences, Massachusetts Institute of Technology - Woods Hole Oceanographic Institution

Lindgren
WITHDRAWN
SEP 24 1975
FROM
MIT LIBRARIES

THE GENERATION, ENERGETICS AND PROPAGATION OF INTERNAL TIDES IN THE WESTERN NORTH ATLANTIC OCEAN

by

Ross MacRae Hendry

Submitted to the Department of Earth and Planetary Sciences on April 11, 1975 in partial fulfillment of the requirements for the degree of Doctor of Philosophy.

ABSTRACT

This thesis reports on an investigation into the structure, energetics and propagation of tidal frequency internal waves. Data from Site D, near the New England continental slope, Muir Seamount northeast of Bermuda, and the Mid-Ocean Dynamics Experiment in the deep Sargasso Sea were used.

Site D, in the near-field of a near-critical semidiurnal generation region, shows variable tidal currents and a marked surface intensification of M_2 energy at the southern Site, related to the beam-like nature of the internal tide. The M_2 tide dominates the semidiurnal band, with about 3 times more energy than at adjacent frequencies at 1/15 cpd separation. There is a significant phase locking between the M_2 baroclinic currents and the equilibrium tide, and evidence for southward propagation of internal wave energy, suggesting generation at the slope to the north. The M_2 baroclinic energy density is about 40% as great as the total barotropic energy density, but the internal tides have more horizontal kinetic energy. A seaward energy flux of $.6 \times 10^6$ erg/s cm in the first three baroclinic M_2 modes is much less than the $.2 \times 10^{10}$ erg/s cm shoreward energy flux in the surface tide. Difficulties in interpreting the measurements are ascribed to the near-singular generation case.

The MODE-1 semidiurnal internal tides are also dominated by the M_2 frequency, with a 3-fold energy increase over adjacent frequencies at 1/15 cpd separation. MODE-1 is far from any major source of internal tides, but the measurements are much less variable than those from Site D. The extensive temperature measurements defining the MODE-1 M_2 internal tide are significantly coherent (phase locked) with the equilibrium tide, with about 80% of the coherent energy deriving from the first baroclinic mode, typical thermocline displacements being 3 m. A horizontal wavenumber spectrum estimate for the first mode M_2 displacement fluctuations gives a peak at 160 km wavelength, in excellent agreement with the theoretical dispersion

relation. The coherent first mode propagates on a bearing of 125°T, with a horizontal energy flux of .3 x 10^8 erg/s cm. Use of the weaker S_2 internal tide and the dispersive nature of oceanic internal waves yields an estimate of 700 km to a common semidiurnal source region. The inferred range and bearing are consistent with generation at the Blake Escarpment and the continental slope to the northwest of the experiment. In one special case current and temperature measurements are combined in a local demonstration of the first mode M_2 propagation, and the less extensive current data gives estimates of the barotropic tidal currents.

Mooring motion, measured by pressure recorders on the mooring lines, accounts for about 15% of the semidiurnal temperature variance, but it is incoherent with the equilibrium tide.

Diurnal tides were examined at all three locations. At the MODE-1 site - near the critical latitude for diurnal period internal waves - the current and temperature fields are dominated by high mode, incoherent, inertial-character motions which mask the tidal events. About 25% of the diurnal band temperature variance is related to mooring motion. Muir Seamount provides a clear example of diurnal period internal tides trapped near their source region north of the critical latitude. A simple analytical model is developed for the diurnal period flow adjustment in a seamount geometry. Site D shows some evidence for diurnal period internal tides, but most of the energy in the diurnal current is not simply related to the local forcing. Diurnal barotropic currents measured at Site D are combined with currents on the New England shelf, showing that the diurnal tidal wave behaves as a Kelvin-Stokes mode trapped to the slope, propagating along the depth contours to the west.

Some aspects of simple generation models are considered. The slope north of Site D is not at all well described as an abrupt step for the M_2 generation problem, but a more realistic model of Baines (1974) predicts the coherent fields observed. But the relatively small energy conversion from the surface tide to internal modes suggests that the globally near-critical slope north of Site D is a poor generator of internal tides into the deep sea, although the local energy density is high. The step shelf generation model is well suited for the steep Blake Escarpment, and predicts a seaward energy flux of .4 x 10^8 erg/s cm in the first mode, comparable to the measurements at MODE-1. This confirms theoretical expectations that the first baroclinic mode is not significantly damped by turbulent diffusion after propagating through the 700 km of ocean between the generation region and the MODE-1 deep ocean site.

Thesis supervisor: Carl Wunsch
Title: Professor of Oceanography

to my father

TABLE OF CONTENTS

ACKNOWLEGEMENTS Page 10

LIST OF FIGURES 11

LIST OF TABLES 17

0.1 Foreword 23

SECTION 1: SEMIDIURNAL TIDES AT SITE D

1.1 Introduction 29

1.2 Oceanic internal waves 34

Field equations 34

Characteristic description of the fields 38

Normal mode description of the fields 40

Energetics of the fields 46

Polarization of horizontal currents 50

WKBJ internal waves 51

1.3 Observational base 54

1.4 Analysis 59

Admittance approach 60

Analysis 61

1.5 Semidiurnal energy levels Page 64

Conclusions based on the distribution of power 77

1.6 Generation of internal tides near Site D 79

Current observations 83

Expansion in normal modes 93

Energetics of the internal tide 105

1.7 Site D barotropic tide 108

1.8 Sources of noise and variability 115

1.9 Conclusions 120

SECTION 2: SEMIDIURNAL TIDES IN MODE-1

2.1 Introduction 123

2.2 Setting, data and analysis 130

2.3 Semidiurnal energy levels 142

Temperature 142

Currents 149

Consistence with internal wave ideas 156

2.4	Deterministic fields	Page 161
	Temperature	161
	Generation sources	175
	S_2 internal tides	177
	Currents	187
	Further evidence for a deterministic internal tide	195
2.5	Barotropic currents	199
	Baroclinic pressure signals	204
	Energetics of the barotropic fields	207
2.6	Variability in the semidiurnal fields	210
	Mooring motion	212
	Energy in mooring motion	222
2.7	Conclusions	225

SECTION 3: DIURNAL TIDES

3.1	Diurnal period internal tides: Introduction	229
3.2	Internal tides at the critical latitude	232
	Observations from MODE-1	234
	Tidal admittances	245
	Horizontal variation in the fields	246

3.3	Muir Seamount experiment	Page 250
	Observations	251
	Time dependent flow adjustment	256
	Density field	264
3.4	Diurnal tides at Site D	271
	Observations	272
	Meteorological effects	279
	Tidal energy in the diurnal band	281
	Barotropic diurnal tide at Site D	287
	Step shelf Kelvin-Stokes normal mode	290
	Conclusions	297
3.5	Summary	299

SECTION 4: OVERVIEW

4.1	Overview of internal tide generation	301
	Step shelf generation models	302
	Baines' characteristic model	311
	Comparison with observations: Site D	313
	Comparison with observations: MODE-1	318

4.2 General remarks Page 322

Statistics 322

Speculations about the dissipation of the internal tide 322

BIBLIOGRAPHY 324

APPENDICES

A.1 Fourier transforming and tapering 330

Finite discrete Fourier transform 330

Tapering 332

A.2 Signal processing 340

A.3 Hydrographic data 344

VITA 347

ACKNOWLEGEMENTS

The author wishes to express his sincere appreciation for the guidance and insight provided by his Supervisor, Professor Carl Wunsch of M.I.T. The apparently unbounded patience of Professor Wunsch in communicating his insights is not the least of the qualities which make working with him a distinct pleasure.

This study was based on field measurements extracted from a sometimes hostile environment, and was possible only as the end result of efforts by many other people. It is impossible to completely acknowlege, or even know, the extent to which we have been dependent on the skills of these other workers. Special thanks must go to the Buoy Group, Woods Hole Oceanographic Institution, as without their efforts at Site D, in the Mid-Ocean Dynamics Experiment, and in a special undertaking at Muir Seamount, this study would simply not have been possible.

Particular thanks go to Mr.G.Volkmann for the use of unpublished average Site D hydrography; to Messers.H.Bryden and R.C.Millard,Jr. for the use of average MODE-1 hydrography from CTD casts in the area; and, to Mr.J.Richman for the use of his computer routine for calculating internal wave modes. Dr.N.Hogg was helpful in the Muir Seamount study, and valuable conversations with him are acknowleged. Dr.R.Beardsley of M.I.T. allowed the use of his New England shelf current measurements, and Mr.B.Zetler and Dr.W.Munk made the recent deep sea pressure observations by them and their co-workers in the MODE-1 experiment freely available.

Help in the extensive computing involved in the study was generously given by personel at both M.I.T. and Woods Hole. Mr.J.Maltais and the whole data processing staff in the Buoy Group at Woods Hole deserve our thanks, as does Ms.B.Grant at M.I.T. Ms.D.Frank was invaluable for her efficient typing.

The support of the Office of Naval Research under contracts N00014-67-A-0204-0048 and N00014-75-C-0291-0048 is gratefully acknowleged.

FIGURES

Figure		Page
1.2.1	Topography and characteristic geometry for M_2 frequency internal waves near Site D, after Fofonoff (1966).	41
1.3.1	Bathymetry of the New England continental shelf, slope and rise, with the Site D study areas indicated. Depth contours are in meters.	55
1.5.1a	Mean squared amplitude of u (east) and v (north) current components in the S_2 band from the south Site, as a function of depth.	65
1.5.1b	Mean squared amplitude of u (east) and v (north) current components in the M_2 band from the south Site, as a function of depth.	66
1.5.1c	Mean squared amplitude of u (east) and v (north) current components in the N_2 band from the south Site, as a function of depth.	67
1.5.2	Average N(z) profile for Site D, from hydrographic data over all seasons in 1965-1972.	71
1.6.1	Near-surface characteristic curves for M_2 frequency internal waves and the average Site D stratification.	81
1.7.1	M_2 cotidal chart for the New England shelf, adapted from Hicks, Goodheart and Isely (1965). The depth contours are shown as dashed lines, with depths in meters. The solid curves are labelled with the interval in lunar hours between the moon's Greenwich transit and high tide. The circles indicate the positions of the earlier measurements described in the text, and the triangle marks the site of the recent bottom pressure measurements also discussed.	110

Figure		Page
2.2.1	Bathymetry of the western North Atlantic Ocean after Heezen and Tharp (1968). The MODE-1 site and Site D are indicated.	131
2.2.2	Local bathymetry (contours in decimeters) and mooring positions for the MODE-1 experiment.	132
2.3.1a	Squared amplitude of S_2 band temperature fluctuations, averaged at depth levels over the entire array.	143
2.3.1b	Squared amplitude of M_2 band temperature fluctuations, averaged at depth levels over the entire array.	144
2.3.1c	Squared amplitude of N_2 band temperature fluctuations, averaged at depth levels over the entire array.	145
2.3.2	Average MODE-1 profile of $N^{-1}(z)(d\theta/dz)^2$ to compare with profiles of temperature variance.	148
2.3.3a	Squared amplitude of S_2 band horizontal current components u (east) and v (north) averaged at depth levels across the entire array.	150
2.3.3b	Squared amplitude of M_2 band horizontal current components u (east) and v (north) averaged at depth levels across the entire array.	151
2.3.3c	Squared amplitude of N_2 band horizontal current components u (east) and v (north) averaged at depth levels across the entire array.	152
2.3.4	Average MODE-1 N(z) profile to compare with profiles of horizontal current variance.	155

Figure		Page
2.4.1	(left) Solid lines join estimates of the coherent (phase locked) M_2 isotherm displacement at Mooring 1 at different depths. The dashed curve is the first baroclinic mode shape, drawn with arbitrary amplitude. (right) The admittance phase of M_2 isotherm displacement at Mooring 1.	164
2.4.2	Theoretical beampattern for 14 moorings in the MODE-1 array. Contour interval -3dB.	170
2.4.3a	Conventional wavenumber spectrum estimate for M_2 first baroclinic mode isotherm displacement at 14 of the MODE-1 moorings. The contour interval is -3 decibels, normalized by the maximum. The peak in the southeast quadrant represents a wave with 163 km wavelength propagating in the direction 125°T.	172
2.4.3b	High resolution wavenumber spectrum of M_2 first baroclinic mode isotherm displacement at 14 of the MODE-1 moorings.	173
2.4.4a	Conventional wavenumber spectrum estimate for S_2 first baroclinic mode isotherm displacement at 15 of the MODE-1 moorings. The weak peak in the far north-west quadrant is a possible alias of the -3 dB sidelobe near the origin in the north-east quadrant.	178
2.4.4b	High resolution wavenumber spectrum estimate for S_2 first baroclinic mode isotherm displacement at 10 of the MODE-1 moorings which showed stable first mode fits.	179
2.4.5	Histogram of the differences in admittance phase of the M_2 and S_2 first baroclinic mode fits to isotherm displacement at 14 of the MODE-1 moorings. The error bars are one standard deviation from the mean.	183

Figure		Page
2.4.6	Horizontal current ellipse for the first baroclinic mode at Mooring 1 for the M_2 band in one 15 day period. The current amplitudes refer to the normalization described in the text. Time of maximum first mode isotherm displacement for the same period of time is indicated by a solid circle near the northern major axis. Together the current and temperature fluctuations define a wave which propagates towards 160°T.	194
2.5.1	M_2 barotropic current ellipse from an overall average of current measurements. High tide occurs at 000°G, defining the direction of horizontal energy flux towards 317°T.	206
2.6.1	Mooring motion effects on coherence of temperature fluctuations and the equilibrium tide in the M_2 band. The coherence estimates are plotted against the ratio of mooring motion related temperature signal inferred from pressure measurements, to measured average temperature signal. A high ratio means that mooring motion is dominating the temperature fluctuations. (upper) Measurements above 1200 m inclusive. (lower) Measurements below 1200 m. Some individual records are marked with mooring number and depth in meters.	214
3.2.1a	Squared amplitude of temperature fluctuations in the O_1 band as a function of depth, averaged across the MODE-1 array.	236
3.2.1b	Squared amplitude of temperature fluctuations in the K_1 band as a function of depth, averaged across the MODE-1 array.	237

Figure		Page
3.2.2a	Squared amplitude of u (east) and v (north) current components in the O_1 band as a function of depth, averaged across the MODE-1 array.	239
3.2.2b	Squared amplitude of u (east) and v (north) current components in the K_1 band as a function of depth, averaged across the MODE-1 array.	240
3.3.1	Muir Seamount mooring geometry. (upper) Horizontal plan view showing 2000, 3000 and 4000 m contours and the mooring site indicated as an open circle. (lower) Vertical sections through the seamount, showing the placement of the current meters.	252
3.3.2	(upper) Diurnal band equilibrium tide periodogram, showing the dominant O_1 and K_1 constituents. (middle) Horizontal current variance at upper and lower depth levels in the diurnal band. (lower) Temperature variance at upper and lower depth levels in the diurnal band.	253
3.4.1a	Squared amplitude of u (east) and v (north) current components as a function of depth for the O_1 band at Site D, averaged over all measurements.	274
3.4.1b	Squared amplitude of u (east) and v (north) current components as a function of depth for the K_1 band at Site D, averaged over all measurements.	275
4.1.1	Dimensionless energy flux into the deep sea for a step shelf generation model, as a function of the shelf to deep ocean depth aspect ratio δ.	307

Figure		Page
4.1.2	Effective mode number of the deep ocean internal waves generated in the anti-resonant step shelf model, as a function of the shelf to deep ocean depth aspect ratio δ. The curve is symmetrical about $\delta = 1/2$.	309
A.1.3	Amplitude spectrum of a 15 day record consisting of a unit M_2 sine wave plus a 40-unit ramp, before tapering (diamonds) and after tapering (circles), showing the filtering effect of the tapering.	338

TABLES

Table		Page
1.3.1	Distribution by depth and location of the current measurements used in the Site D study.	58
1.5.1a	Mean squared amplitude of u (east), v (north), + (anticlockwise rotating), and - (clockwise rotating) current components from the south and north sites, for the S_2 band, as a function of depth. Also the ratios of clockwise to anticlockwise power.	68
1.5.1b	Mean squared amplitude of u (east), v (north), + (anticlockwise rotating), and - (clockwise rotating) current components from the south and north sites, for the M_2 band, as a function of depth. Also the ratios of clockwise to anticlockwise power.	69
1.5.1c	Mean squared amplitude of u (east), v (north), + (anticlockwise rotating), and - (clockwise rotating) current components from the south and north sites, for the N_2 band, as a function of depth. Also the ratios of clockwise to anticlockwise power.	70
1.5.2	Depth integrals of horizontal kinetic energy density for the three semidiurnal bands, at the south and north sites.	73
1.5.3	Ratios of power in horizontal currents in the three semidiurnal bands as a function of depth, showing the dominance of the M_2 band. The 95% confidence intervals for a ratio of unity are given.	75
1.6.1	Amplitudes of coherence between semidiurnal current components and the equilibrium tide, as a function of depth, with the number of degrees of freedom in the estimates and the bias and 95% confidence limits for zero true coherence.	85
1.6.2a	Coherent current amplitudes and phases for the S_2 band as a function of depth for the two areas of Site D.	88

Table		Page
2.2.2a	Temperature data availability. The number of 15 day record lengths at each mooring, by depth, in MODE-1.	136
2.2.2b	Current data availability. The number of 15 day record lengths at each mooring, by depth, in MODE-1.	137
2.2.3	Modal parameters for the first five baroclinic M_2 frequency modes in the MODE-1 area.	140
2.3.1	Numerical values for squared amplitude of temperature fluctuations for the semidiurnal bands in the MODE-1 experiment, averaged at depth levels over the entire array.	146
2.3.2	Numerical values for squared amplitude of u (east) and v (north) current components in the semidiurnal bands in the MODE-1 experiment, averaged at depth levels over the entire array.	153
2.3.3	Average horizontal kinetic energy density, potential energy density, and the ratio of the two for the semidiurnal bands in the MODE-1 experiment. The averages are at depth levels over the entire array. Estimates of the depth integrated energy density in each band are also given.	157
2.4.1	Mooring 1 M_2 frequency average isotherm displacement and admittance phase as a function of depth. Coherences between temperature fluctuations and the equilibrium tide at each depth are also given. With the 7 degrees of freedom in the estimates, the 95% confidence level for zero true coherence is .63. Depths marked * are T-P recorders, unmarked depths are temperature measurements from current meters.	166

Table		Page
1.6.2b	Coherent current amplitudes and phases for the M_2 band as a function of depth for the two areas of Site D.	89
1.6.2c	Coherent current amplitudes and phases for the N_2 band as a function of depth for the two areas of Site D.	90
1.6.3	Modal parameters for M_2 internal waves at Site D. The first five baroclinic modes for the average density profile in all seasons from 1965-1972 are characterized, and the calculation is repeated for the average density during 1971-1972 alone.	97
1.6.4	Mode shapes for currents used in the fits of Site D tidal currents. The weight factors were used in the fits as described in Section 1.2.	99
1.6.5	Modal fits of coherent M_2 currents at the south and north sites, using the two separate modal calculations. The percentage of signal power fit by each mode is given.	101
1.6.6	Inferred wavelengths of the first three baroclinic modes in the M_2 current fits. The first value given is appropriate for southward propagation and the second for northward propagation. Theoretically calculated wavelengths for the modes are given.	104
1.7.1	Barotropic M_2 tidal currents at Site D, by modal decomposition of average currents. The north estimate is suspect as discussed in the text, but the phases of the two fits agree remarkably. Estimates from Magaard and McKee (1973) are included, and agree well with the southern fit.	112
2.2.1	Mooring locations for the MODE-1 array, giving latitude and longitude of the moorings and their position relative to the central Mooring 1.	133

Table		Page
2.4.2	Amplitude of the first baroclinic mode content of M_2 isotherm depth fluctuations at each mooring. The percentage of signal variance accounted for by the first mode in the least-squares fit, and the percentage of the total energy which is represented by the fit are also given for each mooring.	168
2.4.3	Phase differences between the M_2 and S_2 first baroclinic mode fits at the moorings in the MODE-1 experiment. The age of the first baroclinic mode semidiurnal tide.	182
2.4.4	(upper) Currents in the M_2 band for a single 15 day period at the central Mooring 1. (lower) Modal decomposition of the M_2 current profile, using a barotropic mode and the first two baroclinic modes. The percentage of fitted energy in each mode for each component of current is given.	192
2.4.5	Historical evidence from MODE-0 for a phase-locked M_2 internal tide. M_2 temperature fluctuations at comparable depths from Mooring 455 (28°00.2'N,69°37.6'W), Mooring 421 (28°00.2'N,69°41.5'W), and MODE-1 Mooring 1 (27°59.8'N,69°39.0'W) and the admittance phases with respect to the equilibrium tide. Coherence estimates for each measurement and the number of 15 day pieces in the averages are given.	197
2.5.1	(upper) Barotropic current estimates for the major semidiurnal frequencies, and coherences for the overall current averages. (center) Barotropic M_2 currents from modal fits at Moorings 1 and 7. (lower) Barotropic M_2 currents inferred from sea level gradients across the MODE-1 array (ZMMBD, 1974)	201

Table		Page
2.5.2	(upper) Admittances for major semidiurnal barotropic current components, and for the surface tides from Wunsch (1972a) (lower) Normalized admittances of current components to compare with behavior of surface tide.	202
2.5.3	M_2 barotropic current parameters derived from overall current average, combined with estimates of the M_2 surface tide to give the total energy in the tide, and the energy flux in the tidal wave.	208
2.6.1	Modal fits of M_2 isotherm displacements for consecutive 15 day periods at Mooring 1, showing the variability of the fits. The overall average M_2 isotherm fluctuations modal decomposition is also given.	211
2.6.2a	Mooring motion at M_2 frequency at Mooring 6 (see text).	217
2.6.2b	Mooring motion at M_2 frequency at Mooring 3 (see text).	218
2.6.3	Energetics of mooring motion related temperature fluctuations in the semidiurnal and diurnal-inertial frequency bands. The diurnal bands are more seriously influenced by the mooring motion.	223
3.2.1	Airy scales for the first five baroclinic modes at 30°N latitude for the average MODE-1 stratification.	242
3.2.2	Horizontal kinetic energy density and potential energy in the O_1 and K_1 diurnal bands as a function of depth, averaged across the MODE-1 array. Ratios of kinetic to potential energy show relatively less vertical motion at O_1-inertial frequency than at the adjacent K_1 frequency.	244

Table		Page
3.4.1	Eigenvalue k and trapping scale k^{-1} for the barotropic mode and the first five baroclinic modes at Site D for 24 hour period, using the 1965-1972 average density at the Site.	273
3.4.2	Average squared amplitude of u (east), v (north), + (anticlockwise), and - (clockwise) current components at Site D for the O_1 (upper) and K_1 (lower) bands.	277
3.4.3	Coherence amplitude and phase for the diurnal band currents and the equilibrium tide. The averages are by depth level over the whole Site. 95% confidence limits for zero true coherence are given for each case.	282
3.4.4	Coherence amplitude and phase for the O_1 (upper) and K_1 (lower) band currents and the equilibrium tide. These averages were over only those cases where the diurnal current ellipse in a 15 day record showed an anticlockwise rotation. 95% confidence limits for zero true coherence are given for each case.	284
3.4.5	Squared amplitude of u (east) and v (north) current components in the diurnal bands as a function of depth. These averages were made over only the anticlockwise rotating current ellipses.	286
3.4.6	Barotropic diurnal tides in the Site D - New England shelf setting. (upper) Current amplitude and phase for the O_1 and K_1 constituents at Site D and on the shelf. (lower) Surface tide O_1 and K_1 constituents at Bermuda and on the New England shelf.	289
A.3.1	Average Site D hydrography 1965-1972.	344
A.3.2	Average Site D hydrography 1971-1972.	345
A.3.3	Average hydrography of the MODE-1 site.	346

0.1 Foreword

Internal gravity waves are an important source of current, temperature and salinity variance in the oceans. Spectra of horizontal kinetic energy show that the internal wave frequency band is relatively energetic (Fofonoff and Webster, 1971), while vertical motions in this band contribute significantly to the oceanic vertical velocity field (Voorhis, 1968). Internal tides are internal waves with astronomical tidal periodicity, which owe their existence to the astronomical forcing of the sun and moon. Wunsch (1975a) has reviewed the present state of knowledge of oceanic internal tides. The tidal forcing excites oceanic internal waves indirectly, by means of the barotropic tidal currents which would exist even in an unstratified ocean. In the North Atlantic, semidiurnal internal tides are generally most energetic, producing peaks in the frequency spectra of current or temperature variance which stand out from the background continuum. Diurnal period motions are quite energetic in some areas, but in general the diurnal tides are weaker in the North Atlantic Ocean than the semidiurnal species. The purpose of the present work is to investigate in detail the properties of oceanic internal tides as revealed in actual field measurements, to rationalize the observations in

terms of the physics which governs internal waves, and to consider the results in the light of theoretical modelling studies of internal tide generation.

Aside from their high energy levels, internal tides are of special interest because they are the result of a known forcing. Internal waves are driven by winds (Pollard and Millard, 1970), by scattering of barotropic currents from topography (Cox and Sandstrom, 1962), and by non-linear interactions with larger scale flows (Olbers, 1974), for example. Internal tides are generated when barotropic tidal currents in the stratified ocean interact with sloping topography, whether associated with random bottom roughness or more organized continental slopes and mid-ocean ridges. While the surface wind stress or large scale current may show great variability in time at a particular location, the barotropic tides are quite constant and predictable. Thus internal tides have a possibly quite deterministic forcing as opposed to the random forcing which is characteristic of wind-generated internal waves or non-linear transfers of internal wave energy from one frequency to another. Models of oceanic internal waves as completely random fields (Garrett and Munk, 1972) have met with some success in providing a framework for observations: such models contain no mention of either generation or dissipation mechanisms, and while

they do provide a valuable synthesis of the kinematics of the measured fields, they have been characterized as ruling out "almost all the physics" (Wunsch, 1975b). Internal tides are closer to a definite generation process than non-tidal internal waves, making an exploration of the physics of their generation more feasible.

Internal waves interact with other scales of oceanic variability and form part of the ocean as an integral system, as well as contributing to the general level of oceanic motion. Breaking internal waves can generate microstructure and mix heat and momentum (Woods, 1968). This represents a link to the ultimate scales where viscous dissipation dominates and energy is irreversibly removed from the ocean. Müller (1974) has suggested that internal waves interacting with a spatially varying mean flow can cause the diffusion of mean properties which is generally parametrized by an eddy diffusivity coefficient for the mean flow. This relates internal waves and the largest scales of the general circulation. Because of their large energy levels, internal tides seem a promising source of energy for other frequencies of internal waves. Olbers, however, concluded that for a Garrett and Münk internal wave spectrum and a WKBJ approach, the non-linear transfer rates at tidal frequencies are too small to provide a

principal driving mechanism for most of the internal wave frequency band. He does suggest that internal tides could be quite significant in the energy balance for very high frequency internal waves where other non-linear transfer processes are small.

As part of the tidal process, ranging from astronomical considerations to tidal motions in the atmosphere, oceans and solid earth, internal tides have other possible consequences. Dissipation associated with the tides allows the exchange of angular momentum between the earth and moon (see Munk, 1968, for example). At the present time, the moon is being accelerated in its orbit about the earth and receding at a rate of a few centimeters per year, while the earth's rotational period is increasing at a rate of about three-hundredths of a second per year. It is thought that the majority of the dissipation must occur in the earth's oceans (Wunsch, 1975a). Although recent work, including the present study, indicates that the tidal input to internal waves is not of major significance in the overall dissipation problem, the tidal period currents are significantly affected by internal tides, and the generation process is part of the boundary condition on the barotropic tide.

Finally, as part of the generation process on

continental slopes, recent experimental work (Cacchione and Wunsch, 1974) has shown that intense mixing may occur on sloping boundaries in a stratified fluid as a result of instabilities in internal wave motion there. As the continental slopes are important areas for commercial fisheries, for one example, the mixing of nutrients in these areas is of great practical importance.

Observations in the oceans are limited by practical considerations. Internal waves are variable phenomena, and a statistical approach is needed to obtain a true picture of the internal tide. The present study is based mainly on data from two distinct but complementary areas, and the large amount of data available allows a statistical treatment. Site D, instrumented by the Woods Hole Oceanographic Institution for many years, is near the New England continental slope in the near-field of a demonstrated generation region. Its complement in this study is the Mid-Ocean Dynamics Experiment (MODE-1) carried out over the abyssal plain in the Sargasso Sea. An intense effort over a limited time has produced an extremely large amount of data from this source, affording a unique opportunity to examine the internal tide in the deep ocean.

The diurnal period tides have a varying physics

between the MODE-1 Site and Site D. Equatorward of a critical latitude near 30°, diurnal period internal waves can propagate freely just as semidiurnal period internal waves can do over most of the ocean. Poleward of the critical latitude for a given frequency, no free waves are possible but wave motions trapped to topographic features can exist. MODE-1 was nearly at the critical latitude for diurnal period internal tides, and the physics of inertial oscillations is relevant there. A further experiment near Muir Seamount north of the diurnal turning latitude gives a particular example of topographically trapped internal tides. Site D, still further to the north, can also be examined for diurnal internal tides in the constraining slope geometry.

Section 1 following deals with the semidiurnal frequency internal tides at Site D, and with a more detailed description of the generation problem. Section 2 is concerned with semidiurnal tides in the MODE-1 setting, and Section 3 contains all the discussion of diurnal period motions. Finally in Section 4 the individual conclusions of the work are subjected to an overview, in an attempt to draw together the different geographical areas studied. This includes some theoretical considerations of the generation process, and an attempt to relate the observations to the theories. The concluding chapter also contains general observations and speculations, and thoughts about further possible progress in the study of oceanic internal tides.

SEMIDIURNAL TIDES AT SITE D

1.1 Introduction

Site 'D' is the designation of an area centered about 39°10'N, 70°10'W which has been the subject of numerous oceanographic investigations. The Woods Hole Oceanographic Institution has had an extensive measurement program there for the past decade, consisting mainly of moored buoys equipped with current meters which were deployed as routine site moorings or for specific experiments. Site D is about 60 km south of the steep continental slope off Nantucket Island, being on the much gentler continental rise in about 2600 m of water.

Internal tides have been a subject of interest there since the beginning of the program, and Fofonoff (unpublished report, 1966) noted intense horizontal currents of semi-diurnal tidal periodicity in the near surface there. He attributed these to internal waves in the ocean, and noted that the continental slope to the north was a likely source for such waves. This early work established the main characteristics of the process, that it consisted of energetic and depth dependent fluctuations which in this case were most intense near the surface. Gerges (1966) examined the problem of internal waves of tidal period, and looked at several records of horizontal currents from Site D. He concluded that there were cases where the fluctuations had the period of the astronomical M_2 tide, and although his

data included no measurements from below 500 m at Site D, he also concluded that the currents were intensified near the surface as a general rule. Finally he noted what other investigators have had impressed on them, that unlike the predictable rise and fall of the sea surface, the tidal current field in the ocean had tremendous variability. Gerges suggested that low frequency oceanic variability in current and thermal structure could influence the tidal period fluctuations.

It has long been suggested (Zeilon, 1911) that varying topography can couple the barotropic and baroclinic modes of oscillation in a stratified fluid, and the slope north of Site D was a possible generation region for the internal tidal waves observed at the site. The barotropic tidal current would provide the energy source for the internal waves. Wunsch and Hendry (1972) saw energetic tidal period fluctuations in near bottom currents on the continental slope at 1000 m depth, and interpreted the measurements as internal waves propagating northward toward shallower water. The waves could have been generated at a spot just to the south where the bottom slope was the critical slope for M_2 frequency internal waves, a possibility suggested by Fofonoff.

Regal and Wunsch (1973) carried out a study of the baroclinic tides at Site D using all the current measurements available at that time. This study, which was the

motivation for the present chapter, attempted a comprehensive description of the internal tides and contained the significant result that the intense near surface currents seemed to have part of their energy locked into a deterministic relationship with the surface tide, and so also with the barotropic tidal current. However this result was of just marginal statistical significance in their study and there did remain some doubt about this important aspect of the problem. Regal and Wunsch described the variation of tidal period energy with depth, showing strong currents in the upper 100 m of the water column and nearly constant values at depth. They also showed that the variability of the tidal period currents was not confined to the surface layers, as even at 2000 m there was so much variation in the data that the northerly component of velocity was completely unpredictable on the basis of their work. They did note that in the deeper water the stronger easterly component of current was somewhat predictable, and related it to the barotropic tide.

At about the same time, Magaard and McKee (1973) looked at a few specific current records from near the site, and by fitting normal modes to the measurements made an estimate of the depth independent current and the baroclinic contribution. They concluded that there was indeed energetic baroclinic (M_2 period) fluctuations but could detect no

phase locking of the baroclinic currents with the barotropic tide.

The present work was launched with the benefit of all these studies, in the hope of characterizing the semidiurnal baroclinic tides at Site D as a process rather than merely describing the fields. It follows in the vein of Regal and Wunsch in that all the measurements are related to the astronomical tides, and treats the variability in the measurements quantitatively by using coherence estimates between the currents and the equilibrium tide. As well as continuing the overall description of the internal tide, using the greater amount of data which has become available, we make a consistent attempt to describe the nature of the processes in terms of bandwidth, predictability, and origin.

The significant questions to be addressed include: Is the baroclinic tide a completely random, though band limited process, or is it partly deterministic? How can we rationalize the observed variability in terms of seasonal or other low frequency oceanic variability? If there is evidence of a deterministic component in the internal tide, as suggested by Regal and Wunsch, can we detect a direction of propagation and so confirm the importance of the nearby continental slope as a generation region? Also, although the principal lunar M_2 tide is the most energetic semidiurnal

barotropic constituent, there are other semidiurnal lines in the tidal forcing. Internal waves may also be generated at these frequencies, but the energetic M_2 internal waves may dominate the adjacent frequencies as Doppler shifted motions. The frequency behavior in the semidiurnal band gives some insight into these possibilities.

In the following section we adress these questions. Section 1.2 summarizes the theoretical aspects of internal waves which apply to tidal frequency motion. This gives a background for interpreting the results which follow. Section 1.3 defines the geographical area studied and the data used, while Section 1.4 and related appendices describe the statistical analysis. In Section 1.5 the overall energetics of the semidiurnal current field are described as a function of depth and frequency, leaving to Section 1.6 the question of determinism in the internal tide and the most significant results of the study. Section 1.7 deals with the barotropic tide at Site D, and Section 1.8 is devoted to a discussion of variability, noise and measurement problems. Finally the conclusions of the study are summarized in Section 1.9.

1.2 Oceanic internal waves

Field equations

Consider a model ocean with a flat bottom at $z = -H$, a mean free surface $z = 0$, and unbounded in horizontal extent. For motion with horizontal scale small compared to the radius of the earth, the level surfaces are taken as horizontal planes in a coordinate system with x positive eastward, y positive northward, and z positive vertically upward. Gravity g acts in the negative z direction and the ocean is rotating with a constant angular velocity $\hat{k}f/2$, where $\hat{k}$ is a unit vector perpendicular to the level surfaces in the direction of increasing z. The local Coriolis frequency

$$f = 2\Omega \sin\phi$$

is twice the local vertical component of the earth's rotation at the latitude ϕ, and $\Omega = 2\pi/24\ \text{hr}^{-1}$. The horizontal component of rotation is neglected.

The model ocean is vertically stratified with a rest state density distribution $\bar{\rho}(z)$. This results in a rest state hydrostatic pressure gradient

$$d\bar{p}/dz = -\bar{\rho}(z)g \qquad (1.2.1)$$

and a rest state vertical stability characterized by the square of the Brunt-Väisälä frequency

$$N^2(z) = -g(1/\rho_o \, d\bar{\rho}/dz + g/c^2) \qquad (1.2.2)$$

Here ρ_o is a constant reference density, c is the speed of sound in sea water, and the correction to the <u>in situ</u> density gradient by $\rho_o g/c^2$ represents the compressibility of the water.

Small fluctuations in horizontal velocity components u (eastward) and v (northward), vertical velocity component w, pressure p and buoyancy

$$b = -\rho g/\rho_o \qquad (1.2.3)$$

where ρ is a density perturbation are modelled in the rotating frame of reference by linearized, Boussinesq, incompressible and non-dissipative field equations (eg. Eckart, &37, 1960)

$$\partial \underline{u}/\partial t + f\hat{k}x\underline{u} = -1/\rho_o \, \nabla p \qquad (1.2.4)$$

$$\partial w/\partial t = -1/\rho_o \, \partial p/\partial z + b \qquad (1.2.5)$$

$$\partial b/\partial t + N^2 w = 0 \qquad (1.2.6)$$

$$\nabla . \underline{u} + \partial w/\partial z = 0 \qquad (1.2.7)$$

$\underline{u} = (u,v,0)$ and ∇ is the horizontal gradient operator $(\partial/\partial x, \partial/\partial y, 0)$. The approximations involved in this simplified set of equations are discussed in detail in Eckart.

From equations 1.2.4 - 1.2.6,

$$\partial^2\underline{u}/\partial t^2 + f^2\underline{u} = -1/\rho_o \, (\partial/\partial t \, \nabla p - f\hat{k}x\nabla p) \qquad (1.2.8)$$

$$\partial^2 w/\partial t^2 + N^2 w = -1/\rho_o \, \partial^2 p/\partial t \partial z \qquad (1.2.9)$$

relate the velocity fluctuations to the pressure fluctuations. Combining 1.2.8 - 1.2.9 in the continuity equation 1.2.7 gives the single equation in w

$$\nabla^2(\partial^2/\partial t^2 + N^2)w + \partial^2/\partial z^2 \, (\partial^2/\partial t^2 + f^2)w = 0 \quad (1.2.10)$$

For a time-harmonic variation proportional to $\exp(-i\sigma t)$, the spatial variations in the vertical velocity component are governed by the differential equation

$$\nabla^2 w - (\sigma^2 - f^2)/(N^2 - \sigma^2) \, \partial^2 w/\partial z^2 = 0 \qquad (1.2.11)$$

At the rigid bottom $z = -H$, w must vanish. The total pressure $\bar{p} + p$ is constant on the instantaneous free surface $z = \zeta$, and the material derivative

$$D(p + \bar{p})/Dt = D(p - \rho_o g\zeta)/Dt$$

vanishes on $z = \zeta$, where $D/Dt = \partial/\partial t + \underline{u}.\nabla + w\ \partial/\partial z$. Expanding this surface boundary condition is a Taylor series about $z = 0$ and linearizing gives

$$\partial p/\partial t - \rho_o g w = 0 \qquad \text{on } z = 0 \qquad (1.2.12)$$

In terms of p alone, for simple harmonic motion, the boundary condition is

$$((N^2 - \sigma^2)/g)p + \partial p/\partial z = 0 \qquad \text{on } z = 0$$

Typical oceanic values for $N^2 = 10^{-5}\ s^{-1}$ give $N^2/g = 1/1000\ km^{-1}$, while the vertical scales of internal waves are of the order of the ocean depth $H = 5$ km. Thus to a good approximation the surface boundary condition for such waves can be replaced by

$$\partial p/\partial z = 0 \qquad \text{on } z = 0$$

which is equivalent to $w = 0$ there. This rigid lid approximation excludes surface waves. For semidiurnal frequency internal waves, $\sigma^2 = 2 \times 10^{-8}\ s^{-2} << N^2$, and it is also a

good approximation to neglect σ^2 with respect to N^2. This hydrostatic approximation neglects the small kinetic energy of the vertical motion with respect to the potential energy of the isopycnal displacements. The resulting approximate equation for w becomes

$$\nabla^2 w - (\sigma^2 - f^2)/N^2 \partial^2 w/\partial z^2 = 0 \qquad (1.2.13)$$

with $w = 0$ on $z = 0$ and $z = -H$.

Characteristic description of the fields

For the case of semidiurnal frequency internal waves at mid-latitudes, $f^2 < \sigma^2 <$ minimum $(N^2(z))$, and 1.2.13 is a hyperbolic boundary value problem. This is not well-posed mathematically and presents considerable difficulties in the solution. In two dimensions x and z, equation 1.2.13 becomes

$$\partial^2 w/\partial x^2 - (\sigma^2 - f^2)/N^2 \; \partial^2 w/\partial z^2 = 0$$

Defining a characteristic slope γ by

$$\gamma^2(z) = (\sigma^2 - f^2)/N^2(z) \qquad (1.2.14)$$

and characteristic coordinates ξ and η by

$$\xi = x - \int^{z} dz'/\gamma(z') \qquad (1.2.15)$$

$$\eta = x + \int^{z} dz'/\gamma(z')$$

equation 1.2.13 transforms into

$$\partial^2 w/\partial\xi\partial\eta = 0$$

with general solution

$$w = A(\xi) + B(\eta) \qquad (1.2.16)$$

for arbitrary functions A and B (Baines, 1973). However the application of specific boundary and radiation conditions to the general solution is quite complicated.

In physical terms, the wave group velocity and energy flux is tangent to the characteristics, allowing information to propagate in space along such curves. In an inviscid model, discontinuities in the tangential component of velocity are allowable across a characteristic. For an example of an

oceanographic case, Figure 1.2.1 from Fofonoff (unpublished manuscript, 1966) shows the general nature of the characteristics for semidiurnal frequency internal waves in the Site D geometry. The information on a characteristic which intersects the bottom or surface is continued along the second characteristic which passes through the point of incidence. In an incompressible ocean, phase propagation in a group of internal waves occurs normal to the characteristics along which the wave energy travels. Since every point in space has two such characteristics intersecting it in every vertical plane, the apparent local phase propagation can be a complicated function of the spatial coordinates.

Baines (1973, 1974) has derived a scheme to solve a class of hyperbolic boundary value problems of internal wave generation, in terms of the characteristic coordinates. Other theoretical models have used a normal mode approach, which we describe further here.

Normal mode description of the fields

For separable solutions of equation 1.2.13 of the form

$$w = F(x,y)\ \Phi\ (z) \qquad (1.2.17)$$

we find $\nabla^2 F/F = (\sigma^2-f^2)/N^2\ \ d^2\ \Phi/dz^2 \quad = -\kappa^2$

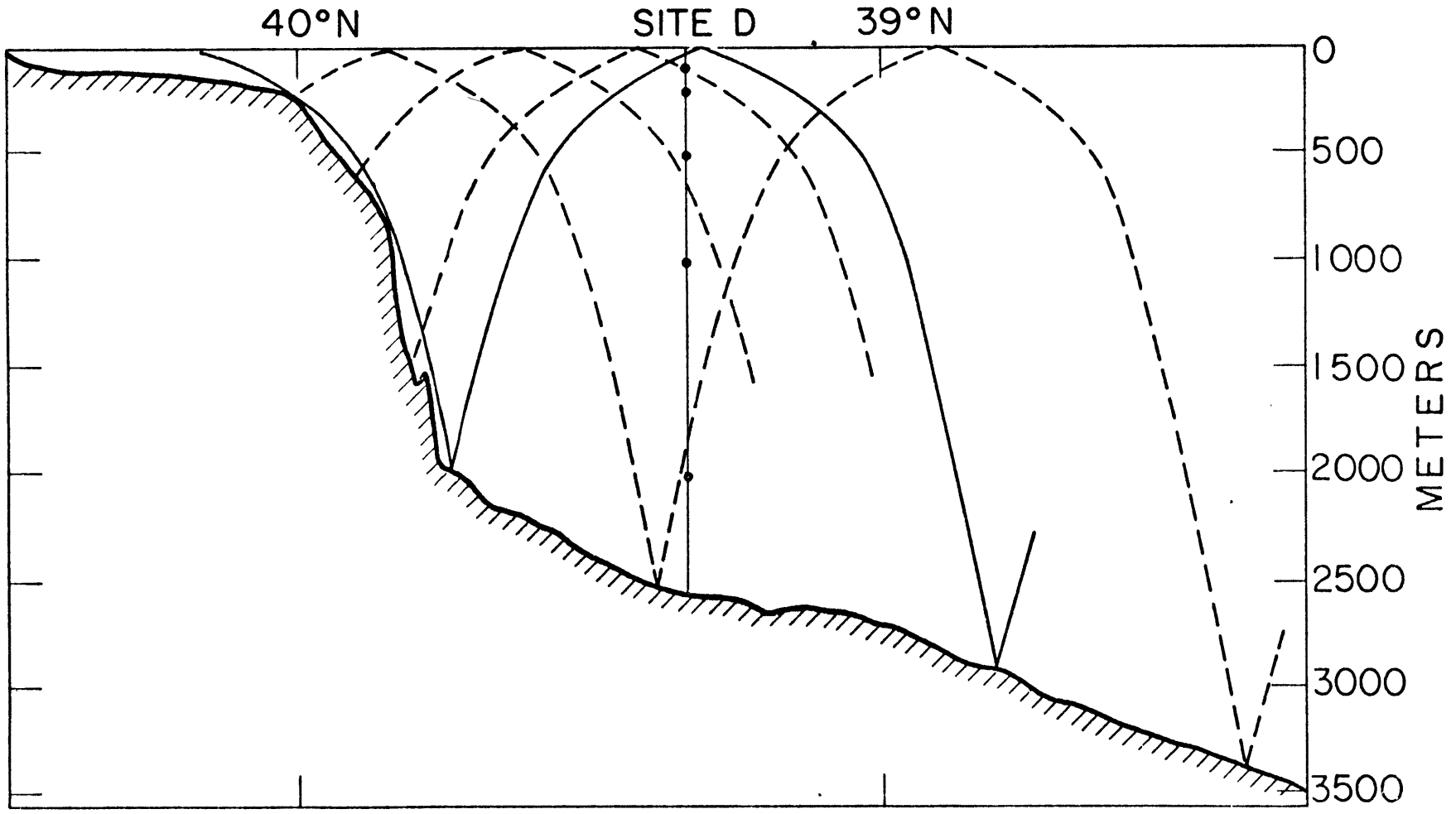


Figure 1.2.1 Topography and characteristic geometry for M_2 frequency internal waves near Site D, after Fofonoff (1966).

where κ^2 is a separation constant. The boundary conditions are also separable in the flat bottom geometry, making $\Phi = 0$ on $z = 0$ and $z = -H$. Then

$$\nabla^2 F(x,y) + \kappa^2 F(x,y) = 0 \qquad (1.2.18)$$

$$d^2\Phi(z)/dz^2 + \kappa^2 N^2(z)/(\sigma^2-f^2)\ \Phi\ (z) = 0 \qquad (1.2.19)$$

The separation constant κ is identified with the horizontal wavenumber in the fields. The problem for Φ, κ^2 is a standard eigenvalue problem (Birkhoff and Rota, Chap. X, 1962) with a denumerable set of solutions Φ_n, κ^2_n, $n = 1,2,\ldots$ which for a given profile of $N(z)$ can be computed numerically.

For a horizontal dependence $F_n(x,y) = \exp(ik_n x)$ representing a plane wave propagating in the x direction, from 1.2.7 - 1.2.9 and 1.2.17,

$$\underline{u} = (i/\sigma k_n)(\sigma, -if, 0)\ \Phi_n'(z) \qquad (1.2.20)$$

$$b = (N^2(z)/i\sigma)\ \Phi_n(z) \qquad (1.2.21)$$

$$p = (i\rho_o/\sigma k_n)\ (\sigma^2-f^2)\ \Phi_n'(z) \qquad (1.2.22)$$

Eigenfunctions of the rigid lid problem are orthogonal

in the sense that for different eigenfunctions $m \neq n$,

$$\int_{-H}^{0} N^2(z)\ \Phi_n(z)\ \Phi_m(z)dz = 0 \qquad (1.2.23)$$

The eigenfunctions provide a complete basis for the expansion of any reasonably smooth function in $-H \leq z \leq 0$, and 1.2.23 implies that the coefficients of such an expansion are unique. For convenience the eigenfunctions will be normalized so that

$$\int_{-H}^{0} N^2(z)\Phi_n^2(z)dz = \overline{N}^2 H \qquad (1.2.24)$$

where $$\overline{N} = \int_{-H}^{0} N(z)dz$$

From 1.2.19, multiplying by $\Phi_n(z)$ and integrating from $z = -H$ to $z = 0$, and using integration by parts and the boundary conditions for w, we can show that

$$k_n^2 = (\sigma^2 - f^2) \int_{-H}^{0} \Phi'^2_n(z)dz \Big/ \int_{-H}^{0} N^2(z)\Phi_n^2(z)dz \qquad (1.2.25)$$

This suggests a variational calculation for the eigenvalues is possible, and it will be used later to calculate the effects of variations in the N(z) profile on the modal parameters. With the given normalization for $\phi_n(z)$, the

pressure or horizontal velocity modes $\Phi_n'(z)$ are normalized by

$$\int_{-H}^{0} \Phi_n'(z)\, \Phi_m'(z)\, dz = k_n^2 \bar{N}^2 H/(\sigma^2-f^2)\ \delta_{mn} \tag{1.2.26}$$

where δ_{mn} is the Kronecker delta function, $\delta_{mn} = 1$ if $m = n$ and 0 if $m \neq n$.

For any smooth enough current profile u(z), there will be an expansion

$$u(z) = \sum_{n=1}^{\infty} B_n\, \Phi_n'(z) \tag{1.2.27}$$

where

$$B_n = (\sigma^2-f^2)/(\bar{N}^2 H k_n^2) \int_{-H}^{0} u(z)\, \Phi_n'(z)\, dz \tag{1.2.28}$$

Instead of the normalization 1.2.26 for horizontal currents, it is convenient to renormalize the $\Phi_n'(z)$ so that

$$\int_{-H}^{0} \Phi_n'(z)\, \Phi_m'(z)\, dz = H\, \delta_{mn} \tag{1.2.29}$$

Modal decompositions in the text for horizontal currents use this normalization, while modal decompositions for vertical velocity or displacement use 1.2.24. For the B_n in 1.2.27,

$$\sum_{j=1}^{J} \{B_j - \frac{1}{H} \int_{-H}^{o} u(z)\ \Phi'(z)\ dz\}^2 \equiv 0 \qquad (1.2.30)$$

A finite approximation to the identity 1.2.30 is used as a basis for fitting a limited number of modes to a similarly limited number of current measurements in a vertical profile. The strict analogy to 1.2.30 is to minimize

$$\sum_{j=1}^{J} \{B_j - \sum_{i=1}^{I} u(z_i)\ \Phi'(z_i)\ \Delta z_i/H\}^2 \qquad (1.2.31)$$
$$= \text{function } (u(z_i),\ B_j,\ \Phi_j'(z_i),\ \Delta z_i)$$

with respect to the B_j, where $J < I$ and for stability $J << I$. Differentiation of 1.2.31 by the B_j and setting the result equal to zero for $j = 1, J$ gives a set of J linear equations in J unknowns B_j which can easily be solved. The Δz_i in 1.2.31 are weight factors proportional to the depth increment represented by the measurement at $z = z_i$. Often Δz_i is taken to be unity for all i, and the results are insensitive to the actual scheme if in fact much of the measured variability is associated with the first J normal modes. For isotherm fluctuations a similar functional

$$\sum_{j=1}^{J} \{A_j - \sum_{i=1}^{I} \zeta(z_i)\Phi(z_i)\ N^2(z_i)\ \Delta Z_i/\bar{N}^2 H\}^2 \qquad (1.2.32)$$

should be minimized to provide the best fitting set of A_j.

In practice, weight factors were usually avoided in the fits of data to modes, but for the Site D currents

(Section 1.6) a set of Δz_i proportional to the depth increments were finally used. There the deep currents were considerable smaller than the surface currents, while the modes had their maximum amplitudes near the surface. Without weighting the levels the least squares fit is somewhat insensitive to the deep currents, which at Site D contain much of the information. In this case the fits were done for $\Delta z_i = 1$ as well, with quantitative but no qualitative changes in the results. All of the fits to MODE data are unweighted in this sense.

Energetics of the fields

Multiplying 1.2.4 by $\underline{u}^*$ (* indicates complex conjugate), 1.2.5 by w^* and 1.2.6 by b^*/N^2 and adding the results gives

$$\partial/\partial t \; 1/2(\underline{u}.\underline{u}^* + ww^* + bb^*/N^2) =$$

$$= -1/\rho_o \; \nabla.p\underline{u}^* - 1/\rho_o \; \partial/\partial z(pw^*) \qquad (1.2.33)$$

where the continuity equation 1.2.7 has also been used. Integrating 1.2.33 over the entire water column and neglecting the term ww^* gives

$$\partial/\partial t \int_{-H}^{o} 1/2(\underline{u}.\underline{u}^* + bb^*/N^2)dz =$$

$$= -1/\rho_o \; \nabla. \int_{-H}^{o} p\underline{u}^* dz \qquad (1.2.34)$$

This relates the time derivative of the energy per unit volume

$$1/2\ \rho_o(u.u^* + bb^*/N^2)$$

integrated over the water column to the divergence of the horizontal energy flux $p\underline{u}^*$. The time average of the total horizontal kinetic energy plus potential energy added over the water column is

$$1/4 \int_{-H}^{o} \rho_o\ (u.u^* + bb^*/N^2)dz \qquad (1.2.35)$$

If there is a net horizontal propagation in the wave field, the energy flux integral in 1.2.34 will have a non-zero time average, while the divergence of the vertically integrated energy flux will vanish for a steady state wave field.

Suppose the w field has a simple modal decomposition where every mode is present with only one direction of propagation,

$$w = \sum_{n=1}^{\infty} A_n\ \Phi_n(z)\exp(ik_nx) \qquad (1.2.36)$$

Then $$\underline{u} = (i/\sigma)(\sigma, -if, 0)\Sigma(A_n/k_n)\Phi_n'(z)\exp(ik_nx) \qquad (1.2.37)$$

$$p = (i\rho_o/\sigma)(\sigma^2-f^2)\ \Sigma(A_n/k_n^2)\Phi_n'(z)\exp(ik_nx) \qquad (1.2.38)$$

$$b = (N^2/i\sigma)\ \Sigma A_n\ \Phi_n(z)\exp(ik_nx) \qquad (1.2.39)$$

The time average horizontal kinetic energy in this field is

$$(1/4)\ \rho_o\ \bar{N}^2H(\sigma^2+f^2)/\sigma^2(\sigma^2-f^2)\ \Sigma\ A_n^2 \qquad (1.2.40)$$

and the time averaged potential energy is

$$(1/4)(\rho_o\ \bar{N}^2H/\sigma^2)\ \Sigma A_n^2 \qquad (1.2.41)$$

The horizontal kinetic energy and potential energy in the waves is partitioned in the ratio

$$(\sigma^2+f^2)/(\sigma^2-f^2) \qquad (1.2.42)$$

The time averaged energy flux in the wave field is the integral

$$(1/2)\int_{-H}^{o} p\underline{u}^*dz =$$

$$= (1/2)(\bar{N}^2H/\sigma)\ \Sigma A_n^2/k_n \qquad (1.2.43)$$

by using 1.2.26. Comparing the energy flux 1.2.43 to the total energy density

$$(1/2)\rho_o \bar{N}^2 H/(\sigma^2-f^2)\ \Sigma A_n^2 \qquad (1.2.44)$$

we can write the energy flux as

$$\Sigma\ (\sigma^2-f^2)/\sigma k_n\ (1/2)\rho_o \bar{N}^2 H/(\sigma^2-f^2)\ A_n^2 \qquad (1.2.45)$$

which is just the sum of the energy densities due to each mode n times the modal group speed defined

$$c_g^{(n)} = (\sigma^2-f^2)/\sigma k_n \qquad (1.2.46)$$

The functional relation between frequency and wavenumber given by the eigenvalue problem 1.2.19 (see also 1.2.25) can be written

$$\sigma^2 = f^2 + k^2/E$$

where E is a constant not depending on either frequency or wavenumber. Then the classical definition of group velocity

$$c_g = \partial\sigma/\partial k$$

gives the same result as 1.2.46.

Polarization of horizontal currents

The earth's rotation affects the partition of potential and kinetic energy in a simple wave (1.2.42). It also affects the polarization of the horizontal current ellipse. From equation 1.2.20, using real arithmetic,

$$u = \sigma S \cos(\sigma t) \qquad (1.2.47)$$

$$v = -fS \sin(\sigma t)$$

at a particular value of x, where S is a real constant. Then defining a complex velocity vector

$$q = u + iv \qquad (1.2.48)$$

where the real part of q represents the eastward current and the imaginary part of q the northward current, using 1.2.47 gives

$$q/S = \cos(\sigma t) - if \sin(\sigma t)$$

$$= (\sigma-f)/2 \exp(i\sigma t) - (\sigma+f)/2 \exp(-i\sigma t) \qquad (1.2.49)$$

The first term in 1.2.49 represents a current vector proportional to $(\sigma-f)$ rotating in an anticlockwise sense, and the second term a larger (in the northern hemisphere) term proportional to $(\sigma+f)$ which rotates in a clockwise sense. The energy in the clockwise polarization of current in this simple wave is

$$(\sigma+f)^2/(\sigma-f)^2 \qquad (1.2.50)$$

times greater than the energy in the anticlockwise polarization. Gonella (1972) has investigated the kinematics of polarized currents in some detail.

WKBJ internal waves

For large vertical mode number n, the spatial scale of the internal wave motion is small compared to the variations in the main features of N(z) and the description of the modes can be simplified. An approximation taking advantage of the two differing scales (WKBJ after its inventors) results in the expressions (Munk and Phillips, 1968)

$$w_n = A_n(\bar{N}/N(z))^{1/2} \sin(\psi_n(z)) \qquad (1.2.51)$$

with

$$\psi_n(z) = n\pi/\bar{N}H \int^z N(z')dz' \qquad (1.2.52)$$

To the approximation $(dN/dz)/N << d\ \psi_n/dz$, the related horizontal velocity component fluctuations are

$$u_n = iA_n(n\pi/k_nH)(N(z)/\bar{N})^{1/2}\ \cos(\psi_n(z)) \qquad (1.2.53)$$

$$v_n = (if/\sigma)u_n$$

Thus the horizontal kinetic energy is modulated by $N(z)$ in the vertical, while the vertical kinetic energy is modulated by $N^{-1}(z)$. In a model spectrum with many high order modes of equal amplitude the vertical variations in phase $\psi_n(z)$ will average out in a real measurement. Density fluctuations associated with the fluctuations in w have amplitude

$$\rho_o\ N^2 w/\sigma$$

and in the WKBJ field the density variance is modulated by $N^3(z)$. Although the temperature variance is formally modulated by

$$N(z)^{-1}(d\theta/dz)^2$$

for θ the mean potential temperature profile, in the areas of the ocean we are considering $N(z)$ is largely determined

by the temperature gradient, and the temperature variance in a high mode field will also be similar to $N^3(z)$.

1.3 Observational base

The current measurements considered here came from the Woods Hole Oceanographic Institution archives. In the final version the study was restricted to between 39°02'N and 30°25'N latitude and 69°51'W and 70°30'W longitude. This area forms a rectangle 40 km north-south by 70 km east-west. The depth contours in the area run generally east-west, parallel to the continental slope to the north, and the depth varies smoothly from 2600 m to 2800 m through the site. The general geometry of the site is shown in Figure 1.3.1.

The records used cover a period from April 1965 to April 1972. Because of recent concern about the effects of mooring motion on measurements taken in deeper levels (see Section 1.8), any measurements from surface moorings at depths below 250 m were excluded from the study. Only records with continuous data for at least 15 days were used. The geographic limits on the study area were set in an attempt to optimize the tradeoff between the stability of a large sample size and the spatial smearing due to the variations in the internal tide across the site. Thus certain records nearby but outside the study area were excluded in the final version, although they were analyzed as a matter of course in the meantime.

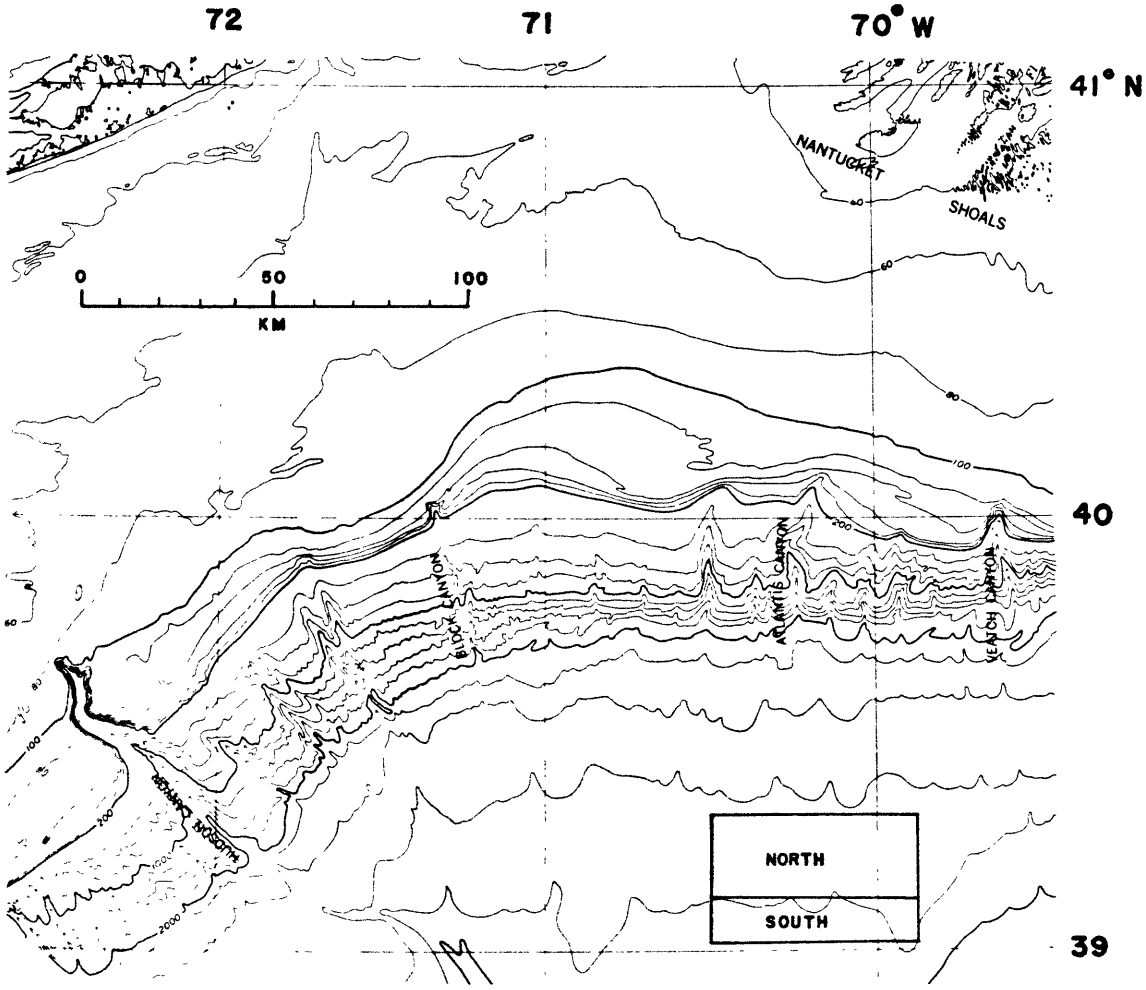


Figure 1.3.1 Bathymetry of the New England continental shelf, slope and rise, with the Site D study areas indicated. Depth contours are in meters.

The resulting ensemble of observations was divided into two groups to attempt horizontal resolution within the study area. All records north of 39°10'N were considered northerly, and all south of and including 39°10'N were considered southerly. Measurements tended to be clustered in longitude about 70°W and no east-west resolution was attempted. Since the southerly measurements were more closely grouped in space, the horizontal partition of the data required to give reasonable numbers of records at all depths resulted in an uneven division in total north and south records. This means that the error bars on averages from the northern measurements will be larger than those for the southern measurements in many cases. The geographical spread in measurements from the nominal northern site was also somewhat greater, with a total north-south variation of ±13 km, while the southern measurements were contained in a ±7 km band. This was unavoidable given the data availability, and has to be considered in the interpretation of the results.

No attempt was made to resolve seasonal variations in the tidal fields, and as is shown in Section 1.8 on variability in the fields, this lack of resolution is a serious limitation. The amount of data needed to resolve the temporal variability would be another quantum jump, so here we attempt to obtain stable estimates of the non-seasonal effects.

Finally, the records were grouped at depth levels, with four levels assigned between the surface and 250 m and nominal levels at 500, 1000, 2000 and 2500 m. The deeper levels were standard ones for essentially all of the historical experiments. The basic unit of information was to be a 15 day long record of horizontal current components, usually sampled at hourly or half-hourly intervals. Table 1.3.1 gives the breakdown of available data as a function of depth and horizontal location. Even the smallest category containing only three 15 day pieces corresponds to a 45 day experiment. The total of the observations used amounted to 232 individual pieces, or 9.5 record-years. The two years since the completion of the Regal and Wunsch analysis produced about 3 extra record-years.

	Nominal depth (m)	Range in depth (m)	No.of pieces
SOUTH	25	8- 32	32
	75	51- 72	32
	125	100- 108	13
	200	197- 206	18
	500	532	3
	1000	1027-1044	14
	2000	2066	7
	2500	2495-2590	30
			149
NORTH	25	7- 13	9
	75	53- 99	16
	125	100- 120	14
	200	200- 207	6
	500	456- 506	9
	1000	958-1007	16
	2000	2000-2012	8
	2500	2575-2582	5
			73
			232

Table 1.3.1

Distribution by depth and location of the current measurements used in the Site D study.

1.4 Analysis

Some thought was given to the overall philosophy of the analysis to be performed. It was felt that baroclinic tides had become firmly established as a phenomenon, and that a more determined examination of their structure was needed. The process is a statistically noisy one, and the noise itself needed characterization. The approach finally decided upon can be described as quasi-harmonic. In the study of sea surface tidal signals, one is interested in the fine structure of the frequency behavior as a probe into the underlying dynamics of the ocean (Munk and Cartwright, 1966; Wunsch, 1972a), and the signal to noise ratio is very favorable to high resolution studies. Ultimately one would like to know the behavior in frequency of the current fields to as high a resolution as the surface displacement, but the poor (some would have zero) signal to noise ratio in the baroclinic fields means that with a finite amount of data the tradeoff between resolution and stability must be heavily biased towards stability considerations.

The surface tide is predictable from the astronomical forcing once measurements define the local admittance of the tide with respect to this forcing, and a high signal to noise ratio means that good predictions are possible with a limited amount of data. If the baroclinic fluctuations

show a significant coherence with the surface tide, or equivalently with the equilibrium tide computed from the astronomical forcing, then some of the energy in the internal tide is also predictable. The usefulness of such predictions depends on the ratio of predictable to total power, which is just the square of the coherence between the tidal fluctuations and the deterministic equilibrium tide. Evidence of even a small real coherence between the internal tide and the equilibrium tide would be scientifically interesting.

Admittance approach

Given a record of physical variation in an oceanic field, a time series of the equilibrium tide can be formed to parallel the record. The equilibrium tide is simply the vertical displacement of the sea surface on a water covered globe which would give a level surface under the combined gravitational potentials of the earth, sun and moon. The form of this level surface changes in time at a point on the earth as the astronomical bodies move relative to each other. The equilibrium tide can be used to define a complex admittance function for the physical variable, s(t),

$$\hat{a}(\sigma) = \hat{S}(\sigma)/\hat{\zeta}_e(\sigma) = |\hat{s}(\sigma)/\hat{\zeta}_e(\sigma)| \exp i(\phi_s - \phi_\zeta) \qquad (1.3.1)$$

where $\zeta_e(t)$ is the equilibrium tide, and $\hat{s}(\sigma)$ and $\hat{\zeta}_e(\sigma)$ the Fourier transforms of the signal s(t) and the equilibrium tide. It is a convenient way to represent the local tidal variability even though there may be no direct link between the local variations in tidal potential and the local signal (Wunsch, 1972a). In a finite numerical calculation with a discretely sampled record, the first order filtering effects of the Fourier transform are removed in a pure admittance approach since only amplitude ratios and phase differences are considered. The admittance approach relates the phases of the harmonic constituents of the local process to the phases of the same constituents in the astronomical tide. It can also correct for modulations in the amplitude and phase of the processes caused by tidal variation at periods longer than the actual record length.

Analysis

It was decided to uniformly analyze the available current records in 15 day piece lengths. This was a practical choice for several reasons, allowing the use of many fairly short records and giving a numerically convenient number of hourly readings. Conventional fast Fourier transform methods (Bingham, Godfrey and Tukey, 1967) were used to convert these pieces, and parallel piece lengths of

the equilibrium tide generated by a computer program, into the frequency domain. The record length used produces adjacent semidiurnal estimates at periods of 12.00, 12.41 and 12.86 solar hours, with a bandwidth of 1/15 cycle/day. In the following chapters these bands will often be referred to as the S_2, M_2 and N_2 estimates respectively, since the variability in the astronomical tide in the three bands is dominated by these constituents.

Each 15 day series of u (eastward) and v (northward) current components had its mean value subtracted out, and the resulting series was multiplied by a tapering window to bring the values smoothly to zero at the beginning and end of the record. The purpose of the tapering procedure was to reduce the contamination of the high frequency part of the records by trends which reflect frequencies lower than resolved by the length of the time series. The equilibrium tide was treated in exactly the same way. A more complete discussion of the Fourier transform techniques and possible numerical problems is given in Appendix A.1.

Once ensembles of Fourier coefficients for the semidiurnal currents and equilibrium tide were assembled, averages could be computed to estimate the coherent tidal signal, correlating with the equilibrium tide, and the apparently random part of the process. The analysis is

described in Appendix A.2, but the averaging gives an estimate of that part of the observed variation which has a linear projection on the equilibrium tide. The effect of averaging over N pieces using the admittance phase is to filter out non-tidal frequencies in the overall semi-diurnal band, and to reduce the variance of the tidal estimates by a factor 1/N. The coherence between the ensemble of Fourier coefficients from different pieces and the equilibrium tide is a measure of the true tidal period signal compared to the total variability in the relatively wide 1/15 cpd frequency band. Thus the noise content can also be discussed in quantitative terms.

1.5 Semidiurnal energy levels

Averages of squared amplitude of current fluctuations at the nominal depth levels described in Section 1.3 were calculated for the north and south sites separately, at the three semidiurnal frequencies in the 15 day piece length analysis. Figures 1.5.1 show the resulting profiles for the u and v components of horizontal current at the southern site, while numerical values for all cases are found in Tables 1.5.1. In general all the profiles show three regimes, with especially strong currents in the upper 50 m, a transition in the surface levels down to 500 m, and relatively constant and weaker current variability in the deep water. Regal and Wunsch (1973) noted the surface intensification for the M_2 frequency motions, and compared the variation of amplitude with depth to the $N^{1/2}(z)$ profile which high mode internal wave fields would resemble in the vertical variation of current. They concluded that the surface currents were more intensified over the deeper currents than the WKBJ approach would predict. Figure 1.5.2 shows the average N(z) profile as calculated from an average of the Site D density field over a seven year period, taken over all seasons. The N(z) profile shows the same general features as the current variance profiles, with surface values about ten times greater than the deep water

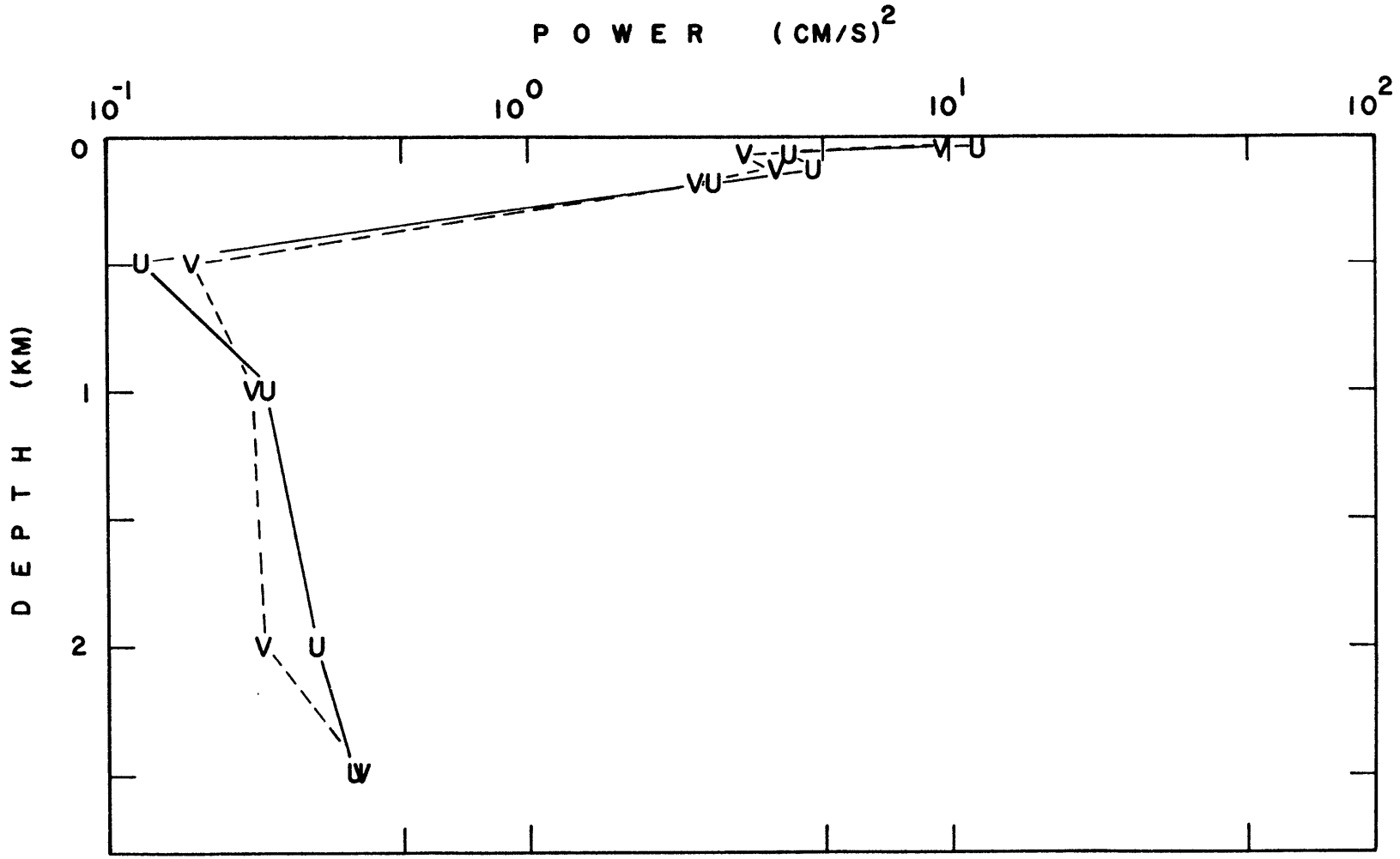


Figure 1.5.1a Mean squared amplitude of u (east) and v (north) current components in the S_2 band from the south Site, as a function of depth.

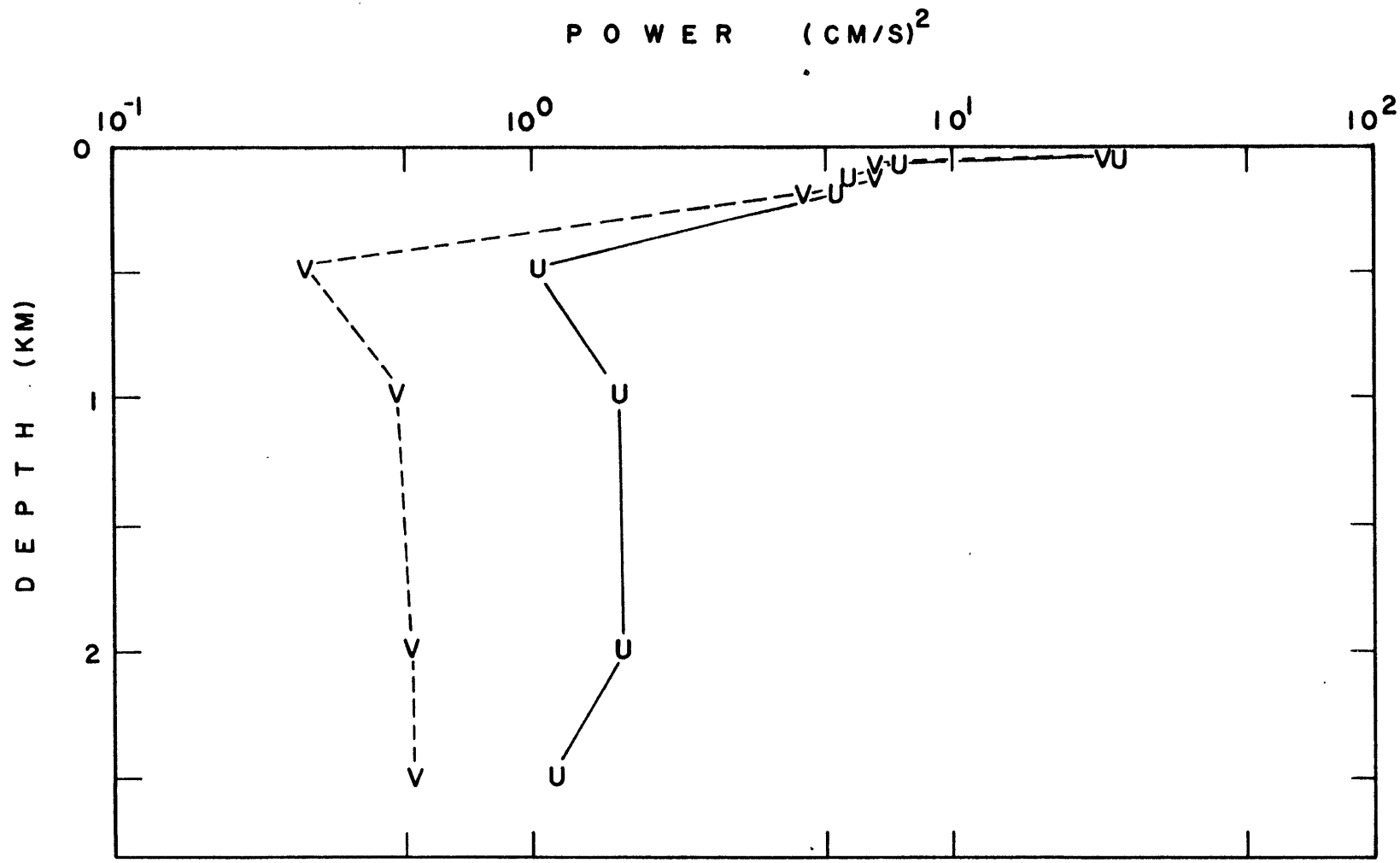


Figure 1.5.1b Mean squared amplitude of u (east) and v (north) current components in the M_2 band from the south Site, as a function of depth.

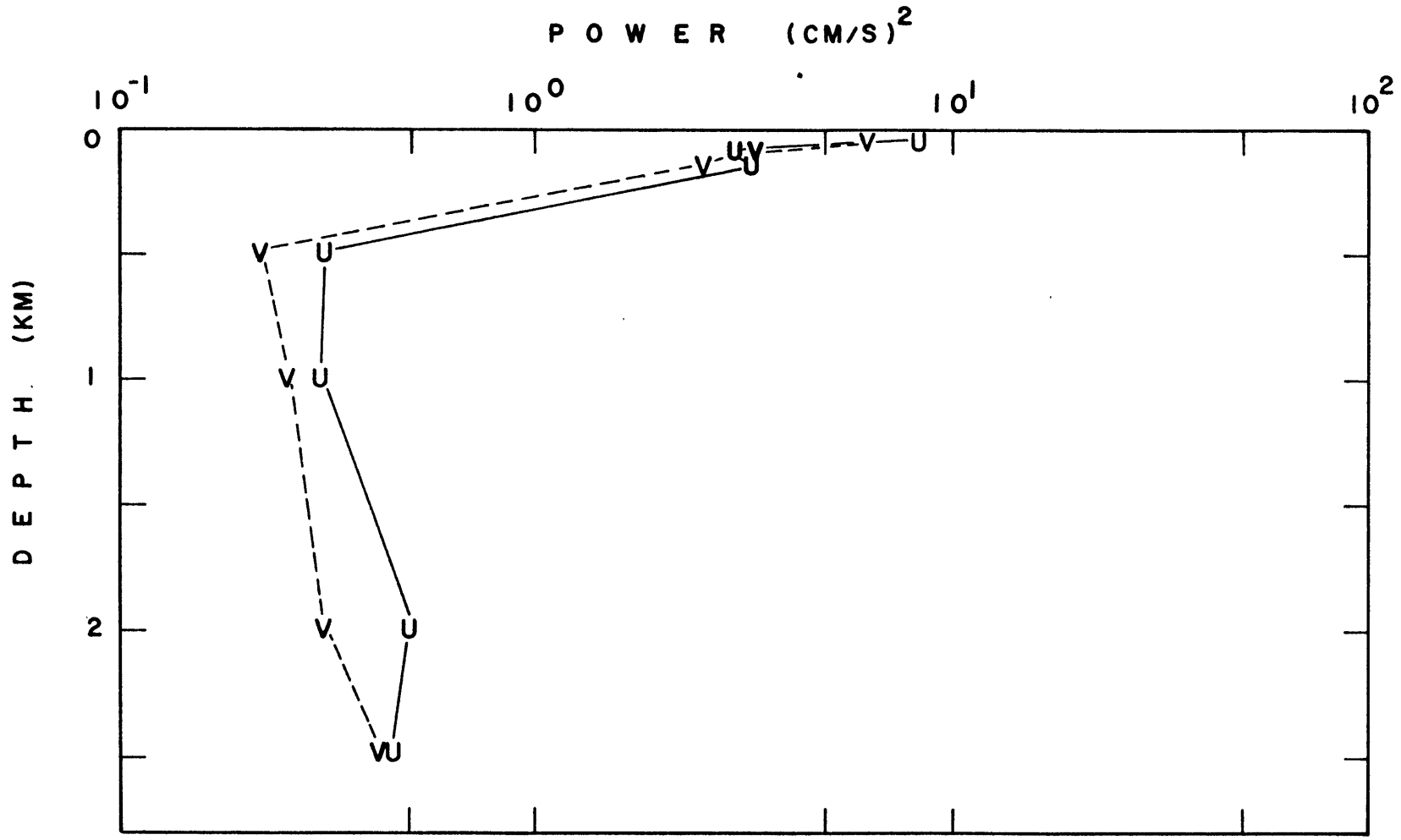


Figure 1.5.1c Mean squared amplitude of u (east) and v (north) current components in the N_2 band from the south Site, as a function of depth.

	Depth (m)	u $(cm/s)^2$	v $(cm/s)^2$	+ $(cm/s)^2$	- $(cm/s)^2$	-/+
SOUTH	25	11.7	9.23	.880	9.58	10.9
	75	4.01	3.27	.416	3.44	8.27
	125	4.81	3.93	.272	4.10	15.1
	200	2.73	2.43	.243	2.35	9.64
	500	.120	.154	.0560	.0812	1.45
	1000	.233	.220	.0275	.199	7.24
	2000	.310	.226	.0217	.247	14.0
	2500	.375	.379	.0374	.340	9.09
NORTH	25	12.3	9.47	1.20	9.72	8.10
	75	4.70	3.68	.442	3.75	8.48
	125	2.67	3.07	.437	2.43	5.56
	200	3.07	4.52	.130	3.67	28.2
	500	.373	.270	.0473	.274	5.79
	1000	.346	.279	.0270	.285	10.6
	2000	.295	.167	.0316	.199	6.30
	2500	.209	.223	.0580	.210	3.62

Table 1.5.1a

Mean squared amplitude of u (east), v (north), + (anticlockwise rotating), and - (clockwise rotating) current components from the south and north sites, for the S_2 band, as a function of depth. Also the ratios of clockwise to anti-clockwise power.

	Depth (m)	u $(cm/s)^2$	v $(cm/s)^2$	+ $(cm/s)^2$	- $(cm/s)^2$	-/+
SOUTH	25	24.9	22.6	1.15	22.6	19.7
	75	7.32	6.48	.579	6.32	10.9
	125	5.69	6.23	.311	5.65	18.2
	200	5.42	4.38	.321	4.58	14.3
	500	1.01	.281	.0812	.565	6.96
	1000	1.60	.472	.142	.896	6.31
	2000	1.65	.513	.222	.859	3.87
	2500	1.12	.521	.131	.689	5.26
NORTH	25	12.6	17.5	2.14	13.0	6.07
	75	9.69	6.57	.630	7.49	11.9
	125	7.17	6.72	.593	6.36	10.7
	200	4.77	4.93	.209	4.64	22.2
	500	1.46	.640	.148	.899	6.07
	1000	.988	.402	.179	.516	2.88
	2000	.635	.175	.0946	.310	3.28
	2500	.960	.680	.113	.707	6.26

Table 1.5.1b

Mean squared amplitude of u (east), v (north), + (anticlockwise rotating), and - (clockwise rotating) current components from the south and north sites, for the M_2 band, as a function of depth. Also the ratios of clockwise to anti-clockwise power.

	Depth (m)	u $(cm/s)^2$	v $(cm/s)^2$	+ $(cm/s)^2$	- $(cm/s)^2$	+/-
	25	8.10	6.09	.648	6.44	9.94
	75	2.99	3.30	.315	2.83	8.98
S	125	3.27	2.49	.128	2.75	21.5
O	200	2.27	2.02	.216	1.94	8.98
U	500	.301	.211	.0189	.237	12.5
T	1000	.295	.247	.0278	.243	8.74
H	2000	.494	.304	.0214	.377	17.6
	2500	.450	.401	.0236	.402	17.0
	25	4.57	3.59	.637	3.44	5.40
	75	2.27	3.78	.227	2.80	12.3
N	125	4.34	4.38	.726	3.63	5.00
O	200	1.46	1.90	.157	1.52	9.68
R	500	.459	.430	.0356	.409	11.5
T	1000	.448	.431	.0253	.414	16.4
H	2000	.375	.301	.0370	.301	8.14
	2500	.348	.299	.0096	.314	32.7

Table 1.5.1c

Mean squared amplitude of u (east), v (north), + (anticlockwise rotating), and - (clockwise rotating) current components from the south and north sites, for the N_2 band, as a function of depth. Also the ratios of clockwise to anti-clockwise power.

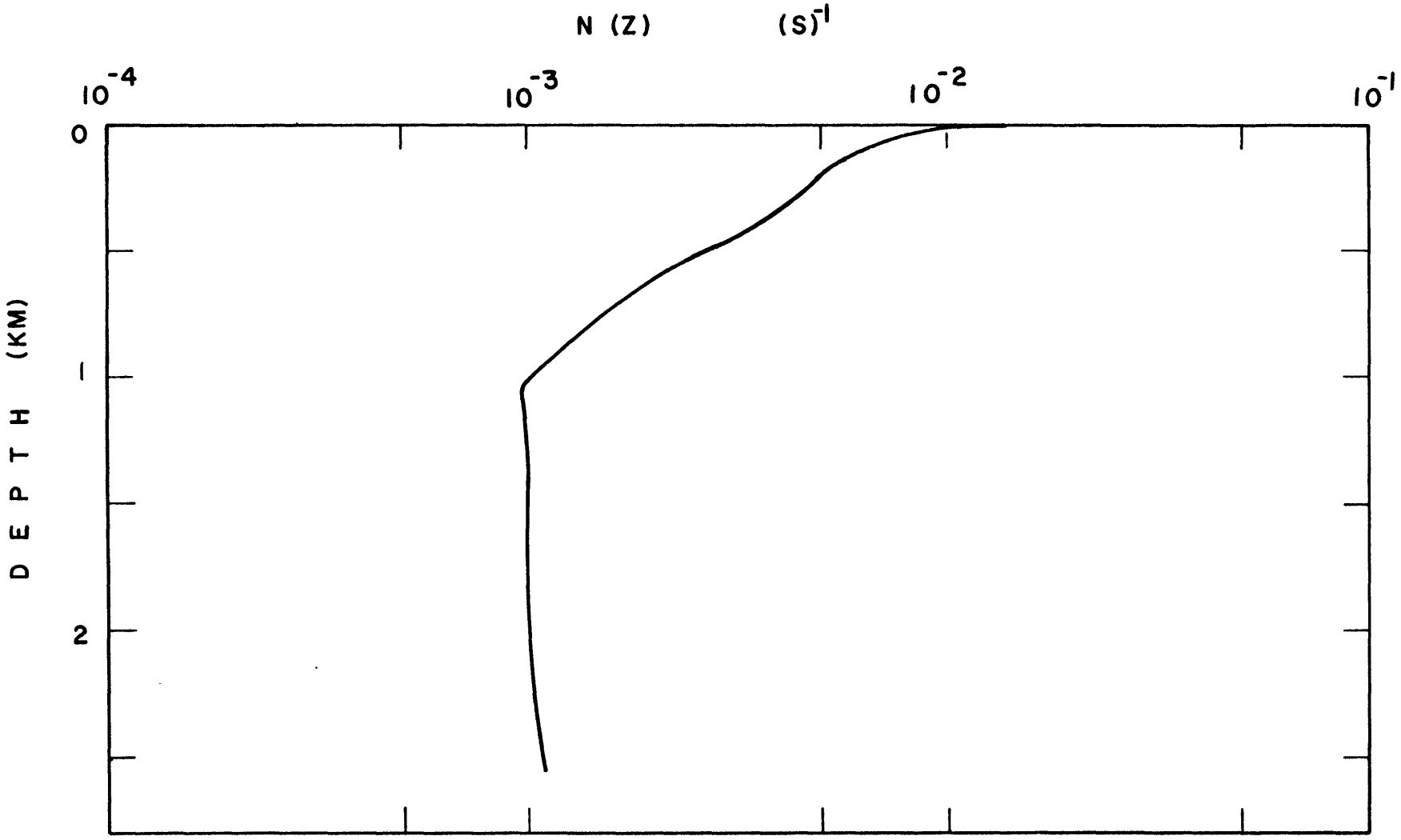


Figure 1.5.2 Average N(z) profile for Site D, from hydrographic data over all seasons in 1965-1972.

values, where N(z) is nearly constant. However the profiles in Figures 1.5.1 all show more intensification of near surface currents than the N(z) profile, as noted by Regal and Wunsch for the M_2 frequency. The sole exception is the M_2 u component, which we will show is dominated by the barotropic current mode.

Table 1.5.2 presents the average over time and depth of the horizontal kinetic energy in the south and north currents for each semidiurnal frequency band. The N_2 and S_2 bands have about the same power, with the M_2 band showing 2 to 3 times greater power than the adjacent bands. The 95% confidence limits on these overall averages are less than ±0.5% of the estimates if the individual Fourier coefficients in the averages are assumed to be independent. Error bars on the individual energy estimates in Tables 1.5.1 can be calculated by assuming that the estimates are from a chi-square distribution with 2N degrees of freedom, where N is the number of pieces in the average at a given depth as found in Table 1.3.1. The 95% confidence limits for N = 5, 10, 20 and 30 are

N =	5	(.325, 2.05)
	10	(.480, 1.57)
	20	(.600, 1.47)
	30	(.667, 1.38)

times the estimate itself, for example.

Frequency band	Energy density South $_2$ (erg/cm^2)	Energy density North $_2$ (erg/cm^2)
N_2	$.82 \times 10^5$	$.83 \times 10^5$
M_2	$.23 \times 10^6$	$.18 \times 10^6$
S_2	$.88 \times 10^5$	$.96 \times 10^6$

Table 1.5.2

Depth integrals of horizontal kinetic energy density for the three semidiurnal bands, at the south and north sites.

Table 1.5.3 gives the ratios of power of the N_2 and S_2 bands to the central M_2 band, and also the ratio of the S_2 to N_2 power. 95% confidence intervals for statistical variations of such ratios are also given, based on the number of degrees of freedom in the individual averages. In this table, it is seen that the M_2 frequency variations are in general more energetic than the neighboring frequencies, by a factor usually between 2 and 3 in power. There is roughly equal power in the u and v components for all three frequencies above 500 m, but in the deeper water the u or along shore variability is consistently greater than the v or on shore variability. This is especially notable for the deep M_2 frequency currents.

The rotary spectra for the currents are also given in Table 1.5.1, giving the energy contained in anticlockwise rotating (+) and clockwise rotating (-) components of the horizontal current at each depth level. For a plane internal wave, equation 1.2.49 predicts that the partition will favor the clockwise rotating part of the current by a factor varying from about 20 to 27 in power for frequency variation from the S_2 to the N_2 band. The currents at all levels are predominantly clockwise, with the near surface M_2 currents showing especially strong clockwise polarization. Although the S_2 and N_2 bands show cases where the deep currents are highly clockwise in power, the M_2 deep currents are generally

	Depth (m)	M_2/N_2 u	M_2/N_2 v	M_2/S_2 u	M_2/S_2 v	S_2/N_2 u	S_2/N_2 v	95%
SOUTH	25	3.1	3.7	2.1	2.4	1.4	1.5	(.65,1.5)
	75	2.4	2.0	1.8	1.7	1.3	1.1	(.65,1.5)
	125	1.7	2.5	1.2	1.6	1.5	1.6	(.44,2.3)
	200	2.4	2.2	2.0	1.8	1.2	1.2	(.53,1.9)
	500	3.4	1.3	8.4	1.8	.40	.73	(.17,5.8)
	1000	5.4	1.9	6.9	2.2	.79	.89	(.48,2.1)
	2000	3.3	1.7	5.3	2.3	.63	.74	(.35,2.9)
	2500	2.5	1.3	3.0	1.4	.83	.95	(.65,1.5)
NORTH	25	2.8	4.9	1.0	1.8	2.7	2.6	(.41,2.5)
	75	4.3	1.7	2.1	1.8	2.1	.97	(.35,2.8)
	125	1.6	1.5	2.7	2.2	.61	.70	(.35,2.8)
	200	3.3	2.6	1.5	1.1	2.1	2.4	(.30,3.3)
	500	3.2	1.5	3.9	2.4	.81	.63	(.41,2.5)
	1000	2.2	.93	2.9	1.4	.77	.65	(.48,2.1)
	2000	1.7	.58	1.8	1.0	.92	.55	(.41,2.9)
	2500	2.8	2.3	4.6	3.0	.60	.74	(.27,3.7)

Table 1.5.3

Ratios of power in the horizontal currents in the three semidiurnal bands as a function of depth, showing the dominance of the M_2 band. The 95% confidence intervals for a true ratio of unity are given.

less biased towards circular polarization.

The profiles from the nominal north and south sites at the same frequency show some differences. The M_2 currents in the southern estimates have about twice as much power as the northern estimates, while the southern site is also more highly clockwise polarized at the surface. The other depth levels for M_2 variability are quite similar. At the N_2 frequency, there is also somewhat more near surface variability at the southern site, while the S_2 profiles for both north and south sites fail to show any consistent differences.

There are differences in the relative surface intensification in the three semidiurnal frequency bands, although all bands do show a considerable degree of this intensification. The N_2 band is the least intensified, with surface powers between 10 and 15 times greater than the deepest currents. The S_2 frequency band, on the other hand, shows currents in the near surface about 30 to 40 times more powerful than in the deep water, with the M_2 band falling between these extremes. The average N(z) profile shows a factor of 10 in surface intensification, and the average over all seasons reduces the near surface maximum which arises in the summer seasonal thermocline. The differences between the S_2 and N_2 bands are illustrated in Table 1.5.3 where it is seen that the S_2 variability is greater than

the N_2 band variability above 500 m depth, but that the situation is reversed at lower levels where the N_2 frequency shows more power. Although the individual levels often do not show significant differences between these two bands, the overall effect of the difference in the deep and shallow levels is quite significant.

Conclusions based on the distribution of power

Since the N_2 and S_2 bands, separated from the M_2 band by a bandwidth of 1/15 cpd on either side, show significant differences in their structure, we can conclude that the more powerful M_2 variability does not dominate these neighboring bands. This means that the effective bandwidth of the M_2 peak is less than the frequency resolution in the 15 day pieces, that is, one cycle per 15 days. The M_2 frequency did show significantly greater power than the neighboring bands at most depth, although the v components in the three semidiurnal bands at depth showed more comparable energies, especially at the northern site. The variation in energy level with depth reconfirms that the semidiurnal current fields have a large baroclinic component.

The S_2 band is centered directly about the astronomical S_2 frequency, while the nominal N_2 band is such that only about half of the astronomical N_2 power in the equilibrium

tide, for example, will fall in this band. While the energy levels in these two bands are comparable, the S_2 band shows considerably more variation in energy with depth. The N_2 band contains some astronomical variability, but it also represents more non-tidal internal wave power than the S_2 band. Since the N_2 band is less variable in power levels with depth, we might conclude that internal tides are more variable in energy levels in the vertical than non-tidal internal waves. This difference may be a result of the different modal compositions of the different types of internal waves: where the background continuum of internal wave may exist as a superposition of many high order modes and give profiles of horizontal kinetic energy resembling the N(z) profile, the true internal tides may exist as lower order modes which would show such a greater relative variation of energy with depth.

1.6 Generation of internal tides near Site D

In Figure 1.2.1, Fofonoff's calculation shows a characteristic for M_2 period internal waves running nearly tangent to the continental slope, with areas of actual critical bottom slope found near 200 m and 1000 m depth. Theoretical studies including those of Hurley (1969) and Baines (1974) have shown that such critical slopes are effective generation regions for internal waves when they form part of the boundary of a fluid which oscillates at the appropriate frequency. The current fields in such cases are characterized by jetting flows in the neighborhood of the characteristics leading from the critical slope regions. For the Site D geometry, where the boundary is globally nearly tangent to a characteristic surface, quite complicated baroclinic motions can be expected.

The tangential characteristic intersects the ocean bottom at the base of the slope, and is continued by reflection along another characteristic rising to the south. This characteristic intersects the surface near the latitude of Site D, and it was Fofonoff's original suggestion that the intense currents noted there at semidiurnal tidal frequency were related to the coincidence of bottom and characteristic geometry. The critical slopes for internal waves of astronomical N_2, M_2 and S_2 frequency differ only slightly, and

at Site D take on values of 2.94°, 3.04° and 3.23° from the horizontal respectively, for an average value of $N = 2 \times 10^{-3}\ s^{-1}$.

Figure 1.6.1 shows a more detailed picture of the near surface characteristic geometry for M_2 frequency internal waves at Site D, based on the average stratification in the upper levels. In a bundle of characteristics rising from the base of the slope, as a continuation of characteristics from a generation region on the slope, the southerly and upward group velocity would be accompanied by a phase propagation in a southward and downward sense, normal to the characteristics (Phillips 5.4, 1969). At a surface which is horizontal, the vertical component of velocity must vanish. For a case of constant N, from Equation 1.2.15 the characteristic coordinates are

$$\xi = x - z/\gamma$$

$$\eta = x + z/\gamma$$

and $\xi = \eta$ is the equation of the free surface $z = 0$. If the vertical velocity component is given by the general solution of the field equation 1.2.13

$$w = A(\xi) + B(\eta)$$

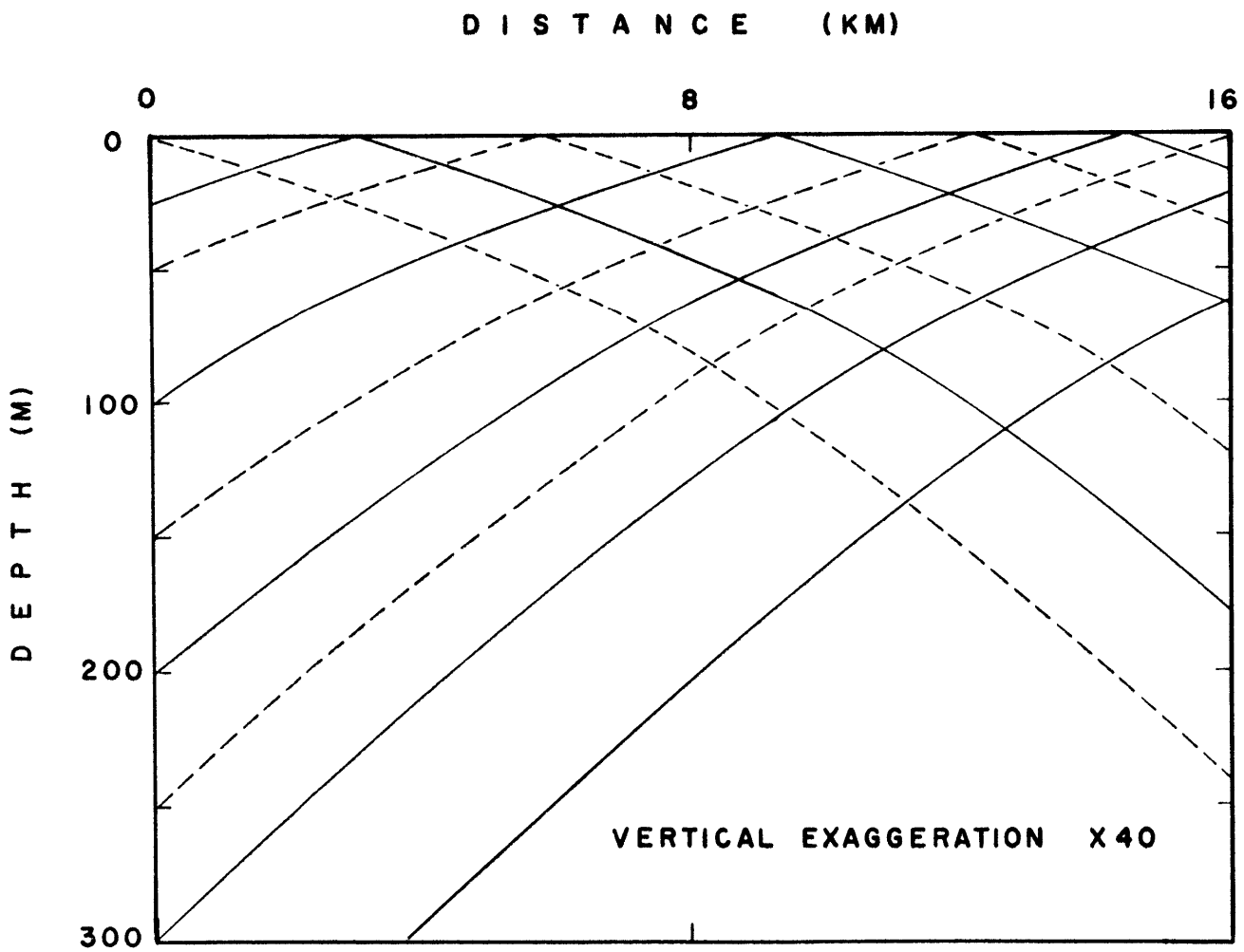


Figure 1.6.1 Near-surface characteristic curves for M_2 frequency internal waves and the average Site D stratification.

then on the upward sloping characteristic to the south, $\xi = \xi_o$,

$$w = A(\xi_o)$$

Following Baines (1973), on a characteristic continuing from the incident characteristic after a surface reflection which is given by the equation $\eta = \eta_o = \xi_o$,

$$w = B(\eta_o)$$

and the surface boundary condition requires

$$A(\xi) + B(\eta) = 0 \qquad \text{on } \xi = \eta$$

or $$A(\xi_o) = -B(\xi_o)$$

The 180° phase difference between A and B as a function of the characteristic coordinates then satisfies the surface boundary condition. For horizontal velocity components, the equation of continuity 1.2.7 can be integrated to give

$$u = (A(\xi) - B(\eta))/\gamma$$

so if $$u = A(\xi_o)/\gamma \qquad \text{on } \xi = \xi_o$$

then $$u = -B(\eta_o)/\gamma = A(\eta_o)/\gamma \qquad \text{on } \eta = \eta_o$$

The horizontal current fluctuations associated with the incident and reflected characteristics have the same phase.

In Figure 1.6.1, energy arriving on characteristics from the north will have a southward component of phase velocity as well as a downward component, while the surface reflected motion will have the same southward component of phase velocity but now an upward component. Near the free surface the vertical components of phase propagation are opposed and set up a standing pattern in the vertical, but the horizontal phase propagation continues and will be to the south for a generation region at the slope to the north. Deeper in the water column, the sharp spatial gradients associated with the characteristics leading back to critical slope regions will make aliasing a major problem in any practical measurement situation.

Current observations

In Section 1.5 it was seen that the total variability in the semidiurnal frequency horizontal currents was notably depth dependent, as is characteristic of internal wave fluctuations. A barotropic current mode contributes equal energy to all depths. The dominant clockwise polarization of internal wave horizontal currents in the northern hemisphere was also observed in the near surface M_2 frequency

currents. Since the barotropic tide has length scales of the same order as the oceanic basins, boundary effects can result in any particular polarization in the barotropic current ellipse.

As described in Section 1.4 and Appendix A.2, coherences between the current components at depth levels and the equilibrium tide were calculated. These estimates are presented in Table 1.6.1. They have a finite number of degrees of freedom, and their significance is a statistical problem. There is evidence for significant coherences between the currents and the tidal forcing, and as the current field may contain both barotropic and baroclinic components it is necessary to separate the two types of motion in order to discuss the question of generation in the internal tides.

As seen in Table 1.6.1, the M_2 frequency motions are significantly coherent at more depth levels than the adjacent frequencies. At the southern site, all depths except 125 m give coherence amplitudes significantly greater than zero at 95% confidence for the u component, while for the v component significant amplitudes are noted at the very near surface and at three deeper levels. At the southern site the deep currents have generally higher values of coherence than the nearer surface currents. The northern site, with fewer degrees of freedom, still has significant coherence amplitudes for the M_2 frequency motion in both u and v

	Depth (m)	N_2 u	N_2 v	M_2 u	M_2 v	S_2 u	S_2 v	No.of pieces	Bias	95%
SOUTH	25	.14	.10	.44	.53	.16	.13	32	.16	.30
	75	.09	.06	.30	.09	.24	.28	32	.16	.30
	125	.14	.03	.38	.16	.30	.12	13	.25	.47
	200	.10	.19	.46	.31	.23	.14	18	.21	.40
	500	.45	.41	.92	.89	.77	.13	3	.53	.88
	1000	.61	.32	.78	.55	.45	.13	14	.24	.46
	2000	.62	.44	.91	.67	.67	.36	7	.34	.63
	2500	.42	.30	.68	.23	.20	.18	30	.16	.32
NORTH	25	.35	.12	.40	.57	.33	.28	9	.30	.56
	75	.16	.26	.70	.75	.39	.28	16	.22	.43
	125	.19	.09	.37	.30	.11	.15	14	.24	.46
	200	.36	.35	.53	.54	.75	.81	6	.37	.67
	500	.65	.52	.50	.51	.29	.10	9	.30	.56
	1000	.35	.22	.47	.23	.28	.15	16	.22	.43
	2000	.51	.24	.48	.14	.51	.27	8	.32	.59
	2500	.39	.40	.29	.37	.36	.39	5	.41	.73

Table 1.6.1

Amplitudes of coherence between semidiurnal current components and the equilibrium tide, as a function of depth, with the number of degrees of freedom in the estimates and the bias and 95% confidence limits for zero true coherence.

components at the near surface level, while the deeper currents and especially the v component show less coherence.

The S_2 and N_2 currents are generally not coherent with the corresponding equilibrium tides at the 95% level, although there are instances of apparent coherence. For a truly incoherent process, we would expect only about one case in 20 to show coherence values greater than the 95% limits quoted in Table 1.6.1. As discussed by Munk and Cartwright (1966), finite estimators of coherence amplitude tend to be positively biased, with the bias decreasing as the true coherence and the number of degrees of freedom in the estimates increases. They use an approximate method to attempt to remove this feature. In Table 1.6.1 we include the expected value of our finite estimates of coherence amplitude for zero true coherence, given the number of degrees of freedom (Amos and Koopmans, 1963). The 95% confidence criterion is much stricter than merely having estimates larger than the expected value for zero true coherence. Coherence phase estimates are unbiased.

Given the evidence for a deterministic part of the tidal current fields, average currents were computed by averaging the individual Fourier coefficients for u and v components, with the phases of each such component referred to the equilibrium tide. The resulting average phases are essentially

equal to the coherence phases, while the amplitudes estimate the coherent tidal period signal. The averages are given in Table 1.6.2 for all three frequencies, but the significance of any individual average is directly related to the corresponding coherence amplitude in Table 1.6.1.

In the profiles of estimated coherent currents, the baroclinicity in the M_2 profiles remains. The very near surface currents are especially strong, with the deeper still uniform. The u component remains the more energetic. The estimates of deep M_2 currents from the northern site are somewhat smaller than those at the southern site, relating to the lower coherence amplitudes at the north. The surface intensification in coherent currents again supports the concept of especially energetic motion near the characteristics leading from the critical slope regions to the north of the site.

The N_2 estimates of coherent current show little depth dependence, even though the overall power near the surface in the N_2 band was generally 15 times greater than in the deepest levels (Table 1.5.1c). The lower coherence amplitudes in the upper depth levels result in most of the variability being averaged out in the coherent estimates. Although the S_2 band apparently shows some intensification in near surface currents at the northern site, they are not very meaningful statistically

	Depth (m)	u (cm/s)	Phase	v (cm/s)	Phase
	25	.33	-147	.28	-110
	75	.49	-129	.54	-048
S	125	.44	146	.09	-152
O	200	.43	-180	.32	-114
U	500	.27	-044	.05	-007
T	1000	.21	031	.05	066
H	2000	.36	081	.16	157
	2500	.11	058	.09	-098
	25	1.2	037	.95	089
	75	.85	104	.48	-130
N	125	.20	-046	.24	007
O	200	1.2	-109	1.6	-014
R	500	.22	138	.06	-076
T	1000	.22	048	.12	147
H	2000	.31	028	.10	046
	2500	.14	-075	.18	063

Table 1.6.2a

Coherent current amplitudes and phases for the S_2 band as a function of depth for the two areas of Site D.[2]

	Depth (m)	u (cm/s)	Phase	v (cm/s)	Phase
SOUTH	25	2.1	012	2.4	084
	75	.79	082	.22	-158
	125	.94	057	.42	132
	200	1.1	048	.64	144
	500	.94	072	.51	143
	1000	.98	062	.37	132
	2000	1.2	055	.48	105
	2500	.72	049	.16	178
NORTH	25	1.5	061	2.4	-147
	75	2.2	064	1.9	169
	125	.94	031	.70	119
	200	1.1	022	1.2	090
	500	.60	023	.42	077
	1000	.48	082	.15	094
	2000	.39	047	.06	-064
	2500	.27	-162	.30	-070

Table 1.6.2b

Coherent current amplitudes and phases for the M_2 band as a function of depth for the two areas of Site D.

	Depth (m)	u (cm/s)	Phase	v (cm/s)	Phase
SOUTH	25	.31	-019	.25	055
	75	.08	160	.07	-017
	125	.63	067	.31	152
	200	.23	-143	.30	002
	500	.38	059	.32	129
	1000	.28	060	.10	144
	2000	.32	050	.15	125
	2500	.27	054	.20	155
NORTH	25	.22	152	.36	088
	75	.09	033	.14	-030
	125	.36	159	.12	092
	200	.55	-022	.40	082
	500	.31	036	.35	103
	1000	.30	061	.21	151
	2000	.31	011	.11	061
	2500	.24	-141	.24	-034

Table 1.6.2c

Coherent current amplitudes and phases for the N_2 band as a function of depth for the two areas of Site D.

as evidence of true surface intensification of a deterministic S_2 internal tide.

Evidence for wave propagation in the current field, and of directionality in the energy flux, must come from the phases of the currents. Since the barotropic wave has very great horizontal scales compared with the resolution of the Site D coverage, we would expect any measurable phase change across the site to be associated with internal modes. Since only the M_2 band shows large enough coherence amplitudes to have any confidence in the results, the discussion of determinism in the baroclinic fields will be confined to the M_2 motion. The lower signal to noise ratios in the adjacent frequency bands can be due to a number of factors, as discussed in Section 1.8. Referring to Table 1.6.2b, the M_2 v component at the northern site leads the v component at the southern site by 129°. The 95% error bars on the individual estimates of v component phase are about ±35° for the southern site and ±50° for the northern site, and the phase difference is quite significant. This phase propagation from north to south gives an effective north-south wavelength of 45 km based on a 16 km separation. From the previous discussion of phase propagation expected near the surface for a generation region to the north, the phase difference implies an energy flux away from the continental slope.

Wunsch and Hendry (1972) interpreted a measured phase progression of M_2 currents across a small array on the continental slope north of Site D as evidence of internal tide generation on the slope to the south of the array, and a resulting shoreward energy flux. The examination of the currents at Site D itself gives the first direct evidence for a seaward energy flux from the slope generation region.

In the tabulation of phases of coherent current estimates in Table 1.6.2b, note that below the very near surface the south site actually tends to lead the north site even though the phase differences are not individually very significant. As discussed earlier, this is consistent with a beam-like structure in the internal wave fields and spatial aliasing. On a single characteristic and its continuation from a surface reflection, the phase of the horizontal currents is constant. Phase progression normal to the characteristics for seaward energy flux would have the currents just seaward of the upgoing incident characteristic lagging the currents just shoreward of the downgoing reflected characteristic. If the internal waves are truly beamlike in their spatial variation, an almost prohibitive amount of spatial coverage would be required for a comprehensive description, given the temporal variability which is also present.

Expansion in normal modes

As described in Section 1.2, any field of internal waves over a flat bottomed ocean can be uniquely expressed as a superposition of discrete, horizontally propagating modes. Both the characteristic description and the normal mode description give the same results, being different ways of describing the same physical situation. Rattray, Dwarski, and Kovala (1969) worked out an internal wave generation model in a constant N ocean with a step continental shelf. A barotropic wave incident on the shelf was the source of excitation of the internal waves, and the physical radiation condition was fulfilled by only admitting modes which carried energy away from the generation region. Matching conditions at the boundary between the deep ocean and the shelf are used to determine the amplitudes and phases of the different modes. For such model generation regions as a step shelf, the sharp corner of the discontinuity at the shelf break is equivalent to a region where the bottom slope is critical, and the jetting current fields require large numbers of modes in any adequate description. Prinsenberg, Wilmot, and Rattray (1974) have extended this model to examine the effects of a sloping shelf by using the shelf normal modes described by Wunsch (1969), and by including dissipation in the step shelf case with a constant eddy diffusivity. Rattray, Dwarski and Kovala used the first 100 normal modes and Prinsenberg, Wilmot and Rattray

at least 45 modes to represent the motion in the deep water for the inviscid case, and the effects of truncation were still evident in the fine details of the calculated fields. The inclusion of friction and diffusion in the latter work smoothed out the current profiles considerably. Higher order modes have a greater rms shear for a given amplitude and are more heavily damped as they propagate away from the shelf, and the resulting currents require fewer terms in a modal expansion for an adequate description.

For the inviscid, constant N models in the two studies described, the amplitude of the n^{th} baroclinic mode in the deep ocean expansion is proportional to

$$\sin(n\pi H_1/H_2)/(n\pi H_1/H_2) = \text{sinc}\ (n\pi H_1/H_2)$$

where H_1 is the depth at the shelf break and H_2 the deep ocean depth. The expansion must match the condition of zero flow into the boundary for $-H_2 \leq z \leq -H_1$, and this is reflected in the behavior of the modal coefficients like the diffraction function $\text{sinc}(n\pi H_1/H_2)$. The slope north of Site D is not a step, but only the steepest parts of the slope near 1000 m and 200 m depth are supercritical slopes for M_2 frequency internal waves. Relating the 1000 m depth area of critical slope to the corner regions in the step shelf models suggests $H_1/H_2 \sim 1000/2600$, and for such a case the first three

baroclinic modes would contain about 90% of the internal wave energy, with the majority in the first baroclinic mode. For a step depth of 200 m however, the first three modes contain less than half the power, and the first 10 modes contain only about 80%. The actual case at Site D is complicated by the finite extent of the slope and the two critical regions, and by the non-constant N(z) profile which determines the actual shape of the normal modes in the vertical. For example the first baroclinic mode has a zero in horizontal current at about 675 m depth, and the bottom current in this mode is less the 20% of the surface current. The structure in both the geometry of the generation region and the current modes means that the uniform decrease in modal amplitude given by the diffraction function will not apply, although for high enough mode number the amplitudes must decrease at least as fast as 1/n for the expansion to converge.

In the models with a vertical continental slope, the region of the deep ocean below the characteristic which glances the shelf break shows a reduced total horizontal current, as the effects of the stratification of the ocean tend to block the flow in this region. The total horizontal transport in the barotropic wave is conserved by the jet-like features in the profiles of horizontal current. At Site D

this glancing characteristic is nearly tangent to the slope over large areas, and so the region of expected near blocking is small. However in this near resonant case of internal wave generation the separation of the baroclinic and barotropic modes is at least a difficult observational problem, and on the slope itself the barotropic and baroclinic parts of the flow will be highly coupled.

We attempted a modal decomposition of the estimated current profiles for the M_2 currents at the two nominal sites. Baroclinic mode shapes for M_2 internal waves in a flat bottomed ocean were calculated numerically, based on average N(z) profiles from Site D. The averages were over all seasons in the years 1965-72, but since the years 1971-72 were anomalous in surface temperature, being notably warmer than in the previous five years, a separate calculation was done for the later period as well to estimate the stability of the modes with respect to such perturbations. The resulting modal wavelengths and propagation speeds for the first five modes are given in Table 1.6.3, where we see that there was little change in the modes over the two periods. Thus the lower order modes are quite stable from year to year, but Section 1.8 contains a discussion of possible seasonal variability which may be quite significant. The average hydrography of the Site is tabled in Appendix A.3 for reference.

Mode number	Wavenumber (km^{-1})	Wavelength (km)	Equivalent depth (cm)	Phase speed (cm/s)	Group speed (cm/s)
1965-1972 average					
1	$.755 \times 10^{-1}$	83.2	20.2	186	107
2	.146	43.0	5.41	96.3	55.1
3	.197	31.9	2.98	71.3	40.8
4	.262	24.0	1.68	53.6	30.7
5	.326	19.3	1.09	43.2	25.7
1971-1972 average					
1	$.752 \times 10^{-1}$	83.6	20.4	187	107
2	.142	44.4	5.74	99.2	56.8
3	.190	33.1	3.21	74.1	42.4
4	.255	24.6	1.77	55.1	31.6
5	.314	20.0	1.17	44.8	25.7

Table 1.6.3

Modal parameters for M_2 internal waves at Site D. The first five baroclinic modes for the average density profile in all seasons from 1965-1972 are characterized, and the calculation is repeated for the average during 1971-1972 alone.

Since there were eight levels in the average vertical profiles, there was a constraint on the number of modes which could be used in a fit without the calculation becoming unstable. Any set of eight modes would give an exact fit to the eight points, but without any dynamical significance. We used a depth independent barotropic mode and the first three baroclinic modes in the final calculation. The modal amplitudes used are given for the standard depth levels in Table 1.6.4. The models of internal wave generation indicate that a relatively large fraction of the energy and energy flux will be associated with the lower order modes, although the detailed structure of the current field depends on all orders of the normal modes. The result of having averaged over finite vertical and horizontal regions, and over all seasons, will be that higher order modes with small spatial scales and greater relative sensitivity to changes in stratification will be severely filtered. Although aliasing is a possibility, the very high order modes will more likely appear as random noise in the averages. Thus the choice of relatively coarse spatial averages, governed by the data availability, and the use of a limited number of low order modes in the fits are internally consistent.

Least square fits were calculated for the M_2 profiles of u and v components at the south and north sites. The

Depth (m)	Mode number 0	1	2	3	Weight
1965-1972 average					
25	1.00	3.33	2.87	3.58	1
75	1.00	2.94	1.62	.786	1
125	1.00	2.60	.732	-.800	1
200	1.00	2.09	-.337	-1.98	2
500	1.00	.374	-1.57	-.093	10
1000	1.00	-.287	-.689	.953	15
2000	1.00	-.620	.756	-.385	15
2500	1.00	-.687	1.17	-.994	11
1971-1972 average					
25	1.00	3.51	3.31	3.70	1
75	1.00	2.97	1.54	.207	1
125	1.00	2.58	.504	-1.27	1
200	1.00	1.99	-.643	-2.12	2
500	1.00	.360	-1.52	.203	10
1000	1.00	-.265	-.647	.966	15
2000	1.00	-.618	.741	-.411	15
2500	1.00	-.682	1.08	-.975	11

Table 1.6.4

Mode shapes for currents used in the fits of Site D tidal currents. The weight factors were used in the fits as described in Section 1.2.

method used is as described in Section 1.2. The four mode fits represented in all cases at least 75% of the summed variance at the eight depths. Since at some levels the actual coherences between the currents and the equilibrium tide were low, it is difficult to assign any error bars to the modal amplitudes and phases. However the fits do represent another projection of the results which we can attempt to interpret. The fitted amplitudes and phases (minus kappa) are presented in Table 1.6.5.

For the southern site, the amplitudes of the three baroclinic modes are quite similar, with the v components associated with modes 1 and 3 being larger than for the corresponding u components. This would be the case for internal waves propagating in a north-south direction. The second mode has nearly equal u and v components. The barotropic estimate from the southern site will be compared to estimates from other investigations in Section 1.5, and we will see that the agreement is quite reasonable. The modal decomposition at the northern site shows a considerably different character. The barotropic mode in the fit is less than half as large as for the southern site, although the phases of the fits at both sites are nearly identical. The weaker apparent barotropic current at the northern site is effectively due to the reduced coherences at the deeper levels there, and resulting small coherent current estimates.

	Mode number	Amplitude u	Amplitude v	Phase u	Phase v	$\%u^2$	$\%v^2$
SOUTH	0	.97	.40	057	125	95.5	67.7
1965-1972 modes	1	.06	.12	341	109	.4	6.4
	2	.17	.15	335	040	3.0	9.3
	3	.11	.20	010	070	1.1	16.6
SOUTH	0	.97	.40	058	126	95.3	65.6
1971-1972 modes	1	.06	.13	342	107	.4	6.8
	2	.18	.17	337	045	3.3	11.9
	3	.10	.20	010	072	1.0	15.7
NORTH	0	.42	.11	054	123	49.1	4.2
1965-1972 modes	1	.36	.31	034	147	35.1	33.4
	2	.11	.32	155	235	3.2	36.0
	3	.21	.28	109	223	12.6	26.4
NORTH	0	.41	.11	054	120	49.7	4.0
1971-1972 modes	1	.36	.32	036	149	37.1	33.5
	2	.12	.35	155	236	3.9	41.3
	3	.18	.25	112	228	9.3	21.2

Table 1.6.5

Modal fits of coherent M_2 currents at the south and north sites, using the two separate modal calculations. The percentage of signal power fit by each mode is given.

The northern fit first mode accounts for much of the total variance in current. While the southern site lies nearly at the intersection of the central characteristic leading back to the slope and the surface, this characteristic cuts the northern site at about the 200 m level. The near surface behavior in the fields is well resolved by the distribution of measurements, but such resolution is lacking below 200 m and the possibility of aliasing is great at the northern site where most of the energy may be located outside of the range of the measurements. Although the true barotropic mode is probably not greatly altered between the north and south sites, phase locking between the internal waves and the barotropic wave means that good resolution in time to average out noise at a finite number of depths is not enough to separate the modes: good resolution in the vertical is also a requirement. At the southern site we are fortunate that the measurements and the principal features of the fields we are trying to measure apparently coincide.

These considerations mean that the northern site modal decomposition is suspect, and the southern site will be used to obtain numerical estimates of the energy density and flux in the low mode internal tide. Except for the first mode, the northern fit gives greater v components than u components, indicating a north-south propagation bias as for modes 1 and 3 at the south. It is still of interest to compare the phases of the fitted modes at the two sites.

The phase differences between the individual baroclinic modes at the two sites can be used to estimate the apparent wavelength of the variations fitted by the modes, and make a comparison with the theoretical values of modal wavelength. This assumes propagation is a north-south sense so that the wavenumbers are not affected by oblique incidence onto the two point "antenna". Table 1.6.6 gives the phase lead of the northern site over the southern site for the modes fitting the u and v components, and the resulting wavelengths based on a 16 km separation. Since there are only two points in the horizontal, and the phases are indeterminate up to a multiple of 360°, the phase differences also show this ambiguity. The wavelengths given in Table 1.6.6 are for the two cases of numerically smallest phase difference, so assuming either northward or southward propagation depending on the resulting sign of the phase difference. The choice between north or south propagation must be made on further physical grounds.

For reasonable wavelengths, the first mode for both u and v components must be assigned southward propagation by choosing the numerically smaller value of the possible phase differences. This gives wavelengths which agree with the calculated first mode wavelength to within a factor of two. The southward phase propagation implies a southward

Mode number	Phase lead of northern site		Apparent wavelength (km)		Theoretical wavelength (km)
	u	v	u	v	
1965-1972 average modes					
1	053	037	109	154	83
	-307	-323	19	18	
2	179	195	32	30	43
	-181	-165	32	35	
3	099	154	58	37	32
	-261	-206	22	30	
1971-1972 average modes					
1	053	043	108	135	84
	-307	-317	19	18	
2	178	192	32	30	44
	-182	-168	32	34	
3	103	156	56	37	33
	-257	-204	22	28	

Table 1.6.6

Inferred wavelengths of the first three baroclinic modes in the M_2 current fits. The first value given is appropriate for southward propagation and the second for northward propagation. Theoretically calculated wavelengths for the modes are given.

energy flux (Equations 1.2.31 and 1.2.37). A choice of propagation direction for modes 2 and 3 on the basis of a consistent wavelength is moot, but both modes show horizontal scales consistent with the shorter wavelengths of the theoretically calculated modes as compared to the first baroclinic mode.

Recalling the discussion of the near surface currents, the phase differences in the upper level v components gave an effective north-south wavelength of 45 km with a southward propagation. The error bars on the phase difference would even accomodate a first mode wavelength at their extremes, but the nominal estimate lies between the values for modes 2 and 3. In general terms, the conclusions from the two approaches are the same, that there is evidence for a southward flux of internal wave energy, away from the slope generation region.

Energetics of the internal tide

Estimates of the depth and time averaged horizontal kinetic energy in the three semidiurnal bands have been given in Table 1.5.2. The agreement between north and south sites is reasonable, and as noted previously the M_2 band has between 2 and 3 times as much energy as either of the adjacent bands. The same integration for the estimated coherent M_2 horizontal kinetic energy gives $.93 \times 10^5$ erg/ cm^2 for the southern site

and .45 x 10^5 erg/ cm^2 for the northern site,so the total incoherent plus coherent power in the M_2 band averages about three times the coherent power. This overall signal to noise ratio of 1:2 is equivalent to a coherence amplitude of about .6, but the noise is not equally distributed in the water column. The M_2 u components at depths show larger coherences than the nominal figure, while the surface currents are much more noise dominated.

Estimation of the baroclinic contribution to the energy flux is more difficult. If the modal composition of the fields were known, the energy flux could be calculated as the sum of modal energies times group speeds. The group speed of the modes decreases with increasing mode number, and in a constant N step-shelf model where the amplitude of the deep ocean internal waves decreases like $\mathrm{sinc}(n\pi H_1/H_2)$, the energy flux contribution from the modes decreases like $(1/n)\mathrm{sinc}^2(n\pi H_1/H_2)$, and the lower order modes are much more effective carriers of energy. For the modal fits to the coherent currents, energy flux estimates were made by assuming a southward propagation and using the v component to define the internal wave major axis for horizontal current. At the southern site the result is an energy flux of .6 x 10^6 erg/s cm in the first three modes. The northern estimate is about four times larger, mainly because of the larger first mode in the fit there, but the northern modal decomposition is highly suspect.

The first baroclinic mode has the largest group speed, and can be used to obtain an upper bound on the energy flux in the internal tide. Assuming that the total horizontal kinetic energy at the southern site is related to a first mode wave, the total kinetic plus theoretically related potential energy multiplied by the first mode group speed gives an energy flux of $.3 \times 10^8$ erg/s cm. This is two orders of magnitude greater than the estimate for the energy flux in the first three baroclinic modes at the southern site, since much of the kinetic energy is actually due to the barotropic and higher order baroclinic modes. The upper bound can be used in the discussion of tidal dissipation in Section 1.7 which follows.

For comparison, Baines (1974) computed the baroclinic energy flux seaward for a realistic slope geometry and stratification modelled after the slope just west of Site D, obtaining an average of $.12 \times 10^7$ erg/s cm over all seasons. This is of the same order of magnitude as the estimates for energy flux in the first three baroclinic modes fitted to the coherent M_2 currents at the southern site. Baines' calculation results in about 70% more energy flux into the deep ocean than onto the shelf on average. Wunsch and Hendry (1972, with a correction for a numerical error) obtained an estimate of the shoreward M_2 energy flux in the internal tide at this more westerly slope to be $.6 \times 10^6$ erg/s cm.

1.7 Site D barotropic tide

The barotropic tide is the suggested source of energy for the observed internal waves. Also the observed current field includes the currents due to the barotropic wave, which is driven directly by the astronomical forcing. The whole eastern coast of the United States and much of the western North Atlantic between 50°N and 20°N show a surface tidal wave dominated by the M_2 frequency, and appearing much like a broad standing wave (Dietrich, 1963). High water occurs about 12 hours after the transit of the moon over the Greenwich meridion. Redfield (1958) did a nice analysis of the surface tides on the Atlantic coast using measurements taken at coastal stations. He assumed that the tidal wave on the continental shelf was a forced co-oscillation with the deep ocean tide, which travelled as a damped wave across the varying shelf. When the coastal high water times were extrapolated back to the 1000 m contour, Redfield found that with a reasonable frictional effect high tide occurred almost simultaneously in the deep water. Actual offshore tidal measurements are scarce. Hicks, Goodheart and Isely (1965) reported on two bottom pressure time series obtained near the 200 m depth contour north of Site D. The M_2 tide showed a phase difference of only about 2° for the 230 km east-west separation, with reported amplitudes of 38 and 40 cm and epochs of 000°G and 358°G for their two

short records after corrections were applied. A 30 day series of bottom pressures on the New England shelf at 40°32'N and 70°55'W in 111 m of water was taken in an experiment for Prof. R. Beardsley at M.I.T. (unpublished data). A preliminary tidal analysis of this record gave an M_2 amplitude of 43 cm and Greenwich epoch of 350°, which agrees reasonably with the earlier measurements of Hicks, Goodheart and Isely and supports their cotidal contours (Figure 1.7.1) which show a slight advance in the time of high water just south of Martha's Vineyard on the New England shelf. At Bermuda, isolated in the western North Atlantic, Zetler, Munk, Mofjeld, Brown and Dormer (1974) report an M_2 amplitude of 35.6 cm with Greenwich epoch 358°, not much different from the continental slope values. For Site D, we use the average of the earlier and deeper shelf measurements, for an amplitude of 39 cm, epoch 359°G.

Figure 1.7.1, adapted from Hicks, Goodheart and Isely, shows the M_2 cotidal lines north of Site D. The positions of the shelf measurements are marked on the chart. Just to the east and north of the site, the wave on the shelf shows a northeast progression into the Gulf of Maine, while to the south and west the tide appears as the more typical coastal standing wave. There is a slight phase propagation from deep to shallow water, an expected effect of coastal dissipation.

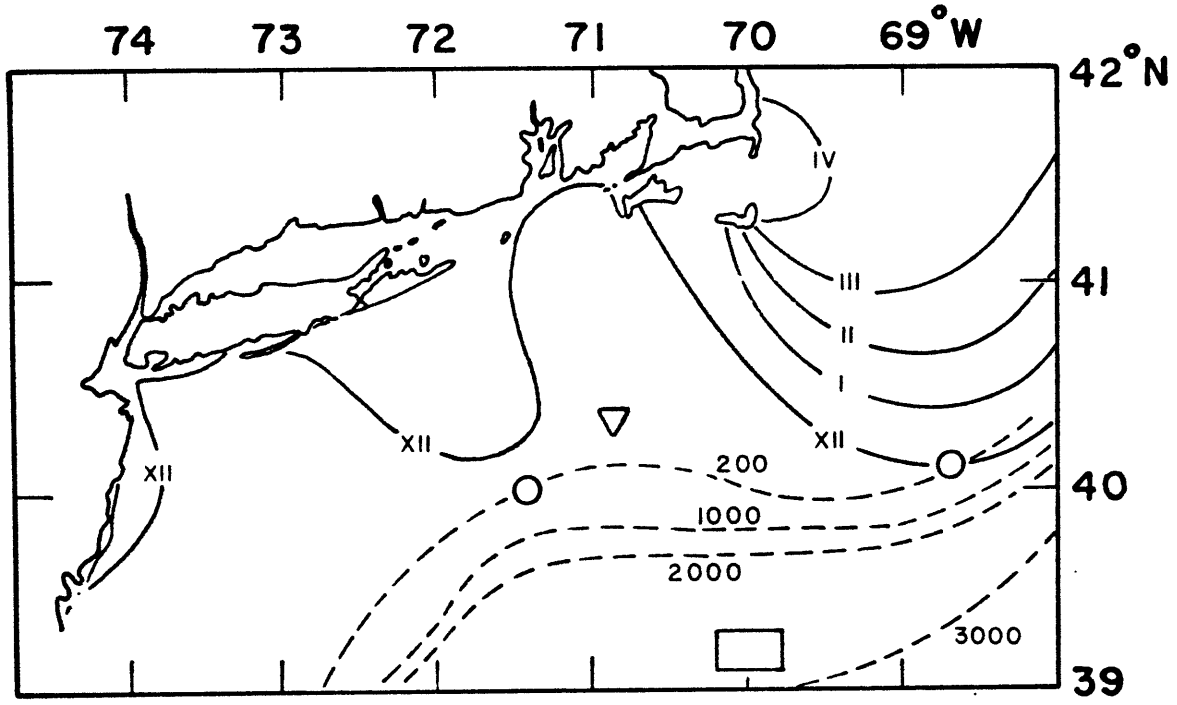


Figure 1.7.1 M_2 cotidal chart for the New England shelf, adapted from Hicks, Goodheart and Isely (1965). The depth contours are shown as dashed lines, with depths in meters. The solid curves are labelled with the interval in lunar hours between the moon's Greenwich transit and high tide. The circles indicate the positions of the earlier measurements described in the text, and the triangle marks the site of the recent bottom pressure measurements also discussed.

Magaard and McKee (1973) have made estimates of the barotropic M_2 tidal currents at Site D by modal decomposition of several months of current records at a single location. Their estimates are reproduced in Table 1.7.1, with the phases expressed as Greenwich epoch rather than with respect to an arbitrary time origin. The barotropic estimates of M_2 currents from the averaged records in the present study are also given there, obtained as described in Section 1.6. As previously noted, the northern site gave much smaller estimates then the southern site, although the phases were similar. The southern site barotropic estimates are in good agreement with the Magaard and McKee estimates in both magnitude and phase, and being further from the slope influence are considered the best estimates of the deep sea barotropic current.

The current and sea surface displacement completely characterize the local barotropic wave at Site D. Taking

$$u = U \cos(\sigma t - G_u) = .97(\text{cm/s}) \cos(\sigma t - 083)$$

$$v = V \cos(\sigma t - G_v) = .40(\text{cm/s}) \cos(\sigma t - 015)$$

$$\zeta = Z \cos(\sigma t - G_\zeta) = 39.(\text{cm}) \cos(\sigma t - 359)$$

then the average over time and depth of the horizontal kinetic energy density is $H(U^2+V^2)/4 = .77 \times 10^5$ erg/cm^2 for water depth 2800 m at the southern site. The potential

Source	u (cm/s)	G^u	v (cm/s)	G^v
South site	.97	083	.40	015
North site	.42	086	.11	017
Magaard and McKee (1)	1.1	083	.48	021
(2)	.85	073	.34	008

Table 1.7.1

Barotropic M_2 tidal currents at Site D, by modal decomposition of average currents. The north estimate is suspect as described in the text, but the phases of the two fits agree remarkably. Estimates from Magaard and McKee (1973) are included, and agree well with the southern fit.

energy in the wave has a time average $gZ^2/4 = .37 \times 10^6$ erg/cm^2, and the total energy density is then $.45 \times 10^6$ erg/cm^2. The volume fluxes in the east and north directions are HU = $.27 \times 10^6$ cm^2/s and HV = $.11 \times 10^6$ cm^2/s respectively. The energy flux in the tidal wave is the correlation between current and pressure, with components

$$(gHUZ/2 \cos(G_u - G_\zeta), gHVZ/2 \cos(G_v - G_\zeta))$$

High water occurs only 16^o before the maximum northward flow, and most of the energy flux is directed towards the north and the continental shelf. The resulting estimates of energy flux are $.54 \times 10^9$ erg/s cm eastward and $.21 \times 10^{10}$ erg/s cm northward. These figures represent the rate of transfer of energy across a strip one cm wide and the depth of the ocean in vertical extent. The horizontal divergence of the energy flux gives the rate of energy dissipation from the surface tide, through bottom friction or conversion to internal waves for example. The flux divergence approach has been a basis for tidal dissipation studies since the classical work of Taylor (1919) in the Irish Sea. A review of tidal dissipation considerations is given by Munk (1968). In Section 1.6, we put an upper bound on the seaward energy flux in the internal wave field for the M_2 band, of $.3 \times 10^8$ erg/s cm, and doubling this to roughly account for shoreward

propagating internal waves still accounts for only about 3% of the northward energy flux in the barotropic wave. Thus the barotropic tide can easily provide the energy for all the internal waves seen, but the internal tides do not appear to figure prominently in the dissipation of the barotropic tide.

Miller (1966) estimated that less than $.1 \times 10^{17}$ erg/s are dissipated from the tides along the whole eastern seaboard of the United States from Cape Cod to Florida. Dividing this upper bound by a 2000 km coastline gives an average onshore energy flux of less than $.5 \times 10^{8}$ erg/s cm and considerably more than this is fluxing up onto the shelf north of Site D. However Miller has the Gulf of Maine - Bay of Fundy system as a relatively large sink of tidal energy, dissipating $.23 \times 10^{18}$ erg/s. A later modelling study of Garrett (1974) estimates that about $.99 \times 10^{18}$ erg/s may be dissipated in the system, increasing Miller's estimate by a factor of three. For the larger estimate and a 400 km distance from Cape Cod to southern Nova Scotia, there is an average net flux of about $.2 \times 10^{11}$ erg/cm s, about ten times greater than the onshore flux of tidal energy at Site D. The tidal wave observed at Site D may be partly dissipated by bottom friction on the continental shelf, but some of the energy fluxing northward through the site may propagate further on the shelf and eventually be dissipated in the Gulf of Maine.

1.8 Sources of noise and variability

The discussion of the semidiurnal internal tides at Site D has been largely in terms of two-dimensional wave theory. The slope to the north is quite lineated in the east-west direction for over 100 km on either side of the longitude of Site D, but it curves sharply to the south at about 71°30'W and the global generation problem is a three dimensional one. Waves arriving at Site D from different points on the slope would arrive at the site with a spectrum of phases and propagation directions, and could present a complex interference pattern. In a limiting case, given the random variability associated with waves from a single generation region, the internal tide at Site D could approximate a random field: band-limited and with a component of phase propagation seaward but without any particular correlation with the local equilibrium tide. However in fact there does seem to be a deterministic component of the internal M_2 tide at the site, but there is also a large fraction of incoherent energy at the tidal frequencies. Some of this may be a result of three dimensional aspects of the process.

Another natural source of variability is the seasonal change in density structure, especially near the surface. We have averaged over all seasons to gain a stable picture of the internal tide, and the seasonal modulations will

appear as noise. In the calculation of Baines (1974), the structure of the internal tide in space was very dependent on the details of the density field, and the overall energy levels on the deep ocean increased about 40% from winter to summer conditions. The average N(z) profiles do not show a surface mixed layer which is sometimes present at Site D, and Baines showed that the lower limits of such a mixed layer acted as a reflector of internal wave energy. Magaard and McKee (1973) used fall hydrographic data from Site D to calculate M_2 frequency internal wave modes. Their calculation gave a first mode wavelength averaging 108 km, compared to the 83 km for the average hydrography of the site, and similar differences for higher modes. Fall conditions at the site include a weakly stratified surface layer and a zone of higher than average N(z) near 50-100 m depth (unpublished seasonal profiles, W.H.O.I.). The experiment of Magaard and McKee was further complicated by the presence of a warm eddy which affected the surface 500 m.

From equation 1.2.25, to first order in small perturbations in N(z) by $\delta N(z)$,

$$\delta k^2/k^2 = - \int_{-H}^{o} \delta N^2(z)\Phi^2(z)dz \Big/ \int_{-H}^{o} N^2(z)\Phi^2(z)dz$$

where $\Phi(z)$ is an eigenfunction of vertical velocity for the unperturbed density profile with eigenwavenumber k. For a

step change in N(z) from .6 x 10^{-2} s^{-1} to 1.2 x 10^{-2} s^{-1} over a 50 m level near 100 m, the average Site D first baroclinic mode is perturbed in squared wavenumber by

$$\delta k^2/k^2 = -.05$$

independent of frequency in the hydrostatic approximation. The relative increase in wavelength is 22%. This would increase a first mode wavelength of 83 km to about 102 km. The suggested perturbation of N(z) is a reasonable one for seasonal changes at Site D. The effect of such changes would be a seasonal modulation of phase measured at a fixed point, as

$$\delta\phi = \delta k\ L$$

where L is the distance from the observation site to the generation region where the phase of the internal mode is fixed by the barotropic tide. Even for the lowest baroclinic mode the perturbation calculated gives a phase modulation of ±40° for L = 50 km, and higher modes are even more seriously affected. The Site D measurements are really in the near field of the generation region and large changes in modal amplitude and phase may be expected as the varying density field in the generation region changes the coupling

between the topography and the barotropic and baroclinic currents. The modal parameters for the seasonal average are stable, as shown by the separate calculations for 1965-72 and 1971-72, but significant seasonal variation is expected. Within a given season, low frequency variations in current and density can cause random phase shifts in the internal tide.

The problem of measurement reliability must also be faced. In Section 1.2 we noted that measurements from surface-moored experiments taken below 250 m were excluded from the study. Indications are that rapid vertical accelerations of the surface float by high frequency surface gravity waves are transmitted down the mooring lines to the current meters. The Savonius rotor used as a speed sensor can give apparent horizontal velocities greater than the true values when it is subjected to such vertical motion (McCulloch, personal communication). Since the actual flow speeds in the deep water are small compared to the surface currents, the deeper measurements are especially vulnerable to this contamination. Near surface measurements are of necessity taken from surface moored instruments, and the effects of mooring motion on such measurements are not completely resolved. This is especially true for the effects of mooring motion on the very near-surface measurements such as those above 50 m in this study. Gould and Sambuco (1975) have studied this problem, and for a

comparison between about 1 record-year of current data from surface moored measurements at Site D at the 100 m level and about a third as much data from sub-surface moored measurements at the same level, they observed that there was three times as much power in the total current field as measured from the surface moored case. The contamination could not increase the coherence of the tidal frequency signal, and the sharp increase of current power at the uppermost level in the southern site in particular, for M_2 frequency waves, is accompanied by a highly significant increase in coherence.

1.9 Conclusions

The semidiurnal current field at Site D is dominated by the M_2 lunar tidal frequency, with power levels 2 - 3 times greater than found at adjacent frequencies with a separation of ±1/15 cpd. For comparison, a 30 day record of bottom pressures on the continental shelf north of Site D showed the astronomical M_2 frequency variation in sea level height to be about 20 times more energetic than the astronomical N_2 frequency, and about 12 times greater than the S_2 frequency. The presence of internal waves in the current field which can be Doppler shifted by low frequency variations in current produces a smoother variation with frequency than in the line spectrum of the surface tide.

The baroclinic components of the current field produce motions highly intensified near the surface, with more constant power at depth. The M_2 and S_2 tidal bands have a greater variation in energy level with depth than the nominal N_2 band. Since the 15 day record length used does not resolve the astronomical N_2 frequency from the M_2 frequency completely, only about half of the astronomical N_2 power turns up in the nominal N_2 band, while in the surface tide the N_2 variability is itself somewhat less than the S_2 tide. The energy levels in the currents in the nominal N_2 and S_2 bands are similar, but more of the N_2 band power is due to background internal waves rather than true tidal period variations. The resulting

differences in structure of the M_2 and S_2 currents, compared to the nominal N_2 currents, suggests that the internal tides are more dominated by low order modes than the background internal wave continuum.

The M_2 frequency currents show significant coherences with the equilibrium tide, and averaged coherent currents still show a variation of energy with depth characteristic of internal waves. This is evidence for a baroclinic current locked in a definite phase relation with the barotropic tide. Near surface currents show a phase propagation with a southerly component, which gives an energy flux away from the continental slope to the north. The average M_2 currents contained about 1/3 of the variance in the nominal M_2 band. Other semidiurnal frequency bands showed much lower coherences with the equilibrium tide. An expansion of the average M_2 currents in normal modes showed no general decrease of modal amplitude with mode number for the first three baroclinic modes. 40% of the observed M_2 power can be related to the barotropic current. Modal fits at an average north and south site gave a smaller barotropic component at the northern site, closer to the slope, which may be a result of measurement problems associated with the coupling of the barotropic and baroclinic modes. The first mode fits at the two sites gave a southward phase propagation with a wavelength in reasonable agreement with the calculated

theoretical first mode wavelength for both the u and v components of the current. Higher modes showed shorter spatial scales, as expected by theory.

Estimates of the baroclinic energy flux at the southern site gave $.6 \times 10^6$ erg/s cm to the south, while an absolute upper bound on the baroclinic energy flux is $.3 \times 10^8$ erg/s cm. The energy flux in the coherent currents is of the same order as theoretical predictions, and comparable to previous estimates of shoreward energy flux from the same slope generation region. The M_2 barotropic wave at Site D is shown to have a shoreward energy flux of about $.2 \times 10^{10}$ erg/s cm, much greater than the energy carried by the internal tides. Thus the barotropic tide can easily provide the energy source for the internal tides, but the internal tides do not figure significantly in the energetics of the barotropic wave.

Seasonal changes in the density field at Site D are an important source of measurement variability. Three-dimensional aspects of the generation problem and mooring motion are other possibilities for the source of the apparently incoherent part of the M_2 tidal current field.

SEMIDIURNAL TIDES IN MODE-1

2.1 Introduction

Since the beginning of the study of internal waves of tidal period in the ocean, dating perhaps from Nansen (1902), observations from coastal areas have been more comprehensive than observations in the deep ocean far from continental boundaries. Early work on internal tides showed that continental slopes or other topographic barriers could be effective sources of internal tides, with the barotropic tides the energy source for the process (Zeilon, 1934). Thus measurements near the continents could be in the near field of generation areas and differ from measurements in the deep ocean. However the great difficulties implicit in obtaining good observations far from centers of human activity have hindered the study of phenomena in the deep sea.

As early as 1910, Helland-Hansen (1930) had made deep ocean observations aimed at internal tides. Defant (1949) gives a review of some of this early work. During the late 1920's, A. Defant (1932) made stations with "Meteor" throughout the central east Atlantic Ocean, where the vessel was anchored in deep water and a series of soundings of temperature and current made. These were some of the first examples of oceanographic time series, designed to obtain information about internal tides. The need for a large research vessel as an observational platform precluded any very long series, and Defant's longest stations lasted only

a few days. He observed energetic fluctuations in isotherm depth and horizontal current, and related them to the tidal forcing and the dynamics of internal waves in a two-layer ocean. The method of anchor stations was continued by others, as Seiwell (1942) and Haurwitz (1952) reported on observations of internal waves of semidiurnal tidal period in the Atlantic Ocean.

The last two studies introduced new techniques into physical oceanography in recognition of the variability or randomness in the internal tide as a process. While the surface tide was predictable and ever present, the fluctuations in the temperature field showed an intermittent nature, sometimes being completely absent. Using the harmonic dial techniques introduced previously to the study of atmospheric tides, Seiwell attempted to average Fourier coefficients for lunar semidiurnal period isotherm displacements over depth to obtain more stability. While the motive was correct the method was not particularly enlightening except that in the particular case considered the phases at the various depths tended to group about two extremes, and could be duplicated by a fit with four normal modes. With longer series of observations, Haurwitz (1952) used the harmonic dial method on consecutive pieces of measurements from a fixed depth. Examining a number of the reported cases of

semidiurnal internal tides, Haurwitz concluded that while some of the observations probably represented true tidal period oscillations, other did not differ significantly from what the harmonic analysis of random noise would give at the tidal frequency. The introduction of statistical techniques to oceanographic analysis represented a step beyond simply generating the Fourier coefficients of the collected data.

With the development of deep sea mooring capabilities, time series of oceanic variables could be obtained for longer periods of time. In particular, the moored current meter program at the Woods Hole Oceanographic Institution showed that wherever measurements were made, there were liable to be energetic fluctuations of horizontal current at tidal period in the deep sea as well as near the coasts, and that these fluctuations were variable with depth in speed and phase. Reports by Day and Webster (1965) and Fofonoff and Webster (1971), while concentrating on other aspects of oceanic variability, noted that semidiurnal period energy was present.

The theoretical aspects of oceanic internal tides were developing as the observational picture improved. Fjelstad (1933) formulated a theory for internal gravity waves in a

continuously stratified ocean. Since the oceanic stratification was known to undergo changes in time and space, the medium in which the internal waves of tidal period travelled was variable one. Haurwitz (1948) investigated the effects of vertical shear in a mean flow on the propagation of internal waves. Some early studies attempted to explain the generation of internal tides by a resonance theory and the direct forcing of the moon and sun, but realistic calculations made it clear that the mismatch in spatial scales of the tide generating forces and oceanic internal waves made this mechanism completely insignificant.

In the last twenty years, much further work has been done. Rattray (1960) modelled the generation of long internal waves by the incidence of a surface wave on a depth discontinuity in a stratified fluid. This had been suggested as a mechanism by Zeilon (1934) who performed some of the earliest experiments in oceanographic geophysical fluid dynamics to demonstrate the feasibility of the method. The coastal generation model has been refined by various investigators, as described in Section 1.1. Further studies inquired into the effects of oceanic turbulence on internal tides as they propagated in space. LeBlond (1966), using a constant eddy viscosity to simulate the effects of turbulence, concluded that long internal waves such as internal tides

should be able to propagate very far into the ocean before being completely damped out, but that the damping effects were great enough to prevent the establishment of ocean-wide standing internal seiches at the tidal periods.

Waves from many different sources could propagate through the ocean to arrive at a given place, and with enough sources a complex interference pattern would result. If each source and propagation path were perturbed by a random forcing, the internal tide could be smeared into a random, though frequency band-limited process. Low frequency oceanic variability could provide such a forcing. Cox and Sandstrom (1962) advanced a linearized model which coupled the surface tide and internal modes by the varying ocean depth, providing a means of generating internal tides. A bottom with random roughness elements would produce an internal wave field with an exceedingly complex phase distribution, and the overall variability of the ocean would effectively randomize the process.

However, the picture of deep sea internal tides as a band limited random process would be accepted largely by default. The measurements that have been available certainly show variability in the tidal period motions which cannot be explained in any deterministic way, but they have generally been too limited to examine the possibility of determinism in the internal tides. With the advent of large mid-ocean

experiments we can begin to address this question. The existence of a deterministic internal tide in some areas of the oceans would give insight into the nature of non-tidal processes which would tend to randomize any signal. Light would also be shed on the overall problem of the generation of such internal waves in the ocean. For the tides themselves, the smaller the degree of determinism the more data would be required to demonstrate it, and the less useful it would be. Thus at some point the practical description of the process would be as a random one, although the bandwidth, modal distribution and propagation characteristics would remain to be determined.

In the following sections, we examine the internal tides in the western North Atlantic Ocean at the site of the Mid-Ocean Dynamics Experiment (MODE-1) during the first half of 1973. The semidiurnal internal tide is described in terms of energy levels, bandwidth, and persistence. From the large amount of data available, we can obtain a statistically reliable determination of the structure of the process. Propagation directions and energy flux can be derived and related to possible sources of the wave energy.

The next Section 2.2, summarizes the experimental setting and the available data. Section 2.3 deals with overall energy levels observed and their consistency with internal wave dynamics. The deterministic internal tide

is the subject of Section 2.4, including measurements of propagation in the M_2 wave and evidence for a noisy but partly deterministic S_2 internal wave. Section 2.6 covers the barotropic M_2 tidal currents measured in the experiment, and 2.6 discusses variability in the observed fields. This includes a consideration of mooring motion as it affects the measurements. The conclusions of the study are restated in Section 2.7.

2.2 Setting, data and analysis

The Mid-Ocean Dynamics Experiment (MODE Scientific Council, 1973) carried out in the spring of 1973 affords a unique look at processes in the deep ocean. The experiment was designed to investigate mesoscale oceanic circulation processes but this report concerns the internal tides as observed in the experiment. Measurements of horizontal currents, temperature and pressure were obtained from 16 fixed moorings centered at 28°N, 70°W. Figure 2.2.1 shows the location of the study area in relation to the overall bathymetry of the North Atlantic Ocean. The MODE setting was the eastern edge of a deep abyssal plain, depth 5400 m, in the Sargasso Sea. The ocean bottom is remarkably smooth in an area about 200 km in east-west extent and over 1000 km in north-south extent in this area. To the west is the Blake Escarpment, about 700 km distant. At about the same distance to the south are the first indications of the islands of the Caribbean, while to the east over 2000 km of rough abyssal hills lie between the plain and the Mid-Atlantic Ridge. The experiment is thus in the far field of any major topographic feature.

Figure 2.2.2 shows the locations of the 16 fixed moorings involved in the program. For reference, the locations of the moorings and their distances from the central Mooring 1 are given in Table 2.2.1. The instrumentation included temperature-

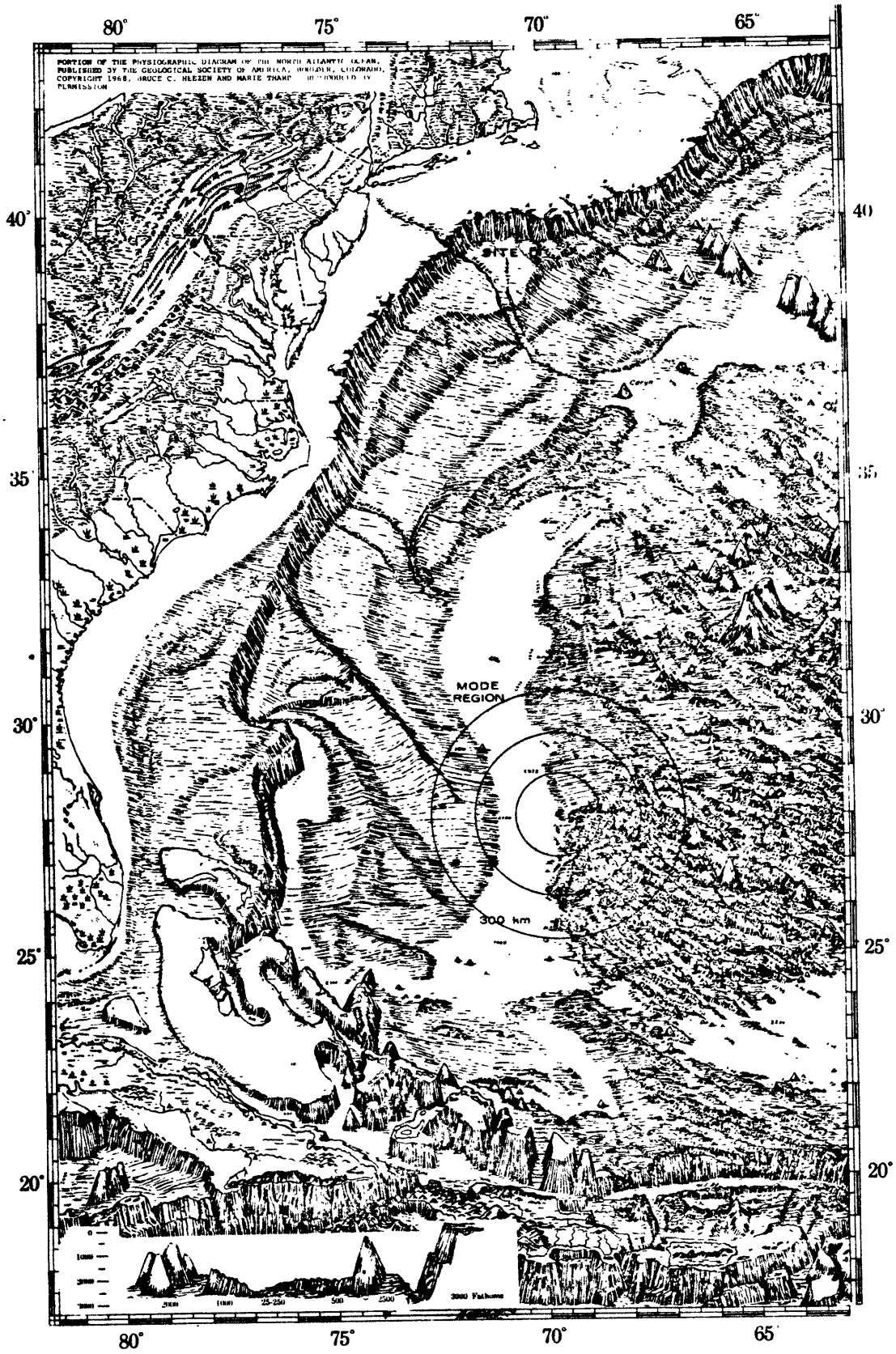


Figure 2.2.1 Bathymetry of the western North Atlantic Ocean after Heezen and Tharp (1968). The MODE-1 site and Site D are indicated.

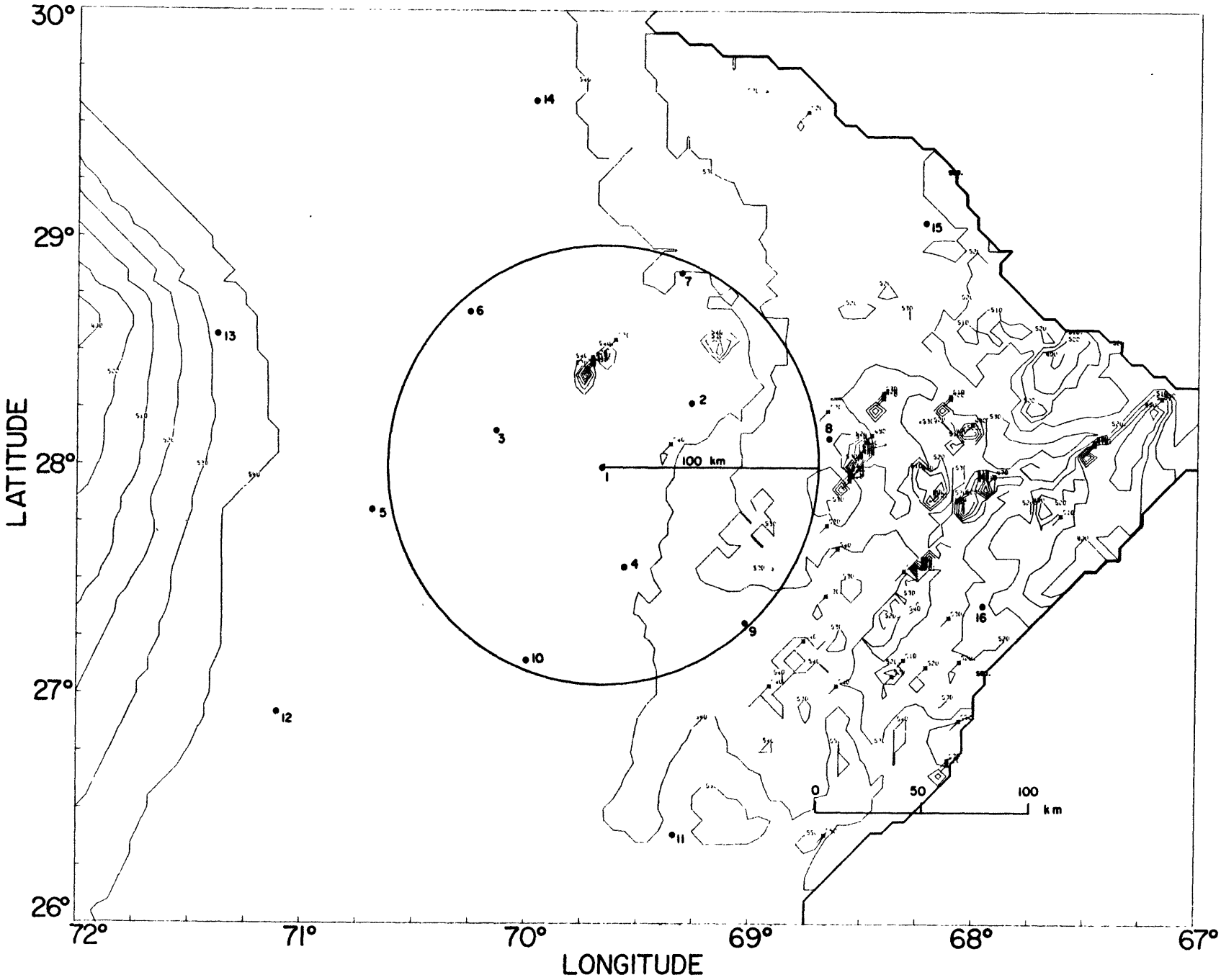


Figure 2.2.2 Local bathymetry (contours in decimeters) and mooring positions for the MODE-1 experiment.

Mooring	Latitude (N)	Longitude (W)	x (east) (km)	y (north) (km)
1	27°59.8'	69°39.0'	0.0	0.0
2	28 17.0	69 16.3	37.1	31.9
3	28 09.0	70 08.1	-47.6	17.0
4	27 33.1	69 34.1	8.0	-49.5
5	27 49.8	70 39.8	-99.6	-18.5
6	28 42.0	70 15.8	-60.0	78.2
7	28 50.1	69 18.0	34.2	93.2
8	28 09.3	68 39.3	97.6	17.6
9	27 18.0	69 01.0	62.4	-77.5
10	27 08.8	70 00.0	-34.5	-94.5
11	26 23.8	69 21.0	29.7	-177.9
12	26 57.7	71 02.3	-137.5	-115.5
13	28 33.1	71 22.9	-169.6	61.7
14	29 35.0	69 59.1	-32.6	176.4
15	29 02.3	68 13.8	138.7	115.8
16	27 25.1	67 59.5	163.3	-64.3

Table 2.2.1

Mooring locations for the MODE-1 array, giving latitude and longitude of the moorings and their position relative to the central Mooring 1.

pressure (T-P) recorders (Wunsch and Dahlen, 1974) and Savonius rotor type current meters (AMF-VACM and Geodyne 850 models). Most of these were of vector averaging type, and included thermistors to measure temperature as well. There were a number of cases when a current meter and a T-P recorder were placed very close together on a mooring, and the temperature intercomparison showed that for tidal frequencies the two instruments were indistinguishable. The T-P recorders also monitored the external pressure, and so the vertical displacement of the sensor in the water column. The effects of mooring motion on the temperature signals can thus be evaluated, and will be discussed in Section 2.6.

On the 16 moorings, over 100 useful records of temperature were obtained, amounting to almost 27 record-years of data. About half of these records included pressure measurements. The current measuring program was less successful, and many of the 50 usuable records were quite short. About 6 record-years of horizontal currents were finally declared usuable. There were at least four levels of temperature available on every mooring, with the exception of Mooring 2, with record length usually at least 75 days and often 105 days. This allowed a very consistent analysis of the temperature field, with uniform statistical treatment as will be described. The current measurements allow a description of the overall energy levels across the experiment,

but had to be treated on a more piecemeal basis.

The analysis proceeded as described in Section 1.3, with non-overlapping 15 day lengths of record treated as the basic unit. Here we describe the results for the semi-diurnal frequency band, consisting of three adjacent Fourier coefficients representing periods 12.86, 12.41 and 12.00 hr and separated by a bandwidth of 1/15 cpd. We refer to these as the N_2, M_2 and S_2 bands respectively, since the astronomical tides designated by these symbols dominate the equivalent bands in the equilibrium tide.

In Table 2.2.2 the number of 15 day pieces of temperature and current records available at each standard depth is given. As an overview, the energy at each of the three frequencies at each depth level was calculated as discussed in Section 2.3. Just as described in Section 1.3, ensembles of the equilibrium astronomical tide Fourier coefficients for the frequencies considered were calculated for each record. The equilibrium tide was calculated for exactly the same period of time and the same discrete time step as the original record, and analyzed in the same way. This allows the calculation of admittance amplitudes and phases for the physical variables relative to the equilibrium tide. Also we project the observations onto the equilibrium tide in a linear sense, and use the coherence between the variables and the equilibrium tide as a means of evaluating the

Nominal depth (m)	Mooring number 1	2	3	4	5	6	7	8	9	10	11	12	13	14	15	16	Overall
400	14	-	5	5	5	5	5	7	5	5	7	7	-	7	7	7	91
500	14	2	5	5	5	5	5	7	5	5	7	-	7	7	7	7	93
700	14	-	5	5	-	6	5	7	5	-	7	-	7	7	14	14	96
900	7	5	5	5	5	5	-	3	5	-	1	-	-	-	-	-	41
1100	7	-	-	-	-	-	-	-	5	-	7	-	-	-	-	-	19
1400	7	-	5	5	5	5	5	7	-	5	7	7	-	7	7	-	72
1900	7	-	-	-	-	-	-	-	-	-	7	-	-	-	-	-	14
2400	7	-	-	-	-	-	-	-	5	-	7	-	-	-	-	-	19
2900	14	-	-	-	5	5	5	7	-	-	-	7	7	7	7	7	71
3400	7	-	-	-	-	-	-	-	5	-	-	-	-	-	-	-	12
4000	-	-	5	5	5	5	5	7	5	5	7	7	7	7	7	7	84
4400	7	-	-	-	-	-	-	-	5	7	-	-	-	-	-	-	19
5200	7	-	-	-	-	-	-	-	5	-	7	-	-	-	7	-	36
																	657

Table 2.2.2a

Temperature data availability. The number of 15 day record lengths at each mooring, by depth, in MODE-1.

Nominal depth (m)	Mooring number 1	2	3	4	5	6	7	8	9	10	11	12	13	14	15	16	Overall
400	4	5	4	5	5	3	4	2	4	3	1	-	1	-	-	3	44
700	-	1	5	3	-	5	-	-	-	5	2	-	2	-	5	3	31
1400	1	1	-	1	-	2	4	-	-	5	-	2	-	1	-	-	17
3000	7	-	5	-	-	1	1	1	-	-	-	5	1	2	-	-	23
4000	7	-	-	-	-	-	1	1	5	-	-	-	-	-	2	1	17
5200	7	-	-	-	-	-	5	-	5	4	-	-	-	-	-	-	21
																	153

Table 2.2.2b

Current data availability. The number of 15 day record lengths available at each mooring, by depth, in MODE-1.

statistical significance of the projection. A detail which should be mentioned here is that the admittance phases are calculated with respect to the local equilibrium tide, and are equivalent to the negative of kappa in the classical nomenclature of tidal analysis. Thus two events which occur simultaneously but at different longitudes have different phases, although their phase relation to the actual forcing of the tidal potential is conserved. It might have been more appropriate to refer all the measurements to a common meridion such as that of Greenwich, which is also a standard approach. However the maximum difference in the quantities kappa and G, the latter value, is only ± 4 degrees across the scale of the experiment for the semidiurnal species and half of this for the diurnal tides.

Once estimates of the deterministic part of the signals are obtained, and their statistical significance is evaluated, it may be justifiable to proceed further. The vertical structure of the fields at a particular mooring can be projected onto a set of normal modes by least squares fitting, where the normal modes are calculated on the basis of internal wave dynamics. The modes which we use here were calculated numerically from average hydrographic parameters over the experiment. Appendix Table A.3.3 gives a smoothed profile

of some of the parameters. The M_2 frequency modal wavelengths and phase and group speeds are given in Table 2.4.3 for the first five modes. Since density fluctuations or isopycnal displacements are the true dynamical variables which are related to the normal modes, the temperature fluctuations are converted to isotherm fluctuations by the relation

$$\zeta_T = - T/\theta_{oz}$$

where ζ_T is the vertical displacement of an isotherm, T the measured temperature fluctuation amplitude and θ_{oz} the potential temperature gradient at the mean depth of the isothermal surface. This assumes linear, non-dissipative internal wave dynamics, which is entirely consistent with the overall procedure since the modes themselves are calculated on the basis of locally linear and inviscid theory. The final formal step in the process is to identify isotherms with isopycnals on the good assumption of a strong correlation between temperature and salinity which together determine the density field.

The highest level sampled in the experiment by the fixed instruments was at 400 m, and to avoid aliasing of energy into higher order modes resembling lower order ones at depth, only two or three baroclinic modes could be used.

Mode number	Wavenumber (km^{-1})	Wavelength (km)	Phase speed (cm/s)	Group speed (cm/s)
1	$.386 \times 10^{-1}$	163.	364.	278.
2	$.905 \times 10^{-1}$	69.4	155.	119.
3	.121	51.9	116.	88.6
4	.158	39.8	88.9	67.8
5	.206	30.5	68.4	52.2

Table 2.2.3

Modal parameters for the first five baroclinic M_2 frequency modes in the MODE-1 area.

These were always chosen to be the lowest order ones. Further evidence will show that this procedure has some hope of achieving useful results in spite of its restrictions.

For the current field, we can treat some cases but little averaging is possible because of the shortness of the records. For the temperature decompositions, the variations of phase of the first baroclinic mode across the array are analyzed to detect any propagation. On an experiment wide scale, the moorings are points in an array or antenna. The MODE array was designed to investigate mesoscale features and the 50 km spacing of the moorings was appropriate for this task. Any waves with wavelengths smaller than 100 km are aliases of longer waves, as perceived by the array. More exactly, any subset of the moorings used as an antenna will have a beam pattern which will be quasi-periodic in wavenumber space, and for a smallest separation of 50 km the period will be about 1/100 cycles per kilometer. Referring to Table 2.2.3, it is seen that all but the first baroclinic mode for the semidiurnal internal tide have wavelengths shorter than 100 km and would appear as aliases in the central zone of the beam pattern.

2.3 Semidiurnal energy levels

To obtain an overview of the general energy levels in the semidiurnal frequency band, we average the observations from different horizontal locations over the whole array for the duration of the experiment. The processes involved may be broadly stationary in time and horizontal placement, but show structure in the vertical and in frequency space which we examine more stably by the averaging. Assuming that the 15 day sections are independent in the statistical sense, the overall averages have a large number of degrees of freedom.

Temperature

Figure 2.3.1 shows the resulting average vertical profiles of temperature fluctuations, while the numerical values are listed in Table 2.3.1. The central M_2 frequency dominates the adjacent semidiurnal bands by a factor of 3 in energy throughout the water column except at the deepest level. There the M_2 and S_2 estimates are nearly equal, while the N_2 estimate is still about a factor of 3 lower in energy. The bands on either side of the M_2 estimate have remarkably similar power levels, with the exception of the lowest depths. This similarity would be expected if the M_2 energy Doppler shifted by random low frequency currents was dominating the

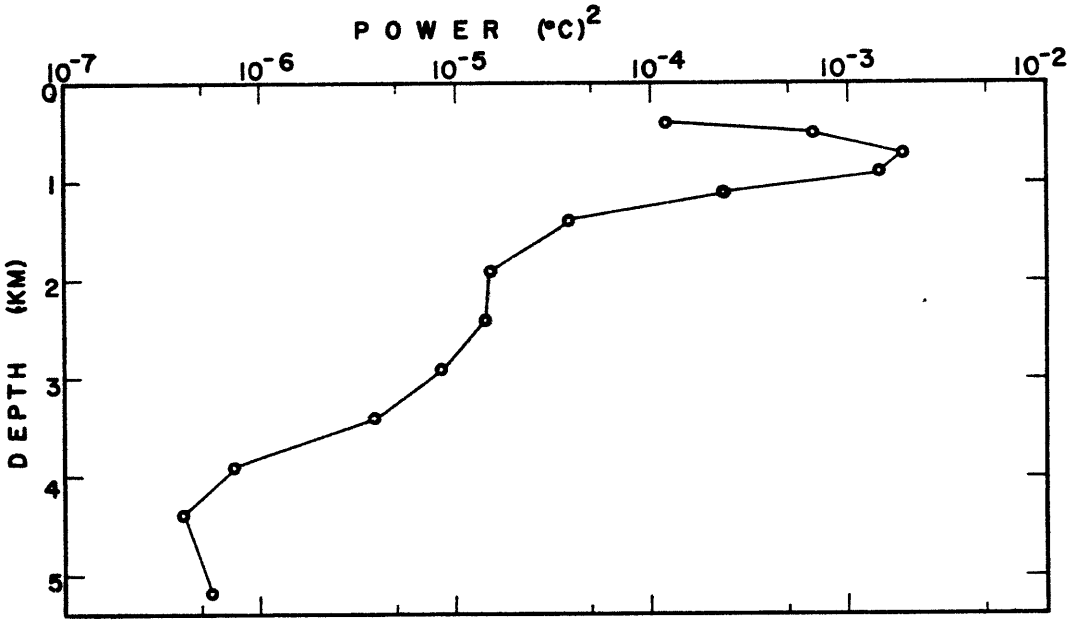


Figure 2.3.1a Squared amplitude of S_2 band temperature fluctuations, averaged at depth levels over the entire array.

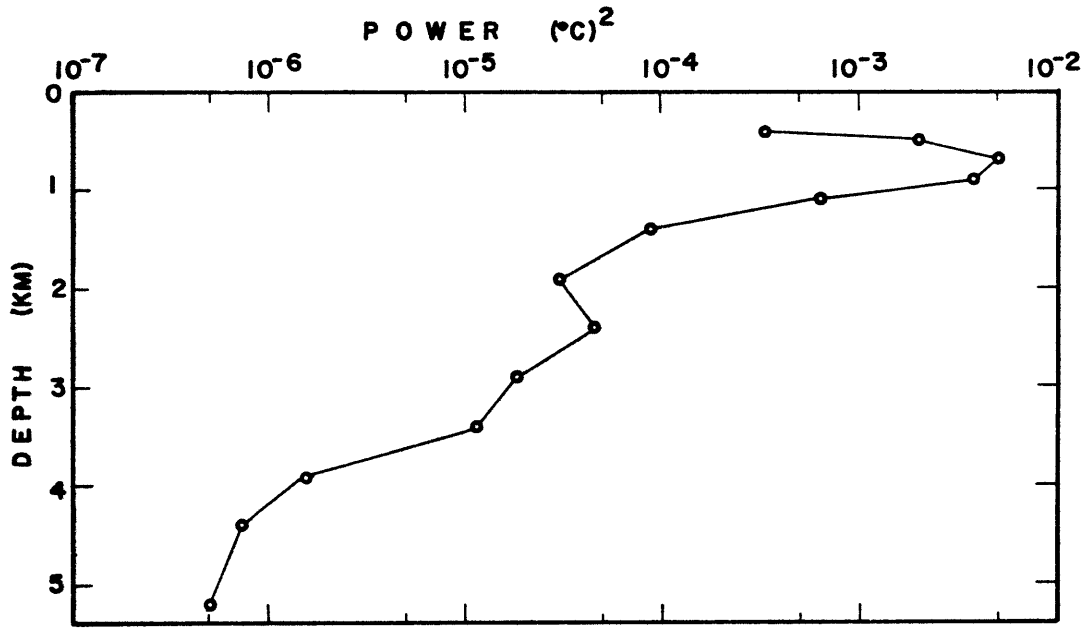


Figure 2.3.1b Squared amplitude of M_2 band temperature fluctuations, averaged at depth levels over the entire array.

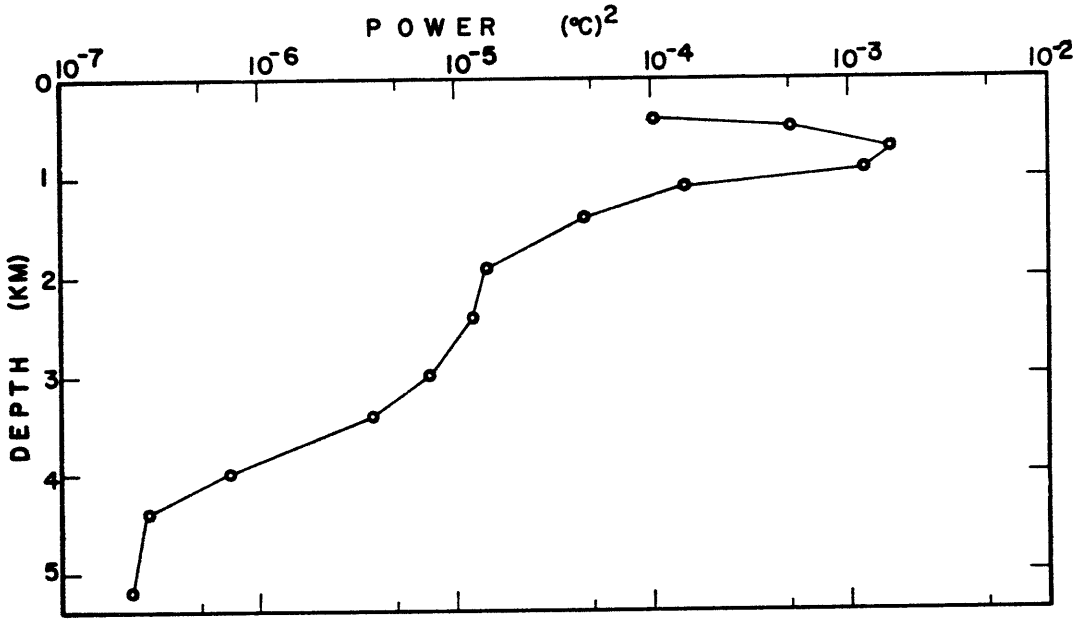


Figure 2.3.1c Squared amplitude of N_2 band temperature fluctuations, averaged at depth levels over the entire array.

Depth (m)	N_2 $(^oC)^2$	M_2 $(^oC)^2$	S_2 $(^oC)^2$
400	$.125 \times 10^{-3}$	$.421 \times 10^{-3}$	$.149 \times 10^{-3}$
500	$.617 \times 10^{-3}$	$.257 \times 10^{-2}$	$.852 \times 10^{-3}$
700	$.205 \times 10^{-2}$	$.631 \times 10^{-2}$	$.240 \times 10^{-2}$
900	$.148 \times 10^{-2}$	$.481 \times 10^{-2}$	$.180 \times 10^{-2}$
1100	$.183 \times 10^{-3}$	$.798 \times 10^{-3}$	$.294 \times 10^{-3}$
1400	$.562 \times 10^{-4}$	$.110 \times 10^{-3}$	$.480 \times 10^{-4}$
1900	$.179 \times 10^{-4}$	$.380 \times 10^{-4}$	$.191 \times 10^{-4}$
2400	$.153 \times 10^{-4}$	$.560 \times 10^{-4}$	$.184 \times 10^{-4}$
2900	$.917 \times 10^{-5}$	$.232 \times 10^{-4}$	$.105 \times 10^{-4}$
3400	$.460 \times 10^{-5}$	$.142 \times 10^{-4}$	$.484 \times 10^{-5}$
4000	$.870 \times 10^{-6}$	$.195 \times 10^{-5}$	$.910 \times 10^{-6}$
4400	$.342 \times 10^{-6}$	$.904 \times 10^{-6}$	$.505 \times 10^{-6}$
5200	$.405 \times 10^{-6}$	$.619 \times 10^{-6}$	$.698 \times 10^{-6}$

Table 2.3.1

Numerical values for squared amplitude of temperature fluctuations for the semidiurnal bands in the MODE-1 experiment, averaged at depth levels over the entire array.

adjacent bands. In terms of the relation

$$\Delta\sigma = \underline{k}.\ \underline{U}$$

relating frequency shift $\Delta\sigma$ to wavenumber $\underline{k}$ and mean current $\underline{U}$, a frequency shift of the first mode M_2 wave whose wavelength is about 160 km by an amount 1/15 cpd could be accomplished by a mean flow of about 10 cm/s. However a more realistic treatment would relate the statistical observation that the 1/3 power points of the M_2 peak have a bandwidth of 1/15 cpd at most, to the combined statistics of the internal wave field and the fluctuating low frequency fields if these were known.

The WKBJ approach, valid for waves with spatial scales less than the characteristic scales of the medium, shows that temperature fluctuations vary like $N^{-1/2}(z)\ \theta_{oz}$ in a field composed of high mode internal waves. Figure 2.3.2 gives a smoothed profile of $N^{-1}(z)\ \theta_{oz}^2$ for the MODE region to compare with the profiles of squared temperature fluctuation amplitude in Figures 2.3.1. All three semidiurnal frequency bands are generally similar to the WKBJ profile, notably in the sharp maximum at 750 m in the main thermocline and the slight inflectional feature between 2000 and 3000 m. However there is more variation in the measured temperature

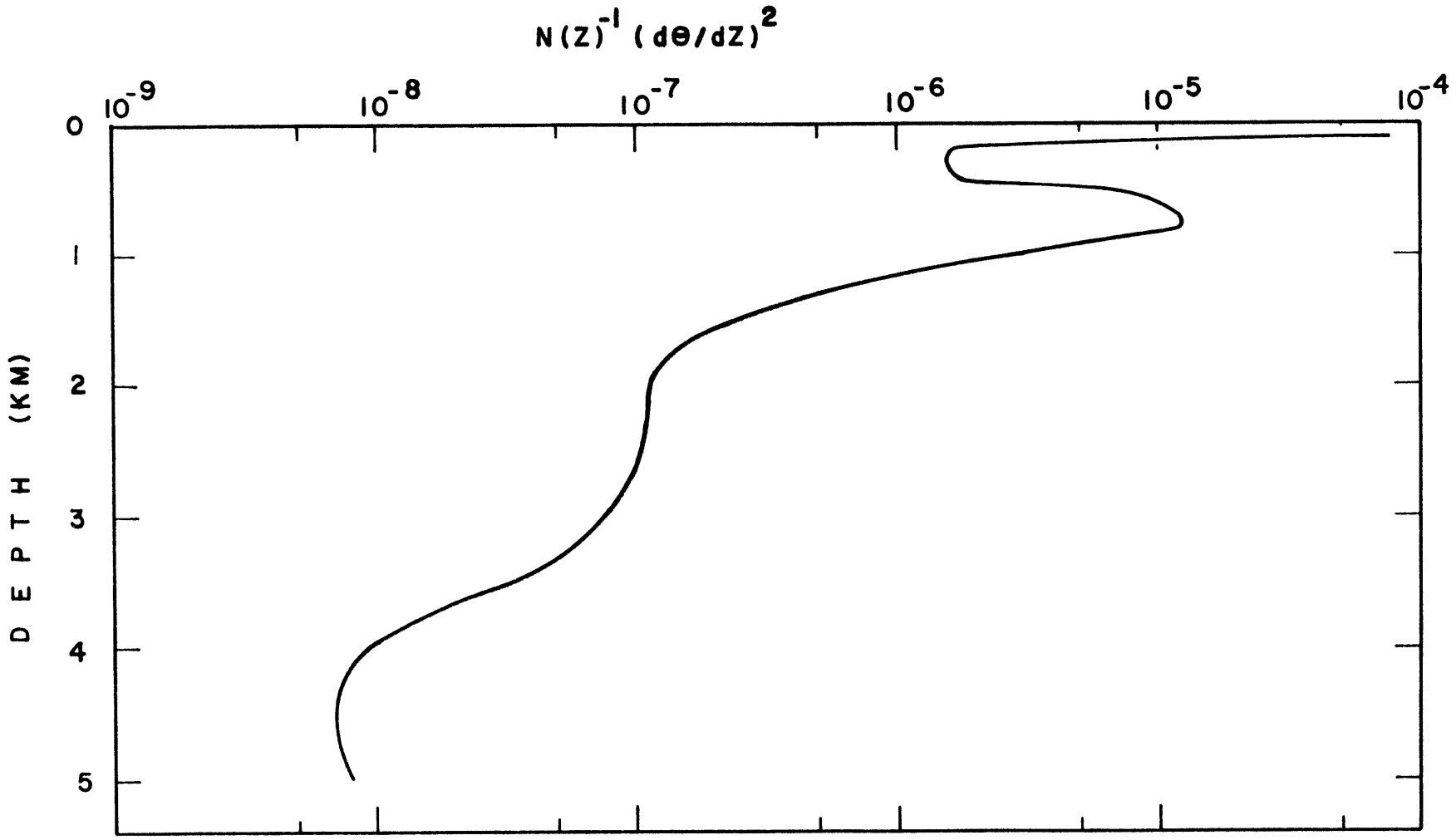


Figure 2.3.2 Average MODE-1 profile of $N^{-1}(z)(d\theta/dz)^2$ to compare with the profiles of temperature variance.

profiles than the theoretical profile: the thermocline values are larger and the deep values smaller than the best fit of the calculated curve. This would be consistent with a modal composition involving lower order, larger scale modes whose vertical structure is not so closely governed by the local density gradient.

Currents

The same averaging over horizontal levels was done for the current components at the three semidiurnal frequencies. Figure 2.3.3 shows the results, with the numerical values given in Table 2.3.2. The currents are a mixture of barotropic and baroclinic modes, with different dynamics, and more information is needed to separate the two. In current as well as temperature, the M_2 band dominates the neighboring bands, by a factor of 5 in power above 1500 m and somewhat more below that level. The neighboring frequency bands show a more depth dependent structure than the central frequency and are approximately equal in power although showing more scatter than the temperature field.

Examining the vertical structure in the three bands, the M_2 energy at 400 and 700 m is greater by a factor of 4 than the values at deeper levels. In the water below 1400 m, the M_2 horizontal kinetic energy is quite constant with depth.

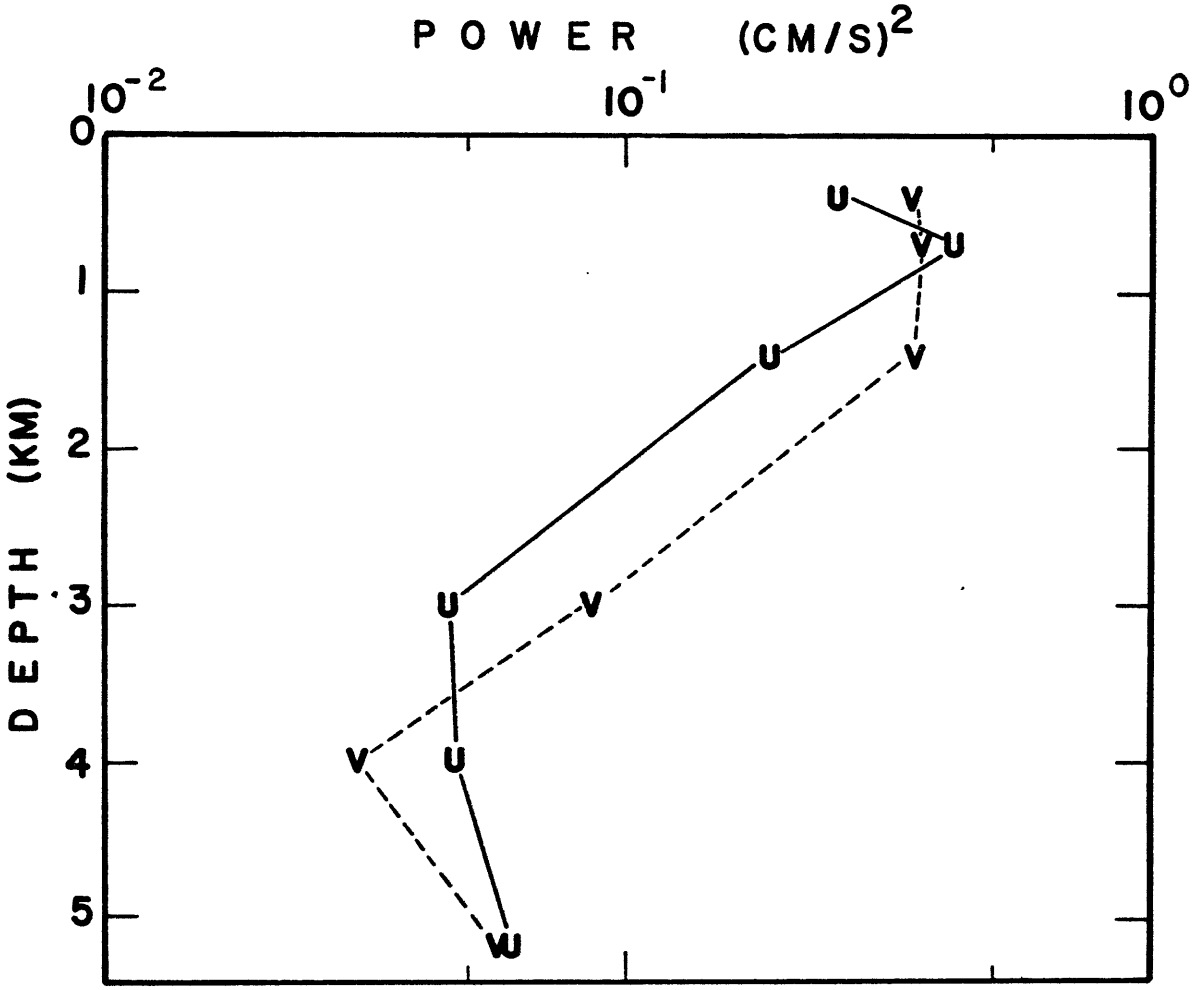


Figure 2.3.3a Squared amplitude of S_2 band horizontal current components u (east) and v (north) averaged at depth levels across the entire array.

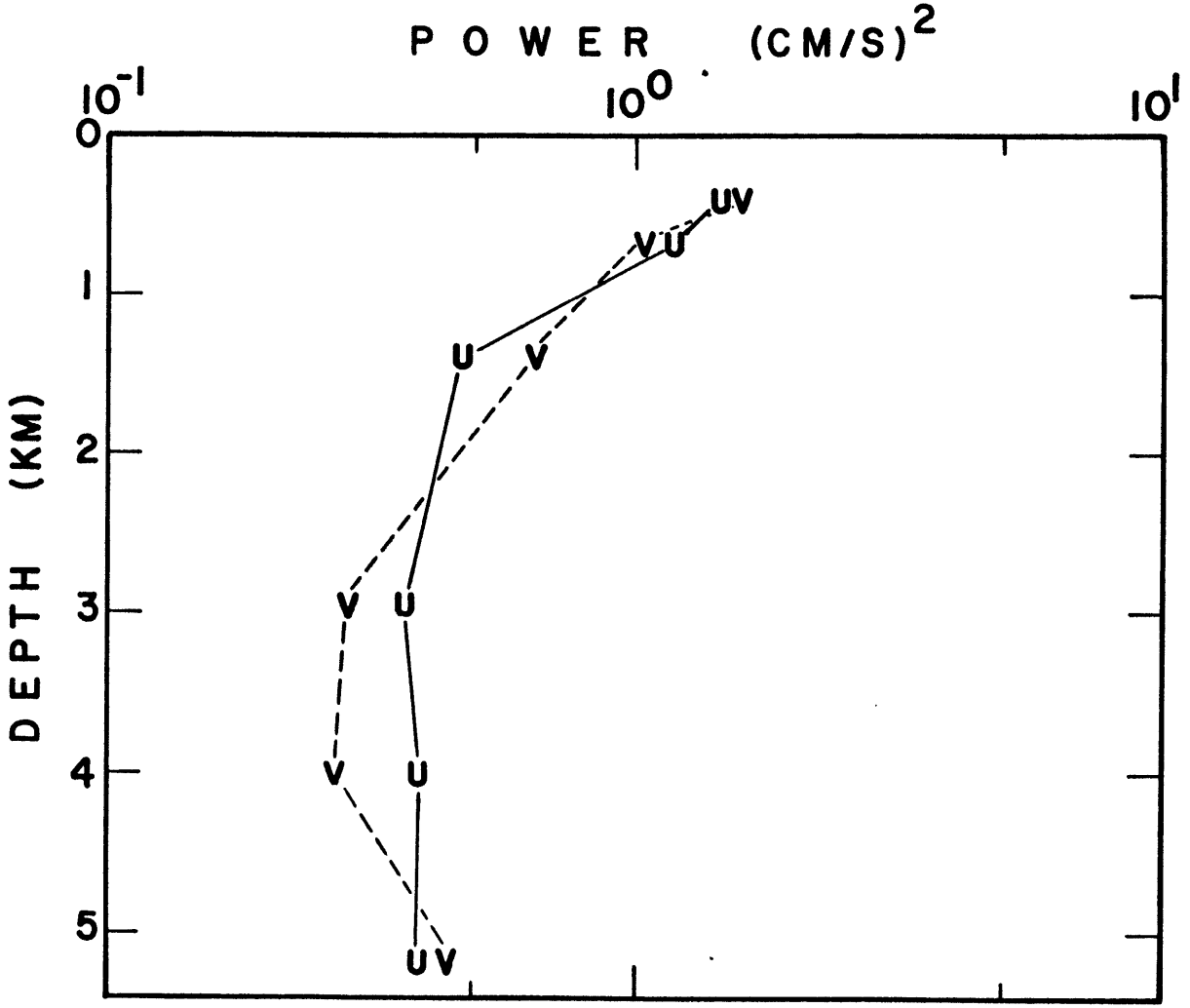


Figure 2.3.3b Squared amplitude of M_2 band horizontal current components u (east) and v (north) averaged at depth levels across the entire array.

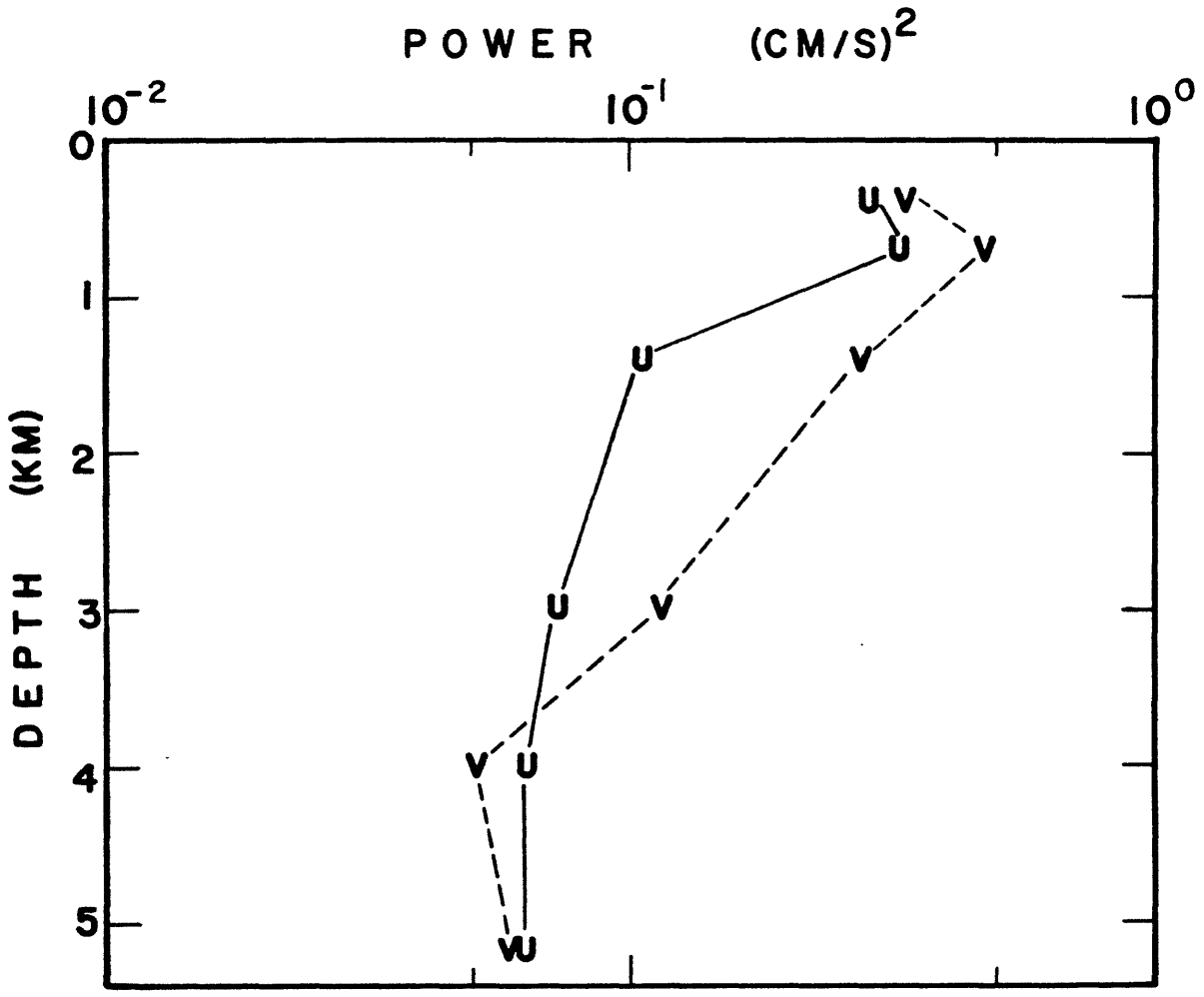


Figure 2.3.3c Squared amplitude of N_2 band horizontal current components u (east) and v (north) averaged at depth levels across the entire array.

Depth	N_2		M_2		S_2	
(m)	u	v	u	v	u	v
400	.314	.437	1.78	1.95	.352	.412
700	.519	.451	1.47	1.26	.401	.579
1400	.233	.441	.583	.814	.127	.338
3000	.0568	.106	.451	.356	.0904	.152
4000	.0574	.0379	.491	.333	.0770	.0621
5200	.0778	.0760	.486	.544	.0747	.0728

Table 2.3.2

Numerical values for squared amplitude of u (east) and v (north) current components in the semidiurnal bands in the MODE-1 experiment, averaged at depth levels over the entire array.

This is consistent with the presence of an energetic barotropic current mode, which is further investigated in Section 2.4. Figure 2.3.4 gives a profile of N(z) to compare with the observed vertical distribution of horizontal kinetic energy in the semidiurnal bands. The N(z) profile varies by about a factor of 10 between the thermocline and the deep water, similar to the behavior of the currents in the adjacent N_2 and S_2 bands but not the M_2 band. The barotropic mode is almost independent of the stratification, and unrelated to the WKBJ considerations.

For the M_2 currents, the east (u) and north (v) components are about equal in power. For the nominal N_2 and S_2 bands, especially the S_2 band, the v component variability is somewhat greater overall in the upper part of the water column. Internal waves have their currents polarized to be greatest in the direction of wave propagation, and this suggests that the north-south direction may be a preferred one for such waves. However the differences in energy of the u and v components are not striking. The baroclinicity of the N_2 and S_2 current profiles compared to the M_2 profile suggests that much of the energy in the former two bands is either Doppler shifted from the M_2 frequency or simply part of the underlying non-tidal internal wave continuum.

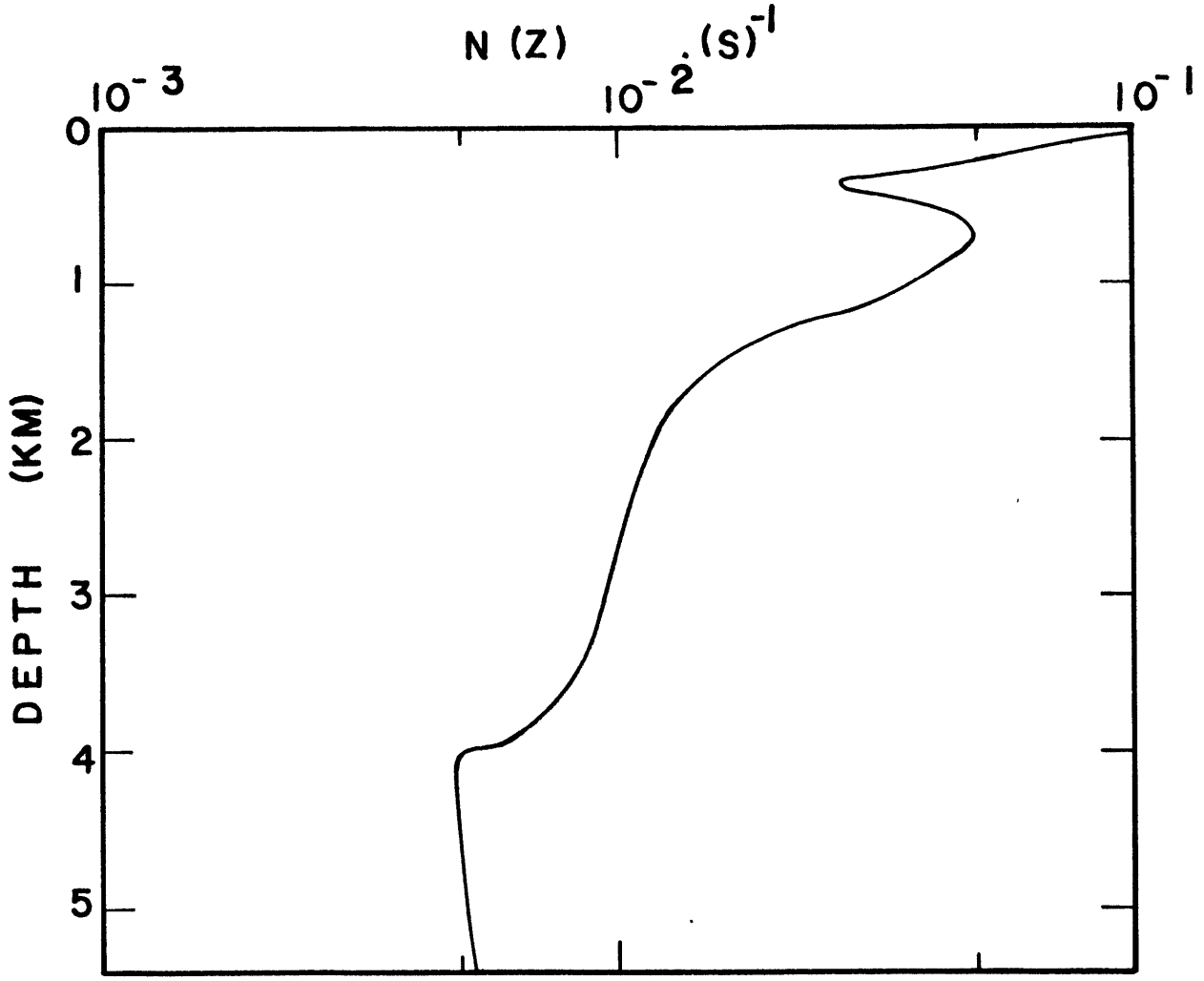


Figure 2.3.4 Average MODE-1 N(z) profile to compare with profiles of horiaontal current variance.

Consistence with internal wave ideas

Given the information we have about the horizontal current field and the vertical displacement field, we are in a position to calculate the overall horizontal kinetic and vertical potential energy levels and compare them with internal wave theory. A simple propagating mode has a partition of average horizontal kinetic energy to average vertical potential energy

$$HKE/VPE = (\sigma^2 + f^2)/(\sigma^2 - f^2) \qquad 2.3.1$$

averaged over the whole water column. At a given vertical level the partition depends on the individual mode. In a field composed of many high order modes with about the same amplitude, the partition 2.3.1 would hold locally. In Table 2.3.3 the average horizontal kinetic energy and potential energy for the semidiurnal bands and the local ratio have been calculated. The average potential energy associated with an isopycnal displacement is

$$VPE = 1/4\ N^2(z)\zeta^2(z)$$

The ratios in Table 2.3.3 show order of magnitude agreement with the kinematical ratio 2.3.1 but have some interesting structure. All three frequencies generally show more kinetic

Depth	N_2			M_2			S_2		
(m)	HKE	VPE	Ratio	HKE	VPE	Ratio	HKE	VPE	Ratio
400	.180	.0554	3.4	.932	.188	5.0	.190	.0664	2.9
700	.242	.223	1.1	.681	.689	.99	.277	.262	1.1
1400	.168	.0789	2.1	.349	.154	2.3	.116	.0675	1.7
3000	.0407	.0294	1.4	.201	.0743	2.7	.0605	.0336	1.8
4000	.0238	.0120	2.0	.206	.0269	7.7	.0347	.0125	2.8
5200	.0385	.0066	5.8	.258	.0101	26.	.0369	.0113	3.3

Depth integral	HKE	VPE	TOTAL
N_2	$.50 \times 10^5$	$.25 \times 10^5$	$.75 \times 10^5$
M_2	$.18 \times 10^6$	$.98 \times 10^5$	$.28 \times 10^6$
S_2	$.47 \times 10^5$	$.25 \times 10^5$	$.72 \times 10^5$

Table 2.3.3

Average horizontal kinetic energy density, potential energy density, and the ratio of the two for the semidiurnal bands in the MODE-1 experiment. The averages are at depth levels over the entire array. Estimates of the depth integrated energy density in each band are also given.

energy than a high mode internal wave field with the measured potential energy. This is partly due to the barotropic tidal currents. The ratios nearest the surface and ocean bottom in all three bands are higher than average. Since vertical motion in the internal wave field vanishes at the bottom and top (to the rigid lid approximation), there is a zero of potential energy for all modes at these extremes. The relatively high values of HKE/VPE there can be related to these boundary effects. Since the highest instrumented level is 400 m from the surface, only internal wave modes with vertical scales larger than 400 m will exhibit the surface boundary effects. This is effectively true only for the first baroclinic mode, whose maximum displacement occurs at about 1300 m below the surface. The second internal mode, for example, has a first maximum about 470 m depth. The barotropic tide increases the horizontal kinetic energy at all levels, especially for the M_2 frequency, and this affects the ratios more near the boundaries where the internal wave potential energy is least. As we show in Section 2.5, the M_2 HKE density for the barotropic mode is about .1 erg/cm^3 so not all of the boundary effects are explainable by this latter mechanism. The conclusion is that some of the intensification of horizontal kinetic energy near the surface and bottom is due to the low mode content of the baroclinic fields.

A further observation concerns the relatively low values of the ratio HKE/VPE near 700 m in the center of the main thermocline. The first baroclinic mode in the setting of the experiment gives a maximum product $N^2.\zeta^2$ at about 860 m depth, while the mode 1 current profile has a zero at near 1300 m depth. For mode 1 alone, the ratio of HKE/VPE is an absolute minimum of zero at the node in the current profile. With the addition of other modes in the averages, including the barotropic mode in the currents, a relative maximum VPE at the 700 m level might be interpreted as a large first mode contribution. Since there are no current measurements between 700 m and 1400 m better vertical resolution is not possible.

Mooring motion can produce spurious temperature signals and apparent vertical potential energy levels higher than actual ones. The 700 m level is near the center of the main thermocline where the spurious temperature signals are greatest, but the real temperature variations are also greatest there. The M_2 frequency showed a mean square pressure amplitude of 2.2 $dbar^2$ at the 500 m level and 1.9 $dbar^2$ at the 900 m level. Converting these to equivalent temperature fluctuations gives about 15% of the total observed temperature variability at the M_2 frequency, so direct mooring motion is not an overwhelming factor. There are not enough pressure

measurements at the 700 m level to define the mooring motion there, but a reasonable interpolation between the 500 and 900 m levels and the use of the 700 m potential temperature gradient gives similar levels of mooring motion to measured temperature energy. Mooring motion is discussed further in Section 2.6.

Table 2.3.3 also includes estimates of the vertically integrated average horizontal kinetic energy and potential energy in the three semidiurnal bands. These will be referred to later in the discussion.

2.4 Deterministic fields

As described in Sections 1.3 and 2.2, when enough data from a given instrument was available an attempt was made to project the tidal period fluctuations onto the equilibrium tide. The coherence between the current or temperature fluctuations and the equilibrium tide provides a statistical comparison of the result to what the projection would give if the temperature or current phases were random. This provides a guide to interpreting the results.

The temperature data set was of uniform coverage and record length and could be treated in a very consistent manner. For the currents the data was much sparser and included many records too short for a meaningful statistical treatment. First we describe the treatment and results for the temperature measurements, and then proceed to the current field. In a special case for the central mooring we synthesize the two fields to obtain a compatible description of the M_2 baroclinic tide. Finally we cite evidence from an earlier experiment in the same area which suggests that the conclusions drawn here are valid generally and can be extended beyond the period of the actual MODE-1 field program.

Temperature

Most of the temperature records provided either 5 or 7 15 day pieces for analysis. As a gross overview of the

statistics of the temperature field, we imagine for a moment that all the records come from the same statistical process, although in reality the process is not at all stationary with depth. Then we note that of the 107 temperature records, 44 of the M_2 estimates of coherence with the equilibrium tide gave amplitudes greater than the corresponding 95% levels for zero true coherence. This would be the expected result if the temperature field were composed of a mixture of random noise and a deterministic signal, with the combination having a true coherence with the tidal potential of about .5 or .6. The predictable energy in such a process would be the square of the coherence. Alternatively, with such a process and 5 degrees of freedom in our estimates, we could expect to get estimates of coherence amplitude greater than the 95% level for zero true coherence only about once in four trials. This gives some insight into the problems of estimation with relatively small samples.

Similarly, for the N_2 band 14 of the 107 records gave coherence estimates above the 95% significance level for zero true coherence, and for the S_2 band the figure was almost the same at 15 of 107 records. In the same sense as above, we would expect this result if the true coherence of the temperature and equilibrium tide were .3 or .4, and the amount of data is not enough to obtain very meaningful statistics for such a process. For these adjacent frequencies, the

effect of Doppler shifted M_2 energy would be potentially critical in the statistics as well. However we will attempt to draw some conclusions from the S_2 band in particular.

For the present, we proceed with the M_2 band. As stated in Section 2.2, we computed the admittance phase at each level on each mooring. Then the temperature signals were converted to isotherm displacement using the appropriate average vertical gradient of potential temperature. The resulting vertical series of amplitude and phase for each mooring was least-squares fitted to the first three normal modes for the displacement field, with the exception of Mooring 13 alone. This mooring was one of the ones having only four sensors, and the three mode fit was unstable in the sense that although the vertical phase differences were small, of order 20°, the spacing of the sensors gave a strong mode 3 signal. Fits were also made of all the moorings using only two baroclinic modes, and in most cases the results were entirely consistent. For Mooring 13 in particular, the two mode fit was used.

Figure 2.4.1 shows the average displacement and phase distribution for the heavily instrumented central mooring. The phase is remarkably constant with depth, characteristic of the first baroclinic mode. The amplitudes of the averages in Figure 2.4.1 show a general increase from the uppermost levels into the main thermocline maximum at about 1200 m which is associated with the first baroclinic mode. At depths

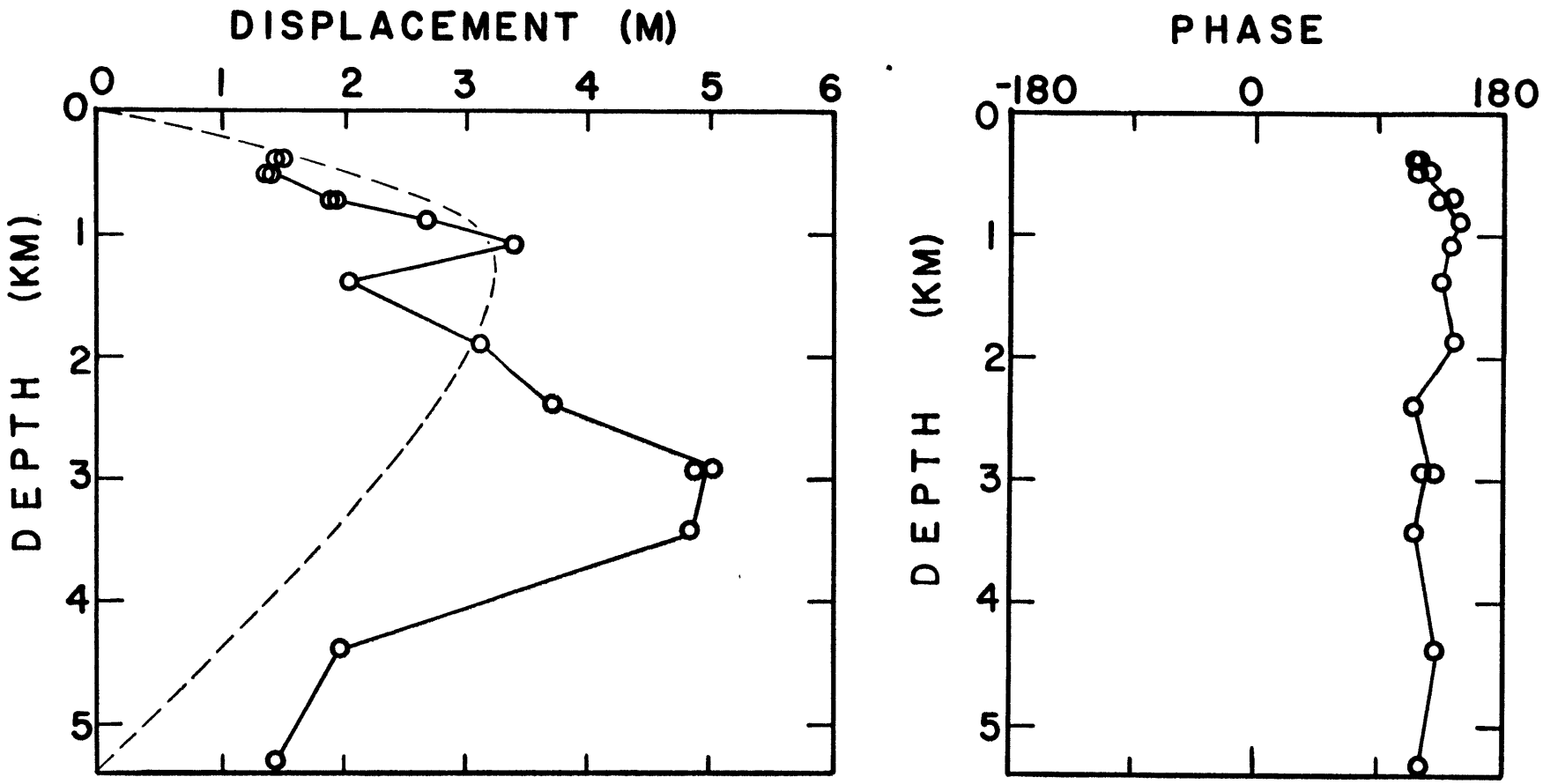


Figure 2.4.1 (left) Solid lines join estimates of the coherent (phase locked) M_2 isotherm displacement at Mooring 1 at different depths. The dashed curve is the first baroclinic mode shape, drawn to arbitrary amplitude.

(right) The admittance phase of M_2 isotherm displacement at Mooring 1.

below 2000 m the isotherm displacements are greater than expected for a pure first baroclinic mode, as sketched in the same figure. In the deeper measurements, θ_{oz} is small and small random temperature fluctuations give large apparent isotherm displacements. Higher order modes with relatively small amplitudes can contribute a greater fraction of the variance in the deep water where the first baroclinic mode amplitude is small. In a modal fit to the isotherm displacements at the central mooring, the first baroclinic mode accounted for about 84% of the variance in the averages, but there was about 12% of the energy in the third baroclinic mode in the three mode fit. The third mode thus has about one third of the amplitude of the first mode, and in the deeper water there is a third mode maximum in vertical excursion at about 3200 m. There is a slight indication that the admittance phases between 2000 and 5200 m are 10 or 20 degrees less than the general values in the main thermocline, but the individual differences are not significant. Table 2.4.1 gives the numerical values represented in Figure 2.4.1, and the estimates of coherence amplitude for the temperature fluctuations and the equilibrium tide. Most levels show quite significant coherence with the background tidal signal. It is interesting to note that the coherence amplitudes estimated are generally largest in the main thermocline between 500 and 1100 m where the first baroclinic mode has its maximum amplitude and that

Depth (m)	Amplitude (m)	Phase	Coherence
389	1.52	118	.57
391	1.56	117	.58
489	1.41	129	.68
490*	1.46	118	.68
691	1.93	145	.76
697*	1.97	136	.75
897*	2.69	151	.69
1095*	3.42	144	.69
1392	2.05	136	.50
1895*	3.13	147	.52
2399*	3.74	115	.50
2916*	5.03	134	.64
2919	4.86	122	.64
3437*	4.85	117	.63
4382*	1.98	134	.39
5348*	1.45	123	.28

Table 2.4.1

Mooring 1 M_2 frequency average isotherm displacement and admittance phase as a function of depth. Coherences between temperature fluctuations and the equilibrium tide at each depth are also given. With the 7 degrees of freedom in the estimates, the 95% confidence level for zero true coherence is .63. Depths marked * are T-P recorders, unmarked depths are temperature measurements from current meters.

there is a secondary maxima of coherence near 3000 m where the third mode has a maxima. Coherence squared is just signal to noise power, and if the signal is distributed in low order modes and the noise more uniformly distributed, we would expect to see high coherences at levels where the low modes had maxima.

Although some of the other moorings have as few as four temperature sensors for vertical resolution, the results from the central mooring give confidence that fits with a limited number of normal modes will be meaningful. Visually, most of the other moorings show very stable M_2 admittance phases with depth for the temperature fluctuations. Table 2.4.2 has the amplitudes and phases of the first baroclinic mode calculated at each of the moorings. The percentage of first mode energy in the fit and the percentage of fitted variance compared to total variance in the signal are given. With the amplitudes and phases of the first baroclinic modes our viewpoint can shift from the local to the global. Using the array as an antenna, we computed estimates of the wave-number spectrum of the first mode field. The technique was somewhat non-standard in that only the phases of the modes were used, rather than cross-spectral estimates between different moorings as might be done in a normal noisy wave detection attempt. All the degrees of freedom have been consumed in the original averaging procedure and we are

Mooring	Amplitude (m)	Phase	% of fit in mode 1	% of fit power to signal power
1	2.56	-042	84	93
2	-	-	-	-
3	2.90	095	69	97
4	3.60	-086	75	75
5	4.34	147	98	90
6	-	-	-	-
7	2.16	-064	94	92
8	3.69	141	84	82
9	3.39	071	68	94
10	4.37	-051	87	98
11	2.41	025	82	83
12	2.19	040	93	99
13	3.17	-071	88	86
14	.93	-164	83	77
15	1.27	-064	68	79
16	3.66	-068	72	84

Table 2.4.2

Amplitude of the first baroclinic mode content of M_2 isotherm depth fluctuations at each mooring. The percentage of signal variance accounted for by the first mode in the least-squares fit, and the percentage of the total energy which is represented by the fit are also given for each mooring.

committed to what is left as the absolute signal. It will still be a noisy finite estimate, but some numerical experiments indicated that the wavenumber techniques would have value is this case as well.

Two methods were tried in the wavenumber analysis. The conventional beamforming approach estimates the wavenumber spectrum in a scalar field $s(\underline{x},t)$ at frequency σ as the sum

$$S(\underline{k},\sigma) = (1/N^2) \sum_{n,m=1}^{N} \frac{\hat{s}(\underline{x}_n,\sigma)\hat{s}^*(\underline{x}_m,\sigma)}{|\hat{s}(\underline{x}_n,\sigma)\hat{s}^*(\underline{x}_m,\sigma)|} \exp(i\underline{k}.(\underline{x}_n-\underline{x}_m))$$

over the N points of the array. $\underline{x}_n$ is the horizontal location of the n'th sensor and $\hat{s}(\underline{x}_n,\sigma)$ the Fourier transform of $s(\underline{x}_n,t)$ at frequency σ. If the signal is a noise free plane wave with phase $\sigma t-\underline{k}_o.\underline{x}$, the beamforming estimate will be just the beampattern

$$B(\underline{k}-\underline{k}_o) = (1/N^2) \Sigma \exp(i(\underline{k}-\underline{k}_o).(\underline{x}_n-\underline{x}_m))$$

centered at $k=k_o$ where B has its maximum of unity. Figure 2.4.2 shows the beampattern of the array of 14 moorings used in the M_2 first mode fit. Mooring 2 had too few points in the vertical to be used, and Mooring 6 appeared to be completely dominated by mooring motion at the M_2 frequency and was not used in the fit. In Section 2.6 Mooring 6 is discussed in

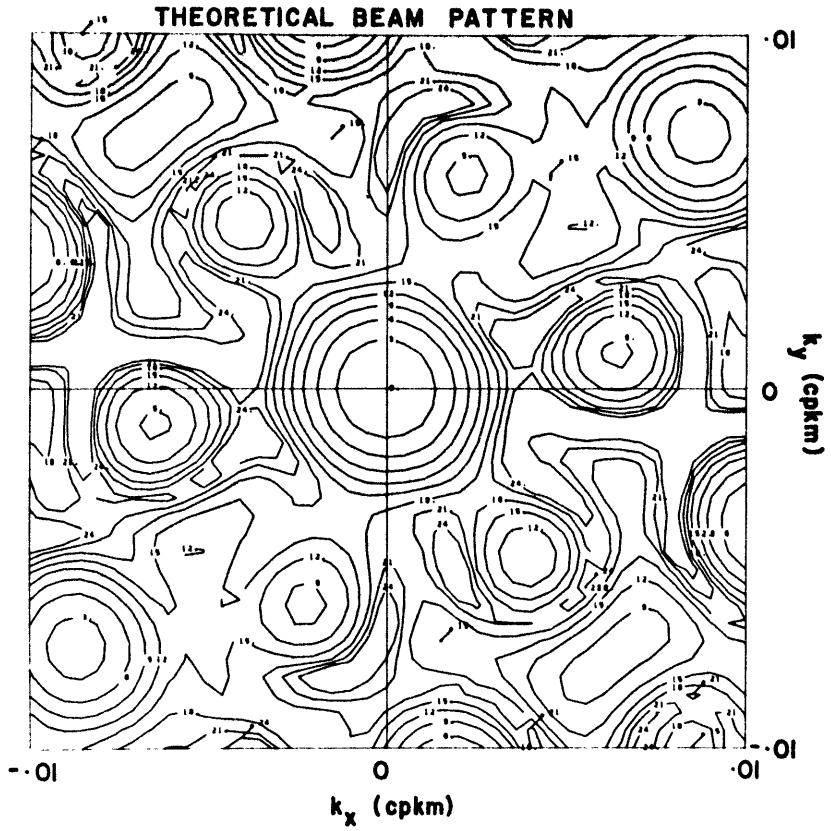


Figure 2.4.2 Theoretical beampattern for 14 moorings in the MODE-1 array. Contour interval -3dB.

detail as an example of serious mooring motion. The results for the conventional wavenumber spectrum estimate are shown in Figure 2.4.3a. The second method used was in inverse estimator which has the property of suppressing a noisy background in an optimal sense if there is a plane wave signal buried in the noise. This maximum likelihood estimator is described by Capon (1969). The results for our fit are given in Figure 2.4.3b. The spectra are normalized to the peak value, and contoured in negative decibels with respect to the peak.

In both cases, the maximum in the spectrum occurs in the southeast quadrant, representing a wave travelling from the origin towards 125°T. The wavenumber resolution of the grid used was .0005 cycles/km. Both estimators gave the same coordinates of the maximum

$$k_x = .0050 \text{ cycles/km}$$
$$k_y = -.0035 \text{ cycles/km}$$

This produces a wavelength of 163 km, which is exactly the calculated wavelength of the first baroclinic M_2 mode as found in Table 2.2.4. At this wavelength the grid resolution is about 15 km, and the exact agreement is fortuitous, but the result is certainly consistent with theoretical expectations.

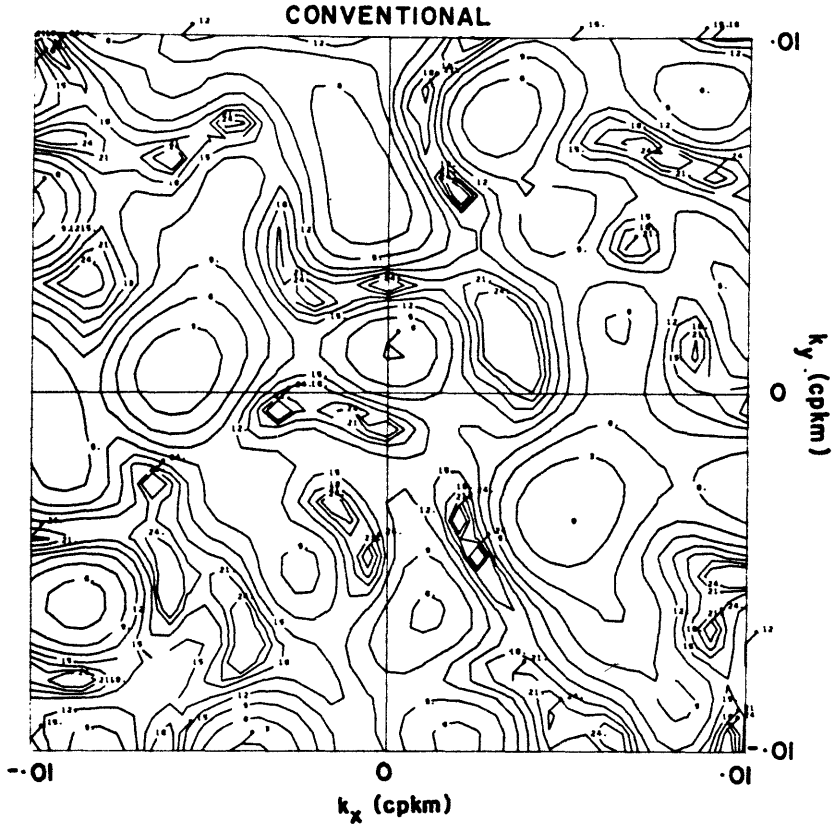


Figure 2.4.3a Conventional wavenumber spectrum estimate for M_2 first baroclinic mode isotherm displacement at 14 of the MODE-1 moorings. The contour interval is -3 decibels, normalized by the maximum. The peak in the southeast quadrant represents a wave with 163 km wavelength propagating in the direction 125°T.

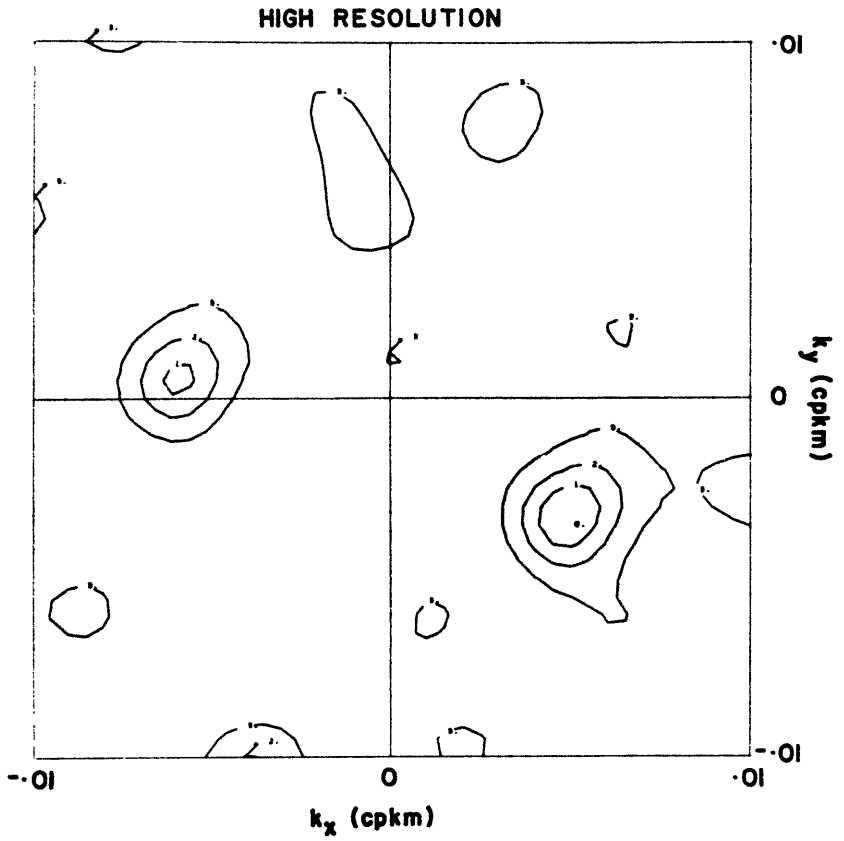


Figure 2.4.3b High resolution wavenumber spectrum of M_2 first baroclinic mode isotherm displacement at 14 of the MODE-1 moorings.

The secondary maximum in the north-west quadrant also gives a wavelength of about 160 km, but falls on an alias of the first peak. The wavenumber difference between the two maxima is 1/93 cycles/km, compared to the nominal 1/100 cycles/km periodicity of the beampattern for a uniform array with spacing of 50 km between sensors. Some indications from the current field which support the rejection of the secondary maxima as an unphysical alias will be discussed later in this section.

An estimation of the total energy contained in the fitted wave is unsure, since the individual first mode amplitudes at different moorings did vary and the distribution of phases is not fitted exactly by any single plane wave. From Table 2.4.2 we take 3 m as a representative amplitude for the deterministic M_2 internal tide. Assuming that this wave has the theoretical partition of kinetic and potential energy for a plane propagating internal wave then gives an estimate of $.9 \times 10^5$ erg/cm^2 for the integrated energy density of the first mode. Multiplying this by the first mode group speed gives an energy flux of $.3 \times 10^8$ erg/s cm in the direction of wave propagation 125°T. The phase and group speeds of the waveguide modes have the same direction. The first mode energy density is just less than 40% of the total barotropic energy density at M_2 frequency (Section 2.5) but the horizontal

kinetic energy in the currents associated with the first mode is about 80% as great as the kinetic energy in the barotropic currents.

Generation sources

The flux of energy to the south and east suggests an energy source in the northwest quadrant, where lies the continental slope of the southern United States between Cape Hatteras and Florida. About 700 km due west of MODE center is the Blake Escarpment, where the ocean depth changes abruptly from 4800 m in the broad Blake-Bahama Basin to less than 1200 m on the Blake Plateau. Shoreward of the Blake Escarpment there is a wide, more gently shoaling continental shelf. Models of internal tide generation (Rattray, Dwarski and Kovala, 1969) for a step continental slope give energy levels in the internal tide which vary as the square of the width of shelf for all other factors held constant. This indicates that regions of particularly wide continental shelf will be effective generation regions, and the shelf south of Hatteras is notably wider than the shelf between Hatteras and Cape Cod, for example (Figure 2.2.1). The widest shelf in the area, about 500 km from the 1200 m line to the shore, is intersected by a line from MODE center bearing about 290°T, giving a range from the slope of about 700 km. The continental slope off Cape Hatteras itself has a steeper aspect ratio, with the largest gradients of depth

occurring between 2400 m and 200 m depth, more like the New England slope north of Site D. MODE center bears 150°T from Cape Hatteras, at a distance of about 950 km from the shelf break.

Generation models show that continental slopes are effective sources of internal tides when forced by the barotropic tide. The models will be discussed in more detail in Chapter 4, where the MODE-1 and Site D results will be considered in concert. The domination of the first baroclinic mode in the M_2 internal tide in the MODE-1 experimental results argues for a distant generation source, since in general the topographic generation mechanisms give near field motions with sharp spatial gradients and a rich modal spectrum. In any particular case, the actual decomposition of the internal waves depends on the relative structure of the topography and the stratification. Even in a field which is initially composed of many modes, the lower order modes tend to contain much of the energy and especially energy flux in the waves. Since higher order modes have shorter spatial scales and greater r.m.s. shear for a given modal amplitude, dissipative effects in a real fluid will damp out the higher modes selectively as the internal tide propagates in space. Prinsenberg, Wilmot and Rattray (1974) have modelled this effect using constant eddy diffusion parameters in a slope generation case. Spatial

variations in the ocean can refract internal waves, and in the geometrical optics limit shorter scale waves are most affected. The same selectivity applies to the Doppler shifting of internal waves by low frequency currents. Thus the ocean acts as a low pass filter for spatial variations, and the lower order modes will persist while higher order modes are dissipated and distorted. Eventually even the first baroclinc mode will be modified enough to lose all memory of its generation source.

The MODE-1 site is special in its very smooth bottom and its relation to the coast of the United States. The Gulf Stream is trapped up onto the continental shelf above 800 m depth until reaching about 33°N latitude (Stommel, 1966), and internal waves generated on the continental slope near the latitude of MODE-1 would have relatively quiet ocean to travel through between the slope and the experimental region. The smoothness of the sea floor makes the bottom scattering mechanism of Cox and Sandstrom (1963) unlikely and removes one possibility of interference. There are areas of rough topography to the east of the site which are possible sources of incoherent internal tides.

S_2 internal tides

We have noted that the S_2 internal tide is not very coherent with the equilibrium tide. However it would be of

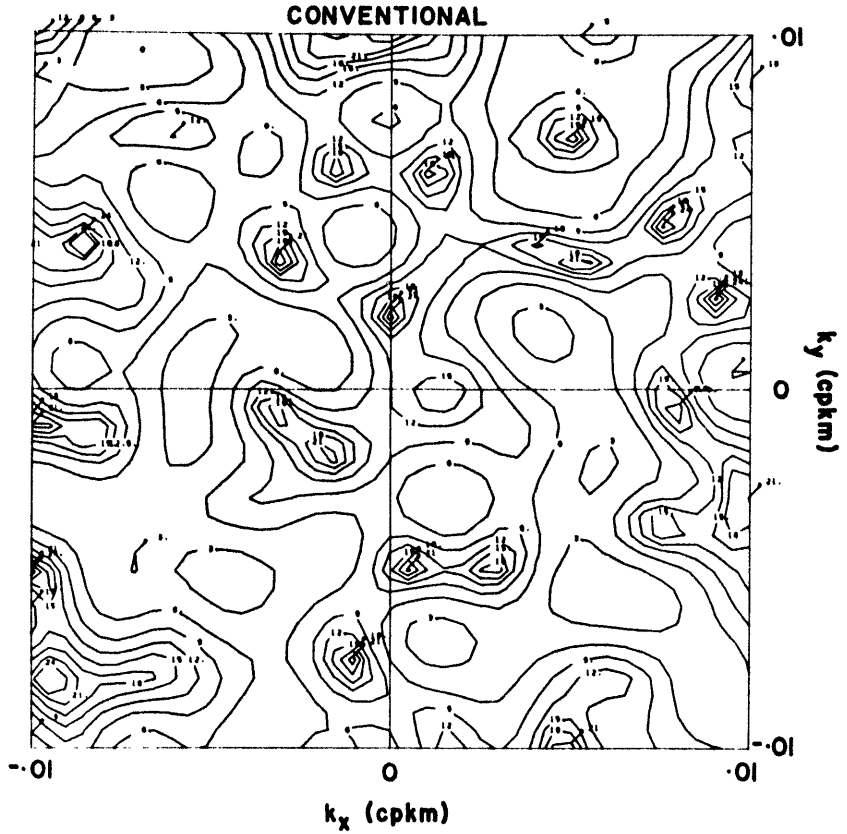


Figure 2.4.4a Conventional wavenumber spectrum estimate for S_2 first baroclinic mode isotherm displacement at 15 of the MODE-1 moorings. The weak peak in the far north-west quadrant is a possible alias of the -3 bB sidelobe near the origin in the north-east quadrant.

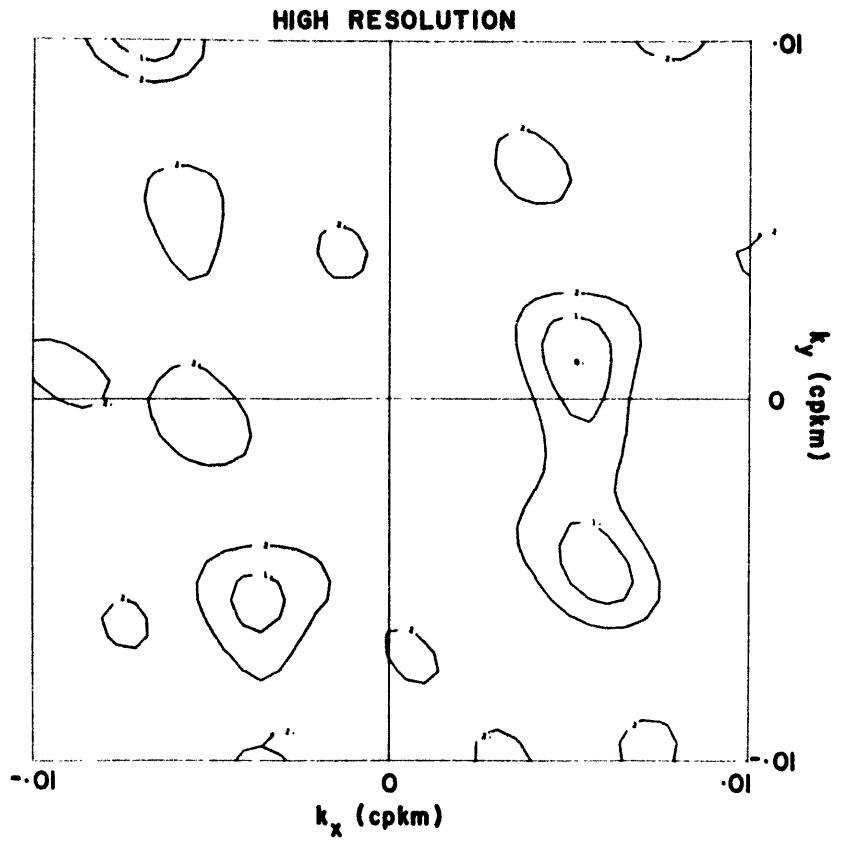


Figure 2.4.4b High resolution wavenumber spectrum estimate for S_2 first baroclinic mode isotherm displacement at 10 of the MODE-1 moorings which showed stable first mode fits.

great interest to extract a meaningful signal from the S_2 frequency band. For example, we could make a direct calculation of the internal tide group velocity if we could compute directly $\Delta\sigma/\Delta k$ for the M_2 and S_2 components. The 12.00 hr period Fourier coefficients for temperature fluctuations were processed in exactly the same way as for the M_2 band. The wavenumber spectrum calculation for the first baroclinic mode content in the S_2 internal tide proved unstable. For the case with 15 moorings used in the conventional spectral estimator, the peak value occurred at $k_x = -.0070$ cycles/km, $k_y = .0095$ cycles/km in a very noisy spectrum (Figure 2.4.4a). The peak value corresponds to a 77 km wavelength, outside the principal alias band of the array. A secondary maximum occurs at a possible alias of the first peak, for $k_x = .0040$, $k_y = .0020$ in the same units. This gives a wavelength of 220 km and propagation direction of 065°T, closer to the behavior of the M_2 first mode. The theoretical wavelength of the first mode S_2 wave is 155 km. Use of various subsets of the moorings gave differing results. For example we chose 10 of the moorings which showed little change in the first baroclinic mode when either two or three modes were used in the least squares fit. Figure 2.4.4b shows the maximum likelihood estimate. There is a weak peak which corresponds to a wavelength of 196 km and a propagation direction 075°T. We conclude that there are some indications

that the S_2 and M_2 frequencies are behaving similarly, but that the low signal to noise ratio in the former frequency band defeats a direct calculation of the group velocity.

However, another approach in the same vein shows some interesting results. The "age of the tide" is a term applied to the surface tide, and depends on the relative lag of the M_2 principal lunar and S_2 principal solar constituents behind the corresponding components of the equilibrium tide. In much of the Atlantic Ocean, the S_2 surface tide lags the S_2 equilibrium tide by about 30° more than is the case for the M_2 tide. This causes the times of spring and neap tides to fall some time after the actual maximum in the combined potential at full or new moon and gives rise to the age of the tide. In the MODE region the actual age corresponds to a 32.0° difference in the admittance phases of the two constituents (Zetler, Munk, Mofjeld, Brown, and Dormer, 1974). We have computed the age of the first mode content of the internal tide by differencing the phases of the modal fits. In spite of the apparent noisiness of the S_2 band, the phase differences show some stability across the array. Table 2.4.3 shows the calculated differences at the various moorings in the experiment, while Figure 2.4.5 is a histogram of the same calculation. Visually there is a concentration of phase differences between 90° and 135°. More precisely, we

Mooring	Phase difference
1	104
2	-
3	-028
4	125
5	138
6	-
7	-161
8	111
9	045
10	180
11	115
12	-022
13	023
14	178
15	104
16	060

Table 2.4.3

Phase differences between the M_2 and S_2 first baroclinic modes at the moorings in the MODE-1 experiment. The age of the first baroclinic mode semidiurnal tide.

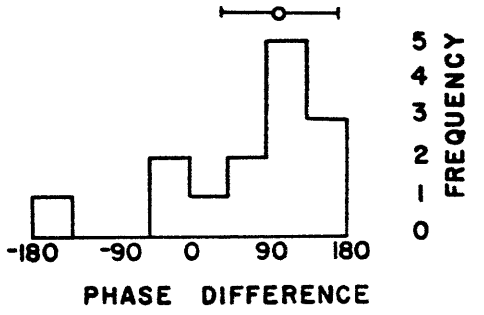


Figure 2.4.5 Histogram of the differences in admittance phase of the M_2 and S_2 first baroclinic mode fits to isotherm displacement at 14 of the MODE-1 moorings. The error bars are one standard deviation from the mean.

calculated the coherence of the collection of phase differences as in the Coherence I approach described in Appendix A.2. This calculation gives a coherence amplitude of .45 for the collection of 14 phase differences, and a phase of 105° for M_2 minus S_2. The 95% level for coherence estimates with 14 degrees of freedom for true coherence zero is about .45, and the chance of obtaining as high a value of coherence amplitude as we did if the difference between the M_2 and S_2 phases is random is only 5%. It may be that the processes which degrade the internal tide signals act upon the M_2 and S_2 frequency waves in the same manner, and so the phase differences at a given mooring are more stable than the total collection of S_2 phases across the array. If we accept this mechanical result by assuming that the phase difference is significant, we can infer a distance to the region of generation on the basis of a number of reasonable assumptions about the behavior of the internal tide.

First we must assume that the deterministic M_2 and S_2 internal tides behave similarly in their generation and subsequent propagation through the ocean. Thus we suppose that both frequencies are generated in the same regions and that there are no resonances, so that the age of the baroclinic tides in the generation regions is the same as the age of the generating surface tide there. As the internal

waves propagate through space their age changes since the ocean is a dispersive medium for such waves. In the MODE region, the S_2 first mode admittance phase is 105° greater than for the M_2 first mode, while the S_2 surface tide admittance phase shows the characteristic 32° increase over the M_2 wave. On the final assumption that the age of the surface tide in the effective integrated generation region is the same as the MODE value, the increase in age has been 73°. For a flat bottomed ocean, the increase in age could be simply related to the expression

$$(\underline{k}_{S_2} - \underline{k}_{M_2}) \cdot \underline{X}$$

where the $\underline{k}$ values are the appropriate ones for first mode internal waves at the S_2 and M_2 frequencies and $\underline{X}$ is the distance the waves have travelled since their generation. The wavenumbers are determined from the dispersion relation between frequency and wavenumber which exists for a given water depth and distribution of N(z). As an illustration, supposing that the waves had propagated in an ocean with the properties of the MODE region, the wavenumber increment between M_2 and S_2 waves would be $.177 \times 10^{-2}$ km^{-1}. A 73° increase in age could be accumulated by propagation over 720 km in such an ocean. More realistically, it can be

shown that for a single internal mode,

$$\Delta k/k = \Delta\sigma/\sigma \cdot (1 - f^2/\sigma^2)^{-1}$$

independent of water depth, since k and Δk decrease together in deepening water. The effect of shallower water in the propagation path is to increase the age of the internal tide proportionally more than deeper water, so the 720 km distance is a lower bound. The 95% confidence limits on the phase difference are about $\pm$ 45° so there is no point in a very detailed calculation of the expected age for generation at the continental slopes to the west and north. In general terms, however, the age calculation is remarkably consistent with the distance to the likely generation regions, and so with a weak but real signal in the S_2 internal wave field. Because of the leakage problems associated with the 15 day piece lengths, we did not make any attempt to resolve the N_2 frequency internal tide, but the results suggest that with about twice as much data there might be a chance to say something about this frequency also. It can be appreciated that this "internal tide spectroscopy" is considerably cruder than the elegant schemes referenced for the surface tide, entirely because of the signal to noise problems here.

Currents

As previously mentioned, the uneven quantity of current measurements made a consistent treatment of the current field difficult. All current records were analyzed in the same way as the temperature records, and when more than one piece was obtained from a particular record an estimate of the stability of the results could be made. The M_2 frequency was again the most coherent, and the effect of the barotropic tidal current was evident. For the M_2 band, 19/34 records gave coherence estimates above the 95% level for zero true coherence, based on the number of degrees of freedom available, for the u component and the equilibrium tide. For the v component the corresponding figure was 17/34. The records from levels below 1400 m were especially coherent, with 10/11 records from these depths showing significant coherence for both u and v components. The barotropic tide greatly influenced the deeper currents, and the spread of admittance phases for the u component below 1400 m was only from 7° to 61° for all records considered. The v component admittance phases showed about twice as much scatter. However there were cases where an apparently significant phase difference existed between two records from the deep water separated in the horizontal.

The M_2 current fluctuations from the thermocline above

1400 m were generally less coherent with the equilibrium tide. The other tidal bands were much less coherent, with only between 4 and 6 records out of the 34 for which estimates could be made showing significant coherence, at the 95% level, for the current components of the N_2 and S_2 bands and the corresponding equilibrium tide. For illustration, we would expect to see 5 out of 34 trials to be greater than the 95% level for zero true coherence if we were using estimates with 7 degrees of freedom from a population with a true coherence of .3. This represents a signal to noise ratio of only 10%.

As seen in the data summary Table 2.2.2b, there are few cases where there is much vertical resolution over long periods of time. Thus no very stable estimates of the vertical modal composition of the current field could be obtained. Moorings 1,6,7 and 10 have at least four levels instrumented simultaneously for at least 15 days, and some attempts were made to calculate modal decompositions from these moorings. Only Mooring 10 has more than one 15 day record at each depth. The results from these attempts were not entirely transparent and a degree of subjectivity is unavoidable in the discussion. This comes in selecting certain cases as reasonable and discarding others on the grounds that they make no physical sense. Again the problems arise because of the small number of degrees of freedom in

these estimates from a noisy process. However there are certain aspects of the current measurements which are quite consistent with the results from the temperature measurements and it is felt that they are worth discussing.

Moorings 6 and 10 had only four instrumented levels and the modal decompositions done with a barotropic mode and one or two baroclinic current modes were not successful in the context of the above discussion. The three pieces for Mooring 10, for which separate calculations were made, showed quite unstable results even for the barotropic mode (discussed further in Section 2.5). The phases of successive estimates of the barotropic components varied by as much as 180° and we can have no confidence in the baroclinic estimates. By inference the current records from Mooring 10 showed little individual coherence with the equilibrium tide. Mooring 6 gave estimates of the barotropic tide which were somewhat consistent with other estimates arrived at in several ways (Section 2.5), although the v component was about twice what we believe the best estimate to be. The first baroclinic mode also showed a large v component. We recall that Mooring 6 behaved anomalously at the M_2 frequency in the temperature measurements, which we believe to be the result of mooring motion. Thus a comparison between the results of the current and temperature measurements would be on uncertain ground on both counts.

Moorings 1 and 7 were instrumented at 5 distinct levels in current and Mooring 1 had a duplicate meter at the 400 m level for part of the time. Both these cases allowed the use of all levels for only one 15 day period. The modal decompositions of the current fluctuations at M_2 frequency gave estimates of the barotropic currents which we include in the next section, comparing well with estimates of another sort. The baroclinic part of the fits had quite different properties for the two moorings, however. Mooring 1 showed an energetic first mode, containing about 40% of the u variability and 70% of the v variability in the three mode fit used. Mooring 7 on the other hand gave only about 5% of the fitted energy on both the u and v components to the first baroclinic mode. Further discussion will be made of the variability in time of the fields in the MODE-1 period (Section 2.6), but for now we note that the current measurements from the two moorings are separated by about three weeks in time, with the Mooring 7 measurements being later. The first baroclinic mode from the Mooring 7 fit gave a current ellipse which rotated anticlockwise, and we must conclude that it represents mostly noise.

This leaves Mooring 1 which we will discuss in detail. Although we can rationalize the scatter in the current measurements on the basis of noise and non-stationary in time, the selection of the currents from the central mooring

for discussion on the basis that the results are consistent with an overall picture must be called a subjective one. However the agreement is quite striking. The first 15 day piece, for which the currents are available, was an especially energetic one in the temperature field at M_2 frequency. A modal decomposition of the first piece of the temperature record alone gave a dominant first mode signal with a displacement amplitude of 4.9 m compared to the average over the full record of about 2.3 m (Table 2.4.2). The currents from the central mooring for this period of time are listed in Table 2.4.4, and the resulting modal decomposition is also given there.

For a simple propagating internal wave mode with displacement shape $\Phi(z)$, the displacement and horizontal currents are related as

$$\zeta = A\ \Phi(z).\cos(\sigma t - kx)$$

$$u = (A\sigma/K)\ \Phi'(z).\cos(\sigma t - kx)$$

$$v = (Af/k)\ \Phi'(z).\cos(\sigma t - kx + \pi/2)$$

where A is the modal amplitude, u is the current component in the direction of wave propagation x, v is the current component 90° anticlockwise of u and k is the wavenumber. For the first baroclinic mode, $\Phi(z)$ has one sign and if positive, then $\Phi'(z)$ is negative above the node for

Depth (m)	u (cm/s)	G_u	v (cm/s)	G_v
389	2.28	125	3.24	357
391	2.02	126	3.03	002
1392	1.12	067	1.24	303
2916	.514	140	.158	235
3963	.208	174	.213	196
5356	.299	141	.208	201

Mode number	u (cm/s)	G_u	v (cm/s)	G_v	$\%u^2$	$\%v^2$
0	.663	109	.616	327	40	20
1	.652	125	1.14	003	38	68
2	.488	167	.228	012	22	12

Table 2.4.4

(upper) Currents in the M_2 band for a single 15 day period at the central Mooring 1.
(lower) Modal decomposition of the M_2 current profile, using a barotropic mode and the first two baroclinic modes. The percentage of fitted energy in each mode for each component is given.

horizontal current at 1300 m. Above this level u and ζ are 180° out of phase. The current vector rotates clockwise, and the major axis to minor axis current ratio is just σ/f.

At the central mooring, a modal decomposition of the horizontal currents gave a first baroclinic mode

u (east) component	.65 cm/s	126°G
v (north) component	1.15 cm/s	003°G

while for the same period of time the temperature measurements gave a first mode isotherm displacement

ζ displacement	4.9 m	014°G

The normalization of the modes is as given in Section 1.2. The currents give an ellipse which rotates clockwise, as illustrated in Figure 2.4.6. The major axis of 1.23 cm/s and minor axis .52 cm/s give a ratio 2.3 compared to the theoretical value 2.1 for the M_2 frequency. The first mode fit has

horizontal kinetic energy	$.24 \times 10^6$ erg/cm^2
potential energy	$.97 \times 10^5$ erg/cm^2

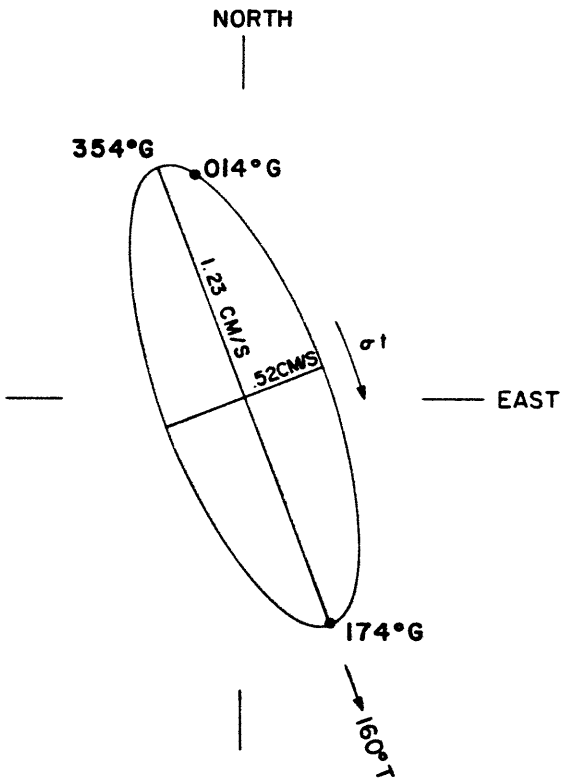


Figure 2.4.6 Horizontal current ellipse for the first baroclinic mode at Mooring 1 for the M_2 band in one 15 day period. The current amplitudes refer to the normalization described in the text. Time of maximum first mode isotherm displacement for the same period of time is indicated by a solid circle near the northern major axis. Together the current and temperature fluctuations define a wave which propagates towards 160°T.

for a ratio of .41 compared to the theoretical partition of .62. The fit has more kinetic energy than exactly consistent with a single plane propagating wave, but the agreement is reasonable in general.

The first mode current ellipse has a major axis directed towards 160°T, with phase 174°G. For the horizontal currents, the phases are appropriate above the 1300 m node. The phase of the opposing major axis is 354°G, compared to the isotherm displacement phase of 014°G. 180° phase difference is expected between the isotherm displacement and current component in the direction of wave propagation, and the southeast major axis must be chosen as indicating the propagation direction with its 160° phase difference much nearer the theoretical expectation. The resulting bearing of 160°T compares reasonably with the 125°T propagation direction inferred from the temperature measurements alone, consistent with the accuracy expected for a single 15 day record from which the currents were derived.

Further evidence for a deterministic internal tide

During the first part of 1972, several pilot experiments were carried out in the MODE region. Many of the moored measurements apparently suffered from the effects of mooring motion induced by surface flotation, and although we examined these measurements no global impressions could safely be

drawn as a result of these problems. There were two moorings located at the site of the present Mooring 1 which were supported by sub-surface flotation, and an examination of the temperature fluctuations at the M_2 frequency from these records proved interesting as an indication of the general validity of the conclusions drawn from the MODE-1 field work.

Table 2.4.5 presents a summary of the results obtained in analyzing three records from the earlier experiments. The moorings involved were numbers 455 and 412 in the terminology of the WHOI Buoy Group, and included two records from 1500 m and one from 500 m. The two moorings were set several months apart in 1972, but the admittance phase of the M_2 temperature fluctuations is remarkably constant over these earlier experiments. On the assumption that the earlier observations were also dominated by the first vertical mode, made plausible by the nearly constant phases between 500 m and 1500 m on Mooring 455, we can compare these observations with those from the MODE-1 experiment. Table 2.4.2 shows that the first baroclinic mode temprature fluctuations at the central mooring in the main experiment had an admittance phase of -42° (minus kappa) and the phases measured in the pilot experiments in the same location differ at most by 34° from this average value (Table 2.4.5). For three degrees of freedom and a true coherence of .7, approximate 95% confidence limits on phase estimates would be $\pm$ 45°. We note that the average amplitude

Record	Depth (m)	Amplitude (mdeg.C)	Phase	Coherence	No.of pieces
4552	514	39.6	-61	.78	3
Mooring 1	489	18.6	-51	.68	7
Mooring 1	490	19.2	-62	.68	7
4121	1502	4.78	-76	.42	3
4553	1516	6.10	-39	.75	6
Mooring 1	1392	4.92	-44	.50	7

Table 2.4.5

Historical evidence from MODE-0 for a phase locked M_2 internal tide. M_2 temperature fluctuations at comparable depths from Mooring 455 (28°00.2'N,69°37.6'W), Mooring 421 (28°00.2'N,69°41.5'W), and MODE-1 Mooring 1 (27°59.8'N, 69°39.0'W) and the admittance phases with respect to the equilibrium tide. Coherence estimates for each measurement and the number of 15 day pieces in the average are given.

of temperature signal from the 500 m record 4552 over 45 days is about twice the average over the entire MODE-1 program at Mooring 1. However the first piece of the seven used for Mooring 1 had a raw M_2 temperature amplitude of 42.0 and 44.2 mdeg C at the two sensors near the 500 m level, so the variation from experiment to experiment is no greater than the variation within the MODE-1 data alone. The earler measurements show some coherence with the equilibrium tide, although only the record from 500 m involving an average over 6 pieces is actually above the 95% confidence limit for true coherence of zero. The record from Mooring 421 has a low coherence amplitude, but the admittance phase is quite comparable to the other measurements. The general agreement is strongly suggestive that the internal waves of M_2 frequency in this region of the western North Atlantic Ocean do have a deterministic relation with the tidal potential. Further comments on the variability in the observations will be reserved to Section 2.6.

2.5 Barotropic currents

The current measurements from MODE can be used to estimate the barotropic, or depth independent component of the semidiurnal current field. Since the 200 km radial scale of the experiment represents only a small fraction of the barotropic wavelength no attempt was made to resolve any propagation in the associated fields across the array. In any such attempt the use of the geographically invariant phase reference G would be vital, while the kappa phase is invariant with respect to the moving astronomical forcing.

First we make use of data from all depths and horizontal locations to make a zero horizontal and vertical wavenumber estimate of the semidiurnal current field. This is accomplished for each frequency and velocity component simply by averaging all the appropriate Fourier coefficients using the admittance phases. Since the average involves a large number of points (153 individual pieces), any random variation will be strongly suppressed in the average. From the known beampattern of the array, any variation with the horizontal wavelength of the first baroclinic mode will be largely filtered out in a simple average. Finally the baroclinic motions involve phases which vary with depth, and the vertical averaging in the overall ensemble will further suppress any baroclinic contributions to the average. Since

in the earlier investigations into the structure of the baroclinic component of the tide it seemed that only the lowest mode had any great stability, the danger of aliasing the overall average by persistent high mode contributions is small. All that remains is the barotropic tide.

Table 2.5.1 shows the average amplitudes and phases obtained by averaging over the 153 individual pieces. The coherence amplitudes between the components and the equilibrium tide are also given. Note that only the v component in the S_2 band gives a coherence estimate less than the 95% confidence level for zero true coherence, and the M_2 field shows quite significant coherences in the overall average. Wunsch (1972a) analyzed a long sea level record from Bermuda and calculated tidal sea level admittances. These values apply reasonably to the MODE region as well, as shown in more recent work by Zetler, Munk, Mofjeld, Brown and Dormer (1974) (henceforth ZMMBD). We have calculated the admittances of the semidiurnal barotropic currents in the sense of Admittance II. (Appendix A.2) for the overall ensemble, as given in Table 2.5.2. The currents are also presented in normalized form to compare with the accompanying sea level admittances. In general the current fields show the same behavior as the associated sea level fluctuations, with the same increase in admittance amplitude towards lower frequencies in the semidiurnal band as noted by Wunsch (1972)

Overall average

Constituent	u (cm/s)	G_u	Coherence	v (cm/s)	G_v	Coherence
N_2	.0886	092	.25	.124	263	.22
M_2	.558	110	.56	.456	297	.45
S_2	.132	137	.32	.0611	355	.13

Modal fits for M_2 barotropic current

Mooring	u (cm/s)	G_u	v (cm/s)	G_v
1	.663	109	.616	327
7	.687	099	.652	302

ZMMBD (1974) results

u (cm/s)	G_u	v (cm/s)	G_v
.49	110	.80	258

Table 2.5.1

(upper) Barotropic current estimates for the major semidiurnal frequencies, and coherences for the overall current averages. (center) Barotropic M_2 currents from modal fits at Morrings 1 and 7. (lower) Barotropic M_2 currents inferred from sea level gradients across the MODE-1 array (ZMMBD, 1974)

Current admittances

Constituent	a_u (s^{-1})	G_u	a_v (s^{-1})	G_v	a_ζ	G_ζ
N_2	.032	096	.031	271	2.5	337
M_2	.030	110	.024	297	2.0	359
S_2	.017	136	.0081	358	1.0	024

Normalized admittances

Constituent	u	Phase	v	Phase		Phase
N_2	2.2	-014	2.6	-026	2.5	-022
M_2	(2.0)	(000)	(2.0)	(000)	2.0	(000)
S_2	1.1	026	.61	061	1.0	026

Table 2.5.2

(upper) Admittances for major semidiurnal barotropic current components, and for the surface tides from Wunsch (1972a). (lower) Normalized admittances of current components to compare with the behavior of the surface tide.

and a similar phase progression. Again the main discrepancy lies in the v component for the S_2 band, which showed very low coherence with the equilibrium tide. The total v component power in the S_2 band was greater than for the u component at upper depths (Figure 2.3.3a), and the low coherence values represent a low signal to noise ratio. The overall agreement with the behavior of the surface displacement supports the scheme for deriving the barotropic current fields.

Barotropic currents can also be estimated by the modal decomposition of vertically separated measurements. Following the discussion in Section 2.4, Table 2.5.1 includes individual M_2 barotropic estimates obtained by fitting the barotropic mode and the first two baroclinic modes to 15 days of record on Moorings 1 and 7. Each of these moorings had five distinct levels of measurement. The general agreement between these estimates and the overall M_2 average is good, with the overall amplitudes being slightly lower. The u component phases are grouped within about a 10° interval and the v component phases scatter through 30°. Based on the calculated coherence values for the overall average M_2 components, approximate 95% confidence limits for the overall phases are $\pm$15°.

Baroclinic pressure signals

Recently, ZMMBD (1974) estimated the M_2 barotropic current field in the MODE area by calculating the tidal sea surface gradient from an array of bottom pressure gauges. Their estimates are reproduced in Table 2.5.1, and as they noted on the basis of a preliminary comparison with our work with the current meter data, the agreement in the two methods is remarkable considering the accuracy needed in their measurements to resolve the small differences in tidal elevation across the experiment. Discussions with this group involving our work recognized the possibility that such arrayed pressure measurements dealing with differences in tidal pressure amplitudes of order 1 cm of sea water could be influenced by the pressure fluctuations of baroclinic tides if these existed in a deterministic relation with the surface tide.

For a simple plane internal wave of mode n, it can be shown (Section 1.2) that the pressure fluctuation at a given level is

$$p = \rho_o u.(\sigma^2-f^2)/(\sigma k_n)$$

where k_n is the wavenumber of mode n and u is the horizontal velocity component in the direction of wave propagation.

This can be written more simply as

$$p = \rho_o c_{gn} . u$$

where c_{gn} is just the group speed of the n^{th} mode. With the values for c_{gn} in Table 2.2.4, a 1 cm/s current in the first baroclinic mode would be accompanied by a pressure fluctuation of .284 cm of sea water. The contribution to the pressure field from higher modes with equivalent current power is proportional to their group speeds, which decrease with higher mode numbers. In the normalizations used here, a vertical displacement amplitude of 3.0 m would give rise to a bottom pressure signal of .103 cm for mode 1, .0594 cm for mode 2, .0330 for mode three and so on. The average over the experiment gave mode 1 amplitudes between 2 and 3 m in general.

The actual differences in bottom pressure reported by ZMMBD were 1.32 cm and 2.55 cm across two base lines of 218 km and 171 km. The effect of the baroclinic pressure fluctuations in pressure on such measurements would depend on the phase differences as well as the amplitude variation over distance, but it seems that such effects could easily have an 0(10)% influence on the ZMMBD case. This would be especially true for the shorter pressure time series, since over shorter periods we have shown that the baroclinic tide

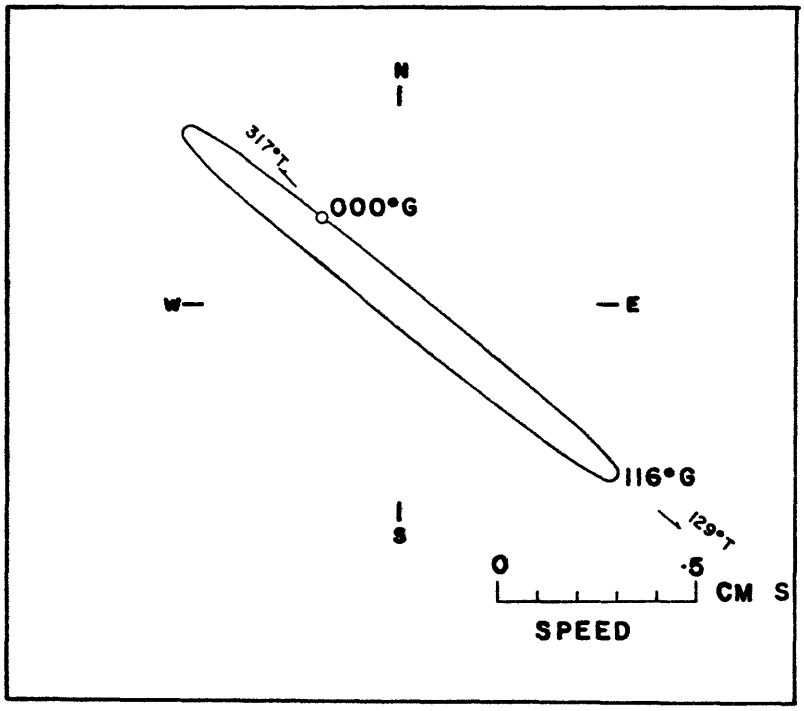


Figure 2.5.1 M_2 barotropic current ellipse from an overall average of current measurements. High tide occurs at 000°G, defining the direction of horizontal energy flux towards 317°T.

can have an apparent amplitude considerably larger than the overall average. These considerations might explain part of the large v component in the ZMMBD estimates, which is the main discrepancy between their results and those presented here from the direct current measurements.

Energetics of the barotropic tide

Using the overall M_2 current estimates and the work of ZMMBD to define the sea surface signal, we can completely characterize the local barotropic tide. Table 2.5.3 summarizes the calculation of the average horizontal kinetic energy and vertical potential energy in the tide, and the energy flux as described in Section 1.4. A sketch of the barotropic current ellipse indicating the time of high water is shown in Figure 2.5.1. Using the calculated values of total energy density and energy flux, we can define an effective group speed by the quotient

$$c_g = \frac{\text{Energy flux}}{\text{Energy density}}$$

$$= .72 \times 10^4 \text{ cm/s}$$

$$= 260 \text{ km/hr}$$

For comparison the theoretical group speed of a long wave

u component	.56 (cm/s)	$110^{o}G$
v component	.46 (cm/s)	$297^{o}G$
sea surface	33.7(cm)	$000^{o}G$
major axis	.72 (cm/s)	$116^{o}G$
minor axis	.043(cm/s)	
orientation	$129^{o}T$	
rotation	clockwise	

horizontal kinetic energy		$.70 \times 10^{5}$ (erg/cm^2)
potential energy		$.28 \times 10^{6}$ (erg/cm^2)
total energy density		$.35 \times 10^{6}$ (erg/cm^2)
energy flux:	amplitude	$.25 \times 10^{10}$ (erg/s cm)
	direction	$317^{o}T$

Table 2.5.3

M_2 barotropic current parameters derived from overall current average, combined with estimates of the M_2 surface tide to give the total energy in the tide, and the energy flux in the tidal wave.

in 5400 m depth is

$$c_g = (gH)^{1/2} \cdot (1-f^2/\sigma^2)^{1/2}$$

$$= 720 \text{ km/hr}$$

The horizontal energy flux is directed towards 317°T, roughly perpendicular to the trend of the co-phase lines in the area(for example, Figure 2 in ZMMBD). Although the tidal wave in the western North Atlantic behaves much like a standing wave, and in the MODE region in particular the maximum current is 64° out of phase with the surface displacement (90° for a pure standing wave), there is still some energy carried by the tide. In this case the energy flux is towards the North American continent, and some of this energy may be reappearing in the MODE-1 area in the form of baroclinic tides.

In conclusion, although the massive effort of the MODE-1 field program was not expended to study tidal processes, the results of different investigators from this experiment make the tidal fields there as well known as in almost any other location in the world's deep oceans.

2.6 Variability in the semidiurnal fields

In Section 2.4 we emphasized the deterministic aspects of the current and temperature fields, especially at the M_2 frequency. In many instances, however, we were reminded of the actual variability in these fields. As an illustration, the seven pieces of record from Mooring 1 temperature measurements provide seven modal decompositions of the vertical displacement field. For the M_2 frequency, modal fits were done for the seven separate cases. Table 2.6.1 shows that the first baroclinic mode varies by a factor of almost 3 in amplitude and has an admittance phase which scatters between 22° and -97°. The second and third modes show great variability in the fits. The average modal decomposition given in Table 2.6.1 has a dominant first mode because the fluctuations fitted by the higher modes tend to cancel in the average. For a coherence with the equilibrium tide of .7, about 50% of the power in a temperature signal is deterministic and the remainder not explainable in terms of a direct relation with the tidal forcing.

We can rationalize part of the variation as general oceanic noise, but some of the energy which appears incoherent at the tidal frequency is undoubtedly of tidal origin also. Time varying currents and density profiles can shift

Piece number	Mode number	Amplitude (m)	Phase	Amplitude squared	% of power
1	1	4.94	126	24.4	90
	2	.69	-126	.5	2
	3	1.51	120	2.3	8
2	1	1.78	128	3.2	29
	2	2.16	114	4.7	43
	3	1.77	-148	3.1	28
3	1	3.82	162	14.6	53
	2	2.94	-017	8.6	32
	3	2.03	091	4.1	15
4	1	2.77	161	7.7	51
	2	.70	047	.5	3
	3	2.62	-005	6.9	46
5	1	1.77	-158	3.1	23
	2	1.91	-066	3.6	28
	3	2.53	065	6.4	49
6	1	2.22	157	4.9	83
	2	.92	-128	.8	14
	3	.41	086	.2	3
7	1	4.38	083	19.2	70
	2	1.28	-019	1.6	6
	3	2.60	135	6.8	24
Overall	1	2.56	138	6.6	84
	2	.54	-040	.3	4
	3	.96	094	.9	12

Table 2.6.1

Modal fits of M_2 isotherm displacements for consecutive 15 day periods at Mooring 1, showing the variability of the fits. The overall average M_2 isotherm fluctuation modal decomposition is also given.

the apparent frequency of propagating waves, and if the frequency shifts are not large enough to completely shift the frequency out of the nominal M_2 band, phase shifts of a random nature will be observed. If the time varying processes are strong enough they could result in a randomization of the whole tidal period field, at least over periods comparable to or shorter than the periods of the low frequency fluctuations. In the MODE-1 tidal fields the result appears to be that the lowest internal M_2 mode still retains its identity while the higher modes have been more randomized. At the central mooring there is an indication of a signal in the third baroclinic mode, but the other moorings do not have enough vertical resolution to explore this possibility. The second mode nearly vanishes in the central mooring average.

Mooring motion

Another source of noise is the motion of the moorings on which the sensors are located. Especially in the main thermocline, vertical motions of the temperature sensors in the vertical gradient of temperature can induce large apparent signals. Since some of the measurements of temperature were accompanied by pressure measurements we can discuss the mooring motion effects. Of special interest

is the level of coherence exhibited by the mooring motion: if the tidal period motions were quite regular, for example if driven by the barotropic currents, the apparent temperature signals would be stable with respect to the surface tide but would not represent internal waves at all.

The general result is that mooring motion induced temperature signals are incoherent with the equilibrium tide and so tend to degrade the measured coherence of the temperature fluctuations. In cases where the internal wave temperature fluctuations are small, or the mooring motion exceptionally great, however, mooring motion can dominate the tidal period signal. We have calculated the apparent mooring motion temperature contribution at the M_2 frequency, as defined by

$$\tilde{T} = -(\bar{P} - \bar{P}_o) \cdot \theta_{op}$$

$\bar{P}$ is the pressure signal at M_2 frequency from the T-P recorders, and $\bar{P}_o$ an estimate of the barotropic tide pressure signal made by using the known admittance of the M_2 surface tide and the actual average equilibrium tide amplitude over the course of the record. θ_{op} is the appropriate temperature gradient. Figure 2.6.1 shows a plot of the ratio $\tilde{T}/\bar{T}$, mooring motion signal over actual

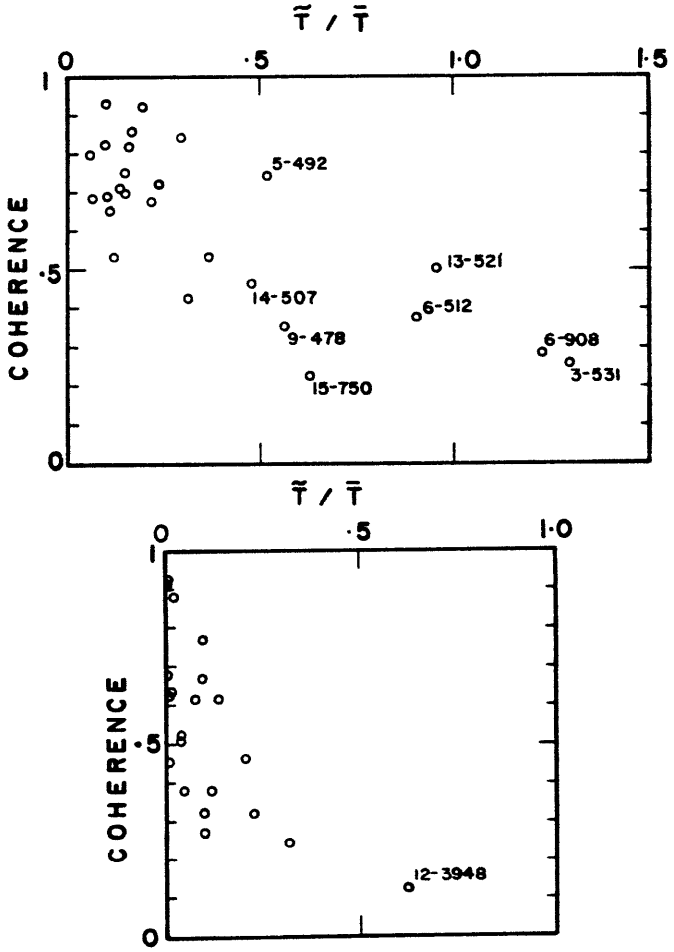


Figure 2.6.1 Mooring motion effects on coherence of temperature fluctuations and the equilibrium tide in the M_2 band. The coherence estimates are plotted against the ratio of mooring motion related temperature signal inferred from pressure measurements, to measured average temperature signal. A high ratio means that mooring motion is dominating the temperature fluctuations. (upper) Measurements above 1200 m inclusive. (lower) Measurements below 1200 m. Some individual records are marked with mooring number and depth in meters.

measured signal, versus the coherence estimate between the temperature and the equilibrium tide for the record. Separate cases are shown for depths above and below 1500 m, in the thermocline and in the deeper water. In both cases there is a trend of lower coherence estimates with increase in the relative effect of mooring motion. The figures also show that in most cases, especially in the deep water, the mooring motion induced temperature signals were considerably smaller than the measured temperature fluctuations on average.

In the deep water the total pressure signals tended to be dominated by the barotropic tide, but there is still an indication of negative correlation in Figure 2.6.1. This figure also shows that the general coherence levels for the M_2 temperature fluctuations were lower in the deeper water. This was also observed (Table 2.4.1) for the central mooring where the two deepest levels had relatively low coherences. This reduction could be explained simply as a greater noise to signal ratio at the lower depths where the first baroclinic mode fluctuations become very small.

The part of Figure 2.6.1 relating to the thermocline observations shows that in some cases the apparent mooring motion signal can be comparable to the observed signal. Of the four records with $\tilde{T}/\overline{T}$ greater than .9, two came from

Mooring 6 which was previously mentioned as exceptional. The two other points with $\tilde{T}/\overline{T}$ greater than .9 came from the 500 m levels on Mooring 3 and 13. Moorings 6 and 3 show particular and different aspects of the mooring motion problem and we discuss them here. Table 2.6.2 shows the average M_2 temperature amplitudes and phases for Moorings 6 and 3, the average pressure fluctuations from levels with T-P recorders, and the resulting pressure amplitudes and phases when the surface tide has been removed. The apparent mooring motion temperature contribution is also given. Mooring 6 appears seriously influenced by mooring motion at the upper levels, with the 512 m ratio $\tilde{T}/\overline{T}$ = .91 and the phase difference between the pressure and temperature fluctuations 174° compared to the 180° which pure mooring motion would give. The 908 m level on this mooring shows almost exactly the same pressure effect of mooring motion, but a smaller measured temperature signal and there appears to be some cancellation between true temperature and mooring motion induced temperature fluctuations. The phase difference at 908 m is about 105°. Finally at 3957 m where there is another pressure record, the pressure signal is mostly the barotropic M_2 tide and mooring motion is insignificant for the temperature measurements. The phases of the temperature fluctuations at the three deepest levels are quite similar,

Mooring 6

Temperature

Depth (m)	$\bar{T}$ (mdeg.C)	Phase	Coherence	No.of pieces
408	8.18	-106	.45	5
512	17.1	-113	.38	5
709	13.7	169	.24	6
908	12.8	-046	.28	5
1410	1.69	058	.24	5
2933	2.67	083	.54	5
3957	.618	053	.39	5

	Pressure			Pressure - P_o		
Depth (m)	$\bar{P}$ (db)	Phase	Coherence	P (db)	Phase	No.of pieces
512	1.16	077	.56	1.05	061	5
908	1.06	077	.57	.964	059	5
3957	.459	099	.57	.306	054	5

	Comparison			
Depth (m)	θ_{op} (mdeg.C/db)	$\hat{T}$ (mdeg.C)	$\hat{T}/\bar{T}$	Phase difference
512	14.8	15.6	.909	-174
908	16.4	15.8	1.23	-105
3957	.230	.070	.114	002

Table 2.6.2a

Mooring motion at M_2 frequency at Mooring 6 (see text).

Mooring 3

Temperature

Depth (m)	$\overline{T}$ (mdeg.C)	Phase	Coherence	No.of pieces
427	4.96	078	.28	5
531	8.92	077	.25	5
728	37.4	091	.54	5
933	57.3	075	.83	5
1428	10.4	104	.85	5
3956	.818	135	.62	5

	Pressure			Pressure - P_o		
Depth (m)	P (db)	Phase	Coherence	P (db)	Phase	No.of pieces
531	.793	080	.42	.697	055	5
933	.762	080	.44	.663	055	5
3956	.453	102	.67	.280	057	5

Comparison

Depth (m)	θ_{op} (mdeg.C/db)	$\tilde{T}$ (mdeg.C)	$\tilde{T}/\overline{T}$	Phase difference
531	16.6	11.6	1.30	022
933	9.62	9.62	.168	020
3956	.230	.0644	.0788	078

Table 2.6.2b

Mooring motion at M_2 frequency at Mooring 3 (see text).

and we can speculate that those levels reflect a first baroclinic mode which is buried in the mooring motion at the upper levels. Since the properties of mooring motion are not well understood, a straightforward linear correction of the temperature signals by subtraction of the apparent mooring motion is not appealing. A linear model by Noble (personal communication, 1974) removes that part of the mooring motion temperature signal which is incoherent with the surface tide and apparently showed promise in a case where mooring motion was small. Generally we can live with the problem in this study, but in the modal decomposition of M_2 temperature fluctuations at Mooring 6 the bistable phase distribution in the vertical results in a fit dominated by the second baroclinic mode, and the mooring was excluded from the wavenumber analysis described in Section 2.4.

The other case which we examine in detail is Mooring 3, which showed a large $\tilde{T}/\overline{T}$ ratio for the M_2 frequency at 531 m. Unlike Mooring 6, the noise introduced by the mooring motion was not great enough to completely dominate the true temperature signal. Referring to Table 2.6.2b, the coherence between the temperature and equilibrium tide at the 400 and 500 m levels is small, and the temperature signal which mooring motion gives is larger than the actual measured temperature at the M_2 frequency. However the mooring motion does not dominate

the temperature signal since the phase difference between the temperature and pressure fluctuations is nearer to 0° instead of the 180° expected for mooring motion. The phase of the temperature fluctuations is quite constant in the vertical on Mooring 3, and the pressure record from 933 m shows that mooring motion is not a significant factor throughout the main thermocline. This appears to be a case where mooring motion has degraded the coherence levels at the upper two levels, but the phase of the energetic temperature signal has survived even in the uppermost levels.

We can only speculate on the reasons why some moorings should be more affected by mooring motion than others. The response of deep sea moorings, which are complicated dynamical systems of distributed buoyancy and drag elements, is very much a current research topic in ocean engineering. Some aspects of the mooring design could lead to a mooring being more susceptible to forcing at tidal period, but in general the normal modes of such systems have periods of a few hours at most. To workers interested in the problems of mooring motion, an analysis of the tidal period fluctuations in mooring displacement might lead to some insight into the response of the moorings. Mooring motion at tidal periods can be forced by tidal period currents, barotropic and baroclinic, and such motion will generate a tidal period

temperature signal when the mooring is permanently tilted over by low frequency currents so that its response to small perturbations in horizontal position is roughly linear in the resulting vertical displacement. For a near-vertical mooring configuration and large enough perturbations in drag, the high frequency variations can give rise to a rectified vertical displacement and temperature signal. The semidiurnal band can be influenced by the second harmonic of the inertial period (25.56 hr at the central mooring), and events of strong bursts of inertial oscillations were noted during the MODE-1 field experiment. The horizontal scales of such events are much less than the scale of the array, and some moorings were affected more than others. In particular, Mooring 13 on the western extreme of the experiment showed a strong event of this nature, which then appeared to propagate towards the east through the array. Moorings 13, 6 and 3 are grouped together in the northwest quadrant of the experiment (Figure 2.2.2) and records from these three moorings show extreme values of $\tilde{T}/\overline{T}$ in the thermocline in Figure 2.6.1. Thus non-stationarity in space of the forces which cause moorings to move is a likely explanation for the differences between a very quiet mooring, such as Mooring 1, and the much noisier moorings mentioned. These effects would be completely unrelated to the tidal periodicity, and would show no coherence with the equilibrium tide.

Energy in mooring motion

As indicated earlier in Section 2.4, the actual energy in the apparent temperature signals induced by mooring motion was substantially less than the total energy in the signals. Some of the characteristics of the mooring motion as it relates to tidal period studies are brought out in Table 2.6.3. The 500 and 900 m levels were instrumented with pressure recorders quite extensively, and allow an overall calculation of mooring motion to compare with the actual temperature signals at those levels. The calculation for the three semidiurnal bands shows that the pressure fluctuations are also peaked at the M_2 frequency. This indicates that a significant part of the mooring motion must be caused by semidiurnal period currents, when the mooring is in an inclined configuration as discussed previously. Since the currents are more energetic at the M_2 frequency than at the neighboring semidiurnal frequencies, the mooring motion is also more extreme there. Rectified mooring displacements caused by near inertial period currents apparently do not dominate the semidiurnal tidal period motions. However there are indications of such rectified motion.

The entries for the nominal N_2 and S_2 mooring motion

Depth (m)	Period (hr)	Pressure variance $(db)^2$	$\frac{\partial\rho}{\partial p}$ $(\frac{mdec.C}{db})$	Mooring motion variance $(^oC)^2$	Measured variance $(^oC)^2$	% Mooring motion
500	25.71	1.38	13.1	$.237 \times 10^{-3}$	$.760 \times 10^{-3}$	31
900		1.69	16.8	$.478 \times 10^{-3}$	$.201 \times 10^{-3}$	24
500	24.00	1.85	13.1	$.317 \times 10^{-3}$	$.128 \times 10^{-3}$	25
900		1.27	16.8	$.359 \times 10^{-3}$	$.160 \times 10^{-3}$	22
500	12.86	.623	13.1	$.107 \times 10^{-3}$	$.617 \times 10^{-3}$	17
900		.590	16.8	$.167 \times 10^{-3}$	$.148 \times 10^{-2}$	11
500	12.41	2.18	13.1	$.375 \times 10^{-3}$	$.257 \times 10^{-2}$	15
900		1.86	16.8	$.526 \times 10^{-3}$	$.481 \times 10^{-2}$	11
500	12.00	.436	13.1	$.748 \times 10^{-4}$	$.852 \times 10^{-3}$	9
900		.368	16.8	$.104 \times 10^{-3}$	$.180 \times 10^{-2}$	6

Table 2.6.3

Energetics of mooring motion related temperature fluctuations in the semidiurnal and diurnal-inertial frequency bands. The diurnal bands are more seriously influenced by the mooring motion.

fluctuations show that at both depth levels there is more mooring motion at the lower frequency, and that the ratios of mooring motion induced temperature fluctuations to measured fluctuations are greater for the N_2 band than the S_2 band. The 12.86 hr period of the nominal N_2 band is the second harmonic of 25.72 hr period fluctuations, compared to the 25.6 hr inertial period at the center of the MODE-1 array.

As previously mentioned, the M_2 ratio of mooring motion is about 15% for the maximum of the two levels in the thermocline for which there is complete pressure coverage. Thus the effects of mooring motion are generally not at all dominant in the temperature measurements. For the N_2 band, the results are about the same, while the S_2 band appears somewhat less affected by mooring motion with ratios at both 500 and 900 m of the mooring motion to recorded variance being less than 10%.

For comparison and future reference, the mooring motion calculations have also been done for the diurnal-inertial frequency bands. The two bands both show considerably greater ratios of contamination, with between a quarter and a third of the temperature variance explainable as mooring motion.

2.7 Conclusions

The analysis of temperature and current measurements obtained in the Mid-Ocean Dynamics Experiment in the western North Atlantic Ocean shows energetic fluctuations at the semidiurnal tidal frequencies. The principal lunar M_2 frequency dominates the adjacent semidiurnal bands, with the energy in the temperature fluctuations typically less by a factor of 3 at a frequency separation of 1/15 cycle per day. The energy levels are roughly symmetric in frequency about the M_2 peak. A comparison of the vertical distribution of temperature variance with WKBJ theory suggests that low order vertical modes are present. Horizontal currents have energy levels four times as great at 400 m as in the deep water for the M_2 tide, and the deep M_2 currents are dominated by the barotropic tide. Barotropic effects are less evident in the neighboring S_2 and N_2 frequency bands, and the current energy at the upper levels is an order of magnitude greater than the deep currents for these fluctuations. A comparison of the horizontal kinetic energy and vertical potential energy at different depths averaged across the experiment gives results consistent with internal wave dynamics, and a further indication of low order modes in the fields.

The M_2 temperature fluctuations show significant coherence with the equilibrium tide, especially in the region of the main thermocline, while the neighboring

frequencies are much more random in their phase distribution. The coherent part of the M_2 temperature field shows isotherm displacements which are in phase throughout the water column, characteristic of the lowest baroclinic mode. Modal decompositions of the vertical distribution of temperature fluctuations at the individual moorings in the experiment quantify this, and show a first baroclinic mode content with a characteristic thermocline displacement amplitude of 3 m. A horizontal wavenumber spectrum estimate of the first mode energy indicates a wave motion through the experiment towards the southeast, with a wavelength consistent with the theoretical value for the first baroclinic mode. Energy propagates from the northwest, away from the continental slope south of Cape Hatteras, and this suggests that the internal tides are generated there. Evidence from a prior experiment in the same geographical area supports the conclusion that the M_2 tidal process includes a deterministic internal tide.

The temperature fluctuations at the neighboring S_2 tidal frequency show too much variability to gain a stable estimate of the properties of the internal tide at that frequency. However there are indications that the weaker S_2 internal tide behaves similarly to the M_2 internal tide. A calculation using the dispersive nature of propagating

internal waves of slightly different frequencies and the age of the internal tide in the experimental region suggests the generation region is o(700) km displaced from the experiment. This is also consistent with the distance to the nearest continental slope.

The current measurements showed much variability and were of less duration than the temperature measurements. At the heavily instrumented central mooring, the results from the M_2 current field support the modal decomposition and directionality inferred form the temperature measurements alone.

Various methods of estimating the barotropic current field from the direct current measurements agree with the general behavior of sea level fluctuations in the area, and with the results of recent bottom pressure measurements used to derive the tidal currents. Pressure fluctuations due to the internal tides may have a significant effect on such bottom measurements in the MODE region.

Variability in the semidiurnal current and temperature fields is noted, with significant portions of the energy unexplainable on the basis of deterministic waves. Many aspects of oceanic variability at lower frequencies can contribute to the variability of the tidal fields, through Doppler shifting and refraction of the propagating tidal waves. Mooring motion can affect the temperature measurements by introducing spurious temperature fluctuations.

In general the mooring motion signals appear as incoherent noise which tends to degrade the true internal wave signal. Generally the mooring motion is smaller than the actual temperature fluctuations at a point, but exceptional cases are noted. Non-stationarity in the horizontal of currents which cause the moorings to move results in large differences in the behavior of separated moorings in the experiment.

DIURNAL TIDES

3.1 Diurnal period internal tides: Introduction

It is of interest to examine the variability in the ocean at the diurnal tidal frequencies, as the tidal forcing represents a known source of energy. As for the semidiurnal tides, the internal waves associated with diurnal period tides will be forced indirectly, rather than by the actual astronomical forcing. Diurnal period internal waves can be fundamentally different from semidiurnal period waves, as freely propagating waves can only exist equatorward of the critical latitudes where $\sigma = \pm f$. For semidiurnal period waves the critical latitudes occur near the poles, but the diurnal turning latitudes are near 30° and much of the oceans are forbidden regions for freely propagating diurnal period internal waves. Poleward of the critical latitude Equation 1.2.11 describing the spatial variation of an internal wave field is elliptical in form. Although three dimensional wave motions are not admitted as solutions, motions which are trapped in one or more spatial direction can exist. For example Kelvin wave modes can propagate along a depth discontinuity, and trapped waves about a localized topographic feature are possible. Since there are normal mode solutions in such cases, resonances are a possibility in a forced problem.

Near the critical latitudes, the problem requires special treatment. Motions with $\sigma \simeq f$ are known as inertial

period motions and the simple f-plane solutions have an apparent resonance there. Munk and Phillips (1968) have discussed inertial period waves in the oceans, showing that the variation of the Coriolis parameter with latitude is of vital importance. Their solutions represent a matching between freely propagating internal wave modes equatorward of the critical latitudes and an exponential fringe poleward of these latitudes. The observations from MODE-1 allow us to examine the diurnal period variability near the critical latitudes for such waves. For the two major lines in the diurnal tidal forcing, the K_1 frequency critical latitude of 30°05'N is just north of the experiment, while the O_1 critical latitude of 27°42'N lies in the center of the array. The moored current and temperature measurements can be examined for diurnal period energy, and for any differences in the two diurnal bands which might relate to the critical latitude considerations.

A special experiment was performed at Muir Seamount about 600 km north of the MODE site. This seamount is north of all the diurnal period critical latitudes, and can be examined for trapped diurnal period internal waves. The observations are analyzed in the context of a simple model for the generation of trapped motions in a seamount geometry.

Finally, the current observations from Site D which

is far north of the diurnal critical latitudes are reexamined for diurnal period motion. The nearby continental slope is expected to constrain the diurnal tides, and we are particularly interested in the possibility of baroclinic waves in this geometry. The barotropic diurnal wave can also be studied.

All three sites show dominant baroclinicity in diurnal period motions. In the following sections we expand on these introductory remarks. Section 3.2 deals with the MODE-1 results and the question of internal tides at the critical latitude. Section 3.3 discusses the Muir Seamount experiment and evidence for trapped diurnal internal tides, and Section 3.4 is concerned with the Site D measurements. A specific model for the barotropic diurnal wave is developed there. The overall conclusions about diurnal period tides in the North Atlantic which we can draw from these three regions are summarized in Section 3.5.

3.2 Internal tides at the critical latitude

In 1964, Hendershott studied the turning latitude problem near 30^{o}N. He assumed that the astronomical tides would dominate the fields, and that the latitudinal variation of diurnal period temperature fluctuations could be used to examine the fine structure of the process. In his model, the barotropic tide generated internal tides through an interaction with bottom roughness. Munk and Phillips (1968) developed a theoretical framework for the internal wave critical latitude problem. Locally the Coriolis parameter is nearly a linear function of north-south position, and the derived solutions are valid in some region about the turning latitude. The Airy function (Abramowitz and Stegun, 1965) solutions of Munk and Phillips are wavelike in the meridional coordinate equatorward of the turning latitude but decay poleward, with the horizontal scale of the motion dependent on the vertical mode. For a first baroclinic mode at 30^{o} latitude the horizontal scale is about 1.5 degrees of latitude, and with higher modes the scale decreases. The actual argument of the Airy function is

$$(\phi-\phi_o)/L - (\sigma-\sigma_o)/2\Omega L \cos \phi_o + (\alpha L)^2 \qquad (3.2.1)$$

where ϕ_o is a reference latitude and $\sigma_o = 2\Omega\sin\phi_o$ a reference frequency. α is the zonal wavenumber in cycles per earth circumference, and

$$L = (2a^2k_o^2 \cot\phi_o)^{-1/3}$$

is the Airy scale. k_o is the horizontal wavenumber in the standard vertical eigenvalue problem for zero frequency for a particular mode, and a is the radius of the earth. From 3.2.1, the horizontal structure in the turning latitude modes depends equally on the spatial and frequency variations, and Munk and Phillips point out that resolution in both frequency and horizontal separation is necessary to resolve such structure.

Miles (1974) discusses the coupling between barotropic and baroclinic motions in the ocean caused by the horizontal component of the earth's rotation. For frequencies which allow a critical latitude, Miles suggests that a resonance condition in the internal wave modes forced by a surface mode could result in large baroclinic waves. This mechanism has not been fully explored to date.

Wind forced inertial period motions can also be present at the critical latitude, and obscure the tidal content.

Pollard (1970) does suggest that for general oceanic stratification inertial period motion in wind generation models seems to be confined largely to the near surface. Olbers (1974) has explicitly calculated the non-linear transfer function for a model internal wave spectrum. He shows that weak wave-wave interactions in the internal wave band tend to transfer energy from higher frequencies towards the inertial frequency, and that if the initial growth rate suggested by the transfer function were maintained, the inertial band energy content would double within a week or two. For an equilibrium spectrum the inertial period energy must itself be dissipated through shear instabilities or some other mechanism, but the near inertial periods may be dominated by this non-linear transfer mechanism.

Observations from MODE-1

The current and temperature data used in Section 2 to examine the semidiurnal internal tides were also looked at for diurnal period energy. The 15 day pieces used give neighboring estimates in frequency space at 24.00 and 25.71 hour periods, which are nearly the true astronomical K_1 and O_1 periods of about 23.9345 hr and 25.8193 hr respectively.

Windowing effects in the finite transform do not contaminate the diurnal resolution, with about 99% of the variance of each diurnal tidal frequency falling in the respective band in the transform. In both horizontal current and temperature, there is considerable energy in the diurnal-inertial band, with a sharp decrease toward lower frequency and a smoother decline into the internal wave band at higher frequency. The peaks are broader in frequency spread than the peaks in the semidiurnal tidal band. In model internal wave studies, the inertial frequency (where the group velocity vanishes) is an accumulation point for internal wave energy rather than an isolated peak.

Figures 3.2.1 give the squared amplitudes of the O_1 and K_1 band temperature fluctuations averaged across the array as a function of depth. The shapes of the two profiles are similar, and show a remarkable resemblance to the average $N^{-1}(z)(d\theta/dz)^2$ profile which was presented in Figure 2.3.2. There is a strong maximum in the main thermocline near 700 m, an inflectional feature between 2000 and 3000 m, and a slight increase in power at the lowest depth. Such behavior is expected for a field of internal waves composed of a random mixture of many modes. The temperature variance in the diurnal bands at 700 m is about a third of the average M_2 frequency variance there with the same bandwidth.

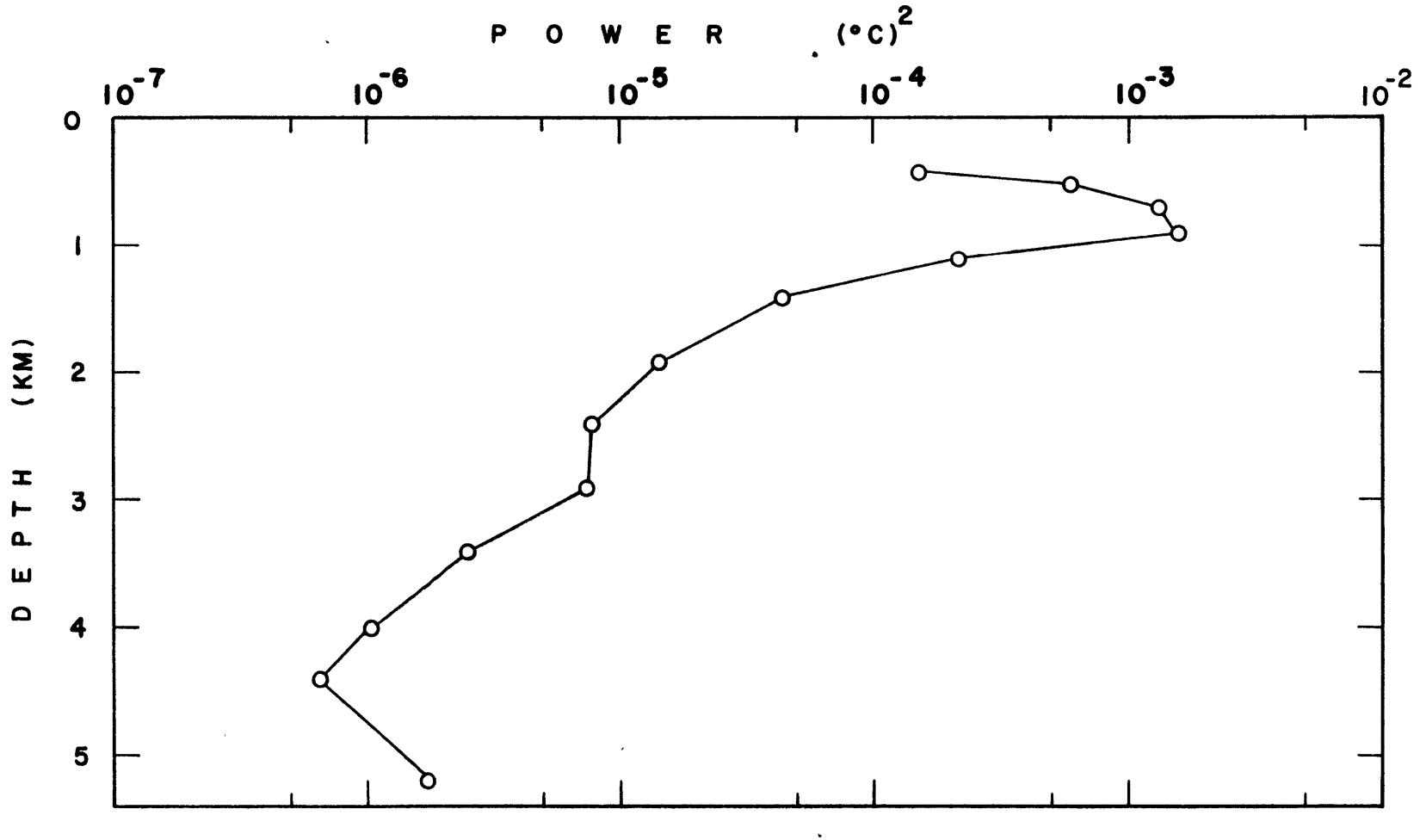


Figure 3.2.1a Squared amplitude of temperature fluctuations in the O_1 band as a function of depth, averaged across the MODE-1 array.

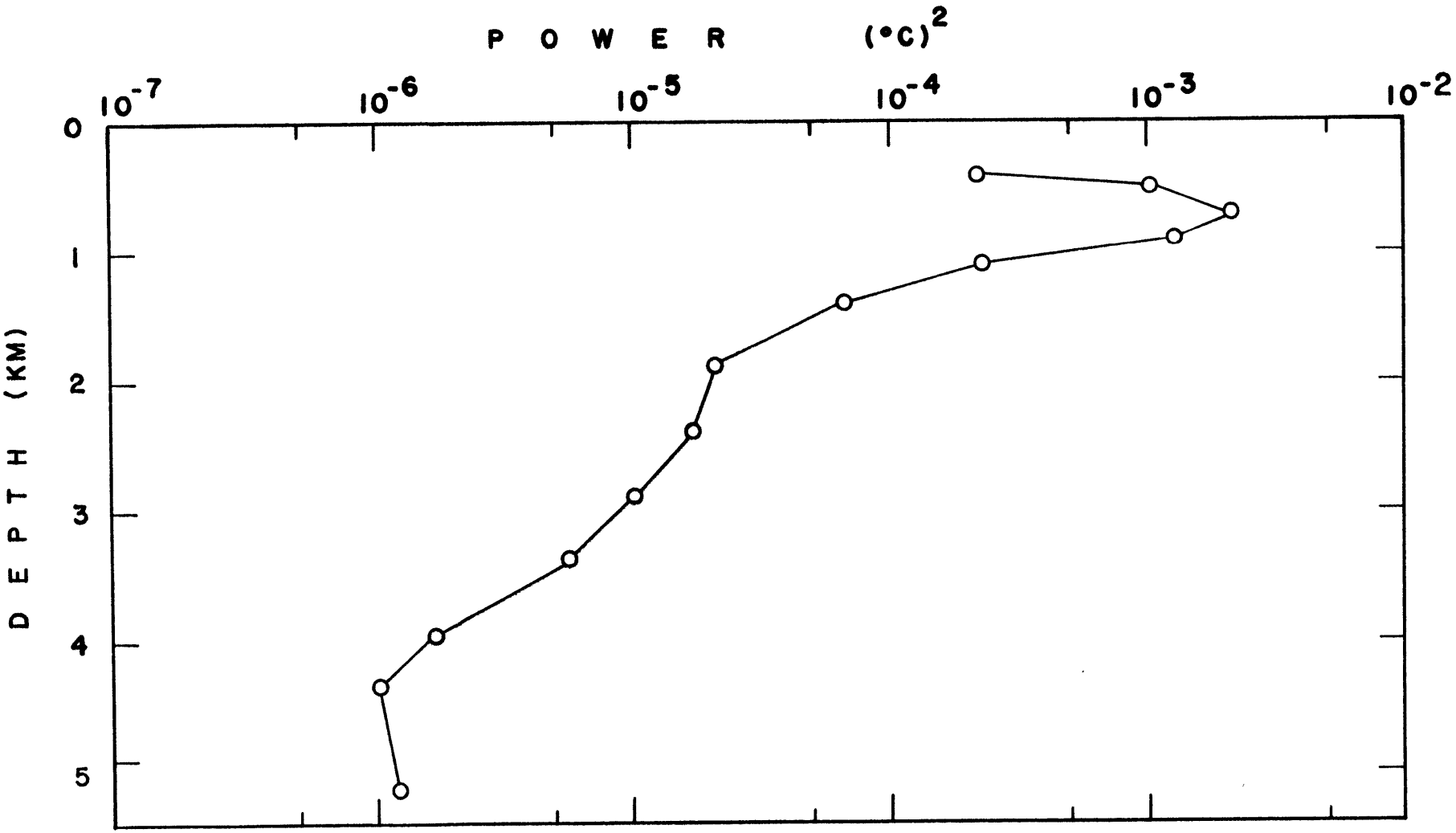


Figure 3.2.1b Squared amplitude of temperature fluctuations in the K_1 band as a function of depth, averaged across the MODE-I array.

Figures 3.2.2 give a similar average for the squared amplitudes of horizontal current components. These show a resemblance to the average N(z) profile in Figure 2.3.4, with maxima in the main thermocline and a monotonic decrease into the deeper water except at the deepest 5000 m level. The u and v components are comparable in magnitude at all depths. An examination of the rotary spectra of the horizontal currents shows that they tend to be nearly circularly polarized, with clockwise rotation characteristic of intertial circles in the northern hemisphere. For a comparison, the currents at 700 m in the diurnal bands are about four times more powerful than the M_2 average at that level (Figure 2.3.3b).

There are differences in the behavior at the two diurnal frequencies, with the O_1-inertial frequency band showing a slight but generally lower level of temperature variance compared to the K_1 band. The current energy in the two bands is nearly equal except at the lowest two levels near 4000 and 5000 m where the average O_1 power is considerably less. We estimated the average potential energy in the fluctuations at different depths from the temperature fluctuations as in Section 2.3, and calculated ratios of horizontal kinetic energy to potential energy at each level for the two diurnal frequencies. An f-plane approximation

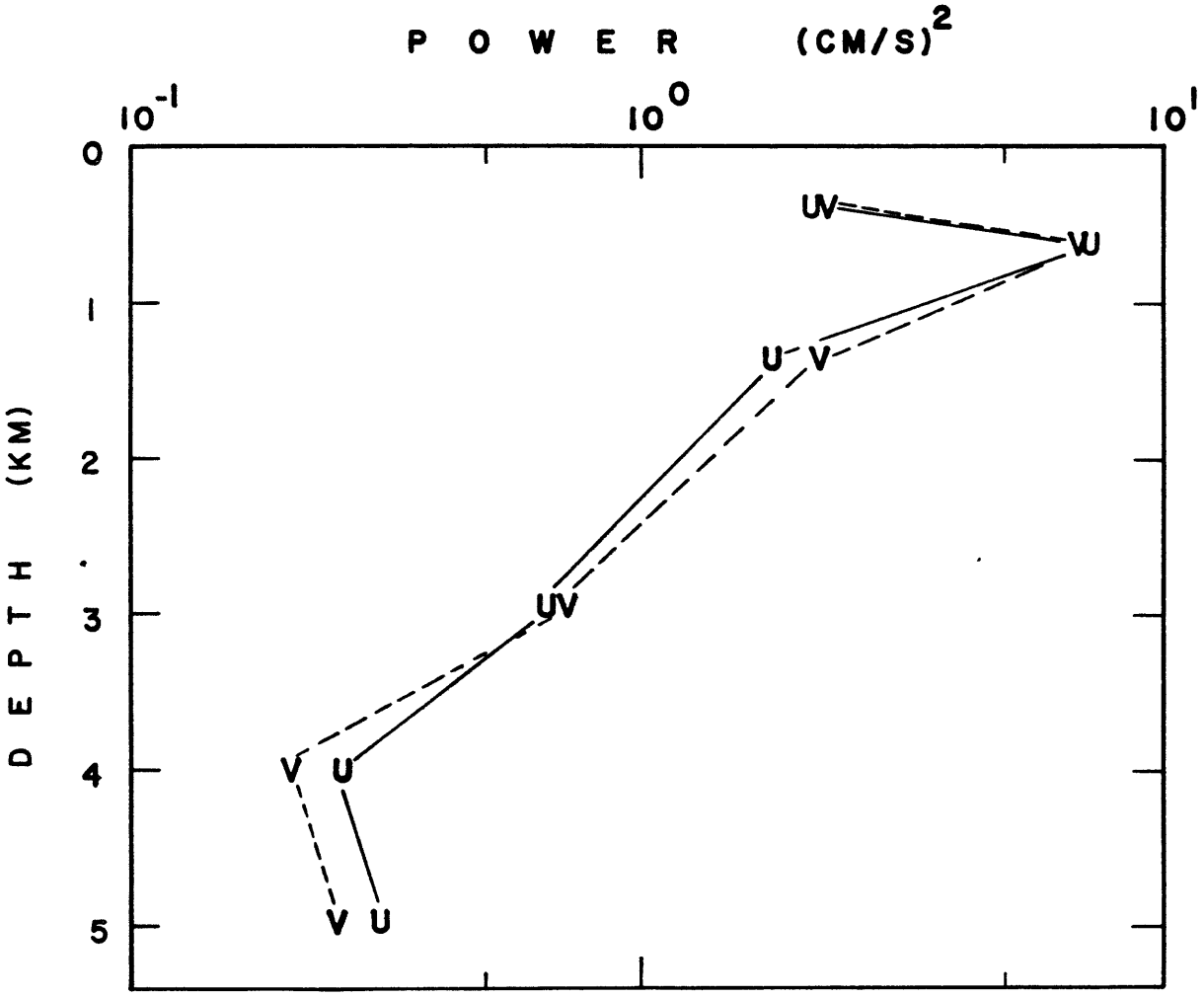


Figure 3.2.2a Squared amplitude of u (east) and v (north) current components in the O_1 band as a function of depth, averaged across the MODE-1 array.

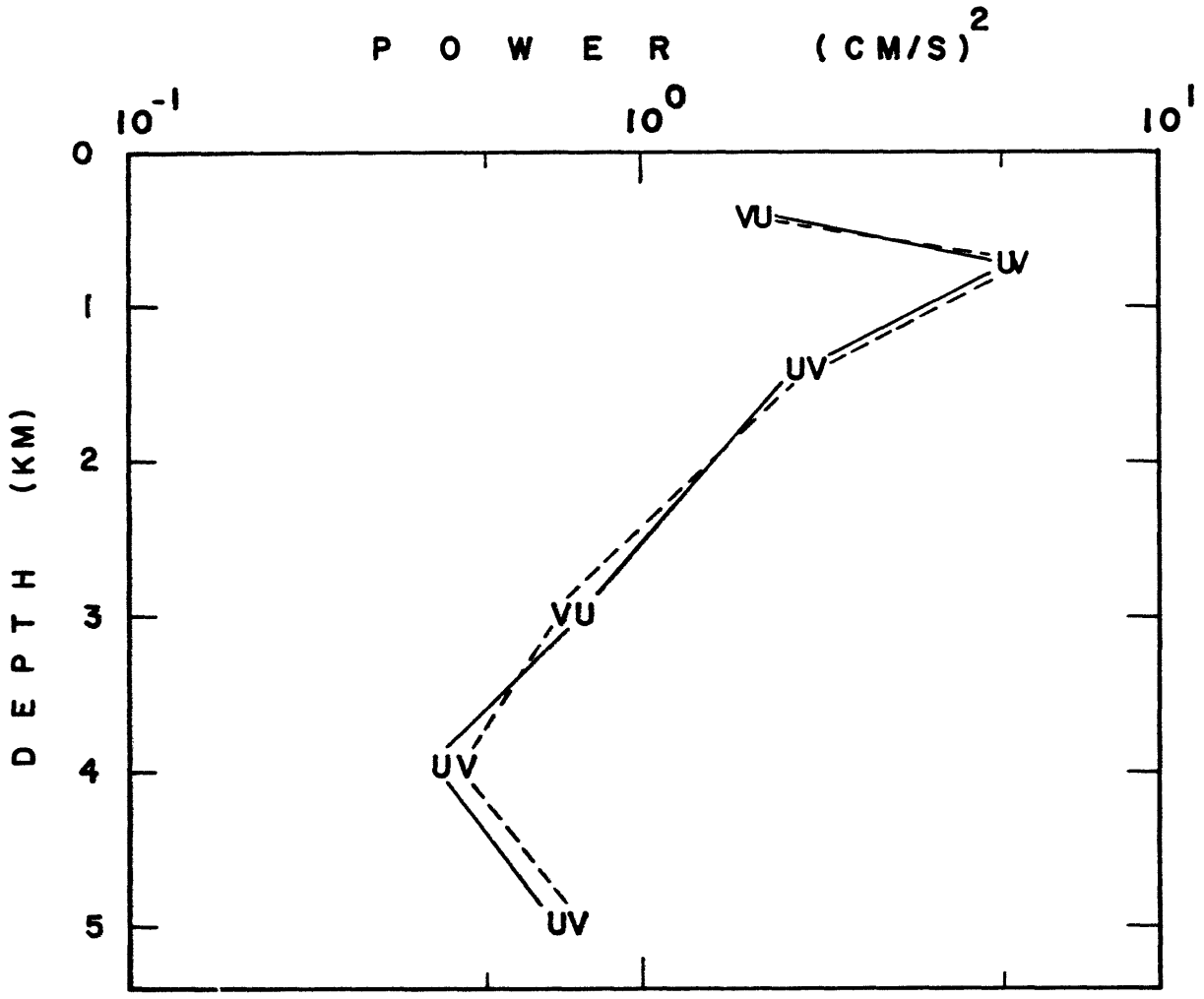


Figure 3.2.2b Squared amplitude of u (east) and v (north) current components in the K_1 band as a function of depth, averaged across the MODE-1 array.

shows that the expected value of such ratios is

$$(\sigma^2 + f^2)/(\sigma^2 - f^2) \qquad (3.2.2)$$

but this is not valid at the critical latitude $\sigma = f$. For the nominal K_1 frequency in the finite transform and f at the center of the MODE array, the theoretical ratio 3.2.2 is 15.9. The K_1 turning latitude is more than one first baroclinic mode scale L from the array center.

For the turning latitude problem, Munk and Phillips (1968) show that the Airy approximation gives a ratio of average horizontal kinetic energy to potential energy in a single mode of

$$(fa/NH)^2(\pi nL)^2(Ai(\eta)/(\alpha LAi(\eta)-Ai'(\eta)))^2 \qquad (3.2.3)$$

where $Ai(\eta)$ is the Airy function with argument 3.2.1. The scale L depends on the mode number n, varying like $n^{-2/3}$ for a WKBJ treatment. Table 3.2.1 gives scale values calculated for the first five baroclinic modes in the average MODE density distribution. The meridional modulation in the ratio arises because the modes are like standing waves in the north-south direction, and any further calculations require a specification of the distribution

Mode number	Airy scale (°latitude)	L (km)
1	1.37	152
2	.775	86.2
3	.638	70.9
4	.535	59.5
5	.449	49.8

Table 3.2.1

Airy scales for the first five baroclinic modes at $30^{\circ}N$ latitude for the average MODE-1 stratification.

energy as a function of east-west wavenumber α and vertical mode number n. For vanishing zonal wavenumber, the partition increases with increasing mode number, unlike propagating internal waves for which it is completely independent of the particular mode.

In Table 3.2.2 we present the observed ratios of horizontal kinetic energy to potential energy for the two diurnal frequencies. The K_1 band ratios are nearly constant with depth down to 4000 m at about 10, while at the lowest two depths there was relatively more kinetic energy. For the O_1 or near inertial band, the ratios are uniformly larger than 10 above 3000 m, with an average of about 18. For nearly the same current amplitudes, the near-inertial band has vertical displacements about 25% less than the neighboring K_1 band. If we assume that the measured temperature variances are 25% too large as a result of mooring motion, as suggested in Table 2.6.3 previously, the ratios of horizontal kinetic energy to potential energy should be increased to 13 and 24 for the K_1 and O_1 bands respectively, while the effect of mooring motion on current measurements is an unknown. The similarity between the profiles of kinetic energy and potential energy and the profiles of $N(z)$ and $N^{-1}(z)(d\theta/dz)^2$ as suggested by the WKBJ theory for an internal wave field composed of many modes suggests that the diurnal bands behave differently than the semidiurnal

O_1 band: Depth (m)	HKE (erg/cm^3)	VPE (erg/cm^3)	Ratio
400	$.13 \times 10^{1}$	$.76 \times 10^{-1}$	18
700	$.44 \times 10^{1}$	$.18 \times 10^{0}$	24
1400	$.12 \times 10^{1}$	$.78 \times 10^{-1}$	16
3000	$.42 \times 10^{0}$	$.29 \times 10^{-1}$	14
4000	$.14 \times 10^{0}$	$.18 \times 10^{-1}$	7.9
5200	$.19 \times 10^{0}$	$.36 \times 10^{-1}$	5.3

K_1 band: Depth (m)	HKE (erg/cm^3)	VPE (erg/cm^3)	Ratio
400	$.10 \times 10^{1}$	$.12 \times 10^{0}$	8.2
700	$.32 \times 10^{1}$	$.30 \times 10^{0}$	10
1400	$.13 \times 10^{1}$	$.12 \times 10^{0}$	11
3000	$.45 \times 10^{0}$	$.41 \times 10^{-1}$	11
4000	$.26 \times 10^{0}$	$.30 \times 10^{-1}$	8.9
5200	$.44 \times 10^{0}$	$.25 \times 10^{-1}$	18

Table 3.2.2

tidal band, where low order modes seemed to dominate the fields. Before drawing any further conclusions about the diurnal period motions, we investigate the relationship between the observations and the tidal forcing.

Tidal admittances

The average current and temperature fluctuations at individual measuring points were computed with the same methods described in earlier sections. The averages used the admittance phases for the individual pieces of a given record, and so tended to filter out any motion not correlated with the equilibrium tide. Coherences between the measured quantities and the equilibrium tide were also calculated. Unlike the semidiurnal frequencies, the diurnal bands showed little evidence of true tidal content.

At the central mooring, the temperature records were generally incoherent with the equilibrium tide at the 95% confidence level, and the admittance phases varied randomly in the vertical. The calculations of overall average horizontal currents as described in Section 2.5 for the semidiurnal tides was repeated for the diurnal bands. If there is a barotropic diurnal tide in the MODE-1 region which stands out from the noise background, the overall average should extract it. In fact, the estimates of

coherence between the equilibrium tide and the overall current ensemble were uniformly not significantly different from zero for both u and v components in both diurnal bands. This places an upper bound on the barotropic component of about .2 cm/s, assuming only that the spatial scale of the barotropic wave is greater than the scale of the array as expected. Even at the deepest levels of measurement, the current phases varied greatly.

The general conclusion from these calculations is that most of the energy in the two diurnal bands is unrelated to the astronomical tides, and that the extraction of a meaningful tidal signal is very difficult. Instead of deriving from a line input, the variance in the diurnal bands appears to be a manifestation of high-mode, wide band internal wave motion of inertial character.

Horizontal variation in the fields

The frequency resolution in the present scheme is dependent on the 15 day piece length used, and is equivalent in the Airy argument 3.2.1 to a spatial separation of about 2.2 degrees of latitude at 30°N. Thus the frequency resolution does not take real advantage of the spatial resolution of the array, and we cannot argue that the diurnal tides dominate the respective bands because the

measurements indicate that they do not. Further work could be done at higher frequency resolution, but an examination of the periodograms from the full temperature records shows an apparent lack of any distinctive features in the general rise of variance at near inertial frequencies. Higher resolution work must face the problems of stability discussed by Munk and Phillips, and we as yet do not have the five or so years of data which they suggest is appropriate to get stable estimates at a frequency resolution necessary to use 1/4 degree of latitude spatial resolution. Such considerations are not special to the diurnal turning latitude, and take us beyond the scope of the present work.

We did examine the 1/15 cycles/day resolution diurnal power estimates for any latitudinal variation. The major result was a demonstration of the effects of mooring motion on near-inertial frequency measurements. Table 2.6.3 shows that on average about 25% of the diurnal temperature variance is explainable as mooring motion, using the measured vertical excursions of the temperature recorders and the vertical temperature gradient. At 700 m there apparently were large features in the latitudinal variation of temperature fluctuations at diurnal period, but each such case was accompanied by large vertical displacement fluctuations at 500 m and 900 m where there were pressure

measurements. Although there were few actual pressure measurements at the 700 m level, the cases that exist show that an interpolation between the two adjacent depths is reasonable. At 700 m, once the apparent energy in the mooring motion related temperature fluctuations was subtracted from the observed energy, there were essentially no features in a plot of energy versus latitude in both diurnal bands. For one case at 500 m, the ficticious temperature signal constructed from the mooring motion and the measured vertical temperature gradient would have three times as much energy as was actually observed, meaning that some cancellation of internal wave and mooring motion related temperature fluctuations apparently took place. These instances implicitly reveal energetic events, but the interpretation of the measurements in terms of ocean dynamics is not easy. The supposition is that such mooring motion is caused by energetic inertial currents causing drag perturbations on a mooring which itself may be inclined in the mean flow.

Moorings 3 and 4 near the O_1 turning latitude showed high values of horizontal kinetic energy in the O_1 band, especially at the 700 m level where they were about three times more energetic than the average. These moorings also produced large vertical motions in the O_1 frequency band.

The K_1 band horizontal kinetic energy was roughly constant across the array at the 400 m level, while at 700 m depth Moorings 15 and 16 showed relatively high energies. These two moorings are widely separated in latitude, but both are near the rougher topography to the east of the array (Figure 2.2.2). The uneven distribution in time of the usable currents makes a comprehensive analysis difficult. In general the inertial-diurnal band currents appear highly non-stationary in time and space, characteristic of intermittent near-inertial frequency wave groups which are localized in space and have a small, though finite group speed. Such groups propagating through the array could cause moorings in the propagation path to show serious mooring motion effects, while nearby moorings remained quite quiet. Intuitively, localized groups would more likely result from a specified generation event, such as wind forcing or an unspecified low frequency catastrophe could provide, rather than from a general non-linear transfer of higher frequency energy to near inertial frequencies. This remains to be seen.

3.3 Muir Seamount experiment

Muir Seamount is a large topographic feature about 270 km northeast of Bermuda in the western North Atlantic (33°40'N, 62°30'W). It rises from the 4800 m depth of the surrounding abyssal plain to a summit relief of 3700 m, with roughly elliptical depth contours. At the 3000 m contour the major axis is about 60 km, oriented towards 330°T, with minor axis of about 10 km. The sides of the seamount slope more than 20° from the horizontal for much of the area above 3000 m depth, making it a very steep feature.

The inertial period at Muir Seamount is 21.65 hr, less than the diurnal tidal period. Internal waves with diurnal periodicity cannot exist as freely propagating modes at this latitude, but trapped modes are possible. It was of interest to examine the oceanic variability near Muir Seamount to test the hypothesis that diurnal period waves would be found trapped to the seamount, forced by the barotropic diurnal tide. An experiment designed by Prof. Carl Wunsch of M.I.T. was deployed by the Buoy Group of the Woods Hole Oceanographic Institution in May of 1972 to look at this problem. Evidence for trapped diurnal period internal tides was indeed found, and here we present some of the observations and a simple analytical model which provides an approach to the dynamics of such waves.

The experiment itself was only a preliminary look at the many interesting facets of oceanic variability near a large topographic feature, and a second experiment was carried out in early 1974 at Muir Seamount. The second experiment, from a preliminary look, tends to confirm the existence of trapped diurnal period oscillations, but will not be dealt with here. A fuller investigation of the new experiment and the other aspects of the interaction between the seamount and ocean flows will be carried out at a future time.

Observations

From the first experiment, measurements of horizontal current and temperature were obtained from a fixed mooring on the western flank of the seamount. Mooring depth was 2998 m, and Geodyne 850 model current meters modified to record temperature were placed at 2015 m and 2898 m depth, respectively 983 m and 100 m above the mooring anchor. The geometry of the mooring location, illustrated in Figure 3.3.1, places the lower instrument only a few hundred meters horizontally from the seamount's side. 150 days of measurement were recorded at the upper meter, number 4561 in the W.H.O.I. terminology, but the lower instrument number 4563 worked for only the first 70 days.

These records were Fourier transformed in 30-day non-overlapping pieces, and power estimates were computed by

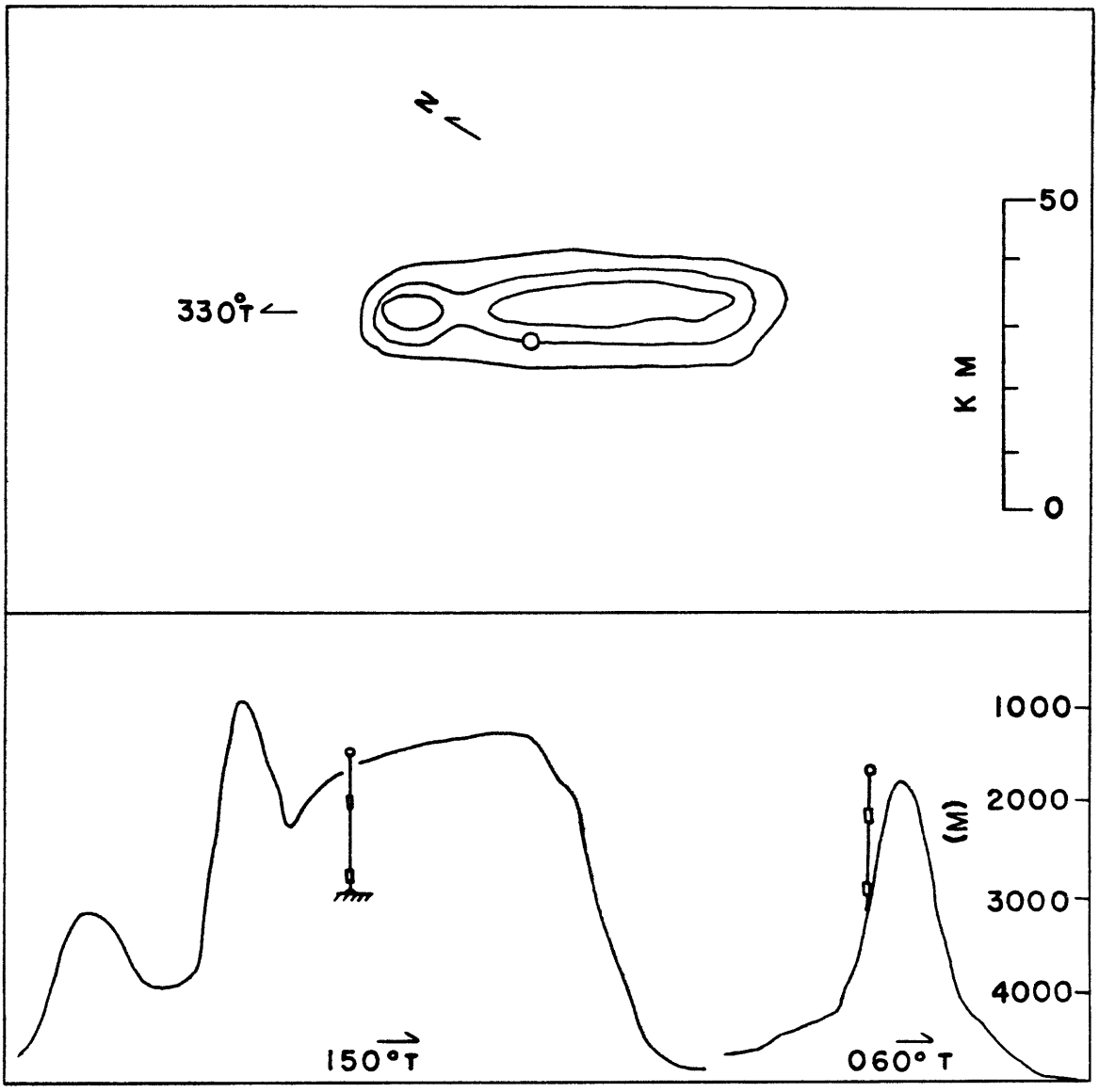


Figure 3.3.1 Muir Seamount mooring geometry. (upper) Horizontal plan view showing 2000, 3000 and 4000 m contours and the mooring site indicated as an open circle. (lower) Vertical sections through the seamount, showing the placement of the current meters.

averaging the pieces. The 30-day length gives estimates almost exactly at the most powerful diurnal lines in the astronomical tide, designated the O_1 and K_1 constituents, with one intermediate estimate. Figure 3.3.2 shows the diurnal region of an equilibrium tide power spectrum calculated for this length of record. The average squared amplitudes of the diurnal current and temperature fluctuations at the two depths are also given in Figure 3.3.2 as periodograms.

The horizontal kinetic energy in the band covered by the five Fourier coefficients presented increased by a factor of 3.1 from the upper to the near bottom measurements. From the periodograms in Figure 3.2.2, the O_1 estimate showed consistently more energy than the other near-diurnal frequencies, while the K_1 estimates are small both in current and temperature power at the upper meter. Near the bottom the K_1 power increases markedly. However there is not a large amount of statistical confidence in the differences as the 95% error bars in Figure 3.3.2 show. Averaged over the diurnal band, assuming the individual frequencies are independent, the energy levels at the two depths are significantly different. For the horizontal kinetic energy a one-sided Fisher F-test suggests that if the upper currents were as energetic as the lower currents, the ratio of lower to upper variance would be less than 1.84

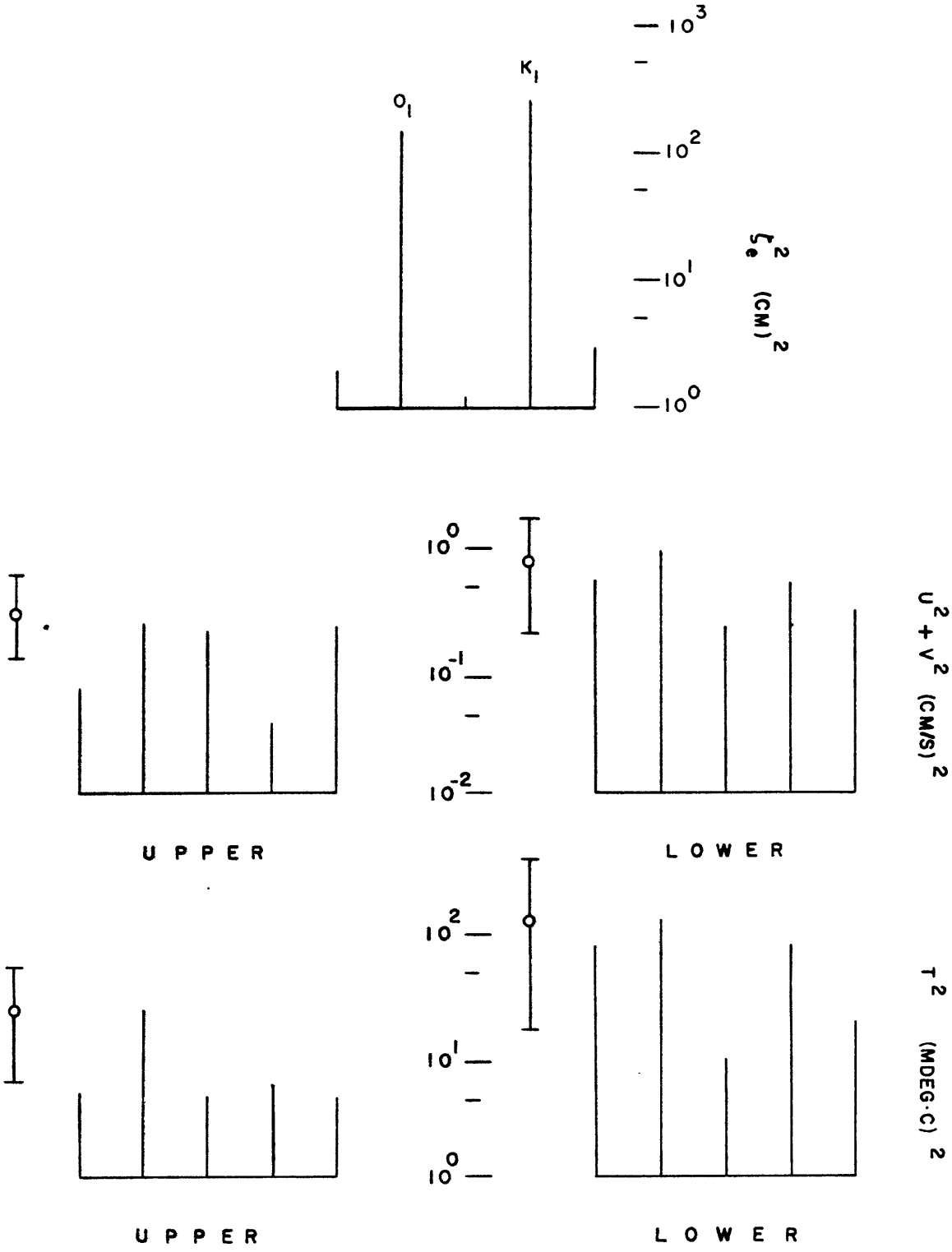


Figure 3.3.2 (upper) Diurnal band equilibrium tide, showing the dominant O_1 and K_1 constituents.
(middle) Horizontal current variance at upper and lower depth levels in the diurnal band.
(lower) Temperature variance at upper and lower depth levels in the diurnal band.

about 95% of the time.

The band averaged temperature variance is increased by a factor of 6.2 at the lower level. The associated average potential energy depends on the vertical temperature gradient, and a hydrographic station, Chain station 1296, was taken on the flank of the seamount near the mooring site. It showed a Brunt-Väisälä frequency of .64 cph at the 2050 m level, and an increased value of .92 cph at the 2564 m level, the lowest estimate. Since these depend only on the difference between two actual bottle values, they are certainly subject to error. However using these estimates, there is an increase of potential energy in the diurnal period fluctuations by a factor of 3.0 at the lower level, about the same as noted for the total horizontal kinetic energy.

Given these observations, we propose a model for the adjustment of the barotropic tide in the vicinity of a steep topographic feature like Muir Seamount, north of the critical latitude for diurnal period internal waves. For the barotropic forcing, measurements from MODE-1 discussed in Section 3.2 failed to resolve the diurnal barotropic tidal currents in the presence of energetic inertial-like motion, and put an upper bound on the barotropic current of about .2 cm/s for both major constituents. The MODE site is some 630 km to the south and 700 km to the west of

Muir Seamount, but given the long wavelength of the barotropic diurnal tide the barotropic fields at the two sites may not be greatly different. Figure 2 in Zetler, Munk, Mofjeld, Brown and Dorner (1974) shows the K_1 surface tide varying smoothly between the MODE site and Bermuda. The root mean square amplitude of current fluctuations in the overall diurnal band at meter 4561 is about .37 cm/s, including both the barotropic and baroclinic currents. The slight peak at the true O_1 frequency suggests that the barotropic tide is present, but in the sea surface signal the K_1 line in the MODE experiment was even slightly stronger than the O_1 line (ZMMBD, 1974). Baroclinic motions generated by the barotropic currents would have much shorter spatial scale and be subject to Doppler smearing effects of variable low frequency currents. We model an idealized situation with an imposed barotropic tide forcing the flow at a single frequency.

Time dependent flow adjustment

The equations presented in Section 1.2 are used here with no further comment, and all the notation remains the same. The equations for horizontal current, pressure, buoyancy and vertical velocity perturbations are

$$-i\sigma\underline{u} + f\hat{k}x\underline{u} = -1/\rho_o \nabla p \qquad (3.3.1)$$

$$0 = -1/\rho_o \partial p/\partial z + b \qquad (3.3.2)$$

$$-i\sigma b + N^2 w = 0 \qquad (3.3.3)$$

$$\nabla.\underline{u} + \partial w/\partial z = 0 \qquad (3.3.4)$$

Then horizontal and vertical velocities are

$$\underline{u} = 1/\rho_o (f^2-\sigma^2) \ (i\sigma\nabla p + f\hat{k}x\nabla p) \qquad (3.3.5)$$

$$w = 1/\rho_o N^2 \ (i\sigma \partial p/\partial z) \qquad (3.3.6)$$

The equation of continuity gives

$$\nabla^2 p + (f^2-\sigma^2)/N^2 \ \partial^2 p/\partial z^2 = 0 \qquad (3.3.7)$$

which for the case we consider here, $f^2>\sigma^2$, is an elliptical equation with no real characteristic curves in space.

As boundary conditions on Equation 3.3.7, we postulate that the flow is driven by a barotropic current which is supported by the sea surface slope of the diurnal tide. On

the scale of the adjustment problem, the horizontal gradients of barotropic current are neglected, and the forcing is taken as horizontally uniform. The vertical velocity in the barotropic wave is also neglected and we assume a rigid lid to filter it out. There can still be a horizontal pressure gradient at the top surface $z = 0$, driving the barotropic component of the flow.

The model geometry consists of an isolated seamount with depth contours $z = -h(x,y)$, with $h \to H$ as $r^2 = x^2 + y^2$ increases to infinity in the horizontal scale of the adjustment problem. The summit of the seamount is at $z = -z_T$ somewhere below the surface of the ocean. Since equation 3.3.7 is elliptical, disturbances in the far field barotropic flow will be trapped about the source region and will not propagate to infinity. Let $\underline{u} = \underline{U}$ be the barotropic flow, and the far field boundary condition on pressure is

$$\nabla p \to \rho_o (i\sigma \underline{U} - f\hat{k}x\underline{U}) \quad \text{as } r \to \infty \qquad (3.3.8)$$

The boundary conditions of no flow normal to the solid boundaries $z = 0$ and $z = -h$ are respectively

$$\partial p/\partial z = 0 \qquad \text{at } z = 0 \qquad (3.3.9)$$

$$[(f^2-\sigma^2)/N^2]\,\partial p/\partial z + (\nabla p.\nabla h + f/i\sigma\ \hat{k}.\nabla p x \nabla h) = 0$$

$$\text{at } z = -h \qquad (3.3.10)$$

The boundary conditions involve only the gradients of pressure, and there is an undetermined constant in the solution which can be taken as zero with no loss of generality.

We scale the problem represented by Equation 3.3.7 and the boundary conditions 3.3.8 - 3.3.10 by a length scale L representing the horizontal extent of the seamount and a vertical scale H, the ocean depth. The horizontal velocity scale is U, set by the boundary condition 3.3.8, and Equation 3.3.5 suggests a pressure scaling by

$$\rho_o L(f^2-\sigma^2)/f \qquad (3.3.11)$$

The term ∇h in the boundary condition is given its own scale s, the slope of the seamount from the horizontal. The scaling of w and b is left indeterminate for now.

In dimensionless variables, which we represent by the same symbols as the original dimensional variables as long as there is no danger of confusion, the equation and

boundary conditions for p become

$$\nabla^2 p + [(1-\sigma^2/f^2)/B^2]\partial^2 p/\partial z^2 = 0 \qquad (3.3.12)$$

$$\partial p/\partial z = 0 \qquad z = 0 \qquad (3.3.13)$$

$$[(1-\sigma^2/f^2)/B^2]\ (H/sL)\partial p/\partial z + (\nabla p.\nabla h + f/i\sigma\ \hat{k}.\nabla p x \nabla h) = 0 \quad \text{on } z = -h \qquad (3.3.14)$$

$$p \to [f/(f^2-\sigma^2)]\ (i\sigma\hat{\imath}-f\hat{\jmath}) \text{ as } r \to \infty \qquad (3.3.15)$$

We have introduced the Burger number

$$B = NH/fL$$

which is a scaled aspect ratio, and for definiteness have taken $\underline{U}$ to be a unidirectional flow parallel to the x axis. $\hat{\imath}$ and $\hat{\jmath}$ are unit vectors in the direction of increasing x and y respectively. The problem is easily generalized to a barotropic current ellipse with any polarization. Taking as a scale length L the geometric mean of the major and minor axes at the 3000 m level for Muir Seamount gives L = 25 km, and H = 5 km. For $N = .3 \times 10^{-2}$ s^{-1} and

$f = .81 \times 10^{-4}\ s^{-1}$, B^2 is about 55. Large B indicates that the seamount acts as a steep obstacle, and that the flow will tend to be around the sides of the seamount rather than across the depth contours. The slope of the seamount s is of order .4. Using these parameters gives a set of scaled equations.

$$\nabla^2 p + (.005)\,\partial^2 p/\partial z^2 = 0$$

$$\partial p/\partial z = 0 \qquad \text{on } z = 0$$

$$(.003)\,\partial p/\partial z + (\nabla p.\nabla h + f/i\sigma\ \hat{k}.\nabla p x \nabla h) = 0 \text{ on } z = -h$$

$$p \to [f/(f^2-\sigma^2)]\ (i\sigma\hat{\imath} - f\hat{\jmath}) \text{ as } r \to \infty$$

Considering a limit $(1-f^2/\sigma^2)/B^2 \to 0$, the zero-order equations in a perturbation expansion give

$$\nabla^2 p = 0 \tag{3.3.16}$$

$$\nabla p.\nabla h + f/i\sigma\ \hat{k}.\nabla p x \nabla h = 0 \quad \text{on } z = -h \tag{3.3.17}$$

$$\nabla p \to [f/(f^2-\sigma^2)]\ (i\sigma\hat{\imath} - f\hat{\jmath}) \quad \text{as} \quad r \to \infty \tag{3.3.18}$$

valid in an interval of z where the slope of the seamount is large enough so that the approximation in the boundary condition 3.3.17 remains valid. For example, as $z \to -z_T$ or $z \to -H$ the slope of the seamount may vanish and the effect of flow over the topography become comparable to the flow around the seamount. Since the governing equation 3.3.12 is elliptical, the solution is governed mainly by the local boundary conditions, and the approach should be valid for the steeper slopes on the seamount.

In the expressions 3.3.16 - 3.3.18, z appears explicitly only in the boundary condition 3.3.17. The equation

$$z + h(x,y) = 0$$

defines one or more closed curves in the plane z = constant which are simply the depth contours of the seamount. For definiteness, consider a seamount with radial symmetry about r = 0 and invert the equation $z = -h(r)$ to $r = F(z)$, a circle whose radius decreases smoothly as z increases. Again this approximation is not critical for the approach.

The resulting problem contains z only parametrically, and in each plane z = constant in the region under consideration, we have a problem of the form

$$\partial^2 p/\partial r^2 + (1/r)\ \partial p/\partial r + (1/r^2)p = 0 \qquad (3.3.19)$$

$$\partial p/\partial r - [f/i\sigma]\partial p/r\partial\theta = 0 \quad \text{on } r = F(z) \qquad (3.3.20)$$

$$\nabla p \to [f/(f^2-\sigma^2)][i\sigma(\hat{r}\cos\theta-\hat{\theta}\sin\theta) - f(\hat{r}\sin\theta + \hat{\theta}\cos\theta)] \text{ as } r\to\infty \qquad (3.3.21)$$

where $x = r\cos\theta$, $y = r\sin\theta$, and $\hat{r}$ and θ are unit vectors for the polar representation. This will be recognized as a potential flow problem, with the boundary condition 3.3.21 suggesting a solution form

$$p = A(r,z)\cos\theta + B(r,z)\sin\theta \qquad (3.3.22)$$

For both A and B this gives equations of the form

$$\partial^2 A/\partial r^2 + 1/r\ \partial A/\partial r + A/r^2 = 0 \qquad (3.3.23)$$

which have solutions

$$A(r,z) = a(z)r \quad \text{and} \quad A(r,z) = a(z)/r \qquad (3.3.24)$$

Matching the boundary conditions at $r = F(z)$ and $r\to\infty$ to

linear combinations of solutions 3.3.24 gives the final solution

$$p = [f/(f^2-\sigma^2)][i\sigma r\cos\theta\ (1 + F^2(z)/r^2) - \\ - fr\sin\theta\ (1 - F^2(z)/r^2)] \qquad (3.3.25)$$

and, much more simply in terms of the horizontal flow,

$$\underline{u} = \hat{\imath} - [F^2(z)/r^2]\ (\cos\theta\hat{r} + \sin\theta\hat{\theta}) \qquad (3.3.26)$$

which is just potential flow about the circle $r = F(z)$ matching up with the uniform flow in the x direction at infinity.

Density field

So far there has been no discussion of the density field, as the approximate equations have decoupled the horizontal velocities in adjacent layers. The solution 3.3.25 describes lamina of fluid which each have their own adjustment scale close to the seamount and slip over one another freely. The hydrostatic balance requires density perturbations to balance any vertical pressure gradients, and such gradients will be introduced in the flow field

near the seamount parametrically by the vertical shear resulting from the change of radius of the seamount with depth. At this point it is convenient to return to the dimensional equations, and from 3.3.25 and the hydrostatic equation 3.3.2,

$$b = U(i\sigma \cos\theta + f\sin\theta) \quad [dF^2(z)/dz]/r$$

$$= (2fU/s) \quad [(i\sigma/f) \cos\theta + \sin\theta] \; F(z)/r \quad (3.3.27)$$

where we have used $dF/dz = 1/s$. The scale of the buoyancy fluctuation is then

$$2fU/s$$

or for the density fluctuations

$$\rho_o(2fU/gs) \quad (3.3.28)$$

An effective coefficient of thermal expansion

$$\alpha = -1/\rho_o \; (d\rho/dT)$$

is defined empirically by the temperature, salinity and pressure at a given depth and the assumption of a functional

temperature-salinity relationship. Then a scale of temperature fluctuations is

$$2fU/gs\alpha \qquad (3.3.29)$$

For the upper level near 2000 m, s = .4 and an estimate of $\alpha = 1.0 \times 10^{-4} °C^{-1}$ based on the local hydrography gives a temperature fluctuation of 4.0 mdeg.C for a 1 cm/s speed. Similarly at the lower level near 3000 m, s = .3 and $\alpha = 6.2 \times 10^{-5} °C^{-1}$ give a temperature scale of 8.6 mdeg.C/(cm/s). The observations showed ratios of temperature variance to horizontal current variance in the diurnal band of 7.4 mdeg.C/$(cm/s)^2$ at the upper level and 120 mdeg.C/$(cm/s)^2$ at the lower level, compared to the squares of the scale ratios of 16. and 74. respectively.

The geometrical factor F(z)/r in 3.3.26 gives both a horizontal trapping proportional to 1/r, and at a fixed r, a trapping in the vertical since the radius of the seamount decreases with increasing z. The approximate solution of the diurnal period adjustment problem separates the horizontal and vertical trapping, while a full solution of the elliptical boundary value problem 3.3.12 with the associated boundary conditions would have a more closely coupled trapping scale for vertical and horizontal distance

from the obstacle. In general the relative scales in the vertical and horizontal would be related by B^{-1}, with the global adjustment depending on the actual geometry of the seamount.

A detailed comparison with the observations would require at least using elliptical geometry, and a knowledge of the actual form of the forcing $\underline{U}$. Even in the case of circular symmetry and linearly polarized far field current, the horizontal kinetic energy proportional to

$$\underline{u}.\underline{u} = 1 - 2F^2(z)\cos 2\theta/r^2 + F^4(z)/r^4$$

and vertical potential energy proportional to

$$b^2/N^2 = (2fU/sN)^2(\sigma^2\cos^2\theta/f^2 + \sin^2\theta)F^2(z)/r^2$$

vary with angle θ and the orientation of the far field flow must be specified before even the ratio of the two quantities at a point can be specified. With the values of s and α used, the intensification of the temperature fluctuations at the 3000 m level over the 2000 m level can be accounted for by the combination of shallower slope and smaller thermal coefficient of thermal expansion, without recourse to the geometrical factor F(z)/r. But the kinetic energy

intensification at the lower level depends entirely on this geometrical factor, and the plan form of the horizontal flow streamlines as given by the angular dependence in 3.3.25. Since the upper measurement point was located some 3 km from the side of the seamount at the 2000 m level where the geometric mean radius of the feature is about 8.5 km, a significant decrease from the geometrical 1/r factor is possible. The lower measurement point is located essentially at r = F(z), only 300 m from the side of the seamount at about 3000 m depth, where the geometric mean radius is about 14 km. Thus if both levels are forced by the barotropic tide with constant amplitude with depth, the horizontal current will be intensified at the lower level over the upper level away from actual stagnation points for the flow.

Since the diurnal barotropic tidal currents are not known, there can be no detailed comparison of the observations and the model. However the mechanism described here gives, in general terms, an explanation of the intensified diurnal period fluctuations observed at the near bottom levels on the side of Muir Seamount. The model resembles that of Hogg (1971) for the steady flow of a current past an island with sloping sides. The increase in radius of the obstacle with depth results in vertical shear in the

horizontal currents near the obstacle, as different levels of the flow adjust to the local radius. The dynamics of the diurnal period adjustment and the steady flow problem are completely different, however, with the steady flow being geostrophic and horizontally non-divergent to order of the Rossby number U/fL, and depending on higher order constraints to close the problem. The time dependent problem is linear to a very good approximation as far as the dynamics are concerned, with Rossby number about $.5 \times 10^{-3}$. The boundary conditions in the finite, three-dimensional seamount problem are non-separable in general, making a complete solution difficult.

The parametric depth dependence in the approximate solution gives a passive flow adjustment. In a right cylinder geometry the adjustment can be expanded in a sum of trapped modes which can propagate azimuthally about the obstacle. Then the possibility of resonances in a forced problem are explicitly realized, in a baroclinic version of a problem considered by Longuett-Higgins (1969) for trapped waves about a circular island. Wunsch (1972b) used a baroclinic island trapped normal mode approach to explain sub-inertial peaks in the temperature spectrum at Bermuda. In a three-dimensional seamount geometry resonances may also be possible, but the calculations are more involved. Experimental work might be done to investigate such sub-inertial trapped modes.

Since Muir Seamount is a truly three-dimensional feature, modelling it by a right cylinder is not appealing, and the approach here does reveal at least part of the dynamics of the actual flow.

3.4 Diurnal tides at Site D

At latitude 39°10'N, Site D has an inertial period of 19.0 hours, and so it is far north of the critical latitude for diurnal period internal waves. The site is about 60 km south of the steep New England continental slope, which may constrain the north-south scale of the motions there. Waves which propagate along the depth contours and are trapped to the slope are possible for both barotropic and baroclinic dynamics. Munk, Snodgrass, and Wimbush (1970) have discussed the full set of barotropic trapped waves in certain simple geometries, and in their study and probably in general trapped waves at periods greater than inertial period propagate with the shallow water to the right in the direction of propagation for a northern hemisphere ocean. A pure barotropic or baroclinic Kelvin wave is a special example of this type of trapped motion.

For $\sigma < f$, a separation of variables gives the same vertical structure equation (1.2.17) as for internal gravity waves, while the horizontal variation is governed by an equation of the form

$$\nabla^2 w - k^2 w = 0 \qquad (3.4.1)$$

For the barotropic mode, to a good approximation

$$k^2 = (f^2 - \sigma^2)/gH \qquad (3.4.2)$$

independent of the stratification, while for the baroclinic modes k is determined by a vertical eigenvalue problem. Table 3.4.1 gives k and k^{-1} for the O_1 diurnal barotropic and first five baroclinic modes at Site D, for the average density profile over all seasons from 1965-1972. k^{-1} is a trapping scale because a simple solution of 3.4.1 is

$$w = \exp(-kx)$$

if there are no boundary conditions to consider. The barotropic trapping scale is comparable to the scale of the ocean basins, while the baroclinic trapping scales are shorter and decrease with higher mode number. We examined the current records from Site D for diurnal period energy.

Observations

Figure 3.4.1 shows vertical profiles of squared amplitude of O_1 and K_1 band current fluctuations at Site D, averaged over all measurements at the depth levels defined in Section 1.3. The same 15 day record length was used for the diurnal analysis, and records from both north and south sites

Mode number	k (km^{-1})	k^{-1} (km)
0	$.39 \times 10^{-3}$	2600
1	$.41 \times 10^{-2}$	250
2	$.79 \times 10^{-2}$	130
3	$.11 \times 10^{-1}$	94
4	$.14 \times 10^{-1}$	70
5	$.18 \times 10^{-1}$	57

Table 3.4.1

Eigenvalue k and trapping scale k^{-1} for the barotropic mode and the first five baroclinic modes at Site D for 24 hour period, using the 1965-1972 average density at the Site.

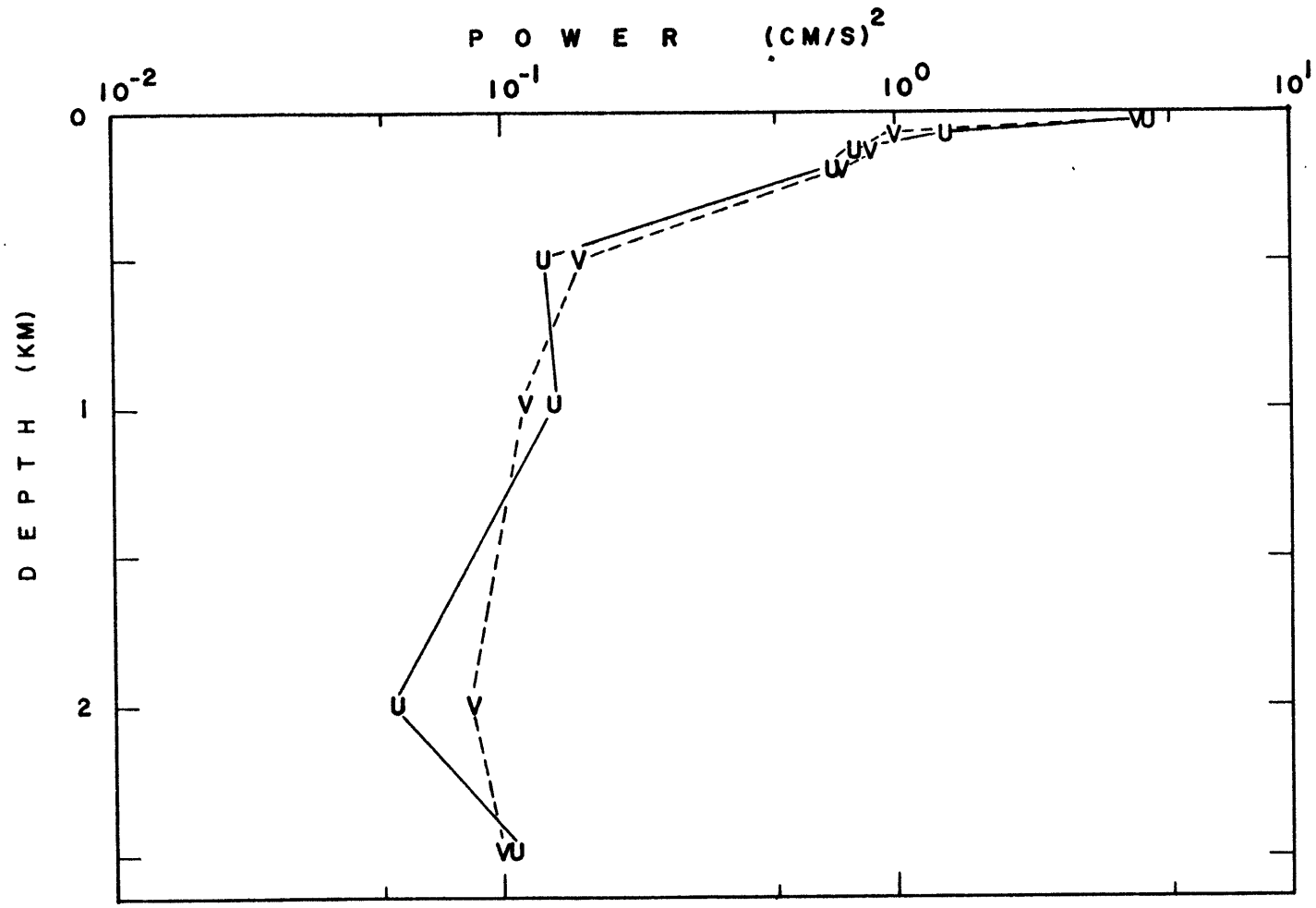


Figure 3.4.1a Squared amplitude of u (east) and v (north) current components as a function of depth for the O_1 band at Site D, averaged over all measurements.

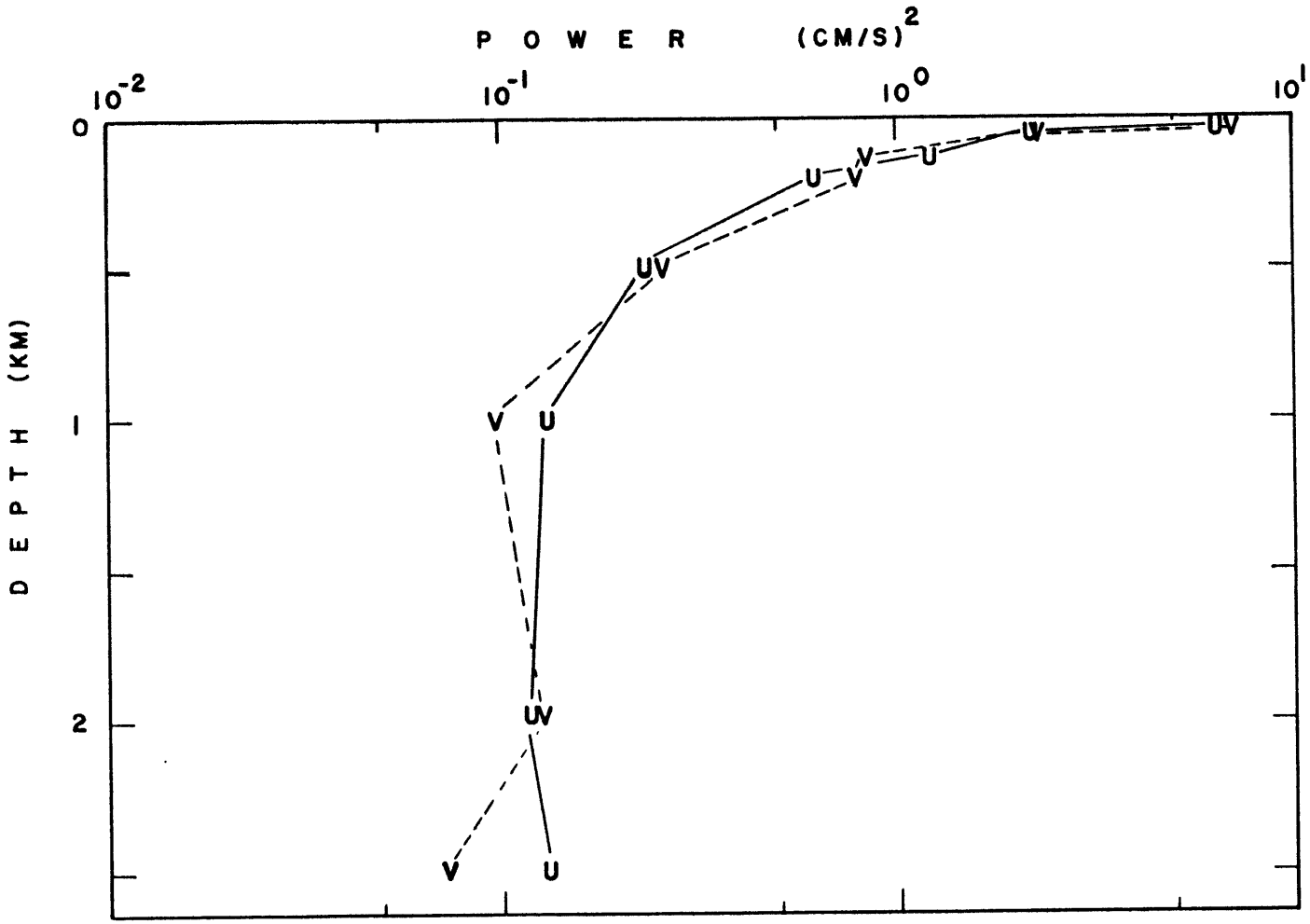


Figure 3.4.1b Squared amplitude of u (east) and v (north) current components as a function of depth for the K_1 band at Site D, averaged ovel all measurements.

are included. The nominal 16 km separation of the two ensembles is small compared to the trapping scales for the low mode baroclinic waves, and an examination of the separate north and south ensembles failed to reveal any systematic differences in energy for the diurnal fluctuations. The average over the whole site can be used to discuss the local behavior of the diurnal motions.

Both the O_1 and K_1 tidal band currents vary with depth, and the currents in the uppermost 50 m are especially intensified. This surface intensification was also noted for the semidiurnal band currents at Site D, and the possibility exists that some of the energy is a result of mooring motion contaminating the current measurements. For the semidiurnal band there were reasons to believe that the surface intensification was real, and a result of the properties of semidiurnal internal wave propagation. These considerations do not apply for the diurnal frequencies, but wind forcing could contribute to the diurnal frequency surface intensification and will be discussed in more detail. At 1000 m and deeper the diurnal energy is nearly constant, and about 50 times less than the near surface values. The u and v components contribute nearly equal amounts to the current variance. Table 3.4.2 gives the numerical values for u and v power, and also the rotary decomposition of the current

O_1 band:

Depth (m)	u $(cm/s)^2$	v $(cm/s)^2$	+ $(cm/s)^2$	- $(cm/s)^2$	-/+	No.of pieces
25	5.3	5.0	.90	4.3	4.8	41
75	1.6	1.2	.91	1.1	1.4	48
125	.99	1.0	.38	.64	1.7	27
200	.85	.90	.29	.58	2.0	24
500	.16	.19	.046	.13	2.8	12
1000	.16	.14	.042	.11	2.6	30
2000	.066	.10	.021	.064	3.1	15
2500	.13	.12	.030	.097	3.2	35

K_1 band:

Depth (m)	u $(cm/s)^2$	v $(cm/s)^2$	+ $(cm/s)^2$	- $(cm/s)^2$	-/+	No.of pieces
25	8.0	8.9	.92	7.5	8.2	41
75	3.0	2.8	.42	2.5	5.9	48
125	1.2	1.0	.36	.96	2.7	27
200	.77	.98	.15	.73	5.0	24
500	.30	.32	.063	.24	3.9	12
1000	.20	.12	.043	.12	2.7	30
2000	.15	.16	.043	.11	2.6	15
2500	.16	.10	.035	.098	2.8	35

Table 3.4.2

Average squared amplitude of u (east), v (north), + (anti-clockwise), and - (clockwise) current components at Site D for the O_1 (upper) and K_1 (lower) bands.

power in the two bands. The K_1 surface currents tend to be more energetic than the O_1 surface currents, while at depth the power in the two bands is more equal. The average currents are polarized in the clockwise sense which is usual in the northern hemisphere, but the partition is far less than the ratio of $(\sigma+f)^2/(\sigma-f)^2$ of about 70 which would apply to freely propagating internal waves with the same frequency difference from the inertial frequency as exists between the diurnal and inertial frequencies. Since the north or nearly upslope current has almost the same energy as the east or alongslope current, the reduction in circular polarization is evidently not due to the constraints of the varying topography, but is more a function of the dynamical difference between sub-inertial motions and internal gravity waves.

The diurnal frequency contribution to current variance is considerably less than that of the inertial frequency (see Figure 5 in Thompson, 1971 for example), and motion near 24 hour periods might be forced by non-linear interaction with the inertial period motions. The known resonances between triads of internal gravity waves (Martin, Simmons and Wunsch, 1972) are not possible since the diurnal fluctuations do not propagate in space, but the vertical structure of motion at the two frequencies is governed by

the same equations and such non-linear forcing seems possible. Another non-tidal source of current energy lies in meteorological forcing, which we consider briefly.

Meteorological effects

A 120 day wind record from a moored surface buoy at Site D was analyzed to examine meteorological influences on the currents at the Site. The record was number 4291 in the W.H.O.I. terminology, taken in spring and summer conditions. Components of the wind-stress-related vector

$$(u^2 + v^2)^{1/2}\underline{u} \qquad (3.4.1)$$

where u and v are the horizontal components of the surface wind were harmonically analyzed, giving a total diurnal power density of $.31 \times 10^{13}$ $(cm/s)^4$/cph with about 80 degrees of freedom over a relatively broad 1/6 cpd band near 24 hours. The power in a 1/15 cpd diurnal band, to compare with the current measurements, is then estimated to be $.86 \times 10^{10}$ $(cm/s)^4$, for a root mean square contribution of $.93 \times 10^5$ $(cm/s)^2$. The surface stress τ and wind stress U are related observationally by

$$\tau = \rho_a C_d U^2 \qquad (3.4.4)$$

where $\rho_a = 1.225 \times 10^{-3}$ gm/cm^3 is the density of air at 15°C and $C_d = 1.0 \times 10^{-3}$ (Deacon and Webb, 1962). The empirical drag law 3.4.4 is valid for steady flow and its use for time dependent motion is unsure, but for a diagnostic calculation we proceed. Using the 1/15 cpd band root mean square of expression 3.4.3 for U^2 gives a wind stress fluctuation with amplitude .16 dyne/cm^2. The simplest models of the response of the ocean to a surface wind stress distribute the stress uniformly as a body force through a surface mixed layer of depth h. In a time dependent forcing with $\sigma < f$, the amplitude of the expected response in the currents is of the order

$$(f\tau/h)/(f^2-\sigma^2) \qquad (3.4.5)$$

For the diurnal period at Site D and the calculated stress, this gives a current amplitude of $.47 \times 10^4/h$ (cm/s)/cm, or 5 cm/s for h = 10 m, and 1 cm/s for h = 50 m. Even a 3 cm/s current in the upper 25 m would explain most of the K_1 band current energy, and the relatively large surface currents which are observed are at least partly a result of wind forcing. The K_1 band is centered about 24 solar hours, and the larger near surface energy in the K_1 band may be related to a slight increase in wind forcing at true

24 hour periodicity, due to the solar heating cycle and associated meteorological variability.

Tidal energy in the diurnal band

We are primarily interested in the currents associated with the astronomical tides. In MODE-1, there was little evidence that the astronomical forcing had anything to do with the diurnal-inertial currents, but at Site D the diurnal and inertial frequencies are well separated and we may expect to see some indication of the true tides. We computed coherences between the current and equilibrium tide exactly as described in Section 1.4, obtaining amplitudes and admittance phases at each standard level. Table 3.4.3 gives the result. In the O_1 band, only one of the depth levels gives a significant coherence at the 95% confidence level for the u component, while four of the eight levels show significant coherence between the v component and the equilibrium tide. For the K_1 band, two levels for u and four for v also show coherence values greater than the null-coherence 95% confidence limit. Thus there does appear to be some true tidal energy in the current fields. The coherence levels are generally low, reflecting a noisy physical situation, and all the features of the tidal signal may not be approachable with the limited sampling

Depth (m)	Coherence amplitude O_1 band u		O_1 band v		K_1 band u		K_1 band v		95% level
25	.04	-151	.14	-009	.12	-171	.22	-048	.27
75	.33	026	.27	025	.22	179	.32	-080	.24
125	.11	107	.16	148	.10	178	.32	-019	.32
200	.34	118	.29	025	.20	059	.23	018	.38
500	.19	-068	.39	047	.49	-005	.60	046	.44
1000	.27	095	.51	030	.36	132	.40	-041	.32
2000	.13	132	.47	-020	.40	082	.33	022	.44
2500	.25	116	.39	-013	.38	077	.15	-044	.29

Table 3.4.3

Coherence amplitude and phase for the diurnal band currents and the equilibrium tide. The averages are by depth level over the whole Site. 95% confidence limits for zero true coherence are given for each case.

we have here. Note that the admittance phases show some stability in the vertical, with the u phases in the deeper water being similar for both hands, and the v phases showing a general similarity throughout the water column. A constant phase in the vertical would be characteristic of a barotropic current. It is also notable that in every case at and below 1000 m, the u component leads the v component, characteristic of a current ellipse with anticlockwise polarization. The phases in Table 3.4.3 are - kappa, and so represent phase leads of the current with respect to the equilibrium tide. Although at every depth the overall power was predominantly in clockwise rotating currents (Table 3.4.2), it seems that the part of the current field associated with the tide might be rotating in the opposite sense.

On the above assumption, we created sub-ensembles of currents at each level by including only those 15 day piece lengths in which the diurnal period current ellipse had an anticlockwise rotations sense. This was done separately for the O_1 and K_1 bands. Although each such sub-ensemble will have fewer degrees of freedom, the signal to noise ratio will be larger if the tidal process is actually in the anticlockwise current. Table 3.4.4 gives the resulting estimates of coherence amplitude and phase, as well as the number of records actually involved and the appropriate

O_1 band: Depth (m)	u	v	No.of pieces	95% level
25	.76 040	.71 -082	7	.63
75	.58 023	.23 -019	12	.49
125	.22 170	.34 -135	10	.53
200	.40 101	.54 032	7	.63
500	- -166	- 158	1	-
1000	.65 087	.88 007	9	.56
2000	.94 064	.85 001	4	.80
2500	.67 132	.59 -014	12	.49

K_1 band: Depth (m)	u	v	No.of pieces	95% level
25	.33 -013	.37 108	5	.73
75	.39 051	.07 110	11	.51
125	.62 082	.37 -019	8	.59
200	.68 039	.54 011	5	.73
500	.80 088	.86 048	2	.98
1000	.46 152	.65 -008	8	.59
2000	.47 093	.52 000	6	.67
2500	.57 057	.46 -022	11	.51

Table 3.4.4

Coherence amplitude and phase for the O_1 (upper) and K_1 (lower) band currents and the equilibrium tide. These averages were over only those cases where the diurnal current ellipse in a 15 day record showed an anticlockwise rotation. 95% confidence limits for zero true coherence are given for each case.

confidence limits. In these ensembles, the O_1 band shows more coherence, with five out of eight of the u component ensembles and four of eight levels for the v component showing significant coherences. The surface u phases for the O_1 band have changed to nearer the deep values, and now have some statistical significance. In the K_1 band there are fewer cases of significant coherences for the fewer degrees of freedom in the sub-samples currents, but the phases are roughly constant in the vertical with the exception of the very near surface levels.

Table 3.4.5 gives the energy associated with the u and v components in the sub-ensembles of anticlockwise rotating currents. The energy still varies with depth but the very large currents in the uppermost layer in the overall averages (Table 3.4.2) are relatively reduced. The deeper levels owe the coherences to currents of the order of .2 cm/s. The near surface estimates of coherent current, on the other hand, obtained by multiplying the coherences in Table 3.4.4 by the square root of the total variance as given in Table 3.4.5, are a large fraction of a centimeter per second. If we believe these results, based on a very finite number of degrees of freedom, we must conclude that there is a phase locked baroclinic portion of the O_1 tide, in particular, at Site D. An attempt at a modal decomposition of the

Depth	O_1 band		K_1 band	
(m)	u $(cm/s)^2$	v $(cm/s)^2$	u $(cm/s)^2$	v $(cm/s)^2$
25	2.0	1.6	1.2	1.1
75	1.6	1.1	1.5	.62
125	.86	1.1	.62	.65
200	.37	1.2	.40	.26
500	.51	.095	.33	.086
1000	.050	.048	.13	.078
2000	.033	.057	.12	.070
2500	.068	.058	.082	.062

Table 3.4.5

Squared amplitude of u (east) and v (north) current components in the diurnal bands as a function of depth. These averages were made over only the anticlockwise rotating current ellipses.

estimates of coherent current gave no interpretable results in terms of baroclinic modes, where the decomposition was done with a barotropic and the three lowest baroclinic modes as in Chapter 2 for the semidiurnal tide. The near surface u admittance phases for the O_1 currents are, however, slightly but significantly different from the average of, say, the u phases below 1000 m. We might expect that a coupled barotropic-baroclinic mode would exist in the sloping geometry, and from the current records we conclude that there is some indication of the true tidal period energy in the baroclinic fields. The low coherences indicate that most of the current energy is not simply related to the tidal forcing, and the noise levels obscure the actual tidal signal. The next section considers a specific model for the diurnal barotropic tide in the slope region, and even with the noise levels present some of the critical features of the model can be verified.

Barotropic diurnal tide at Site D

We noted that the phases of the currents in Table 3.4.4 were stable with depth, as characteristic of a barotropic wave. A depth average of the phases at the different levels (Coherence I., Appendix A.2) for the anticlockwise rotating currents gives stable estimates of the diurnal barotropic

current phases, with suggested error bars of $\pm$ 20° for 95% confidence. These phases are given in Table 3.4.6, converted to Greenwich epoch G. It is more difficult to obtain stable estimates of the actual amplitude of the diurnal currents, and after trying various schemes the best that we cna do is to estimate the u component of both constituents at about .2 cm/s and the v components at somewhat less, say .1 cm/s, as strictly order of magnitude figures. There is unequivocal evidence in the distribution of phases for currents of this order. Table 3.4.6 also presents estimates of the O_1 and K_1 surface tides based on a 30-day series of bottom pressure measurements from a Wunsch-Dahlen temperature-pressure recorder deployed in a tide gauge mode in about 112 m depth on the New England continental shelf at 40°32.5'N, 70°55.4'W (unpublished data). For comparison the tidal constituents from Bermuda are included (ZMMBD, 1974). Although the surface tide is relatively constant over the whole western North Atlantic between Cape Cod and Bermuda, there are local changes near the coast and the shelf measurements seem the optimal ones to use for Site D even though they are in shallower water.

To compare with the deep water currents, Table 3.4.6 also presents O_1 and K_1 barotropic current estimates for the New England shelf, from a single current record 18 m

Current:	Constituent	u (cm/s)	G_u	v (cm/s)	G_v
Site D:	O_1	(.2)	348	(.1)	095
	K_1	(.2)	353	(.1)	085
Shelf:	O_1	4.4	166	3.6	076
	K_1	2.9	171	1.2	081

Sea level:	Constituent	Amplitude (cm)	Phase (^oG)
Bermuda:	O_1	5.3	192
	K_1	6.6	187
Shelf:	O_1	5.6	197
	K_1	4.6	163

Table 3.4.6

Barotropic diurnal tides in the Site D - New England shelf setting. (upper) Current amplitude and phase for the O_1 and K_1 constituents at Site D and on the shelf. (lower) Surface tide O_1 and K_1 constituents at Bermuda and on the New England shelf.

from the bottom in 60 m depth at 40°45'N, 71°03'W (Beardsley and Butman, 1974). The measurements were taken in winter conditions when no vertical stratification exists, and a 15 day series was made available for the current analysis. On the basis of the Site D and shelf measurements, we can postulate and verify a model for the local diurnal period tidal wave.

Step shelf Kelvin-Stokes normal mode

The work of Munk, Snodgrass and Wimbush (1970) (hereafter MSW) provides a comprehensive summary of trapped barotropic modes in a step shelf and exponential slope model ocean. Using the step shelf as appropriate for the Site D and New England shelf case, and following MSW, we consider an ocean of depth D* on an f-plane with an adjoining shelf of constant depth D'*. The shelf break lies at y*=0, and the shore at y*=L*. The depths and surface elevation η^* are made dimensionless by scaling with the deep ocean depth D*, and distances and wavelengths are scaled by the barotropic radius of deformation

$$\lambda = (gD^*/f^2)^{1/2}$$

Speeds are scaled by the long wave phase speed

$$C = (gD^*)^{1/2}$$

and time is scaled by the inverse of the Coriolis parameter f. For the Site D setting, $D^* = 2600$ m, $D'^* = 130$ m and $f = .92 \times 10^{-4}$ s^{-1} give $\lambda = 1740$ km, $C = 160$ m/s. A shelf width $L^* = 200$ km and the O_1 tidal frequency give the resulting non-dimensional parameters

shelf depth $D' = .0500$

shelf width $L = .115$

frequency $\sigma = .736$

Assuming a solution of equation 3.4.1 for vertical displacement η of the form

$$\eta = \eta(y) \exp i\,(\beta x - \sigma t) \qquad (3.4.6)$$

the alongshore velocity component u and onshore component v are given by

$$\begin{Bmatrix} u \\ iv \end{Bmatrix} = \frac{1}{\sigma^2 - 1} \begin{Bmatrix} \beta\sigma + \partial/\partial y \\ \beta - \sigma\,\partial/\partial y \end{Bmatrix} \eta(y) \exp i\,(\beta x - \sigma t) \qquad (3.4.7)$$

corresponding to equations (7) and (8) in MSW.

From 3.4.1 and 3.4.2, equations for $\eta(y)$ have exponential solutions for deep ocean (unprimed) and shelf (primed) variables

$$\eta(y) = a \exp(py) \qquad y<0 \qquad (3.4.8)$$

$$\eta'(y) = (a-B')/2 \exp(-p'y) + (a+B')/2 \exp(p'y) \qquad 0<y<L \qquad (3.4.9)$$

where $$p^2 = \beta^2 - \sigma^2 + 1 \qquad (3.4.10)$$

$$D'p'^2 = D'\beta^2 - \sigma^2 + 1 \qquad (3.4.11)$$

For $\sigma<1$, p and p' are both real, the y variation of the surface displacement being exponential in nature both on and off the shelf, and the solution 3.4.8 excluding the exponentially growing wave in the deep ocean. The boundary conditions on the wave motion are

$$v = 0 \quad \text{at } y = L \qquad (3.4.12)$$

$$D'v^{y=0^+} = Dv^{y=0^-} \qquad (3.4.13)$$

$$\eta'^{y=0^+} = \eta^{y=0^-} \qquad (3.4.14)$$

requiring the vanishing of the onshore flow at the coast, and the continuity of onshore transport and surface displacement at the shelf break. In terms of η, 3.4.12 and 3.4.13 become

$$(\beta + \sigma\partial/\partial y)\eta' = 0 \quad \text{at } y = L$$

$$D'(\beta + \sigma\partial/\partial y)\eta' = D(\beta + \sigma\partial/\partial y)\eta \quad \text{at } y = 0$$

The boundary conditions 3.4.12 - 3.4.14 relate a and B' in 3.4.8 - 3.4.9 as

$$B'/a = -[\beta + p'\sigma\tanh(p'L)]/[\sigma p' + \beta\tanh(p'L)] \qquad (3.4.15)$$

and there is a dispersion relation between σ, p and β as a solubility condition. In terms of the ellipticity of the horizontal currents

$$\varepsilon = -iv/u \equiv \sin\mu \qquad (3.4.16)$$

and impedence of the sea surface amplitude with respect to the longshore current

$$\P = \eta/u \equiv - \cos\mu \qquad (3.4.17)$$

defined by MSW, they show that

$$\beta = -\sigma\sec\mu - \tan\mu \qquad (3.4.18)$$

$$p = \sigma\tan\mu + \sec\mu \qquad (3.4.19)$$

and finally as the dispersion relation

$$L \tanh(p'L)/p'L = \sigma\tan\mu/(\sigma^2 - D'\beta^2 - \beta\tan\mu) \qquad (3.4.20)$$

A free solution of the equations of motion of the form 3.4.8 - 3.4.9 exists with very small ellipticity ε, in which the currents are nearly linearly polarized along the depth contours. To first order in ε and L, MSW show that this mode satisfies

$$\beta = -\sigma - \mu \qquad (3.4.21)$$

$$p = 1 + \sigma\mu \qquad (3.4.22)$$

and so $$\mu = \sigma(1-D')L \qquad (3.4.23)$$

Then from 3.4.21 - 3.4.22,

$$\beta = -\sigma[1 + (1-D')L] \qquad (3.4.24)$$

$$p = 1 + \sigma^2(1-D')L \qquad (3.4.25)$$

Using the parameters quoted gives $\beta = -.816$, $p = 1.06$, $p' = 3.14$ and $\mu = .0802$.

This wave has a dimensional trapping scale of 1680 km in the deep water, and 490 km on the shelf, and a longshore wavelength of about 14,000 km. As shown in Figure 12 in MSW, the currents in the wave rotate in an anticlockwise sense in the deep water, but for the chosen parameters the onshore component of the deep ocean flow is only 1/12 as large as the alongshore component. The deep water impedance is close to -1, and the sea surface displacement nearly 180° out of phase with the positive longshore flow as for a pure Kelvin wave. The dimensional impedance is nearly $(D^*/g)^{1/2}$, giving an alongshore current of .062 cm/s for each cm of sea surface displacement. For a tidal amplitude of 5.6 cm (Table 3.4.6) an alongshore current amplitude of .34 cm/s would be expected, which is comparable to the rough estimate of .2 cm/s for the deep currents at Site D. Other aspects of the model agree well with the measurements at the Site

and on the nearby shelf, even though the flat ocean and shelf are only approximations to the real geometry.

The free mode satisfying 3.4.24 - 3.4.25 has surface displacement in phase on and off the shelf, as is observed for the New England shelf and the deep sea values from Bermuda in Table 3.4.6. The onshore or v component is in phase on and off the shelf, while the u or alongshore component is discontinuous at the shelf break. Between the shelf break at y = 0 and some interior point on the shelf the alongshore current is 180° out of phase with the deep ocean u component, and the current ellipse on the shelf has a clockwise polarization as opposed to the anticlockwise deep ocean currents. The ellipticity of the shelf currents varies with y. The reverse flow on the shelf occurs in an interval from y = 0 to about y = .51 in dimensionless terms for the chosen parameters, and shoreward of this interval the u component is again in phase with the deep ocean flow. Since the real shelf is not of constant depth, the model may not be applicable to the very near-shore currents.

The deep sea u component lagged the surface tide by 151° for the O_1 estimates and 190° for the K_1 estimates, compared with the 180° predicted by the model. For the O_1 alongshore current amplitude of .34 cm suggested by the model, the onshore flow would be only .03 cm/s and there

does seem to be evidence for a somewhat larger onshore component in the actual measurements. The noise in the measurements prevents any definite conclusions about this feature of disagreement. The measured shelf currents (Table 3.4.6) are in accord with the model and show the reversal of alongshore flow predicted. The v components for both the O_1 and K_1 frequencies have phases identical to the deep sea currents to within the accuracy of the measurements, while the u components are nearly 180° out of phase with the deep flow. This gives a shelf current ellipse with a clockwise polarization. The shelf currents are considerably larger than the deep ocean currents, consistent in general terms with the 20-fold decrease in depth on the shelf, although the step shelf model does not allow a realistic comparison. The discontinuity in alongshore flow at the shelf break predicted by the model is non-physical and would be smoothed out by friction in a real fluid. However strong horizontal shears in the diurnal period alongshore currents might be expected near the shelf break.

Conclusions

The diurnal period currents at Site D show strong surface intensification and relatively constant power at depth. There is no apparent decrease in total current

variance across the Site to suggest a strong contribution from trapped baroclinic tides. The currents are not strongly circularly polarized in the deep water, but the total variance in onshore and alongshore current fluctuations is comparable, suggesting that the continental slope to the north and the general topographic trend do not dominate the character of the motions there. The strong surface intensification can be ascribed largely to meteorological forcing, while the deeper currents show the influence of the barotropic tide. Although mooring motion cannot be ruled out as contributing to the surface intensification, the wind forcing gives a physical explanation of the observations without mention of mooring motion.

The currents show some coherences with the equilibrium tide, especially in the deep water, and there are indications of phase locked baroclinic motions as well as the barotropic tide. The baroclinic signal is not strong enough relative to the total current variance to allow any definite picture to emerge. The barotropic currents, with magnitudes of the order of .2 cm/s in alongshore flow, are well explained by a free Kelvin-Stokes barotropic mode which is trapped to the slope and propagates to the west along the depth contours. This mode exhibits a reversal in alongshore flow on the shelf which is observed in measurements there, and the correlation between deep ocean current and surface tide is consistent with the requirements of the model.

3.5 Summary

The varying physics of diurnal period internal waves from the MODE-1 area north to Site D means that these different areas will not fit together in one dynamical framework. North of the critical latitude, the diurnal period process is a local one, which depends critically on specific boundary conditions. The three areas considered do provide an insight into this varying physics, and a realization that the diurnal tidal process is relatively less energetic than the semidiurnal tides in areas north of the diurnal critical latiude, and that a separation of the tidal content of the diurnal band from other sources of energy is difficult.

The MODE-1 field observations, at the turning latitude for diurnal tides, are dominate by high mode, incoherent inertial-character motions in the diurnal band. The noise levels are so great that we can only put an upper bound on the diurnal barotropic current of about .2 cm/s, and there is no evidence for a global tidal process in either the temperature or current fields.

Muir Seamount, north of the turning latitude, provides a clear example of diurnal period internal waves trapped to their source. An analytical model developed to explain the observations at Muir Seamount describes a local adjustment in horizontal planes, with the fluid constrained to

feel only the local features of the seamount so far as vertical variations are concerned. The sloping sides of the seamount then induce a density signal as vertical shear in the horizontal flow is introduced parametrically. The approach gives current and temperature fluctuations which are generally consistent with the observations, but does exclude free seamount modes which might be found in a full treatment.

Finally, Site D showed some evidence of baroclinic diurnal tides, but most of the energy in diurnal period current fluctuations appears to be of non-tidal origin. The near surface currents are highly intensified over the deeper flow, and part of this is related to meteorological forcing. The noise levels prevent an accurate estimation of the barotropic current amplitudes, but stable estimates of the phases of the O_1 and K_1 barotropic current constituents in the deep water are combined with observations from the nearby New England shelf to obtain a consistent picture of the diurnal surface tide. The tidal currents show a reversal in along shore flow on and off the shelf which is a feature of a free shelf mode we use to model the observations.

OVERVIEW

4.1 Overview of internal tide generation

Sections 1 and 2 dealt separately with the semidiurnal internal tides in two widely separated areas. Specific estimates of the energy density and energy flux in the two cases were obtained for the M_2 tide, as well as a general feeling about the variability in the tidal fields. Here we review some theoretical considerations about the generation process at continental slopes, in order to apply some of these ideas to the observational sites and contrast the two. Site D is in the near field of a generation region while MODE-1 was in the far field of another slope generation region, but the differences between the two sets of measurements are greater than just this consideration would suggest. The currents at Site D showed a great deal of variability, while the temperature field and to a lesser extent the current field in MODE-1 appeared to be behaving relatively simply. This runs counter to intuition, which might suggest that the signal should be strongest near the generation region and more degraded by noise in the far field. However, physical differences between the two generation regions could account for some of the observed differences.

Step shelf generation models

First we discuss the generation process at a step continental shelf in a constant N ocean, as in the model of Rattray, Dworski and Kovala (1969) and extended by other workers. Some of the simple aspects of these models have not been discussed completely previously. For a constant Brunt-Väisälä frequency N, giving a constant characteristic slope

$$\gamma = (\sigma^2 - f^2)^{1/2}/N$$

a surface wave with amplitude ζ_o incident on a step shelf of depth H_1 and width L in a deep ocean with depth H_2 will generate a seaward propagating train of internal waves with isopycnal displacement of the form

$$\zeta \simeq (2\zeta_o \gamma L)/H_2 \sum_{m=1}^{\infty} \frac{\sin(m\pi H_1/H_2)}{(m\pi H_1/H_2)} \sin(m\pi z/H_2) \cdot$$

$$\cdot \sin(m\pi\gamma x/H_2 - \sigma t) \qquad (4.1.1)$$

The expression is exact for a particular anti-resonance case (Rattray, Dworski and Kovala), which occurs when the shelf width is an integral number of shelf internal wavelengths, and the node in onshore flow at the shore is

duplicated at the shelf break for each mode. The internal waves on the shelf have no influence on the deep ocean internal waves in this case. For the alternate resonance case where the shelf internal waves have a maximum in current at the shelf break for each shelf mode, the structure of the deep ocean currents can be highly complicated. The anti-resonance case is tractable and contains some interesting features.

At the shelf break, the internal waves add up to cancel the barotropic current from $-H_2<z<-H_1$, and the anti-resonant case gives a current profile which is constant for $-H_1<z<0$. This velocity signal propagates out to sea between the two characteristics leading from the shelf break, and since the internal waves have a progressive nature there is also a signal which is out of phase with the forcing surface tidal currents away from the actual shelf break.

From 4.1.1, since

$$\sum_{m=1}^{\infty} \frac{\sin(m\pi\delta)}{(m\pi\delta)} = (1-\delta)/2\delta \qquad (4.1.2)$$

(Gradshteyn and Ryzhik, 1965, §1.444.1), the internal wave amplitude is of order

$$[2\gamma L\zeta_o/H_2]\ [(1-\delta)/2\delta] \qquad (4.1.3)$$

in isopycnal displacement, where $\delta = H_1/H_2$. The shelf width L enters more naturally in terms of the volume flux in the surface tide, which by continuity is of the order

$$Q = \sigma\zeta_o L = UH_2 \qquad (4.1.4)$$

where U is the deep sea barotropic velocity component normal to the shelf (Baines, 1973). Thus the displacement ζ is of order

$$(2\gamma Q/\sigma H_2)\ (1-\delta)/2\delta \qquad (4.1.5)$$

and the currents in the internal waves are of the order

$$w/\gamma = \sigma\zeta/\gamma = 2U(1-\delta)/2\delta \qquad (4.1.6)$$

Shallow aspect shelves with $\delta << 1$ produce large velocities in the deep water, but the region in space where these high speeds occur is also small, of order $2H_1$ in the vertical. The time-averaged and depth integrated energy density in the anti-resonant case is

$$(Q^2/H_2)\ \Sigma\ \frac{\sin^2(m\pi\delta)}{(m\pi\delta)^2} \qquad (4.1.7)$$

$$= (Q^2/H_2)\ (1-\delta)\ /2\delta \qquad (4.1.8)$$

(Gradshteyn and Ryzhik, from §1.443.3) For a given volume flux and deep ocean depth, shallow shelves $\delta << 1$ produce the largest internal wave energy density. In the constant N step shelf, the anti-resonant internal wave field has total energy independent of the stratification, depending only on the presence of some stratification to allow internal waves to exist.

The energy flux in the seaward propagating waves is the sum of modal energy times group speed, where the group speed of mode m is

$$NH_2(1-f^2/\sigma^2)^{1/2}\ /\ m\pi \qquad (4.1.9)$$

For the anti-resonant case the energy flux is

$$Q^2N(1-f^2/\sigma^2)^{1/2} \cdot \Sigma \frac{\sin^2(m\pi\delta)}{(m\pi)\ (m\pi\delta)^2} \qquad (4.1.10)$$

$$= \quad Q^2N(1-f^2/\sigma^2)^{1/2}\ F(\delta) \qquad (4.1.11)$$

The energy flux depends on the stratification since the

group speeds vary with N. Alternately the surface tide must do more work to generate the necessary flow adjustment when the stratification is greater. The total energy flux is independent of the actual ocean depth, depending only on the aspect ratio of the shelf and deep ocean depths. The sum $F(\delta)$ in 4.1.11 apparently has no simple analytical form, but it was evaluated numerically and is shown in Figure 4.1.1 as a function of δ. Shallow shelves are again more effective than deeper shelves for generating internal waves, when all other factors are equal.

The modal decomposition in the generated fields depends on the geometry of the shelf. For example the percentage of the energy density in the first baroclinic mode is

$$[\sin^2(\pi\delta)/(\pi\delta)^2] \;/\; [(1-\delta)/2\delta] \qquad (4.1.12)$$

which is a maximum of 81% for $\delta = 1/2$ and vanishes as $\delta \to 0$ or 1. The percentage of energy flux in the first baroclinic mode is

$$\{\sin^2(\pi\delta)/\,\pi(\pi\delta)^2\} \;/\; F(\delta) \qquad (4.1.13)$$

and about 95% for $\delta = 1/2$. On the other hand, for $\delta = 1/20$ only 10% of the energy density and 37% of the energy flux

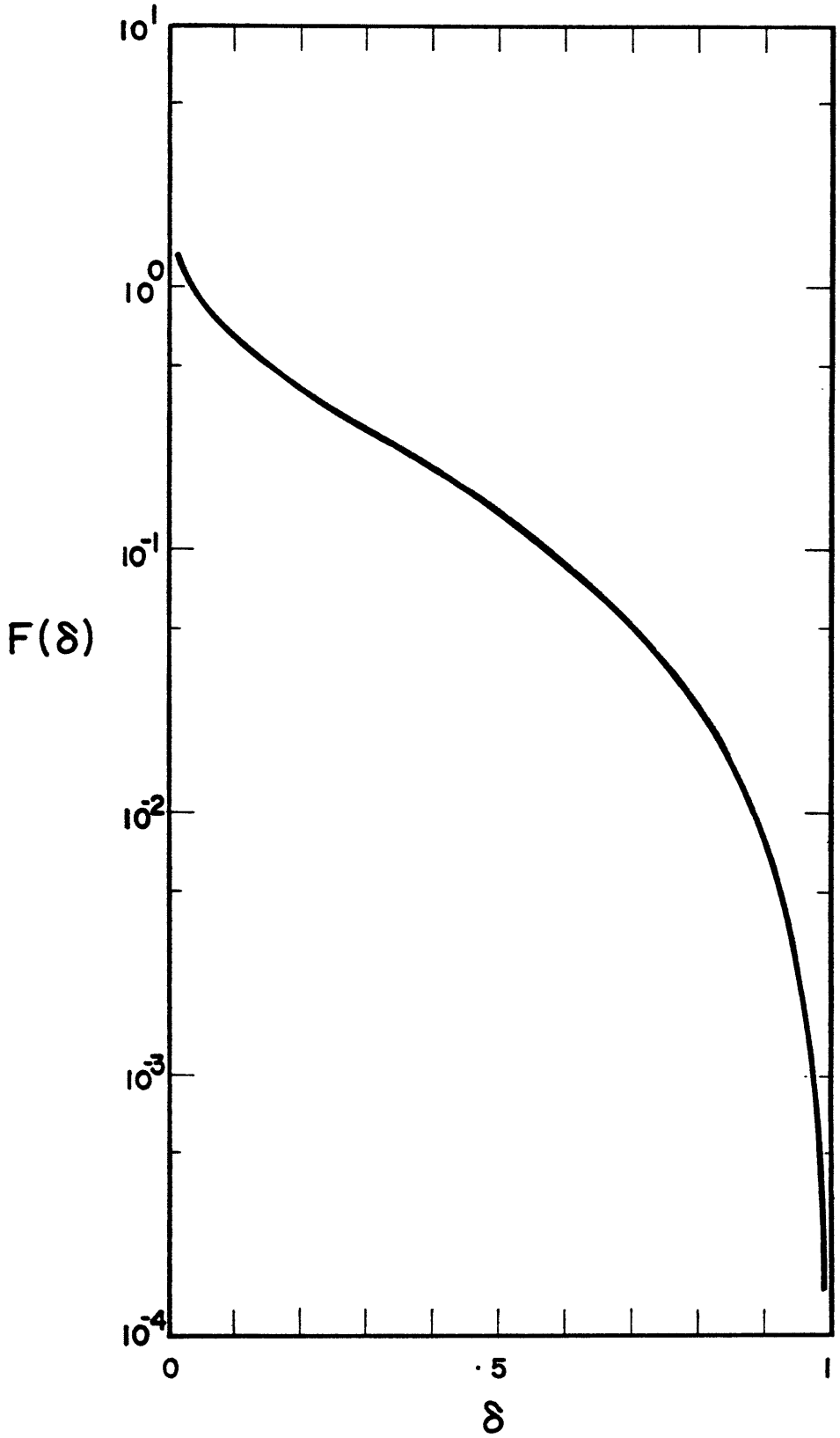


Figure 4.1.1 Dimensionless energy flux into the deep sea for a step shelf generation model, as a function of the shelf to deep ocean depth aspect ratio δ.

are contained in the first baroclinic mode. The effective group speed in the field (Baines, 1973) is the ratio

$$\frac{NH_2(1-f^2/\sigma^2)^{1/2}}{\pi} \Big/ \frac{F(\delta)\pi}{(1-\delta)/2\delta} \qquad (4.1.14)$$

$$= \frac{NH_2(1-f^2/\sigma^2)^{1/2}}{\pi n_{effective}}$$

which defines an effective mode number

$$[(1-\delta)/2\delta] \; / \; [F(\delta)\pi] \qquad (4.1.15)$$

which we have plotted in Figure 4.1.2. Shallow shelves need more high mode energy to build up the confined currents, and have less energy flux for a given energy density. The effective mode number is symmetrical about $\delta = 1/2$ for constant stratification because of the symmetry of the model shapes about $z = -H_2/2$.

The resonance or intermediate cases are not easily treated analytically, although the details of these cases are explicitly contained in the generation models. The part of the wave field generated by the coupling of shelf and deep ocean internal waves does depend on the stratification and shelf width, specifically through the ratio

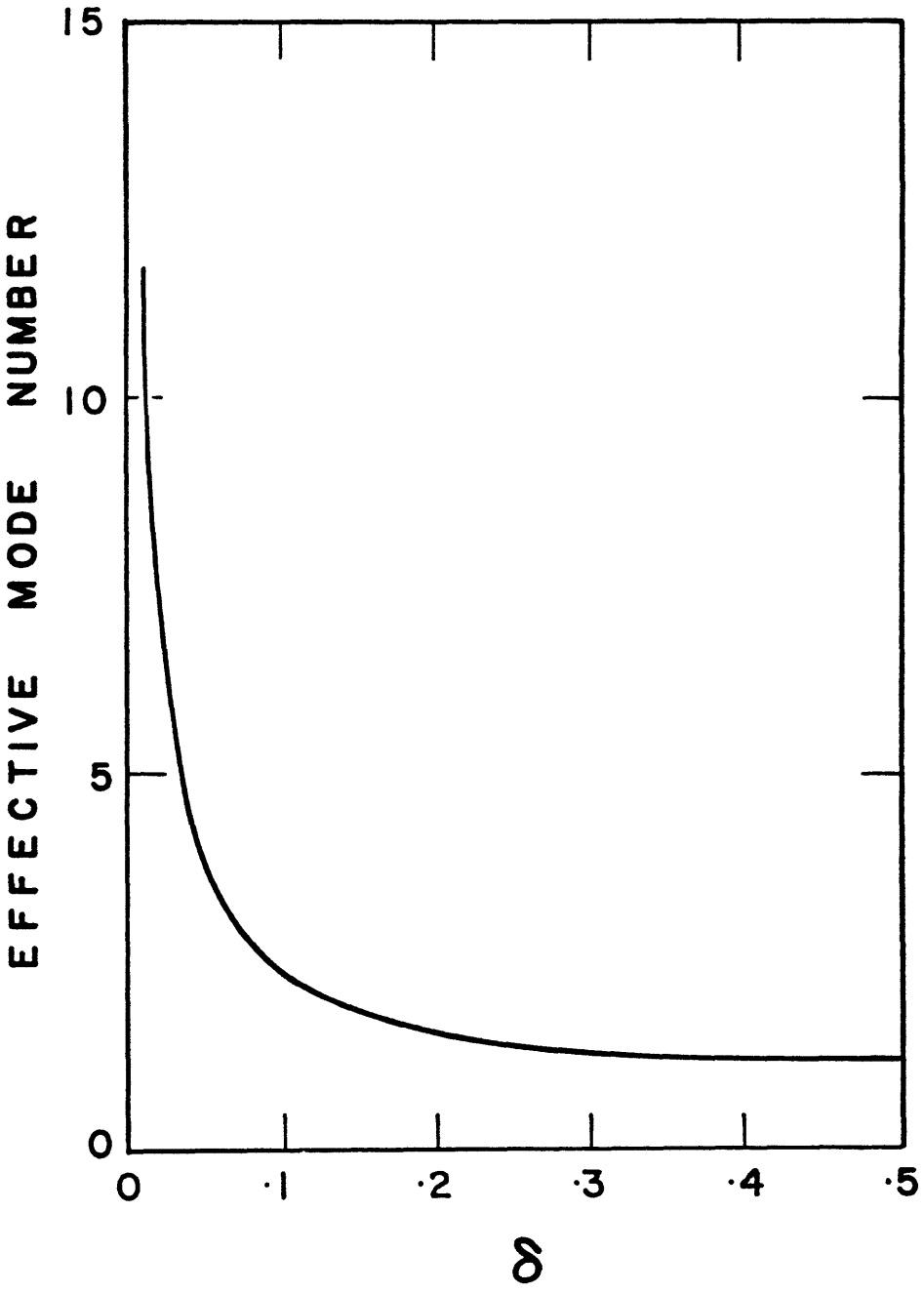


Figure 4.1.2 Effective mode number of the deep ocean internal waves generated in the anti-resonant step shelf model, as a function of the shelf to deep ocean depth aspect ratio δ. The curve is symmetrical about $\delta = 1/2$.

($H_1/\gamma L$) which relates the shelf internal wave lengths to the shelf width. The energy density in the deep ocean waves thus depends on the details of the process, and the published calculations of Rattray, Dworski and Kovala show that in a resonance case the deep sea current profiles have peaky and irregular features which tend to increase the total energy in the wave field.

Since low order modes are less sensitive to perturbations in the propagation path than higher order modes, and also less damped, the energy flux in the generated waves associated with the low modes is most important for determining the overall energy levels of the internal tide in a real ocean far from the generation regions. Some shelf geometries can produce high local energy densities, but be less effective in influencing the deep ocean than a shelf with less local energy density but a more efficient shape for generating low mode internal waves. For the anti-resonant step shelf case, the absolute amounts of energy and energy flux in the first baroclinic mode continue to increase as δ decreases. We briefly consider another model which includes different features of the generation process.

Baines' characteristic model

Baines (1973, 1974) has considered a model of internal wave generation by the interaction of a surface wave with varying bottom topography in a stratified ocean. He uses the characteristic coordinates of the internal waves, and by assuming a special form of the stratification can obtain separable solutions in these coordinates. Then the radiation condition is formulated as an integral relation on the general solution, and this relation and the boundary conditions define a mathematical problem which can be solved numerically. Quite general topographic variations and density profiles are permitted in this approach, although the numerical complications become greater with more realistic cases. Baines has calculated the internal waves generated in various sorts of continental slope models, where the formulation gives effectively an infinitely wide shelf.

For shallow linear slopes, less than the characteristic slope γ, Baines (1973) finds that the energy flux and energy density in the generated waves generally increase with steeper slope and with smaller aspect ratio H_1/H_2, but that the dependence fluctuates with the details of the geometry in both slope and aspect ratio. In this case the energy fluxes into the deep and shallow water are nearly constant,

and the shallow water energy density greater because of the slower group speeds in the shallow water. For a transition from such shallow slopes to slopes steeper than the characteristic slope γ, Baines (1974) finds an apparently discontinuous increase in seaward energy density and flux by about a factor of 2, and a decrease in shoreward energy density and energy flux. For the steep slopes the energy density and energy flux depend less on the actual slope, but still increase with shallower aspect ratio. The energy flux is predominantly into the deep ocean for the steep linear slopes, and some of the considerations of effectiveness in generation are revealed by Baines' calculation that for steep slopes which approach the critical slope γ, the energy density in the deep ocean increases but the energy flux to the deep ocean actually decreases. Because of the predominantly seaward bias for the energy flux, near-critical steep linear slopes appear to be actually less efficient in generating internal waves than steeper slopes. This contrasts to the shallow slope case where the energy density and energy flux both increase as the topographic slope approaches the critical slope from below. For very steep linear slopes, the seaward energy flux which Baines calculates agrees quite well with expression 4.1.11 for the anti-resonant step shelf case. The energy flux is predominantly carried in the low

order modes which are somewhat insensitive to the fine detail of the generation process, and the individual differences in the models.

For Baines' formulation, the energy density in the internal waves varies directly with N for tidal frequencies, as opposed to the direct generation response in the step shelf model which is independent of stratidication, and the indirect response where the energy density can vary as the square of N. Thus the infinite shelf formulation appears to be somewhere between an anti-resonant and resonant case as compared to the step shelf, in the steep slope limit. For a real ocean, diffusive effects would tend to remove the distinction. Prinsenberg, Wilmot and Rattray (1974) concluded that with the inclusion of friction in the step shelf model, the internal waves on the shelf would be quickly damped and would not set up the standing wave pattern required for a resonance.

Comparison with observations: Site D

The theoretical models can be used to calculate the expected fields in the observational areas, using the parameters appropriate for each setting. The agreement or lack of it gives some insight into the generation process, and tests the validity of the idealized models to the real ocean.

For Site D, we choose H_1 = 130 m, H_2 = 2600 m, L = 200 km and ζ_o = 39 cm for the M_2 tide. This gives a barotropic volume flux onshore of Q = .11 x 10^6 cm^3/s, which is consistent with an onshore velocity component of .40 cm/s at the 2800 m depth of the southern site. N = .19 x 10^{-2} s^{-1} is chosen so that the constant N group speeds of the low modes agree with the calculations for the actual density distribution. For δ = 1/20, the geometrical factors for the step shelf case are $(1-\delta)/2\delta$ = 9.5 and $F(\delta)$ = .846. Then the step shelf model gives an energy density on the deep ocean side of .44 x 10^6 erg/cm^2 and a seaward energy flux of .14 x 10^8 erg/s cm. By comparison, the very steep linear slope model of Baines for constant stratification gives deep sea energy density .18 x 10^7 erg/cm^2 and seaward energy flux .13 x 10^8 erg/s cm for γ = .056. The steep slope energy density is greater than the anti-resonant step shelf value, but the energy fluxes are quite comparable. Baines' near critical shallow slope model gives considerably less deep sea energy density at about .18 x 10^6 erg/cm^2, and a seaward energy flux .34 x 10^7 erg/s cm.

Baines carried out a particular calculation in his 1974 work for a continental slope modelling the slope about 100 km west of Site D, and used a realistic variable stratification. This calculation gave an average over summer and winter

conditions of .22 x 10^5 erg/cm^2 for deep sea energy density, and .12 x 10^7 erg/s cm for seaward energy flux. Both these figures are considerably less than any of the idealized models give. In the more realistic model, Baines used topography which was sub-critical in slope for M_2 internal waves except for a localized region near 1000 m depth, but the slope was globally nearly critical as is the case for the actual New England slope.

We have estimated the total coherent plus incoherent energy density in the M_2 band internal waves at the southern site to be .18 x 10^6 erg/cm^2, which is about 40% of the total barotropic energy there. For δ = 1/20, both the step shelf and very steep linear slope models give deep sea energy densities which are considerably greater than the observed total, and we conclude that neither is applicable to this generation region. However the step shelf model may still be useful in estimating the contribution of the first three modes to the overall energetics of the generated fields. The total energy density in the first three baroclinic modes for the fit of coherent currents at the southern site is far less than the total energy there at .10 x 10^5 erg/cm^2. For the special step shelf case, 30% of the deep sea energy is contained in the first three modes, and we might multiply the estimate given by three for about .3 x 10^5 erg/cm^2 expected in the generated fields. The higher modes would tend to be lost in

the average over variable oceanic conditions and a finite spatial region. This estimate of energy density would agree with the calculation of Baines for the realistic slope model.

The three mode fit at the southern site gave a seaward energy flux of $.6 \times 10^6$ erg/s cm on the basis of a number of assumptions. For the step shelf case about 70% of the total energy flux is carried by the first three modes, and the low modes are expected to be most effective for any geometry. The currents were averaged over all seasons, and since the energy is quadratic in the currents the energy flux estimate is probably low. However the flux estimates for a step shelf or steep linear slope are both 50 times greater than our estimate, and this strengthens the conclusion that neither model can be used for this case. The near-critical shallow slope model gives energy density comparable to the total coherent plus incoherent baroclinic energy density at the southern site, but the model gives energy flux about 10 times greater than the measurements indicate, and is not a very realistic model for the process. The more detailed calculation of Baines, which applies more closely to the slope north of Site D than any of the idealizes models, gives an energy flux about twice our estimate and within the accuracy of our calculation this is good agreement.

Thus it seems that theory still leads experiment for internal tide generation, and that Baines' modelling efforts in particular are quite useful in reproducing the signal which we have extracted from the very noisy fields at Site D. The comparisons point out that the simple step-like models have very limited applicability on continental slopes where the topography is only locally super-critical as at the slope north of the Site. The continental slopes on the east coast of North America north of Cape Hatteras average about 4^{o} inclination (Emery, 1965), which is comparable to the M_2 internal wave critical slope for the usual stratification. The near-critical slope generation problem is therefore a very relevant one, and the results from Site D indicate that it may be a singular one. In a field composed of extremely high mode waves, there can be large energy density with relatively little actual energy flux out to sea, and the realistic calculation of Baines shows that for a more realistic geometry and nearly critical slope over much of the depth range, the energy flux is only about a third of the figure calculated for a linear slope which is just less than critical. The estimates for the linear slopes depend on an average effective stratification, but the number which we use is a reasonable choice.

Baines (1974) has discussed the high shear produced in the velocity profiles near a critical slope, and the

possibility of flow instabilities mixing the fluid. An experimental demonstration of the dramatic instabilities which can occur when internal waves interact with a critical slope has been given by Cacchione and Wunsch (1974). These aspects of real fluid behavior may be the truly significant ones for the near-critical slope generation process.

Comparison with observations: MODE-1

The MODE-1 experiment provides a much fairer case for the application of the simple generating models. As described in Section 2.4, there are a variety of slope types along the eastern seaboard of North America, and south of 30^{o}N the Blake Escarpment is a special situation. This massive fault forms a deep sea slope region, with a shelf break at about 1200 m depth on the edge of the Blake Plateau and a precipitous drop to the Blake-Bahama Rise at 4800 m depth. The slopes on the Escarpment have been estimated at 15^{o} inclination, but it is believed that slopes of 30^{o} and greater are found there which defy traditional echo sounding techniques to resolve (Shepard, 1967). The aspect ratio of 1/4 generates internal tides with a large low-mode content, making the observational problems less difficult and explaining the well-behaved nature of the internal tide far from the generation region.

The widest part of the Blake Plateau is adjacent to the northern end of the Escarpment where the depth contours curve sharply. A shelf width L = 500 km and the estimates of Redfield (1958) for the M_2 surface tide at the shelf break give an onshore volume flux of $.32 \times 10^6$ cm^3/s, while the geometrical factors for the step shelf case we have discussed are $(1-\delta)/2 = 1.5$ and $F(\delta) = .340$. The deep shelf is not particularly efficient in generating internal tides, but the volume flux is about three times the estimate at Site D and the energy flux in the internal tide varies as the square of the volume flux. With $N = .18 \times 10^{-2}$ s^{-1}, the anti-resonant step shelf case gives a deep sea energy density of $.31 \times 10^6$ erg/cm^2 and seaward energy flux of $.52 \times 10^8$ erg/s cm. A rough estimate of the total barotropic energy density at the Blake Escarpment is $. 6 \times 10^6$ erg/s cm, about twice as much as the predicted energy in the internal tide. Since most of the energy in the barotropic tide is potential energy of sea surface displacement in this setting, the internal tides are a dominant factor in the horizontal current field. The aspect ratio of 1/4 results in 54% of the energy density and 76% of the energy flux in the internal tide accounted for by the first mode, for the simple model we have duscussed. This gives a seaward energy flux in the first mode of $.4 \times 10^8$ erg/s cm, providing remarkable agreement with the $.3 \times 10^8$ erg/s cm observed in the MODE-1 field

experiment. The likely generation region is located about 700 km from the array center, and the 108°T bearing of the experiment from the northern end of the Blake Escarpment to the experiment is consistent with the 125°T direction of energy flux in the internal tide which was derived from the measurements. The observations will be influenced by the integrated generation region all along the coast, but the dominant coherent signal is explained as a low mode internal tide generated at the Blake Escarpment and propagating smoothly out to sea. The calculations of Prinsenberg, Wilmot and Rattray (1974) indicate that even for large constant eddy diffusivity, a first mode M_2 internal wave in a 5 km deep ocean is essentially undamped after propagating the four or five wavelengths equivalent to the distance from the Escarpment to the observing area. Thus although the observations are in the far field of the generation source, the shelf geometry, energetic barotropic tide and benign propagation conditions allow a strong signal at the MODE-1 location.

As discussed in Section 1.7, Miller (1966) gives an upper bound on the average energy dissipation from the M_2 barotropic tide on the coast between Cape Cod and Florida of $.5 \times 10^8$ erg/s cm, and our analysis indicated that about this amount is being diverted to the generation of internal tides in some regions of this continental margin. This area

of the world has relatively small dissipation relative to the global process, but here the baroclinic tides appear to be an important part of the boundary condition for the surface wave.

4.2 General remarks

Statistics

For the seimdiurnal tide, the M_2 frequency was most energetic in the two areas we studied. The M_2 tide was also most coherent with the equilibrium tide, while the adjacent bands were considerably noisier. The analysis was designed to look specifically for determinism in the internal tide, and the 1/15 cpd bandwidth used was the widest possible with any reasonable hope of separating the major seimdiurnal constituents. The internal tides were quite variable, with signal to noise ratios of at best 1, but there was definite evidence for determinism. Any studies hoping to look at such determinism seem to be constrained to using at least the frequency resolution we have used here, and the use of a wider bandwidth is essentially admitting mostly noise with very little signal, and degrading the statistics of the process.

Speculations about the dissipation of the internal tide

The MODE-1 experiment, while showing interesting results for the semidiurnal tides, does not give the ultimate fate of the internal tides generated at the continental margin. We did not observe any consistent decrease of first mode amplitude across the array, and the modal fits of temperature

fluctuations at the eastern moorings near the rough topography were not atypical of the whole MODE-1 area. The several thousand kilometers of rough topography between the MODE-1 site and the Mid-Atlantic Ridge could scatter the energetic first mode we observed into higher modes, which would be quickly dissipated by turbulent processes. This is somewhat the reverse of Cox and Sandstrom's motivation for their bottom scattering model, since it involves dissipation in the internal tides rather than generation, but the distinction is a formal one. Further observations over the abyssal hills which might become available in the planned successor of the MODE program would clarify this possibility.

BIBLIOGRAPHY

Abramowitz,M.,and I.A.Stegun,ed.,Handbook of Mathematical Functions,p.446,Dover,New York 1965

Amos,D.E.,and L.H.Koopmans,Tables of the distribution of the coefficient of coherence for stationary bivariate Gaussian processes,Sandia Corp. Monograph SCR-483 1963

Baines,P.G.,The generation of internal tides by flat-bump topography,Deep-Sea Res.,20,179-205 1973

Baines,P.G.,The generation of internal tides over steep continental slopes,Phil.Trans.Roy.Soc.London,A227, 27-58 1974

Beardsley,R.C.,and B.Butman,Circulation on the New England continental shelf: response to strong winter storms, Geophys.Res.Letters,1,181-184 1974

Bingham,C.,M.D.Godfrey,and J.W.Tukey,Modern techniques of power spectrum estimation,I.E.E.E.Trans.,AU-15,56-66 1967

Birkhoff,G.,and G-C.Rota,Ordinary Differential Equations, Blaisdell,Waltham 1962

Cacchione,D.,and C.Wunsch,Experimental study of internal waves over a slope,J.Fluid Mech.,60,223-239 1974

Capon,J.,High-resolution frequency-wavenumber analysis, Proc.I.E.E.E.,57,1408-1418 1969

Cox,C.,and H.Sandstrom,Coupling of internal and surface waves in water of variable depth,J.Oceanog.Soc.Japan, 20th Anniv.Vol. 1962

Day,C.G.,and T.F.Webster,Some current meter measurements in the Sargasso Sea,Deep-Sea Res.,12,805-814 1965

Deacon,E.L.,and E.K.Webb,Interchange of properties between sea and air,The Sea,M.N.Hill ed.,p.57,Interscience, New York 1962

Defant,A.,Tides and internal tidal waves in the Atlantic Ocean,METEOR Work VII/I,de Gruyter,Berlin 1932 (in German)

Defant,A.,Internal waves and their stability conditions, Arch.Met.Geophys.Bioklimat.,A1,39-61 1949 (in translation)

Dietrich,G.,General Oceanography,Chart 6,Interscience, New York 1963

Eckart,C.,Hydrodynamics of Oceans and Atmospheres,Pergammon, London 1960

Emery,K.O.,Geology of the continental margin off eastern United States,Submarine Geology and Geophysics, W.F.Whittard and R.Bradshaw ed.,p.4,Butterworths, London 1965

Fjelstad,J.E.,Interne Wellen,Geophys.Publ.,10,1-35 1933 (in German)

Fofonoff,N.P.,Internal waves of tidal period,(unpublished manuscript) 1966

Fofonoff,N.P.,and T.F.Webster,Current measurements in the western Atlantic,Phil.Trans.Roy.Soc.London,A270, 423-436 1971

Garrett,C.,Normal modes of the Bay of Fundy and the Gulf of Maine,Can.J.Earth Sciences,11,549-556 1974

Garrett,C.,and W.Munk,Space-time scales of internal waves, Geophys.Fluid Dyn.,2,225-264 1972

Gerges,M.A.,Variation of tidal currents measured at deep-sea moorings,M.S.Thesis,Department of Meteorology, Massachusetts Institute of Technology 1966

Gonella,J.,A rotary-component method for analysing meteorological and oceanographic time series,Deep-Sea Res., 19,833-846 1972

Gould,W.J.,and E.Sambuco,The effect of mooring type on measured values of ocean currents,Deep-Sea Res.,22, 55-62 1975

Gradshteyn,I.S.,and I.W.Ryzhik,Tables of Integrals,Series and Products,4th ed.,Academic Press,New York 1965

Haurwitz,B.,The effect of ocean currents on internal waves, J.Marine Res.,7,217-228 1948

Haurwitz,B.,On the reality of internal lunar tidal waves in the ocean,Tech.Report 52-71,Woods Hole Oceanographic Institution 1952

Helland-Hansen,B.,Physical Oceanography and Meteorology, MICHAEL SARS N.Atlantic Deep-Sea Expedition 1910, Scientific results 1930

Hendershott,M.C.,Inertial oscillations of tidal period, Ph.D.thesis,Harvard University 1964

Hicks,S.,A.Goodheart and C.Isely,Observations of the tide on the Atlantic continental shelf,J.Geophys.Res.,70, 1827-1830 1965

Hogg,N.,The influence of topography on steady currents and internal waves,Ph.D.thesis,Department of Earth and Planetary Sciences,Massachusetts Institute of Technology 1971

Hurley,D.G.,The emission of internal waves by vibrating cylinders,J.Fluid Mech.,36,657-672 1969

LeBlond,P.H.,On the damping of internal gravity waves in a continuously stratified ocean,J.Fluid Mech.,25, 121-142 1966

Longuet-Higgins,M.S.,On the trapping of long-period waves round islands,J.Fluid Mech.,37,773-784 1969

Magaard,L.,and W.D.McKee,Semi-diurnal tidal currents at 'site D',Deep-Sea Res.,20,997-1009 1973

Martin,S.,W.F.Simmons and C.Wunsch,Resonant internal wave interactions,Nature,224,1014-1016 1969

Miles,J.W.,On Laplace's tidal equations,J.Fluid Mech.,66, 241-260 1974

Miller,G.R.,The flux of tidal energy out of the deep oceans, J.Geophys.Res.,71,2485-2489 1966

MODE Scientific Council,A mid-ocean dynamics experiment, Available from the Department of Meteorology, Massachusetts Institute of Technology,(unpublished manuscript) 1973

Müller.P.,On the interaction between short internal waves and larger scale motion in the ocean,Hamburg.Geophys. Einzelschrift.23,Wittenborn,Hamburg 1974

Munk,W.,Once again - tidal friction,Q.J.Roy.Astr.Soc.,9, 352-375 1968

Munk,W.,and N.Phillips,Coherence and band structure of inertial motion in the sea,Rev.Geophys.,6,447-472 1968

Munk,W.,and D.E.Cartwright,Tidal spectroscopy and prediction,Phil.Trans.Roy.Soc.London,A259,533-581 1966

Munk,W.,F.Snodgrass,and M.Wimbush,Tides off-shore: transition from California coastal to deep-sea waters,Geophys. Fluid Dyn.,1,161-235 1970

Nansen,F.,The Norwegian North Polar Expedition 1893-1896, Scientific results III,No.9,London 1902

Olbers,D.J.,On the energy balance of small-scale internal waves in the deep-sea,Hamburg.Geophys.Einzelschaft.24, Wittenborn,Hamburg 1974

Phillips.O.M.,The Dynamics of the Upper Ocean,Cambridge University Press,Cambridge 1969

Pollard,R.T.,On the generation by winds of inertial waves in the ocean,Deep-Sea Res.,17,795-812 1970

Pollard,R.T.,and R.C.Millard,Jr.,Comparison between observed and simulated wind-generated inertial oscillations,Deep-Sea Res.,17,813-821 1970

Prinsenberg,S.J.,W.L.Wilmot,and M.Rattray,Jr.,Generation and dissipation of coastal internal tides,Deep-Sea Res.,21,263-281 1974

Rattray,M.,Jr.,J.G.Dworski,and P.E.Kovala,Generation of long internal waves at the continental slope,Deep-Sea Res.,supp.16,179-195 1969

Redfield,A.C.,The influence of the continental shelf on the tides of the Atlantic coast of the United States, J.Marine Res.,17,432-448 1958

Regal,R.,and C.Wunsch,M_2 tidal currents in the western North Atlantic,Deep-Sea Res.,20,493-502 1973

Seiwell,H.R.,An analysis of vertical oscillations in the southern North Atlantic,Proc.Am.Phil.Soc.,85,136-158 1942

Shepard,F.P.,The Earth Beneath the Sea,Johns Hopkins Press, Baltimore,p.100 1967

Stommel,H.,The Gulf Stream,University of California Press, Berkeley,p.68 1966

Taylor,G.I.,Tidal friction in the Irish Sea,Phil.Trans.Roy. Soc.London,A120,1-93 1919

Thompson,R.O.R.Y.,Topographic Rossby waves at a site north of the gulf Stream,Deep-Sea Res.,18,1-19 1971

Voorhis,A.D.,Measurements of vertical motion and the partition of energy in the New England slope water, Deep-Sea Res.,15,599-608 1968

Woods,J.D.,Wave-induced shear instability in the summer thermocline,J.Fluid Mech.,32,791-800 1968

Wunsch,C.,Progressive internal waves on slopes,J.Fluid Mech., 35,131-144 1969

Wunsch,C.,Bermuda sea level in relation to tides,weather, and baroclinic fluctuations,Rev.Geophys.Space Phys., 10,1-49 1972a

Wunsch,C.,The spectrum from two years to two minutes of temperature fluctuations in the main thermocline at Bermuda,Deep-Sea Res.,19,577-593 1972b

Wunsch,C,Internal tides in the ocean,Rev.Geophys.Space Phys., (in press) 1975a

Wunsch,C.,Deep ocean internal waves: What do we really know?, J.Geophys.Res.,80,339-343 1975b

Wunsch,C.,and R.Hendry,Array measurements of the bottom boundary layer and the internal wave field of the continental slope,Geophys.Fluid Dyn.,4,101-145 1972

Wunsch,C.,and J.Dahlen,A moored temperature and pressure recorder,Deep-Sea Res.,21,145-154 1974

Zetler,B.,W.Munk,H.Mofjeld,W.Brown,and F.Dormer,MODE Tides, (Submitted to) J.Phys.Oceanog. 1975

Zeilon,N.,On tidal boundary-waves and related hydrodynamical problems,Kungl.Svenska Vet.Akad.Handl.,47,1-46 1911

Zeilon,N.,Experiments on boundary tides,Goteborgs Kengl. Vetensk.Handl.,5B,1-8 1935

Appendix A.1 Fourier transforming and tapering

In the western North Atlantic Ocean, the semidiurnal surface tide is dominated by the 12.4206 hour period principal lunar M_2 constituent. Separated in frequency from the M_2 line by 1/14.77 cpd is the principal solar line at 12.0000 hour period, and at a separation of 1/27.55 cpd to lower frequency from the M_2 line is the lunar N_2 constituent with period 12.6582 hours. These three frequencies account for most of the semidiurnal variance in sea level. For example in the Sargasso Sea, the M_2, S_2 and N_2 surface tides have amplitude 35 cm, 7 cm and 8 cm respectively, and together account for all but a fraction of a per cent of the total semidiurnal band energy (Zetler, Munk, Mofjeld, Brown and Dormer 1974). In order to resolve the weaker lines from the M_2 frequency, conventional harmonic analysis requires a record length the reciprocal of the frequency difference, and classical tidal prediction schemes favor 15 and 29 day record lengths when dealing with short series, because in round numbers these allow resolution of the M_2 - S_2 pair and all three major frequencies respectively.

Finite discrete Fourier transform

Consider a time series of N discrete data points at equal intervals of time, which consists of a sinusoid at

frequency σ which may not be one of the fundamental frequencies of the analysis

$$\sigma_k = 2\pi\{(k-1)/\Delta T\} \qquad (A.1.1)$$

for ΔT the time step in the discrete series. If

$$s(t\Delta T) = s_t = \exp\{2\pi i(K-1)(t-1)/N\}$$
$$t = 1, N \qquad (A.1.2)$$

is the signal, where K is a real number, then the Fourier transform of s_t is

$$\hat{s}(\sigma_k) = \hat{s}_k = \frac{1}{N} \sum_{t=1}^{N} s_t \exp\{-2\pi i(k-1)(t-1)/N\}$$
$$= \frac{\exp\{\pi i(K-k)\}}{\exp\{\pi i(K-k)/N\}} \frac{\sin\{\pi(K-k)\}}{\sin\{\pi(K-k)/N\}} \qquad (A.1.3)$$

If $(K-k)/N << 1$, then

$$\hat{s}_k \simeq \exp\{\pi i(K-k)\}\frac{\sin\{\pi(K-k)\}}{(K-k)}$$
$$= \exp\{\pi i(K-k)\}\text{sinc } \pi(K-k) \qquad (A.1.4)$$

where $\text{sinc}(x) = \sin(x)/x$.

For example, the N_2 line with frequency .0790 cph would be split into two main contributions in the frequency grid of the 15 day record Fourier transform, with about 50% of the total power in the nominal N_2 band centered at 12.86 hour period. 31% of the astronomical N_2 line input will influence the nominal M_2 band. On the other hand, much less than 1 percent of the astronomical M_2 line input leaks into the bands adjacent the nominal M_2 band, and since the M_2 variation is greatest, this is desirable. The S_2 astronomical frequency and the nominal S_2 frequency are exactly equal, and there is no leakage from the S_2 band of true S_2 power.

Tapering

The 15 day record lengths were tapered smoothly to zero at the beginning and end of record after the individual piece means had been removed. The tapering function used was a one-tenth cosine window

$$W_t = 0.5 - 0.5 \cos\{10\pi(t-1)/N\}, \quad t = 1, N/10 \text{ or } t = 9N/10, N$$

$$W_t = 1, \quad t = N/10, 9N/10 \qquad \text{(A.1.5)}$$

which has a Fourier transform $\hat{W}_k$

$$\hat{W}_k = .90 \qquad ,k = 1$$

$$\hat{W}_k = -\frac{1}{2N}\exp\{\pi i(k-1)/N\}\frac{\sin\{\pi(k-1)/5\}}{\sin\{\pi(k-1)/N\}} -$$

$$-\frac{1}{4N}\exp\{\pi i(k-6)/N\}\frac{\sin\{\pi(k-6)/5\}}{\sin\{\pi(k-6)/N\}} -$$

$$-\frac{1}{4N}\exp\{\pi i(k+4)/N\}\frac{\sin\{\pi(k+4)/5\}}{\sin\{\pi(k+4)/N\}} \quad , k = 2,N$$

(A.1.6)

For a one-sided transform, since W_t is real valued, we can write

$$W_t = \hat{W}_1 + (-1)^t\hat{W}_{N/2+1} +$$

$$+ \sum_{k=2}^{N/2} \hat{W}_k \exp\{2\pi i(t-1)(k-1)/N\} +$$

$$+ W_k^* \exp\{2\pi i(t-1)(k-1)/N\}$$

(A.1.7)

These expressions will be used to show the effect of the tapering process on the data series. The purpose of the proceedure is to remove end effects from the series which could contaminate the high frequency content of the actual process we want to study. A strong trend in the data,

which may reflect low frequency energy from the "red" geophysical spectrum which is not resolved by the record length, will generate spurious high frequency energy. Consider a simple ramp function

$$R_t = (t-1)/(N-1) - 1/2 \quad , \; t = 1,N \qquad (A.1.8)$$

so that R_t increases uniformly from - 1/2 to 1/2 over the record of N points. Then the Fourier transform of R_t is

$$\hat{R}_k = 0 \quad , \quad k = 1$$

$$\hat{R}_k = - \frac{1}{2(N-1)} \{1 - i \cot\{\pi(k-1)/N\}\} \quad , \; k > 1 \qquad (A.1.9)$$

For $(k-1)/N << 1$,

$$\hat{R}_k \simeq (i/2)\; 1/\{\pi(k-1)\} \; , \quad k > 1 \qquad (A.1.10)$$

which is the analogue of the infinite Fourier sine expansion of a continuous ramp. The point is that such a ramp will generate Fourier coefficients whose amplitude decreases like k^{-1}, and that if the ramp is large enough relative to the actual signal at harmonic k, it could seriously contaminate the high frequency process as derived

in the finite transform. For a 15 day record length, a trend with a peak to peak range of unity shows up at the M_2 estimate with an amplitude of .011. An extreme case of a 50 cm/s total trend corresponding to a low frequency wave with amplitude 25 cm/s could produce over .5 cm/s of apparent M_2 frequency current, comparable to the signals in the water column below 250 m depth.

There are various schemes for eliminating the effect of trends for time series analysis. The taper acts as a non-linear filter, with the Fourier transform of a tapered series s_t, whose true Fourier transform is $\hat{S}_k$, being the convolution

$$(\hat{s_w})_k = (1/N) \sum_{t=1}^{N} (W_t \cdot s_t) \exp\{-2\pi i (k-1)(t-1)/N\}$$

$$= (1/N) \sum_{t=1}^{N} \sum_{r=1}^{N} \hat{W}_r \exp\{2\pi i (r-1)(t-1)/N\} \cdot$$

$$\cdot \sum_{p=1}^{N} \hat{S}_p \exp\{2\pi i (p-1)(t-1)/N\} \exp\{-2\pi i (t-1)(k-1)/N\}$$

$$= \sum_{r,p=1}^{N} \hat{W}_r \hat{S}_p \sum_{t=1}^{N} \exp\{2\pi i (t-1)(r+p-t-1)/N\}$$

$$= \hat{S}_k \hat{W}_1 + \sum_{p=1}^{k-1} \hat{S}_p \hat{W}_{k+1-p} + \sum_{p=k+1}^{N} \hat{S}_p \hat{W}_{N-p+k+1}$$

(A.1.11)

More graphically, the tapering window smooths out the leading edges of the ramp, and reduces its high frequency content markedly. At the M_2 frequency for the 15 day record length, a tapered ramp has only about .06% as much power as the original untapered ramp. As with all such techniques, there is a price to pay which shows up here in the effect of the windowing on a line input. The non-linearity of the taper/filter implied in the convolution A.1.11 means that the line will be somewhat smeared in frequency, with a unit input sine wave giving an amplitude of .90 at the input frequency and some power at other frequencies as well. The estimates can be corrected for the first order reduction in variance to give the estimate at the input frequency the correct amplitude, and this was done for all the values quoted in the text. The correction simply involves dividing the raw estimates by the numerical factor .9. For the particular window here, $\hat{W}_2 = \hat{W}_{360} = .10$, so

$$(\hat{S}_w)_k = \hat{S}_k\hat{W}_1 + \hat{S}_{k-1}\hat{W}_2 + \hat{S}_{k+1}\hat{W}_N + \cdots$$

$$= .90\ \hat{S}_k + .10\ \hat{S}_{k-1}\exp(i\mathrm{Arg}\hat{W}_2) +$$

$$+ .10\ \hat{S}_{k+1}\exp(i\mathrm{Arg}\hat{W}_N) + \cdots$$

(A.1.12)

The leakage from a strong line into the immediately adjacent band is about .10 of the line in magnitude or 1 per cent in energy. Within a few harmonics, the k^{-2} decay of the spectrum of the tapering function reduces any leakage to insignificance. An actual numerical run with a unit sine wave input at 12.4206 hour period gave an amplitude of .897 at the nominal M_2 frequency, .115 at the N_2 estimate and .0853 at the S_2 estimate. This is mainly the result of the taper, with a small effect from the input not being exactly at the frequency of one of the record length harmonics. Since the observations showed that the energy in the adjacent bands was typically one-third of the energy at M_2 frequency for the current and temperature field, the leakage from the M_2 band is not significant at about 1 per cent of the M_2 power. The N_2 frequency, however, is not well-resolved from the M_2 frequency in the 15 day analysis, and the results for the N_2 coherent tides resultingly less stable. The necessity of averaging many shorter pieces together to filter out the noise content, and the desire to have good resolution in frequency space, are diametrically opposed, and the 15 day record length represents the compromise we have selected.

Although the tapering proceedure has some undesirable features, it does accomplish its primary purpose. Figure A.1.3 shows the amplitude spectrum of a unit sine wave at M_2 frequency added to a ramp with range 40 units, for the cases when no tapering was applied and when it was used.

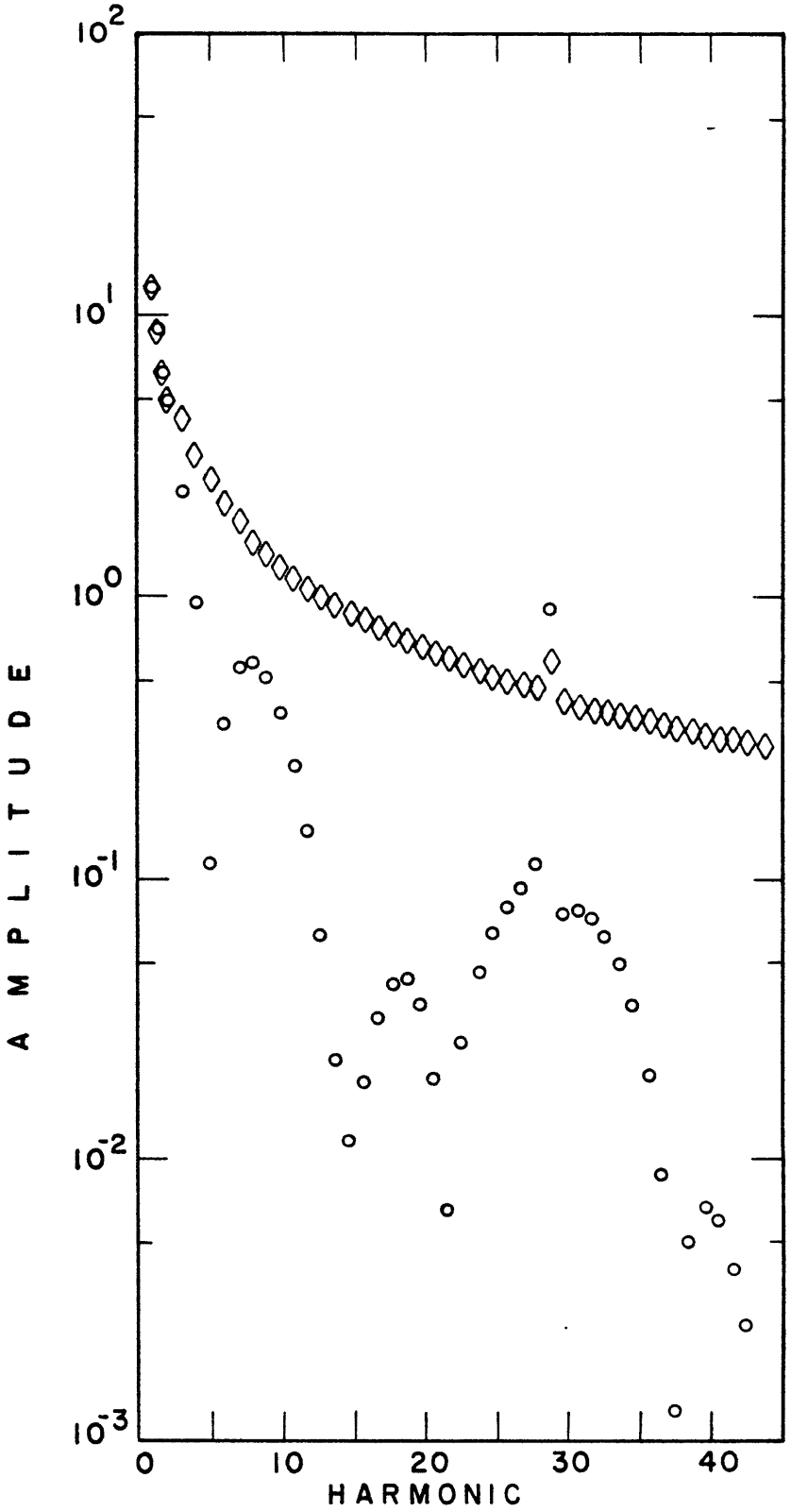


Figure A.1.3 Amplitude spectrum of a 15 day record consisting of a unit M_2 sine wave plus a 40-unit ramp, before tapering (diamonds) and after tapering (circles), showing the filtering effect of the tapering.

In this case the Fourier coefficient in the untapered case at M_2 frequency is less than the input wave, while in other cases the phases of the ramp and input sine wave could add and give a greater value there than the unput wave. The tapered ramp has insignificant energy at M_2 frequency, and the input sine wave can be completely recovered.

Appendix A.2 Signal processing

The general approach is called quasi-harmonic since the Fourier coefficients of current, temperature and equilibrium tide were inputs to further steps. The most general linear projection of a measured field s(t) onto the equilibrium tide $\zeta_e(t)$ can be written

$$s(t) = \int a(t') \, \zeta_e(t-t')dt' + n(t) \qquad (A.2.1)$$

where a(t) is the time domain admittance function and n(t) is uncorrelated noise. In the frequency domain, this gives

$$\hat{s}(\sigma) = \hat{a}(\sigma) \, \hat{\zeta}_e(\sigma) + \hat{n}(\sigma) \qquad (A.2.2)$$

Given a suitable ensemble, the admittance function $\hat{a}(\sigma)$ can be derived by averaging out the uncorrelated noise. Denote by <> an ensemble of Fourier coefficients derived from the measurements. Then multiplying expression A.2.2 by its complex conjugate and averaging gives the raw power in the process s(t) as

$$P_s = \langle (\hat{a}\hat{\zeta}_e + \hat{n})(\hat{a}^*\hat{\zeta}_e^* + \hat{n}^*) \rangle$$

$$= (\hat{a}\,\hat{a}^*)(\hat{\zeta}_e\,\hat{\zeta}_e^*) + \langle \hat{n}\,\hat{n}^* \rangle$$

$$= |\hat{a}|^2 \, P_{\zeta_e} + P_n \qquad (A.2.3)$$

This includes both the power correlated with the tidal forcing and the noise power. Define the coherence between the signal s and the equilibrium tide at a given frequency as

$$C = \frac{\langle \hat{s}(\sigma)\ \hat{\zeta}_e^*(\sigma) \rangle}{\langle \hat{s}(\sigma)\hat{s}^*(\sigma) \rangle^{1/2}\ \langle \hat{\zeta}_e(\sigma)\hat{\zeta}_e^*(\sigma) \rangle^{1/2}} \qquad (A.2.4)$$

Then it follows that

$$(\hat{a}\ \hat{a}^*)(\hat{\zeta}_e\hat{\zeta}_e^*) = C^2\ P_s \qquad (A.2.5)$$

is the correlated power, while

$$P_n = (1-C^2)\ P_s \qquad (A.2.6)$$

is the uncorrelated, or noise power. Since the equilibrium tide is a deterministic fuction, the power which is correlated with the equilibrium tide is in principle subject to prediction, as for the usual case of tidal prediction of sea level.

Of the possible forms of finite averages using the three basic inputs

$$\hat{s} = \hat{s} \exp(i\phi_s)$$

$$\zeta_e = \exp(i\phi_\zeta)$$

and a raw admittance

$$\hat{A} = |\hat{s}/\hat{\zeta}_e| \exp i(\phi_s - \phi_\zeta) = A \exp(i\phi_A)$$

a number were actually computed over the various ensembles. These were

Coherence I. $\langle \exp(i\phi_A) \rangle$ (A.2.7)

Coherence II. $$\frac{\langle \hat{s}\,\hat{\zeta}_e \rangle}{\langle \hat{s}\hat{s}^* \rangle^{1/2} \langle \hat{\zeta}_e \hat{\zeta}_e^* \rangle^{1/2}}$$ (A.2.8)

Admittance I. $\langle |\hat{A}| \exp(i\phi_A) \rangle$ (A.2.9)

Admittance II. $$\frac{\langle \hat{s}\hat{\zeta}_e^* \rangle}{\langle \hat{\zeta}_e \hat{\zeta}_e^* \rangle}$$ (A.2.10)

Average $\langle |\hat{s}| \exp(i\phi_A) \rangle$ (A.2.11)

Most of the discussion in the text is in terms of Coherence II. estimates, average currents or temperatures, and raw power. Coherence II. amplitude estimates from a finite sample have a statistical distribution which depends on the true coherence and the number of points in the average. Tables of this distribution by Amos and Koopmans (1963) allow the 95% confidence levels for zero true coherence and the given number of degrees of freedom to be evaluated to compare with the estimates actually derived. Coherence amplitude estimates are positively biased, with the actual bias also depending on the true coherence and the number of degrees of freedom. Coherence phase estimates are unbiased, with 95% confidence limits of about

$$\pm \quad 2.5 \{(|C|^{-2} - 1)/2N\}^{1/2} \qquad \text{(A.2.12)}$$

for estimates with N degrees of freedom (which we assume to be the same as the number of pieces) from a population with true coherence C. The actual numerical factor in A.2.12 varies slowly as a function of N and C, but the given value is fairly accurate for $\{(|C|^{-2} - 1)/2N\}^{1/2} < 2$ (Munk and Cartwright, 1966, Appendix B).

Depth (m)	Temperature (deg.C)	Salinity (ppt)	θ (deg.C)	σ_θ	N(z) (s^{-1})
0	16.58	34.57	16.58	25.30	$.14 \times 10^{-1}$
25	15.37	34.90	15.36	25.83	$.13 \times 10^{-1}$
50	14.24	35.17	14.23	26.29	$.92 \times 10^{-2}$
100	13.24	35.47	13.22	26.73	$.62 \times 10^{-2}$
150	12.40	35.51	12.38	26.93	$.54 \times 10^{-2}$
200	11.16	35.39	11.13	27.07	$.49 \times 10^{-2}$
300	8.62	35.14	8.59	27.31	$.45 \times 10^{-2}$
400	6.70	35.02	6.67	27.50	$.35 \times 10^{-2}$
500	5.54	34.98	5.49	27.62	$.27 \times 10^{-2}$
600	4.91	34.97	4.86	27.69	$.20 \times 10^{-2}$
700	4.62	34.97	4.56	27.72	$.16 \times 10^{-2}$
800	4.44	34.97	4.38	27.75	$.14 \times 10^{-2}$
900	4.29	34.97	4.22	27.76	$.13 \times 10^{-2}$
1000	4.15	35.97	4.07	27.78	$.92 \times 10^{-3}$
1100	4.06	34.96	3.97	27.78	$.91 \times 10^{-3}$
1200	3.98	34.96	3.89	27.79	$.10 \times 10^{-2}$
1300	3.92	34.96	3.82	27.80	$.10 \times 10^{-2}$
1400	3.84	34.96	3.73	27.80	$.11 \times 10^{-2}$
1500	3.76	34.96	3.64	27.81	$.99 \times 10^{-3}$
1600	3.70	34.96	3.57	27.82	$.10 \times 10^{-2}$
1700	3.64	34.96	3.50	27.83	$.97 \times 10^{-3}$
1800	3.58	34.96	3.43	27.84	$.96 \times 10^{-3}$
1900	3.51	34.96	3.36	27.84	$.10 \times 10^{-2}$
2000	3.44	34.96	3.28	27.85	$.97 \times 10^{-3}$
2100	3.37	34.96	3.20	27.85	$.11 \times 10^{-2}$
2200	3.28	34.96	3.10	27.86	$.11 \times 10^{-2}$
2300	3.19	34.95	3.00	27.87	$.11 \times 10^{-2}$
2400	3.09	34.95	2.90	27.87	$.11 \times 10^{-2}$
2500	2.99	34.94	2.79	27.88	$.11 \times 10^{-2}$
2600	2.93	34.94	2.71	27.89	-

Appendix Table 3.1 Average Site D hydrography 1965-19

Depth (m)	Temperature (deg.C)	Salinity (ppt)	θ (deg.C)	σ_θ	N (s^{-1})
0	17.37	34.55	17.37	25.10	$.12 \times 10^{-1}$
25	16.73	34.88	16.73	25.50	$.16 \times 10^{-1}$
50	14.86	35.15	14.85	26.14	$.10 \times 10^{-1}$
100	13.45	35.48	13.44	26.69	$.65 \times 10^{-2}$
150	12.23	35.44	12.21	26.91	$.60 \times 10^{-2}$
200	10.89	35.36	10.86	27.10	$.48 \times 10^{-2}$
300	8.50	35.13	8.47	27.32	$.44 \times 10^{-2}$
400	6.86	35.06	6.82	27.51	$.35 \times 10^{-2}$
500	5.71	35.01	5.67	27.62	$.27 \times 10^{-2}$
600	5.08	35.00	5.03	27.69	$.19 \times 10^{-2}$
700	4.73	34.99	4.68	27.72	$.16 \times 10^{-2}$
800	4.52	34.99	4.46	27.75	$.12 \times 10^{-2}$
900	4.37	34.98	4.30	27.76	$.13 \times 10^{-2}$
1000	4.24	34.98	4.16	27.77	$.10 \times 10^{-2}$
1100	4.13	34.97	4.05	27.78	$.10 \times 10^{-2}$
1200	4.05	34.97	3.96	27.79	$.10 \times 10^{-2}$
1300	3.96	34.97	3.86	27.80	$.11 \times 10^{-2}$
1400	3.87	34.97	3.76	27.81	$.10 \times 10^{-3}$
1500	3.79	34.97	3.67	27.82	$.91 \times 10^{-2}$
1600	3.73	34.97	3.60	27.82	$.11 \times 10^{-3}$
1700	3.67	34.97	3.53	27.83	$.94 \times 10^{-3}$
1800	3.60	34.97	3.45	27.84	$.98 \times 10^{-2}$
1900	3.52	34.96	3.37	27.84	$.11 \times 10^{-3}$
2000	3.45	34.96	3.28	27.85	$.98 \times 10^{-2}$
2100	3.36	34.96	3.19	27.86	$.11 \times 10^{-2}$
2200	3.27	34.96	3.10	27.86	$.10 \times 10^{-2}$
2300	3.18	34.95	3.00	27.87	$.11 \times 10^{-2}$
2400	3.10	34.95	2.90	27.87	$.10 \times 10^{-2}$
2500	3.01	34.94	2.80	27.88	$.92 \times 10^{-3}$
2600	2.95	34.94	2.74	27.88	-

Appendix Table 3.2 Average Site D hydrography 1971-1972.

Depth (m)	Temperature (deg.C)	Salinity (ppt)	θ (deg.C)	dθ/dz (mdeg.C/m)	N(z) (s^{-1})
10	26.69	36.44	26.69	43.	-
50	21.91	36.54	21.90	48.	$.98 \times 10^{-2}$
100	20.17	36.51	20.16	24.	$.70 \times 10^{-2}$
150	19.30	36.49	19.28	14.	$.65 \times 10^{-2}$
200	18.74	36.48	18.70	9.1	$.57 \times 10^{-2}$
250	18.30	36.48	18.25	8.7	$.47 \times 10^{-2}$
300	17.89	36.47	17.84	7.5	$.38 \times 10^{-2}$
350	17.55	36.45	17.49	6.8	$.31 \times 10^{-2}$
400	17.21	36.40	17.14	7.1	$.28 \times 10^{-2}$
450	16.81	36.33	16.83	9.8	$.32 \times 10^{-2}$
500	16.23	36.23	16.15	14.	$.38 \times 10^{-2}$
550	15.42	36.09	15.33	18.	$.42 \times 10^{-2}$
600	14.42	35.92	14.33	21.	$.45 \times 10^{-2}$
650	13.33	35.75	13.02	22.	$.48 \times 10^{-2}$
700	12.19	35.58	11.86	23.	$.48 \times 10^{-2}$
750	11.00	35.42	10.90	24.	$.48 \times 10^{-2}$
800	9.83	35.28	9.73	22.	$.46 \times 10^{-2}$
850	8.80	35.18	8.70	19.	$.46 \times 10^{-2}$
900	7.91	35.12	7.82	17.	$.43 \times 10^{-2}$
950	7.14	35.08	7.05	14.	$.41 \times 10^{-2}$
1000	6.53	35.06	6.44	11.	$.39 \times 10^{-2}$
1050	6.06	35.06	5.97	8.4	$.36 \times 10^{-2}$
1100	5.70	35.06	5.60	6.4	$.33 \times 10^{-2}$
1150	5.41	35.05	5.31	5.1	$.30 \times 10^{-2}$
1200	5.19	35.05	5.08	4.1	$.28 \times 10^{-2}$
1250	5.01	35.05	4.90	3.5	$.25 \times 10^{-2}$
1300	4.84	35.04	4.73	3.2	$.24 \times 10^{-2}$
1350	4.70	35.04	4.58	2.8	$.20 \times 10^{-2}$
1400	4.57	35.03	4.45	2.4	$.18 \times 10^{-2}$
1450	4.46	35.03	4.34	2.4	$.17 \times 10^{-2}$
1500	4.35	35.02	4.22	2.2	$.16 \times 10^{-2}$
2000	3.69	34.99	3.53	1.1	$.12 \times 10^{-2}$
2500	3.17	34.97	2.97	1.0	$.10 \times 10^{-3}$
3000	2.76	34.94	2.52	.83	$.95 \times 10^{-3}$
3500	2.48	34.92	2.19	.53	$.84 \times 10^{-3}$
4000	2.34	34.91	2.00	.23	$.54 \times 10^{-3}$
4500	2.31	34.90	1.90	.18	$.48 \times 10^{-3}$
4900	2.28	34.89	1.83	.26	$.49 \times 10^{-3}$
5400	2.16	34.86	1.65	.20	$.54 \times 10^{-3}$

Appendix Table A.3.3 Average hydrography of the MODE-1 site.

VITA

ROSS MACRAE HENDRY

Born: 1 May 1948, Geraldton, Canada.
Canadian citizen.

Marital Status: Single.

Education: Massachusetts Institute of Technology
Woods Hole Oceanographic Institution

Ph.D in Oceanography, April 1975.
Thesis supervisor Prof. Carl Wunsch.

University of Waterloo

B.Math. in Applied Mathematics, May 1970.

Research interests: Generation and energetics of oceanic baroclinic tides. Internal waves. Dynamics of the interaction of steady and unsteady flows with topography. Oceanic time series analysis.

Professional Associations: American Geophysical Union

Publications:

Hendry, Ross and Carl Wunsch, High Reynolds number flow past an equatorial island, J.Fluid Mech.,58,97-114 (1973)

Wunsch, Carl and Ross Hendry, Array measurements of the bottom boundary layer and the internal wave field on the continental slope, Geophys.Fluid Dynamics,4, 101-145 (1972)

Abstract:

Hendry, Ross, Phase stable baroclinic tides in the Sargasso Sea, Trans.Am.Geophys.Un.,56,1138 (1974)